

SPECTROSCOPY OF SMALL MOLECULES AND CLUSTERS

Victoria Louise Ayles

Submitted to the University of Nottingham
for the degree of Doctor of Philosophy

July 2008

Abstract

The $3s$, $3d$ and $4s$ Rydberg states of nitric oxide (NO), bound to a rare gas (Rg) atom in a van der Waals complex (NO–Rg), are probed using resonance-enhanced multiphoton ionisation, in order to investigate the effect of electronic excitation on these complexes. The spectroscopy is interpreted in terms of interactions between the Rydberg electron, the nitric oxide (NO^+) core and the Rg atoms. Larger NO–Rg_x clusters are investigated offering the prospect of bridging the spectroscopic gap between van der Waals dimers and the bulk. The spectroscopy is determined by an NO^+ –Rg₂ moiety and formation of the Rydberg state provokes a dynamic response from the Rg_x cluster, similar to that observed in matrix studies.

High-resolution zero electron kinetic energy spectroscopy is employed to derive vibrational frequencies of the *para*-fluorotoluene cation and assignments for previously unidentified (or in some cases, erroneously assigned) features have been presented. The first electronically-excited state of *para*-fluorotoluene (*p*FT), where a *p*FT chromophore is bound to several *p*FT molecules in a van der Waals cluster, has been studied. The effects of laser power and the internal temperature of the clusters on the fragmentation are considered.

A model potential analysis is carried out to determine whether binding in metal cation/rare gas (M^+ –Rg) complexes is physical (due to electrostatic, dispersion and induction interactions), or whether a chemical component (classical covalent interactions) must be considered. For alkali metal (Alk⁺)/Rg complexes, the model potential successfully describes the binding (the interaction is purely physical). For Au^+ –Rg, the model potential analysis reveals the emergence of a chemical component to the interaction, which becomes more significant as Rg gets larger.

Publications

Electronic spectroscopy of the 3*d* Rydberg states of NO–Rg (Rg = Ne, Ar, Kr, Xe) van der Waals complexes, D.E. Bergeron, A. Musgrave, R.T. Gammon, V.L. Ayles, J.A.E. Silber, T.G. Wright, B. Wen, H. Meyer, *J. Chem. Phys.* **124** (2006) 214302.

Electronic spectroscopy of NO–(Rg)_x complexes (Rg = Ne, Ar) via the 4*s* and 3*d* Rydberg states, D.E. Bergeron, A. Musgrave, V.L. Ayles, R.T. Gammon, J.A.E. Silber, T.G. Wright, *J. Chem. Phys.* **125** (2006) 144319.

Electronic spectroscopy of the $\tilde{E}^2\Sigma^+ \leftarrow \tilde{X}^2\Pi$ transition of NO–Kr and shielding/penetration effects in Rydberg states of NO–Rg complexes, B. Wen, H. Meyer, V.L. Ayles, A. Musgrave, D.E. Bergeron, J.A.E. Silber, T.G. Wright, *Phys. Chem. Chem. Phys.* **10** (2008) 375-379.

The $\tilde{A}^2\Sigma^+$ state of NO–Ne, V.L. Ayles, R.J. Plowright, M.J. Watkins, T.G. Wright, J. Klos, M.H. Alexander, P. Pajón-Suárez, J. Rubayo-Soneira, R. Hernández-Lemoneda, *Chem. Phys. Lett.* **441** (2007) 181-186.

Progress in understanding the intramolecular vibrational redistribution dynamics in the *S*₁ state of *para*-fluorotoluene, C.J. Hammond, V.L. Ayles, D.E. Bergeron, K.L. Reid, T.G. Wright, *J. Chem. Phys.* **125** (2006) 124308.

Zero electron kinetic energy spectroscopy of the *para*-fluorotoluene cation, V.L. Ayles, C.J. Hammond, D.E. Bergeron, O.J. Richards, T.G. Wright, *J. Chem. Phys.* **126** (2007) 244304.

Electronic spectroscopy of *para*-fluorotoluene clusters, D.E. Bergeron, V.L. Ayles, O.J. Richards, T.G. Wright, *Chem. Phys. Lett.* **430** (2006) 282-286.

Analysis of the bonding in alkali-cation/Rg complexes (Rg = He–Xe) using a simple model potential, W.H. Breckenridge, V.L. Ayles, T.G. Wright, *Chem. Phys.* **333** (2007) 77-84.

Evidence for Emergent Chemical Bonding in Au⁺–Rg Complexes (Rg = Ne, Ar, Kr, and Xe), W.H. Breckenridge, V.L. Ayles, T.G. Wright, *J. Phys. Chem. A* **112** (2008) 4209-4214.

Reinvestigation of the electronic spectroscopy of the Au–Ar complex, R.J. Plowright, V.L. Ayles, M.J. Watkins, A.M. Gardner, R.R. Wright, T.G. Wright, W.H. Breckenridge, *J. Chem. Phys.* **127** (2007) 294308.

Interaction potentials and transport properties of coinage metal cations in rare gases, A. Yousef, S. Shrestha, L.A. Viehland, E.P.F. Lee, B.R. Gray, V.L. Ayles, T.G. Wright, W.H. Breckenridge, *J. Chem. Phys.* **127** (2007) 154309.

Acknowledgements

First and foremost I wish to thank Tim Wright. It's been a pleasure to work with Tim; he's supported me throughout the last three years, he's always been willing to listen and has helped me through some of the tougher times. I owe a lot to Denis Bergeron. His infectious enthusiasm and passion for research made him a joy to work with.

I've had a lot of fun working with everyone in A40, and there are a number of people I've been glad to meet during my PhD, apologies if I've missed anyone out: Adrian Boatwright, Jay Jeffs, Owen Richards, James Silber, Richie Plowright, Chris Hammond, Paul Hockett and Julia Davies.

Contents

1 Introduction.....	18
1.1 Intermolecular forces.....	18
1.2 Rydberg states.....	21
1.3 Previous work on open-shell species.....	23
1.4 Previous work on ground state NO–Rg complexes.....	29
1.5 Implications of previous work on the present thesis.....	31
1.6 Research presented in the current thesis.....	32
1.7 References.....	33
2 Experiment.....	38
2.1 Van der Waals complex generation.....	38
2.2 Resonance-enhanced multiphoton ionisation.....	40
2.3 Zero electron kinetic energy spectroscopy.....	46
2.4 References.....	49
3 Electronic spectroscopy of the $3d\lambda$ Rydberg states of NO–Rg (Rg = Ne, Ar, Kr, Xe) van der Waals complexes.....	51
3.1 Introduction.....	51
3.1.1 $3d\lambda$ states in nitric oxide.....	51
3.1.2 Energetic ordering of the $3d\lambda$ states.....	51
3.1.3 Previous work on the lower Rydberg states.....	55
3.1.4 Previous work on the $3d\lambda$ Rydberg states.....	56
3.2 Experiment.....	59
3.2.1 Experimental set-up.....	59
3.2.2 Calibration.....	60

3.2.3 Rotational temperatures.....	65
3.3 Results.....	66
3.3.1 Spectral redshift.....	68
3.3.2 Convergence of the $\tilde{F}^2\Delta$ and $\tilde{H}^1\Pi$ states.....	69
3.3.3 NO–Xe.....	70
3.4 Discussion.....	72
3.4.1 $\tilde{F}^2\Delta$ and $\tilde{H}^1\Pi$ state origins and vibrational constant determination.....	72
3.4.1.1 $\tilde{F}^2\Delta$ state origin determination.....	72
3.4.1.2 $\tilde{H}^1\Pi$ state origin determination.....	75
3.4.1.3 $\tilde{H}^1\Pi$ state vibrational constant determination.....	76
3.4.2 $\tilde{F}^2\Delta$ and $\tilde{H}^1\Pi$ states.....	79
3.4.3 Predissociation of the $\tilde{H}^1\Pi$ state.....	82
3.4.4 Dissociation energies.....	85
3.4.5 Orientation effects.....	88
3.5 Conclusions.....	90
3.6 References.....	93
4 Electronic spectroscopy of NO–Rg _x complexes (Rg = Ne, Ar) via the 4s and 3d Rydberg states.....	96
4.1 Introduction.....	96
4.1.1 Previous work on NO in Ne and Ar matrices.....	96
4.1.2 Previous work on NO–Rg _x clusters.....	100
4.2 Experiment.....	102
4.3 Results.....	104
4.4 Discussion.....	106
4.4.1 Electronic structure NO–Ar _x (x = 1–6).....	106

4.4.2 Electronic structure NO–Ne _x (x = 1–2).....	110
4.4.3 Vibrational structure NO–Ne _x (x = 1–2).....	111
4.4.4 Vibrational structure NO–Ar _x (x = 1–6).....	115
4.4.5 Disappearance of the $\tilde{C}^2\Pi$ ($v' = 4$) and $\tilde{H}'^2\Pi$ bands.....	117
4.4.6 Implications of the present results for bulk studies.....	118
4.5 Conclusions.....	119
4.6 References.....	121
5 Electronic spectroscopy of the $\tilde{E}^2\Sigma^+ \leftarrow \tilde{X}^2\Pi$ transition of NO–Kr and shielding/penetration effects in Rydberg states of NO–Rg complexes.....	124
5.1 Introduction.....	124
5.1.1 Previous work on the $\tilde{E}^2\Sigma^+$ state of NO–Ne and NO–Ar.....	125
5.2 Experiment.....	128
5.2.1 Experimental set-up.....	128
5.2.2 Calibration.....	128
5.3 Results and discussion.....	130
5.3.1 NO–Kr $\tilde{E}^2\Sigma^+$ state.....	130
5.3.2 4s and 3d Rydberg states with $v_{\text{NO}} = 1$	139
5.4 Conclusions.....	145
5.5 References.....	147
6 The $3s\sigma \tilde{A}^2\Sigma^+$ Rydberg state of NO–Rg (Rg = Ne–Xe).....	149
6.1 Introduction.....	149
6.1.1 Previous work on the $\tilde{A}^2\Sigma^+$ state of NO–Rg (Rg = Ar–Xe)..	149
6.2 Experiment.....	156
6.2.1 Experimental set-up.....	156
6.2.2 Calibration.....	157

6.3 Results.....	159
6.4 Discussion.....	161
6.5 Theory.....	165
6.6 Conclusions.....	168
6.7 Conclusions from the study of NO–Rg Rydberg states.....	170
6.8 References.....	173
7 Zero electron kinetic energy spectroscopy of <i>para</i> -fluorotoluene.....	176
7.1 Introduction.....	176
7.1.1 Previous work on the S_1 state of <i>para</i> -fluorotoluene.....	177
7.1.2 Previous work on the <i>p</i> FT cation.....	179
7.2 Experiment.....	182
7.2.1 Experimental set-up.....	182
7.2.2 Calibration.....	183
7.3 Results.....	184
7.4 Discussion.....	201
7.4.1 Assignment of the spectra and the $\Delta v = 0$ propensity rule.....	201
7.4.2 Symmetry effects.....	203
7.4.3 $6a$ dominance.....	204
7.4.4 Unresolved $S_1(9b^1/16a^2)$ feature.....	206
7.4.5 Assignment of the 12^1 level.....	207
7.5 Conclusions.....	209
7.6 References.....	211
8 Electronic spectroscopy of <i>para</i> -fluorotoluene clusters.....	214
8.1 Introduction.....	214
8.2 Experiment.....	217
8.3 Results and discussion.....	218

8.3.1 Fragmentation.....	218
8.3.2 Spectroscopy.....	223
8.3.2.1 Structure in the dimer spectrum.....	223
8.3.2.2 Trends for pFT_n	226
8.3.3 Structural considerations.....	230
8.4 Conclusions.....	231
8.5 References.....	232
9 A simple model potential analysis of the bonding in alkali metal cation/Rg complexes (Rg = He–Xe) and Au^+ –Rg complexes (Rg = Ne, Ar, Kr, and Xe).....	235
9.1 Introduction.....	235
9.2 Model potential.....	237
9.3 Results and discussion.....	240
9.3.1 Alk^+ /Rg complexes.....	240
9.3.1.1 Damping functions.....	244
9.3.1.2 <i>Ab initio</i> calculational inaccuracies.....	244
9.3.1.3 Neglect of higher-order attractive terms in the model potential.....	245
9.3.1.4 Errors in C_6	245
9.3.1.5 The form of the repulsion term.....	245
9.3.1.6 Effects of polarisation of the outer-shell electron cloud of Rg towards Alk^+	246
9.3.2 Au^+ /Rg complexes.....	251
9.4 Conclusions.....	255
9.5 Future work.....	257
9.6 References.....	258

Figures

Figure 1(i): general form of an intermolecular potential energy curve.....	20
Figure 1(ii): radial distributions functions with respect to the electron-nucleus separation.....	22
Figure 1(iii): laser excitation spectrum of SH–Kr	26
Figure 1(iv): potential curves for ground and excited state NO–Ar.....	30
Figure 2(i): LIF (left-hand side) and REMPI (right-hand side) schematic.....	42
Figure 2(ii): schematic of the experimental set-up used for REMPI spectroscopy.....	43
Figure 2(iii): extraction grid configuration used to extract NO/Rg and <i>p</i> FT cluster ions in the REMPI experiments.....	44
Figure 2(iv): schematic of ZEKE spectroscopy.....	46
Figure 2(v): dye lasers and vacuum chambers used in the ZEKE experiment.....	48
Figure 2(vi): the voltages applied to the extraction grids and the MCP detector used in the ZEKE experiment.....	49
Figure 3(i): Rydberg states and non-Rydberg states of nitric oxide.....	52

Figure 3(ii): observed ordering (T_{obs}) of the $3d\lambda$ and $4s\sigma$ Rydberg states of NO. T^* shows ordering predicted by the long-range model.....	54
Figure 3(iii): (a) IR-REMPI spectrum exciting NO $v'' = 2$ and one quantum of intermolecular bend; (b) IR-REMPI spectrum exciting NO $v'' = 2$; (c) (2 + 1) REMPI spectrum of NO–Ar.....	57
Figure 3(iv): rotational energy levels of the $X^2\Pi$ and $E^2\Sigma^+$ states of NO, corresponding to Hund's coupling cases (a) and (b) respectively.....	63
Figure 3(v): (2 + 1) REMPI $E^2\Sigma^+$ state spectrum of NO used to calibrate data.....	64
Figure 3(vi): (2 + 1) REMPI spectra of NO and NO–Rg (Rg = Ne, Ar, Kr) showing the $3d$ and $4s$ Rydberg states.....	67
Figure 3(vii): $\tilde{F}^2\Delta$ and $\tilde{H}^2\Pi$ states of NO–Ar and NO–Kr recorded at low and high laser power.....	70
Figure 3(viii): REMPI spectrum recorded in the Xe^+ mass channel.....	71
Figure 3(ix): (2 + 1) REMPI spectrum of the $\tilde{F}^2\Delta$ and $\tilde{H}^2\Pi$ states of NO–Ar	73
Figure 3(x): expanded view of the (2 + 1) REMPI spectrum of NO–Ar shown in Figure 3(ix).....	74

Figure 3(xi): (2 + 1) REMPI spectrum of the $\tilde{F}^2\Delta$ state of NO–Kr, from the contemporaneous study of Meyer <i>et al.</i>	75
Figure 3(xii): (2 + 1) REMPI spectrum of the $\tilde{F}^2\Delta$ and $\tilde{H}^1\Pi$ states of NO–Kr.....	76
Figure 3(xiii): Birge-Sponer extrapolation to determine ω_e and $\omega_e x_e$ for NO–Kr $\tilde{H}^1\Pi$ state.....	78
Figure 3(xiv): observed relative energies (T_{obs}) of the $3d\lambda$ and $4s\sigma$ Rydberg states of uncomplexed NO. The change in energy of each state upon addition of a rare gas atom to the NO chromophore is shown ($T_{obs (NO-Rg)}$).....	80
Figure 3(xv): (2 + 1) REMPI spectrum of NO–Ar showing the $\tilde{F}^2\Delta$ and $\tilde{H}^1\Pi$ states, recorded using 2 mJ/pulse (low laser power) by H. Meyer <i>et al.</i>	82
Figure 3(xvi): (2 + 1) REMPI spectrum of NO–Ar showing the $\tilde{F}^2\Delta$ and $\tilde{H}^1\Pi$ states, recorded using a low laser power by H. Meyer and coworkers.....	83
Figure 3(xvii): (2 + 1) REMPI spectrum of NO–Kr showing the $\tilde{F}^2\Delta$ and $\tilde{H}^1\Pi$ states, recorded using a low laser power by H. Meyer and coworkers.....	84
Figure 3(xviii): orientation of the d_{yz} and d_{xz} orbitals with respect to the Rg atom in the two $3d\pi$ components of the $\tilde{H}^1\Pi$ state.....	89
Figure 3(xix): orientation of the $d_{x^2-y^2}$ and d_{xy} orbitals with respect to the Rg atom in the two $3d\delta$ components of the $\tilde{F}^2\Delta$ state.....	89

Figure 4(i): neutral NO–Ar _x (x = 1–6) geometries.....	100
Figure 4(ii): (2 + 1) REMPI spectra of the NO–Ar _x clusters (x = 1–6). The $\tilde{E}^2\Sigma^+$, $\tilde{F}^2\Delta$ and $\tilde{H}'^2\Pi$ states are shown, as are the vibrationally-excited $\tilde{C}^2\Pi$, $\tilde{D}^2\Sigma^+$ and $\tilde{E}^2\Sigma^+$ states.....	104
Figure 4(iii): (2 + 1) REMPI spectra of the NO–Ne _x clusters (x = 1–2). The $\tilde{E}^2\Sigma^+$, $\tilde{F}^2\Delta$ and $\tilde{H}'^2\Pi$ states are shown, as are the vibrationally-excited $\tilde{C}^2\Pi$ and $\tilde{E}^2\Sigma^+$ states.....	105
Figure 4(iv): (2 + 1) REMPI spectra of the $\tilde{E}^2\Sigma^+$ state of NO–Ne and NO–Ne ₂	111
Figure 4(v): two views of the optimised "cross" structure geometry of NO ⁺ –Ne ₂	113
Figure 4(vi): neutral NO–Ar ₂ and cationic NO ⁺ –Ar ₂ geometries.....	115
Figure 4(vii): (2 + 1) REMPI spectra of the NO–Ar _x (x = 1–2) $\tilde{E}^2\Sigma^+$ state.....	116
Figure 5(i): (2 + 1) REMPI spectrum of the $\tilde{E}^2\Sigma^+$ state of NO–Ne.....	125
Figure 5(ii): (2 + 1) REMPI spectrum of the $\tilde{E}^2\Sigma^+$ state of NO–Ar.....	127
Figure 5(iii): (3 + 1) REMPI spectrum recorded in the Xe ⁺ mass channel.....	130
Figure 5(iv): (2 + 1) REMPI spectra of the $\tilde{E}^2\Sigma^+$ state of NO–Ne, NO–Ar and NO–Kr with $\nu_{\text{NO}} = 0$	131

Figure 5(v): (2 + 1) REMPI spectrum of the $\tilde{E}^2\Sigma^+$ state of NO–Kr recorded in the present work, and a comparable spectrum collected by Meyer <i>et al.</i>	132
Figure 5(vi): simulated and experimental (2 + 1) REMPI spectra of the $\tilde{E}^2\Sigma^+$ ($v_{\text{NO}} = 0$) $\leftarrow \tilde{X}^2\Pi$ transition in NO–Kr, recorded by Meyer <i>et al.</i>	133
Figure 5(vii): the dimensions r_{NO} , $R_{\text{NO-Kr}}$, and the Jacobi angle θ , together with the a inertial axis for NO–Kr, used to simulate the $\tilde{E}^2\Sigma^+$ state (2 + 1) REMPI spectrum.....	136
Figure 5 (viii): (2 + 1) REMPI spectra of the NO–Kr $\tilde{E}^2\Sigma^+$ state, with $v_{\text{NO}} = 0$ and $v_{\text{NO}} = 1$	140
Figure 5(ix): (2 + 1) REMPI spectra of the NO–Ar $\tilde{F}^2\Delta$ and $\tilde{H}^2\Pi$ states, with $v_{\text{NO}} = 0$ and $v_{\text{NO}} = 1$	141
Figure 5(x): (2 + 1) REMPI spectra of the NO–Ne $\tilde{E}^2\Sigma^+$ state, with $v_{\text{NO}} = 0$ and $v_{\text{NO}} = 1$	141
Figure 6(i): (1 + 1) REMPI $\tilde{A}^2\Sigma^+$ state spectrum of NO–Ar.....	151
Figure 6(ii): (1 + 1) REMPI $\tilde{A}^2\Sigma^+$ state spectrum of NO–Kr.....	152
Figure 6(iii): (1 + 1) REMPI $\tilde{A}^2\Sigma^+$ state spectrum of NO–Xe.....	154
Figure 6(iv): (1 + 1) REMPI spectrum of the NO $A^2\Sigma^+$ state. The rotational lines $Q_{11}(1/2)$, $Q_{21}(1/2) + R_{11}(1/2)$ and $R_{21}(1/2)$ are labelled.....	157

Figure 6(v): (1 + 1) REMPI spectra of the $\tilde{A}^2\Sigma^+ \leftarrow \tilde{X}^2\Pi$ transition of NO and NO-Rg (Rg = Ar-Xe).....	160
Figure 6(vi): contour plot of the total electron density of the $A^2\Sigma^+$ state of NO.....	164
Figure 6(vii): contour plot of the total electron density of the $X^2\Pi$ state of NO.....	165
Figure 6(viii): calculated vibrational wavefunctions for the $\tilde{A}^2\Sigma^+$ state of NO-Ne for the $\nu = 0$ and $\nu = 1$ levels.....	167
Figure 6(ix): contour map (cm^{-1}) of the $\nu = 0$ levels of the $\tilde{X}^2\Pi$ and $\tilde{A}^2\Sigma^+$ states..	168
Figure 7(i): pictorial representations of the vibrational modes of a di-substituted benzene.....	176
Figure 7(ii): fluorescence excitation spectrum of <i>para</i> -fluorotoluene (<i>p</i> FT).....	178
Figure 7(iii): two-colour REMPI spectra of the S_1 state of <i>p</i> FT and <i>p</i> FT-Ar.....	179
Figure 7(iv): MATI spectra of <i>p</i> FT via $S_1(0^0)$ and $S_1(9b^1)$	181
Figure 7(v): (1 + 1) REMPI spectrum of <i>p</i> FT.....	186
Figure 7(vi): ZEKE spectrum recorded using the $S_1(0^0)$ level as the intermediate resonance.....	186

Figure 7(vii): ZEKE spectrum recorded using $S_1(6a^1)$ as the intermediate resonance.....	188
Figure 7(viii): ZEKE spectrum recorded using $S_1(1^1)$ as the intermediate resonance.....	188
Figure 7(ix): ZEKE spectrum recorded using $S_1(12^1)$ as the intermediate resonance.....	190
Figure 7(x): ZEKE spectrum recorded using $S_1(6a^2)$ as the intermediate resonance.....	190
Figure 7(xi): ZEKE spectrum recorded using $S_1(18a^1)$ as the intermediate resonance.....	191
Figure 7(xii): ZEKE spectra recorded using $S_1(13^1$ and $7a^1)$ as the intermediate resonances.....	192
Figure 7(xiii): ZEKE spectrum recorded using $S_1(11^1)$ as the intermediate resonance.....	194
Figure 7(xiv): ZEKE spectrum recorded using $S_1(6b^1)$ as the intermediate resonance.....	194
Figure 7(xv): ZEKE spectrum recorded using $S_1(15^1)$ as the intermediate resonance.....	196

Figure 7(xvi): top trace: (1 + 1) REMPI spectrum of the overlapped $S_1(9b^1/16a^2)$ features showing three energetic regions of this band probed (labelled I, II and III). Bottom three traces: ZEKE spectra recorded using three different regions (I, II and III) of the overlapped $S_1(9b^1/16a^2)$ levels as the intermediate resonances.....	197
Figure 7(xvii): (a) equilibrium geometry of neutral <i>para</i> -difluorobenzene (<i>p</i> DFB); arrows indicate atomic displacements upon ionisation magnified by 10; (b) equilibrium geometry of cationic <i>p</i> DFB; arrows indicate the eigenvector of ν_{6a} of the cation.....	206
Figure 8(i): (a) sandwich; (b) T-shaped and (c) parallel-displaced configurations of the benzene dimer.....	215
Figure 8(ii): (1 + 1) REMPI spectrum of the S_1 state of <i>p</i> FT.....	217
Figure 8(iii): mass spectra acquired at increasing delay between firing of the pulsed valve and firing of the laser.....	219
Figure 8(iv): (a) mass spectra collected at increasing laser power I–IV; (b) fragmentation pattern in the low-mass region of trace III.....	221
Figure 8(v): (1 + 1) REMPI spectra of <i>p</i> FT and (<i>p</i> FT) ₂ with expanded views of the higher energy regions – factors of ×3 and ×5 for <i>p</i> FT and (<i>p</i> FT) ₂ respectively...	225
Figure 8(vi): (1 + 1) REMPI spectra for (<i>p</i> FT) _{<i>n</i>} (<i>n</i> = 1–11).....	227
Figure 8(vii): J- and H-type dimer geometries for species with a donor and acceptor substituent in the <i>para</i> positions.....	230

Figure 9(i): comparison of the fitted, undamped model potential with the
calculated *ab initio* points for $\text{Li}^+\text{-He}$ and $\text{Cs}^+\text{-Xe}$243

Figure 9(ii): a plot of the induced dipole on the Rg atom (μ_{ind}) against $N \cdot \Delta R$ for
 $\text{Li}^+\text{-Rg}$, $\text{Na}^+\text{-Rg}$, $\text{K}^+\text{-Rg}$, $\text{Rb}^+\text{-Rg}$ and $\text{Cs}^+\text{-Rg}$, (Rg = He-Xe).....248

Tables

Table 1(I): experimentally derived ground and excited state dissociation energies for OH–Rg and SH–Rg.....	27
Table 1(II): measured bond lengths for OH–Rg and SH–Rg.....	28
Table 3(I): $\tilde{F}^2\Delta$ and $\tilde{H}'^2\Pi$ state origins and vibrational constants of NO and NO–Rg (Rg = Ne–Kr). $\tilde{F}^2\Delta$ and $\tilde{H}'^2\Pi$ state origins and vibrational constants of NO ⁺ –Rg are shown for comparison.....	79
Table 3(II): calculated dissociation energies of the $\tilde{F}^2\Delta$ and $\tilde{H}'^2\Pi$ states of NO–Ne, NO–Ar and NO–Kr.....	87
Table 5(I): atomic (3 + 1) Xe transitions used for calibration.....	129
Table 5(II): $\tilde{E}^2\Sigma^+$ state dissociation energies for NO–Ne, NO–Ar and NO–Kr with the corresponding cationic values. The stretch and bend frequencies (the 1–2 separation) for NO–Kr and the 0–1 spacings for the intermolecular stretch and bend for NO–Ne and NO–Ar are also shown, as are the harmonic stretch and bend frequencies for the cationic complexes NO ⁺ –Rg (Rg = Ne–Kr).....	138
Table 5(III): measured NO 0–1 vibrational spacings for the 4s and 3d Rydberg states of NO and NO–Rg, with errors of $\pm 1.5 \text{ cm}^{-1}$	143
Table 6(I): Rydberg state binding energy (D_0') in cm^{-1} with respect to Rg dipole polarisability (α_{Rg}) in \AA^3	171

Table 6(II): Rydberg state binding energy (D_0') in cm^{-1} with respect to the Rydberg orbit radius (r) in \AA	172
Table 6(III): NO 0–1 vibrational spacings for the 4s and 3d λ Rydberg states of NO and NO–Rg and NO^+	172
Table 7(I): <i>para</i> -fluorotoluene cationic vibrational level assignments made, with a brief description of the vibrational modes. The cationic vibrational frequencies derived in previous work and calculated frequencies are also presented.....	200
Table 9(I): values of A , b and Z for Li^+ –Rg (Rg = He–Xe) calculated using the model potential analysis with D_e , ω_e and R_e values determined from previous <i>ab initio</i> calculations. Values in parentheses are obtained employing damping functions.....	241
Table 9(II): values of A , b and Z for Na^+ –Rg (Rg = He–Xe) calculated using the model potential analysis with D_e , ω_e and R_e values determined from previous <i>ab initio</i> calculations. Values in parentheses are obtained employing damping functions.....	241
Table 9(III): values of A , b and Z for K^+ –Rg (Rg = He–Xe) calculated using the model potential analysis with D_e , ω_e and R_e values determined from previous <i>ab initio</i> calculations. Values in parentheses are obtained employing damping functions.....	242
Table 9(IV): values of A , b and Z for Rb^+ –Rg (Rg = He–Xe) calculated using the model potential analysis with D_e , ω_e and R_e values determined from previous <i>ab initio</i> calculations. Values in parentheses are obtained employing damping functions.....	242

Table 9(V): values of A , b and Z for $\text{Cs}^+\text{-Rg}$ ($\text{Rg} = \text{He-Xe}$) calculated using the model potential analysis with D_e , ω_e and R_e values determined from previous *ab initio* calculations. Values in parentheses are obtained employing damping functions.....243

Table 9(VI): calculated values of R_e , ΔR , $N \cdot \Delta R$, and induced-dipole moments (μ_{ind}) for the $\text{Alk}^+\text{/Rg}$ species ($\text{Alk}^+ = \text{Li}^+\text{-Cs}^+$, $\text{Rg} = \text{He-Xe}$).....249

Table 9(VII): values of A , b and Z for $\text{Au}^+\text{-Rg}$ ($\text{Rg} = \text{Ne-Xe}$) calculated by applying the undamped model potential analysis to the R_e , ω_e and D_e values calculated by T. G. Wright. Values shown in parentheses are obtained by incorporating damping functions into the model potential.....252

Table 9(VIII): effects on Z of successively deleting all but the R^{-4} terms in the model potential. Damped values are shown in parentheses.....253

1 Introduction

This thesis presents a series of spectroscopic studies of small molecules and clusters. The systems studied experimentally include the van der Waals complexes NO–Rg_x, where nitric oxide (NO) is bound to one or more rare gas (Rg) atoms, and the first electronically-excited state and the cationic ground state of para-fluorotoluene. A theoretical investigation of the binding of a singly-charged metal cation to a rare gas atom is also presented. The intermolecular forces present in the van der Waals complexes investigated herein will be discussed below.

The NO–Rg complexes, where the NO chromophore is excited to a number of low-lying Rydberg states form a significant proportion of the present thesis. An introduction to Rydberg states will be given below, together with a summary of work carried out on similar complexes, also containing an open-shell species. In addition, the work performed to date on the NO–Rg complexes where NO is in the electronic ground state will be described. Previous work relevant to the study of *p*FT and M⁺–Rg complexes will be confined to the appropriate chapters.

1.1 Intermolecular forces

The van der Waals complexes investigated herein are bound together not by chemical bonds, but by electrostatic interactions, which arise as a result of the distribution of charged particles within the atoms and molecules. There are three main attractive contributions to the interaction in a neutral van der Waals complex: a dipole/dipole (electrostatic) interaction (for molecules containing a permanent dipole moment), a dipole/induced-dipole (induction) interaction and an induced-dipole/induced-dipole (dispersion) interaction, all of which have an inversely proportional dependency on the separation between the charges, R . The electrostatic interaction arises between polar

molecules and the average potential energy of two rotating molecules, separated by a distance R varies with R^{-6} . The induction interaction exists between a polar molecule and a polarisable molecule, where the polar molecule induces a dipole in the latter;¹ the strength of the interaction depends on R^{-6} . Within polar and non-polar molecules the electron positions are changing and as a result form instantaneous dipoles that are constantly changing in magnitude and direction. The formation of an instantaneous dipole moment can induce a dipole in a neighbouring molecule resulting in a dispersion interaction; the strength of the dispersion interaction is dependent upon the polarisability of both molecules and is proportional to R^{-6} . Molecules often have a more complicated distribution of charge, for example, NO^+ has a quadrupolar distribution of charges and these higher-order multipoles can also contribute to the attractive interaction.

For a van der Waals complex between a charged and a neutral species (for example, a singly-charged metal cation, M^+ and a neutral Rg atom), the attractive interaction is dominated by the charge/induced-dipole interaction, the strength of which depends upon the charge on the ion and the polarisability of the neutral atom or molecule and varies with R^{-4} .

When the separation between the molecules is very short, the van der Waals interaction is dominated by a repulsive interaction, the magnitude of which increases dramatically with decreasing separation (R). There are three contributions to the repulsive interaction: the repulsion between the positively charged nuclei of the approaching molecules, the repulsion between the negatively charged electron cloud of the approaching molecules and, most importantly, the Pauli repulsion. The latter is pertinent when the electron clouds of the approaching atoms (or molecules) overlap, and restricts electrons of the same spin from sharing the same region of space. The general form of an intermolecular potential energy curve is shown in Figure 1(i).

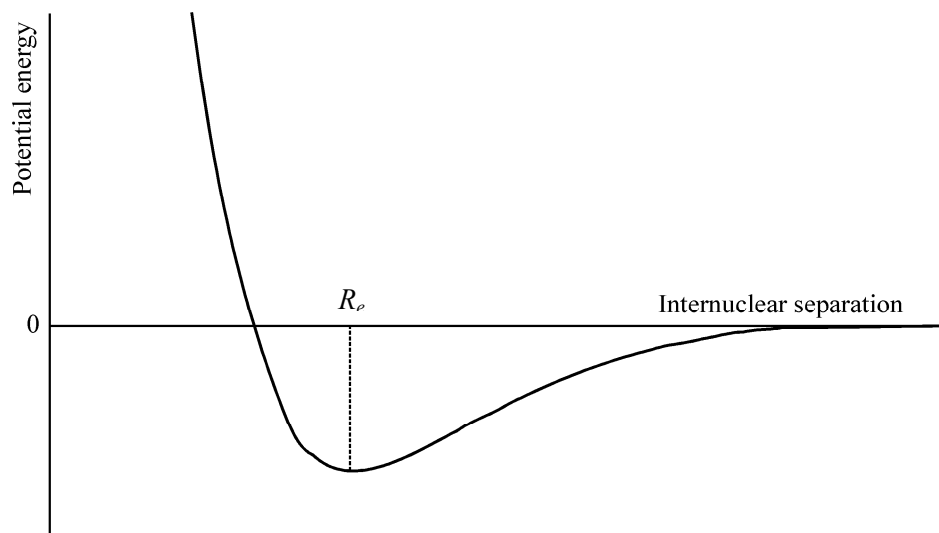


Figure 1(i): *general form of an intermolecular potential energy curve.*

As the molecules approach each other, the strength of the attractive interaction (with electrostatic, induction and dispersion contributions) increases. If the attractive interaction is sufficient to reduce the potential energy of the system to $V(R) < 0$ then a van der Waals complex will be formed, with a separation centred around the equilibrium intermolecular separation (R_e). At distances much lower than the equilibrium separation ($R \ll R_e$), the repulsive interaction will dominate. At a long separation, one power of R usually dominates (for example, the interaction between M^+ and Rg will be dominated by the ion/induced-dipole term, proportional to $1/R^4$); at smaller values of R where R is near to R_e , higher-order terms (representing contributions arising from the interactions of quadrupolar and higher-order multipoles) contribute to the attractive interaction to an increasing extent.² These long-range forces at still smaller values of R must be lessened ("damped") in order for the repulsive interaction to take effect as the internuclear separation shortens further.

1.2 Rydberg states

The majority of the experimental work performed as part of the present thesis has involved the formation and study of Rydberg states of NO, bound to a Rg atom in a van der Waals complex. Rydberg states are defined as a state where an electron has undergone a transition to an orbital that is large compared to the rest of the molecule,³ and can be approximated by a single electron orbiting a positively charged ion core. The energy (E) of a Rydberg state in a many-electron atom (in cm^{-1}), more specifically the energy required to remove the excited electron, is given by:³

$$E = R_H / (n - \delta)^2 \quad 1(a)$$

R_H is the Rydberg constant (in cm^{-1}), n is the principal quantum number and δ is the quantum defect. The Rydberg state energies vary with $1/n^2$ as for the hydrogen atom (for hydrogen $E = R_H/n^2$), although now the quantum defect must be considered. The quantum defect can be regarded as a measure of the interaction between the Rydberg electron and the ion core *i.e.* it represents the penetrating character of the electronic wavefunction. For hydrogen (and non-hydrogenic atoms where the Rydberg electron does not penetrate towards the ion core), the electron-core interaction is dominated by a Coulomb attraction. However, as the Rydberg electron becomes increasingly able to penetrate the inner electronic shells, it will experience a greater effective core charge (and will interact with electrons in the inner electronic shells). These effects are responsible for the differences between Rydberg states of the hydrogen atom and non-hydrogenic Rydberg states.⁴ The degree of penetration (and therefore the quantum defect) of the electronic wavefunction in the core region decreases as the orbital angular momentum (l) increases. The wavefunction gives the probability of finding an electron at a particular location, although it is useful to know the probability of finding

an electron at a given radius (*i.e.* distance from the core) regardless of the direction. This probability can be determined using the radial distribution function.⁵ Radial distributions functions for an *s*, *p* and *d* electron ($l = 0, 1$ and 2 respectively) are shown in Figure 1(ii). These relate the probability of finding each electron at a particular distance from the core⁵ and show that a *1s* electron is likely to be found nearer the core (it is more able to penetrate towards the core) than a *2p* or *3d* electron.

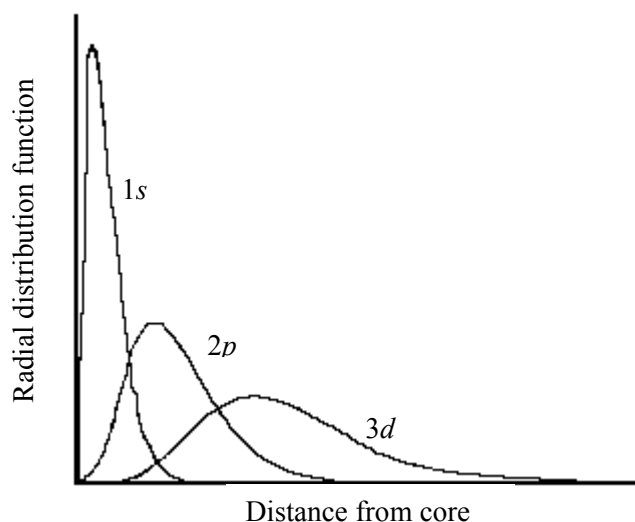


Figure 1(ii): *radial distributions functions with respect to the electron-nucleus separation.*

A comprehensive account of the properties and spectroscopy of low-*n* Rydberg states of NO has been given by Mulliken^{3,6,7} and Miescher *et al.*^{8,9} and more recently by Jungen,¹⁰ Meyer *et al.*^{11,12} and Sándorfy.¹³ The properties of Rydberg states vary rapidly with *n* and *l*: as *n* increases, the average distance between the electron and the core increases as n^2 and as *l* increases, the degree of penetration of the electronic wavefunction in the core region decreases (as shown in Figure 1(ii)). The *l* dependence of the quantum defect leads to Rydberg states in non-hydrogenic atoms and molecules forming several series, each characterised by their *l* value.⁴

1.3 Previous work on open-shell species

Nitric oxide is an open-shell molecule and represents the class of radicals with a single electron occupying an antibonding π^* -orbital.¹⁴ It is of relevance here to summarise the work involving the van der Waals complexes OH–Rg (where the OH radical represents a system with a triply filled π -orbital) and SH–Rg (S has the same valence electronic configuration as O) – OH and SH are also open-shell. The complexes NH–Rg and CH–Rg have also been investigated and the work reviewed by Heaven.¹⁵ These complexes are of interest since the effects of van der Waals forces are widespread – they determine many of the properties of liquids and molecular solids. As a result of the weak binding associated with these van der Waals complexes, few such systems exist under ambient conditions although by studying isolated complexes using a supersonic expansion (as in the present thesis), a detailed description of the interactions in such complexes can be derived.¹⁶

Of the X–Rg species, where X = OH, SH, NH or CH and Rg = Ne, Ar, Kr, the OH–Ar complex has received the most attention, both via experiment^{17, 18, 19, 20, 21, 22} and theory.^{23, 24, 25} In the experimental work on OH–Ar, laser-induced fluorescence (LIF) has been used to study the $\tilde{A}^2\Sigma^+ \leftarrow \tilde{X}^2\Pi$ electronic transition, a transition from the $\tilde{X}^2\Pi$ electronic ground state to the lowest energy Rydberg state $\tilde{A}^2\Sigma^+$, and rotationally resolved LIF excitation spectra have been obtained.¹⁷⁻²² The complexes OH–Ne and OH–Kr have also received attention.^{26, 27, 28, 29, 30} The $\tilde{A}^2\Sigma^+ \leftarrow \tilde{X}^2\Pi$ electronic transition in SH–Rg complexes has also been investigated experimentally using LIF.^{31, 32, 33, 34, 35} A review of the spectroscopy of OH–Rg, SH–Rg, CH–Rg and NH–Rg complexes is given in Reference 15 and the complexes OH–Rg and SH–Rg are discussed in Reference 16. The ground state ($\tilde{X}^2\Pi$) of the OH–Ar complex has been probed experimentally using stimulated emission spectroscopy³⁶ and the $\tilde{X}^2\Pi$

state of SH–Rg (Rg = Ne, Ar, Kr) complexes has been investigated using dispersed fluorescence,³⁷ although for both SH–Rg and OH–Ar complexes, it remains less well characterised experimentally than the $\tilde{A}^2\Sigma^+$ state. The ground state for the OH–Rg and SH–Rg complexes is the $\tilde{X}^2\Pi_{3/2}$ spin-orbit component, which lies lower in energy than the $\tilde{X}^2\Pi_{1/2}$ component. This is contrary to NO–Rg complexes, where the $\tilde{X}^2\Pi_{1/2}$ state lies lower in energy. In the cold environment of the supersonic expansion used in the present work and in the work on OH–Rg and SH–Rg, electronic transitions originate from the spin-orbit component which lies lower in energy. The following discussion will focus upon the lowest energy Rydberg state (the $\tilde{A}^2\Sigma^+$ state) of the OH–Rg and SH–Rg complexes and in particular on the vibrational structure observed in the LIF spectra of this state.

The analysis of the vibrational and rotational structure contained in the LIF spectra of the $\tilde{A}^2\Sigma^+ \leftarrow \tilde{X}^2\Pi$ electronic transition is necessary for understanding the electronic and geometric structure of the complexes. Some general statements can be made regarding the rotational and vibrational structure in the spectra, which apply to all but the most weakly bound complexes (OH–Ne and SH–Ne) and are exemplified in the review of Carter *et al.*,¹⁶ using the LIF $\tilde{A}^2\Sigma^+$ state spectrum of the SH–Kr complex (see below). The spectra are found to have a significant progression in the intermolecular van der Waals stretch vibration (between the diatom chromophore and the Rg atom). In addition, some van der Waals stretch-bend combinations are likely although their progressions are shorter and less intense.¹⁶ Rotational analysis of the vibrational structure shows that two categories of vibronic band exist, which arises as result of the bending motion (or hindered internal rotation) of the diatomic moiety and its projection along the internuclear axis.¹⁶ The first type of vibronic bands are attributable to the pure intermolecular stretch vibration or stretch-bend combinations, where there is no component of diatom rotational angular momentum along the

internuclear axis (the projection of rotational angular momentum is denoted by K). The second type of vibronic band is a stretch-bend combination (or rarely a pure bending vibration) with a projection K of diatom rotational angular momentum along the internuclear axis where $K \neq 0$.

The vibrational levels of the excited $\tilde{A}^2\Sigma^+$ state are denoted by $(v_{\text{XH/D}}, n^K, v_s)$, where $v_{\text{XH/D}}$ is the diatom stretch vibrational quantum number and $X = \text{O}$ or S , n^K describes the bending motion (or hindered internal rotation) of the diatomic moiety with quantum number n and projection (K) along the internuclear axis, and v_s is the quantum number associated with the van der Waals stretch vibration.¹⁶

The two types of vibronic bands were apparent in the laser-induced fluorescence study of Chang *et al.*²¹ who recorded rotationally-resolved spectra of the $\tilde{A}^2\Sigma^+$ state of OH–Ar with five quanta in the intermolecular van der Waals stretch vibration ($v_s = 5$); the authors labelled the two distinct vibronic bands A and U . The A band involves only excitation of the OH–Ar van der Waals stretch vibration; the U band involves the OH–Ar stretch vibration and at least one quantum of the bend (internal rotation of the OH moiety). The U band ($K \neq 0$) has a strong spin-rotation coupling effect (the electron spin angular momentum couples with the rotation of the diatom); the spin-rotation splittings are clearly visible. This splitting is not clearly resolved in the A bands.

The vibrational and rotational analysis of the $\tilde{A}^2\Sigma^+ \leftarrow \tilde{X}^2\Pi$ transition in SH–Kr was outlined in a review by Carter *et al.*,¹⁶ using the LIF spectrum of Yang *et al.*,³⁴ shown in Figure 1(iii). Three progressions were identified, the first of which is the van der Waals stretch vibration, labelled v_A in Figure 1(iii). Two additional progressions were present, which had rotational contours consistent with the U band in the OH–Ar LIF spectrum of Chang *et al.*²¹ These progressions, labelled v_α and v_β were therefore

assigned to stretch-bend combination bands, involving hindered rotation of the SH moiety.

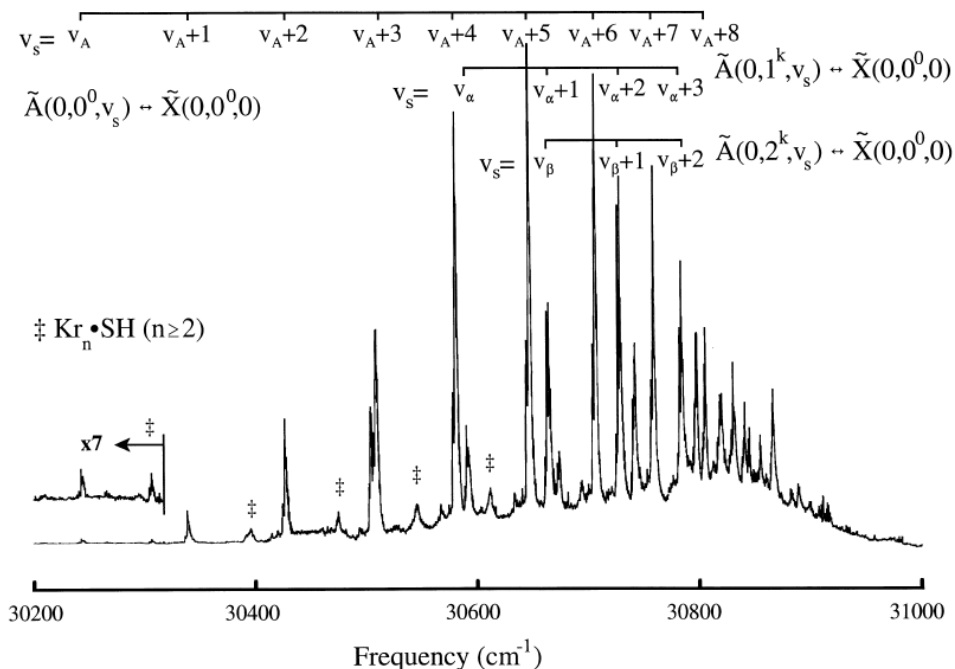


Figure 1(iii): laser excitation spectrum of SH–Kr from the LIF study of Yang *et al.*,³⁴ taken from Reference 16.

Although it is possible to assign a vibrational progression to the intermolecular stretch, or to a stretch-bend combination using a rotational analysis, it is not possible to assign specific vibrational quantum numbers. Isotopic substitutions are typically used for such purposes, although are not relevant to the present thesis and will not be discussed herein. The assignment of specific quantum numbers to members of a vibrational progression allows the dissociation energy of the complexes in the excited state ($\tilde{A}^2\Sigma^+$) to be determined, which can be compared with those for the ground state complexes. The ground and excited state dissociation energies for the OH–Rg and SH–Rg (Rg = Ne, Ar, Kr) complexes are given in Table 1(I).¹⁶

Complex	D_0''	D_0'
OH-Ne	28 ^a	47-52
SH-Ne	13-35	22-44
OH-Ar	107	717
SH-Ar ^b	83	458
OH-Kr	117	1752
SH-Kr ^c	104	1273

Table 1(I): *experimentally derived ground and excited state dissociation energies taken from Reference 16; (a) Reference 38; (b) Reference 17; (c) Reference 27. Data for the SH-Rg complexes is taken from Reference 34. All values given in cm^{-1} .*

For a given rare gas, the OH-Rg complex has a greater excited state dissociation energy than the analogous SH-Rg complex, indicating a much stronger bond. As the rare gas is varied from Ne to Kr in either OH or SH complexes, the bond strength increases rapidly: for the $\tilde{A}^2\Sigma^+$ state of the Kr and Ar complexes, the bonding between the open-shell radical and Rg is strong ($>1000 \text{ cm}^{-1}$ in the Kr complexes), the $\tilde{A}^2\Sigma^+$ states of the Ne complexes indicate a weaker bond. The ground states of all the species have much lower dissociation energies in comparison to the excited state; the trend of a stronger bond in the OH-Rg versus SH-Rg complex is still observed though to a lesser extent. The difference in dissociation energy between the excited and ground states is significant for all the species except for the Ne complexes which have only a slightly stronger bond in the excited $\tilde{A}^2\Sigma^+$ state.¹⁶

Rotational analyses of the LIF spectra for OH-Rg and SH-Rg have provided the bond length between the Rg atom and the centre of mass of the diatom.^{21,22,27,28,32,33} The

bond lengths for the OH–Rg and SH–Rg complexes are shown in Table 1(ii), taken from Reference 16. The excited state bond lengths are determined for the (0, 0⁰, 0) band.

Complex	State	Ne	Ar	Kr
OH–Rg	$\tilde{X}^2\Pi$	3.6884 ^a	3.7049 ^c	3.7814 ^e
	$\tilde{A}^2\Sigma^+$	3.1635 ^a	2.8961 ^c	2.8060 ^e
SH–Rg	$\tilde{X}^2\Pi$	4.2116 ^b	4.2093 ^d	4.2771 ^d
	$\tilde{A}^2\Sigma^+$	3.8928 ^b	3.4613 ^d	3.2950 ^d

Table 1(II): *measured bond lengths taken from Reference 16 and calculated using data presented in (a) Reference 28; (b) Reference 32; (c) Reference 22; (d) Reference 33; (e) Reference 27. All values given in Å.*

In the excited state the diatom–Rg bond length decreases on going from Ne to Kr despite the large increase in the Rg van der Waals radius (1.54 Å, 1.88 Å and 2.02 Å for Ne, Ar and Kr respectively).³⁹ This demonstrates the strong bonding in the heavier Rg complexes (as seen from the D_0' values given in Table 1(I)), which compensates for the increasing van der Waals radius of the Rg atom.

In the ground state, the bond length decreases on going from Ne to Kr, although it is considerably smaller than would be expected from the increase in the van der Waals radius of the Rg atom. In the $\tilde{X}^2\Pi$ state, as for the $\tilde{A}^2\Sigma^+$ state, the bond lengths for the OH complexes are shorter than those for the SH complexes, indicative of the increased binding energy in the former.

1.4 Previous work on ground state NO–Rg complexes

In the work performed as part of the present thesis, a number of low-lying Rydberg states of NO are prepared following an electronic excitation from the electronic ground state, where the NO chromophore is bound to one or more Rg atoms. The electronic spectra of these species, as for the OH–Rg and SH–Rg complexes discussed above, will contain vibrational structure associated with the complex. In order to assign this structure it is necessary to consider the geometry change as a result of excitation, which necessitates a knowledge of the ground state complex geometry.

The first spectroscopic observation of the NO–Ar complex was reported in the laser-induced fluorescence (LIF) study of Langridge-Smith *et al.*⁴⁰ They identified a broad feature lying to lower energy of the band origin of the $\tilde{A}^2\Sigma^+ \leftarrow \tilde{X}^2\Pi$ transition in the monomer spectrum. This feature was attributed to transitions from the electronic ground state of the complex terminating on the repulsive wall of the excited state surface; in Reference 40 the authors suggest that the NO–Ar potential in the $\tilde{A}^2\Sigma^+$ state is shifted so that the repulsive wall lies above the minimum of the ground state potential. Such bound-free transitions were also observed in the work of Miller *et al.*^{41,42}

The first direct observation of bound rotational levels in the electronic ground state was accomplished by Mills *et al.* for NO–Ar⁴³ and NO–Rg.⁴⁴ The rotational structure of the observed microwave spectrum was analysed to give a near T-shaped structure for the NO–Ar complex, with an averaged bond distance of 3.71 Å and a bond angle of 85°. The bond angle is defined as the angle between the N–O bond and the vector between the Ar atom and the centre of mass of NO. This geometry was originally established in the collision studies of Thuis *et al.*^{45,46} Bound levels of the complex

involving intermolecular vibrations have been observed in an IR-REMPI double resonance experiment.⁴⁷

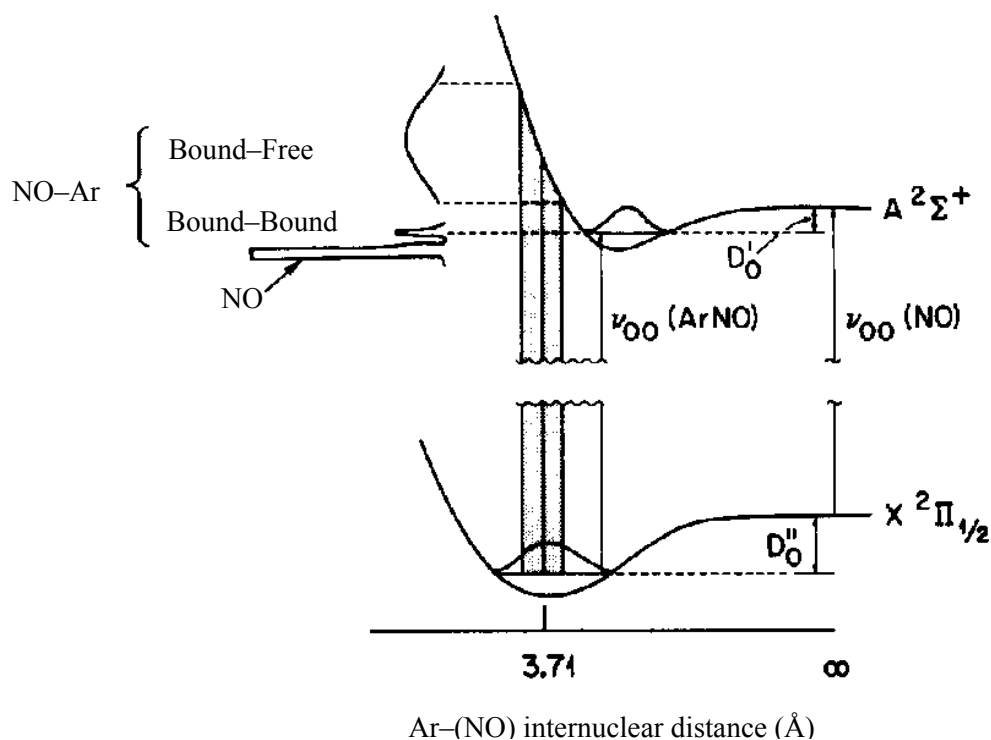


Figure 1(iv): adapted from Reference 48. Potential curves for ground and excited state NO–Ar given with respect to the van der Waals stretch coordinate, where NO–Ar is treated as a pseudodiatom molecule.

Using the experimentally determined bond length for the NO–Ar $\tilde{X}^2\Pi$ state, Miller⁴⁸ presented a schematic representation of the $\tilde{X}^2\Pi$ and $\tilde{A}^2\Sigma^+$ state NO–Ar potentials. The bound-free transitions observed using LIF by Langridge-Smith and coworkers⁴⁰ and multiphoton absorption by Miller *et al.*,^{41,42} which constitute the first experimental observations of the NO–Rg complexes are shown in Figure 1(iv).⁴⁸

1.5 Implications of previous work on the present thesis

The Rydberg states of NO–Rg van der Waals complexes probed in this work correspond to transitions of the outermost $2p\pi^*$ electron in NO to the $3s$, $3d$ and $4s$ orbitals. A transition to the lowest energy Rydberg state for the NO–Ne complex has yet to be observed experimentally. The binding in OH–Ne and SH–Ne in the $\tilde{A}^2\Sigma^+$ state was found^{16,33} to be weak and as a result the long progression of the van der Waals stretch vibration seen in the $\tilde{A}^2\Sigma^+$ state spectra of the more strongly-bound complexes (OH or SH with Ar or Kr) was not observed.³² The aim of the present thesis is to attempt to record this transition ($\tilde{A}^2\Sigma^+ \leftarrow \tilde{X}^2\Pi$) in NO–Ne and use the successful recording of this transition in other NO–Rg complexes to investigate the nature of the interaction in the $\tilde{A}^2\Sigma^+$ state.

The preparation of Rydberg states with different l (orbital angular momentum) and therefore different quantum defects, allows the effect of Rydberg electron penetration on the NO–Rg interaction to be probed. Interactions between the $3d$ Rydberg electron and the NO^+ core are well documented (a review of these interactions is given in Chapter 3); the effect that potential interactions between the $3d$ Rydberg electron and the Rg atom may have on the spectroscopy of these complexes is less well known. In order to elucidate a more detailed account of the interactions between the weakly-penetrating $3d$ Rydberg electron and a Rg atom, the $3d$ Rydberg states of NO–Rg (Rg = Ne, Ar, Kr, Xe) complexes are investigated.

The $\tilde{E}^2\Sigma^+ \leftarrow \tilde{X}^2\Pi$ transition has been observed for the complexes NO–Ne and NO–Ar (a review of previous work on this Rydberg state is given in Chapter 5) although not for the heavier NO–Kr complex. In order to examine the trends in the binding of

the $\tilde{E}^2\Sigma^+$ state as the Rg atom increases in size and polarisability, an attempt will be made to observe this transition in NO–Kr.

The binding in the electronically-excited states of NO–Rg complexes can be broadly interpreted according to the size of the Rydberg orbit in comparison with the average NO–Rg separation.¹⁴ When the Rydberg orbit is smaller than the average separation between the NO chromophore and the Rg atom, the interaction is weak and dominated by dispersion forces. In contrast, a large Rydberg orbit radius will lead to a stronger attractive induction interaction. The low- n Rydberg states of NO–Rg complexes investigated herein offer the opportunity to study this transition from dispersion dominated bonding to ion-induced interactions.

1.6 *Research presented in the current thesis*

As a stable open-shell molecule, the interaction of NO (both in the electronic ground state and in electronically-excited states) with closed-shell Rg atoms is considered a prototype for the study of van der Waals interactions involving open-shell molecules. In the present thesis, NO is excited to a number of electronically-excited states in order to investigate how the electronic excitation affects these interactions. The interaction of electronically-excited NO with more than one Rg atom is also investigated; this offers the prospect of bridging the spectroscopic gap between van der Waals dimers and the bulk.

A spectroscopic study of para-fluorotoluene (p FT) has been performed, where the assignment of vibrational levels of the p FT cation, together with their energies is presented for the first time. The high resolution offered by the spectroscopic technique employed reveals spectral details that were previously inaccessible. The assignment of

vibrational levels (and their energies) in the first electronically-excited state (S_1) of neutral p FT, also presented in this work provides independent confirmation of previously reported assignments. In addition, the observation of several p FT molecules bound together in a van der Waals cluster, allows the effect of complexation (and the fragmentation of these relatively large, weakly-bound clusters) on the electronic excitation of a single p FT chromophore to be investigated.

In addition to the experimental work described above, a theoretical investigation of the interaction between a singly-charged metal ion (M^+) and a Rg atom is presented. The interaction between a single M^+ cation and a single solvent atom is the most straightforward to probe, and the understanding of interactions present in such a system necessitates the understanding of interactions between M^+ and multiple solvated atoms. In particular, the work presented herein focuses on whether the interaction in the M^+ /Rg van der Waals dimer can be described by purely "physical" bonding (where M^+ and Rg are bound by an electrostatic and dispersive attraction), or whether an additional "chemical" component exists (where M^+ and Rg are bound together by a covalent interaction). The interaction of a singly-charged metal ion with a single atom or molecule is important for many areas (for example, for understanding the ion transport properties of M^+ ions in low-pressure plasma discharges) hence this investigation is applicable to many different fields.

1.7 References

¹ P.W. Atkins, *Physical Chemistry, Seventh Edition*, Oxford University Press, Oxford, (1986) pp. 857.

² J. Koperski, *Phys. Rep.* **369** (2002) 177-326.

- ³ R.S. Mulliken, *J. Am. Chem. Soc.* **86** (1964) 3183.
- ⁴ F. Merkt, *Annu. Rev. Phys. Chem.* **48** (1997) 675-709.
- ⁵ P. Atkins, R. Friedman, *Molecular Quantum Mechanics, Fourth Edition*, Oxford University Press, Oxford, (2007) pp. 573.
- ⁶ R.S. Mulliken, *J. Am. Chem. Soc.* **88** (1966) 1849.
- ⁷ R.S. Mulliken, *J. Am. Chem. Soc.* **91** (1969) 4615.
- ⁸ K.P. Huber, E. Miescher, *Helv. Phys. Acta.* **37** (1963) 257-268.
- ⁹ K. Dressler, E. Miescher, *Astrophys. J.* **141**(1964) 1266-1283.
- ¹⁰ Ch. Jungen. *J. Chem. Phys.* **53** (1970) 4168-4182.
- ¹¹ H. Meyer, *J. Chem. Phys.* **107** (1997) 7721-7731.
- ¹² Y. Kim, H. Meyer, *Chem. Phys.* **301** (2004) 283-292.
- ¹³ C Sándorfy , *The Role of Rydberg States in Spectroscopy and Photochemistry: Low and High Rydberg States*, Springer-Verlag New York, (1999) pp. 540.
- ¹⁴ Y. Kim, H. Meyer, *Int. Rev. Phys. Chem.* **20** (2001) 219-282.
- ¹⁵ M.C. Heaven, *J. Phys. Chem.* **97** (1993) 8567-8577.

- ¹⁶ C.C. Carter, *J. Mol. Struct.* **525** (2000) 1-45.
- ¹⁷ W.M. Fawzy, M.C. Heaven, *J. Chem. Phys.* **92** (1990) 909-916.
- ¹⁸ M.T. Berry, M.R. Brustein, J.R. Adamo, M.I. Lester, *J. Phys. Chem.* **92** (1988) 5551.
- ¹⁹ M.T. Berry, M.R. Brustein, M.I. Lester, *J. Chem. Phys.* **90** (1989) 5878-5879.
- ²⁰ W.M. Fawzy, M.C. Heaven, *J. Chem. Phys.* **89** (1988) 7030-7031.
- ²¹ B.-C. Chang, J.M. Williamson, D.W. Cullin, J.R. Dunlop, T.A. Miller, *J. Chem. Phys.* **97** (1992) 7999-8008.
- ²² B.-C. Chang, L. Yu, D. Cullen, B. Rehfuss, J. Williamson, T.A. Miller, W.M. Fawzy, X. Zheng, S. Fei, M. Heaven, *J. Chem. Phys.* **95** (1991) 7086-7098.
- ²³ C. Chakravarty, D.C. Clary, A. Deglei-Esposti, H.-J. Werner, *J. Chem. Phys.* **93** (1990) 3367-3378.
- ²⁴ J. Klos, M.H. Alexander, M. Brouard, C.J. Eyles, F.J. Aoiz, *J. Chem. Phys.* **129** (2008) 054301.
- ²⁵ J.M. Bowman, B. Gazdy, P. Schafer, M.C. Heaven, *J. Phys. Chem.* **94** (1990) 2226-2229.
- ²⁶ B.-C. Chang, D.W. Cullen, J.W. Williamson, J.R. Dunlop, B.D. Rehfuss, T.A. Miller, *J. Chem. Phys.* **96** (1992) 3476-3483.

- ²⁷ C.C. Carter, T.A. Miller, H.-S. Lee, P.P. Korambath, A.B. McCoy, E.F. Hayes, *J. Chem. Phys.* **110** (1999) 1508-1520.
- ²⁸ B.-C. Chang, J.R. Dunlop, J.M. Williamson, T.A. Miller, *J. Opt. Soc. Am. B* **11** (1994) 198-207.
- ²⁹ H.-S. Lee, A.B. McCoy, L.B. Harding, C.C. Carter, T.A. Miller, *J. Chem. Phys.* **111** (1999) 10053-10060.
- ³⁰ G.W. Lemire, R.C. Sausa, *J. Phys. Chem.* **96** (1992) 4821-4824.
- ³¹ M.-C. Yang, A.P. Salzberg, B.-C. Chang, C.C. Carter, T.A. Miller, *J. Chem. Phys.* **98** (1993) 4301-4304.
- ³² C.C. Carter, T.A. Miller, H.-S. Lee, A.B. McCoy, E.F. Hayes, *J. Chem. Phys.* **110** (1999) 5065-5078.
- ³³ C.C. Carter, T.A. Miller, *J. Chem. Phys.* **107** (1997) 3447-3459.
- ³⁴ M.-C. Yang, C.C. Carter, T.A. Miller, *J. Chem. Phys.* **107** (1997) 3437-3446.
- ³⁵ B.E. Applegate, M.-C. Yang, T.A. Miller, *J. Chem. Phys.* **109** (1998) 162-169.
- ³⁶ M.T. Berry, R.A. Loomis, L.C. Giancarlo, M.I. Lester, *J. Chem. Phys.* **96** (1992) 7890-7903.
- ³⁷ M.-C. Yang, C.C. Carter, T.A. Miller, *J. Chem. Phys.* **110** (1999) 7305-7315.

- ³⁸ B.-C. Chang, J.R. Dunlop, J.M. Williamson, M.C. Heaven, T.A. Miller, *Chem. Phys. Lett.* **207** (1993) 62.
- ³⁹ A. Bondi, *J. Phys. Chem.* **68**(3) (1968) 441.
- ⁴⁰ P.R.R. Langridge-Smith, E. Carrasquillo, D.H. Levy, *J. Chem. Phys.* **74** (1981) 6513.
- ⁴¹ J.C. Miller, W.C. Cheng, *J. Phys. Chem.* **89** (1985) 1647.
- ⁴² J.C. Miller, *J. Chem. Phys.* **86** (1987) 3166.
- ⁴³ P.D.A. Mills, C.M. Western, B.J. Howard, *J. Phys. Chem.* **90** (1986) 4961.
- ⁴⁴ P.D.A. Mills, C.M. Western, B.J. Howard, *J. Phys. Chem.* **90** (1986) 3331.
- ⁴⁵ H. Thuis, S. Stolte, J. Reuss, *Chem. Phys.* **43** (1979) 351.
- ⁴⁶ H. Thuis, S. Stolte, J. Reuss, J.J.H. van den Biesen, C.J.N. van den Meijdenberg, *Chem. Phys.* **52** (1980) 211.
- ⁴⁷ Y. Kim, K. Patton, J. Fleniken, H. Meyer, *Chem. Phys. Lett.* **318** (2000) 522.
- ⁴⁸ J.C. Miller, *J. Chem. Phys.* **90** (1989) 4031-4036.

2 Experiment

In the present thesis, two spectroscopic techniques are employed. Resonance-enhanced multiphoton ionisation (REMPI) spectroscopy is used to investigate the interaction of electronically-excited NO bound with one or more Rg atoms, and to probe the first electronically-excited state of *para*-fluorotoluene, bound to several *p*FT molecules in a van der Waals cluster. Zero electron kinetic energy (ZEKE) spectroscopy is employed in order to derive vibrational frequencies of the *p*FT cation. In the following is an account of how these van der Waals complexes are formed, together with a description of the REMPI and ZEKE experiments employed to probe the excited states of NO/Rg and *p*FT van der Waals complexes and larger clusters, and the electronic ground state of the *p*FT cation.

2.1 Van der Waals complex generation

The weakly-bound van der Waals complexes investigated in this thesis are generated by the expansion of an appropriate, high-pressure gas mixture (either NO in the rare gas of interest, or by passing Ar gas through a liquid sample of *p*FT) through a narrow aperture into a vacuum. If the ratio of the aperture diameter to the pressure of the gas mixture before it passes through the aperture is appropriate, then a free-jet expansion is formed. More specifically, if the aperture diameter $d \gg \lambda$ where λ is the mean free path (the average distance travelled by a gas particle between collisions, which is inversely proportional to the pressure), then a free-jet expansion will result.

A free-jet expansion is characterised by a highly directional flow of particles with a narrow range of velocities, and is generated if the gas pressure is high enough to result in collisions between species in and just beyond the nozzle, leading to cooling of the internal energy of the particles.^{1,2} The resulting free-jet expansion will have a

rotational and vibrational temperature as well as a translational temperature, which is related to the spread of the molecular speeds in the expansion and can be as low as 1 K.³ Rotational temperatures of < 10 K are common. Vibrational cooling is less efficient and vibrational temperatures of 20–50 K are typical, although this cooling is sufficient to stabilise weakly-bound complexes. Temperature in this context is defined as the temperature that describes the Boltzmann population distribution amongst the pertinent energy levels.¹ The advantage of using such a method to generate species for spectroscopic investigation is that the very low pressures involved result in little or no pressure broadening of the spectroscopic line widths, leading to improved resolution. Also, if detection is carried out perpendicularly to the direction of the expansion, the narrow range of one-dimensional velocities of the expansion will lead to a reduction in Doppler broadening.

The term "supersonic expansion" is derived from the fact that the particles in the free-jet expansion have a velocity very much higher than the local speed of sound. Their speed is expressed in terms of a Mach number M , defined as the velocity of the particles in the expansion v , relative to the local speed of sound a , $M = v/a$. If $M > 1$ the expansion is supersonic.² The local speed of sound is proportional to the translational temperature (T_{Tr}) of the expansion, and the very low values of T_{Tr} resulting from supersonic expansion of a gas lead to the very high Mach numbers of such expansions (M can be as high as 100).¹ To avoid disruption of the free-jet expansion, and a subsequent increase of T_{Tr} , a skimmer, or collimator, can be placed in the expansion path. This disruption may occur from collisions between the background gas in the vacuum chamber and particles that deviate from the main expansion path.² By maintaining a low background pressure, such disruption can be minimised so that a skimmer may not be necessary. (Note that the term molecular beam is appropriate if a skimmer is employed. If this is not the case, as in this work, then the resulting flow is more correctly known as a free-jet expansion.)

Clustering takes place as the gas passes through the nozzle and in the region of the supersonic expansion lying just beyond the nozzle where collisions are still occurring. Initial clustering will proceed through three-body associations with the excess energy from the collision carried away by the third-body. For example with Ar:



The cluster may continue to grow by three-body reactions until it reaches a size that is large enough to absorb the energy of the collision where then it may continue to grow by two-body associations.²

2.2 Resonance-enhanced multiphoton ionisation

The excited states of NO bound to one or more Rg atoms in a van der Waals complex, and the first excited state of *p*FT bound to other *p*FT molecules in a van der Waals cluster are probed using resonance-enhanced multiphoton ionisation (REMPI) spectroscopy. REMPI spectroscopy will be described below and compared to laser-induced fluorescence, which can also be applied to the systems investigated herein.

Electronic transitions can be probed using a laser spectroscopic technique such as laser-induced fluorescence (LIF). One of the requirements for LIF to be successful is that the excited state should have a fluorescence quantum yield with a magnitude sufficient for detection. The fluorescence quantum yield is defined as the rate of photon emission by the excited state relative to the rate of photon absorption.⁴ Once formed, an excited state may lose excess energy by several processes in addition to fluorescence. Such processes include dissociation, intersystem crossing (a collision-induced radiationless transition between states of different multiplicity) or internal

conversion (a radiationless conversion to a state of the same multiplicity).³ The lifetime of the excited state with respect to these process affects the fluorescence quantum yield and is therefore crucial to the success of an LIF experiment. An additional requirement for LIF spectroscopy is that the excited state of interest should have a symmetry that allows a one-photon transition from the ground state.

Both of these constraints can be overcome by employing a multiphoton ionisation (MPI) process. Ionisation is achieved by an initial excitation to an intermediate state, followed by the absorption of an additional ionising photon. If the intermediate state is real rather than virtual then the efficiency of the ionisation process is increased (the excited state acts as a "stepping-stone" to ionisation)⁵ and the process is known as resonance enhanced multiphoton ionisation (REMPI) spectroscopy. The structure seen in the REMPI spectrum will be associated with the intermediate state. The ionising and excitation photons may be of the same wavelength (one-colour REMPI), or of a different wavelength (two-colour REMPI). A one-colour scheme is preferable to a two-colour scheme since it requires a single dye laser. However, an excess of energy in the ionising photon can lead to fragmentation of larger species, which then contribute to the REMPI spectra of the species of interest. Employing a two-colour process to minimise the energy of the ionising photon means that fragmentation of higher clusters can be avoided. Figure 2(i) illustrates the principle of REMPI spectroscopy and shows a comparison with laser-induced fluorescence.

The lifetime of the excited state which gives rise to the resonance enhancement is not as critical in REMPI as it is in laser induced fluorescence. For example, an intermediate state with a short lifetime with respect to predissociation can still provide significant enhancement, provided that the rate of ionisation is comparable to other loss processes.⁶

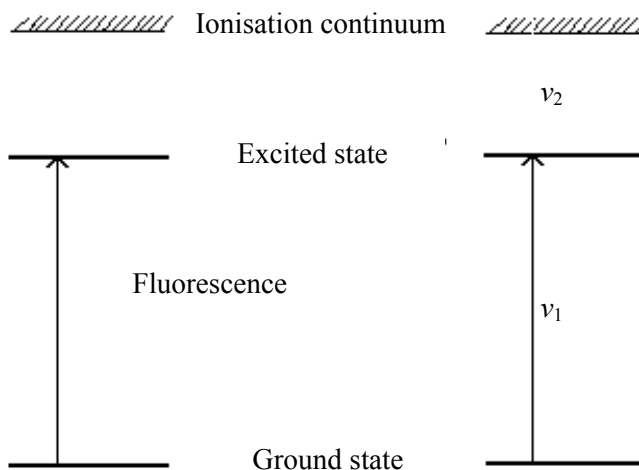


Figure 2(i): *adapted from Reference 6. LIF (left-hand side) and REMPI (right-hand side) where $\nu_1 = \nu_2$ (one-colour) or $\nu_1 \neq \nu_2$ (two-colour).*

The initial excitation may involve the absorption of one, two or even three photons. Generally the selection rules associated with multiphoton absorption are less restrictive than for one-photon processes and provide a greater number and range of excited states capable of enhancing ionisation.⁶ This allows electronic transitions involving excited states, which may not be accessible via one-photon absorption processes due to their high energy or to the relevant selection rules, to be probed. The mass spectrometric detection employed in most REMPI experiments (so that it is possible to attribute a REMPI spectrum to a mass-selected species), offers an additional advantage over laser-induced fluorescence.

The REMPI apparatus employed in the present work comprises a free-jet expansion of NO in a suitable Rg mix or *p*FT in Ar, a laser system and a time-of-flight mass spectrometer for detection. A schematic of the experimental set-up is shown in Figure 2(ii).

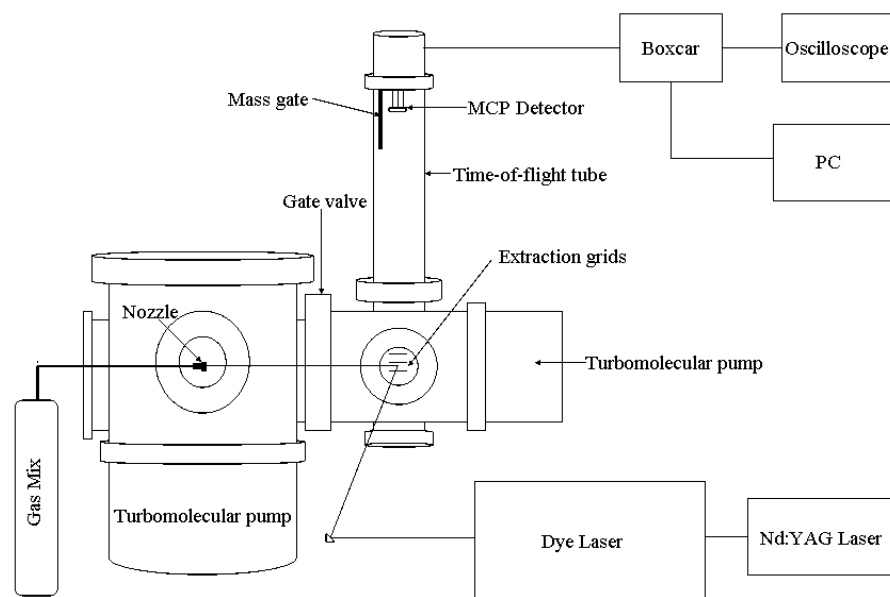


Figure 2(ii): *schematic of the experimental set-up used for REMPI spectroscopy.*

The apparatus used to carry out REMPI spectroscopy consists of two chambers, separated by a thin gate valve and held under vacuum, with typical pressures of approximately 10^{-6} mbar. The first chamber contains the free-jet expansion source, a General Valve pulsed nozzle with an orifice of $750\ \mu\text{m}$ diameter and a pulse repetition rate of 10 Hz. The nozzle chamber is pumped by a $2000\ \text{l s}^{-1}$ turbomolecular (Pfeiffer TPH 2000), backed by a $40\ \text{m}^3\ \text{h}^{-1}$ rotary pump (Leybold TRIVAC D40B). The second (ionisation) chamber contains the ion/electron extraction grids – two plates mounted parallel to the free-jet expansion, onto which voltages can be supplied to deflect the charged species into the time-of-flight tube for detection, with a third plate, located above the extraction region, maintained at ground voltage. A photograph of the extraction grids is shown in Figure 2(iii).



Figure 2(iii): *extraction grid configuration used to extract NO/Rg and pFT cluster ions in the REMPI experiments.*

The ionisation chamber is pumped by a 1000 l s^{-1} turbomolecular pump (Leybold TURBOVAC 1000C), backed by a $40 \text{ m}^3 \text{ h}^{-1}$ rotary pump (Leybold TRIVAC D40B). The time-of-flight (TOF) tube is mounted above the extraction grids, at the top of which is a multichannel plate (MCP) detector to detect ion signal (a detector is also positioned just below the extraction grids in order to collect electron signal although this detector is not employed in the REMPI studies). An additional turbomolecular pump (150 l s^{-1} Leybold TURBOVAC 151) is mounted on the TOF tube, backed by a rotary pump (Leybold TRIVAC D10E). Due to the mass spectrometric detection employed in this REMPI experiment, the procedure is mass selective: the signal intensity is monitored as a function of photon energy over a narrow time range, which can be selected for the species of interest. The MCP detector amplifies the ion signal of the mass-selected species before passing it onto an oscilloscope (LeCroy LT342 Waverunner) for monitoring and a boxcar integrator (SRS SR250) for averaging, before collection and storage on a personal computer.

A strongly absorbing species can result in saturation of the detector; the effects of saturation can be minimised by the use of a mass gate, located near the detector in the TOF tube (the position of the mass gate is shown in Figure 2(ii)). The mass gate comprises a metal rod, 3 mm in diameter and ~150 mm in length, extending down the flight tube. A high positive voltage (typically 500–800 V) is pulsed onto the rod using a high voltage pulse generator with an additional offset (DC Power Supply, Hewlett-Packard, 6515A), at a time chosen to coincide with the time-of-flight of the species whose signal is to be eliminated. The positive voltage applied to the mass gate deflects the species whose ion signal is to be minimised, so that it is no longer on a collision trajectory with the MCP detector.

The laser system used in the REMPI studies generates a range of photon energies and consists of a tuneable dye laser (Sirah Cobra Stretch; 1800 lines/mm grating), pumped by the output of an Nd:YAG laser (Surelite III). The dye laser beam is directed into the ionisation chamber so that it intersects the free-jet expansion between the lower and middle extraction grids. The beam is focused into the ionisation chamber to increase the light intensity and enhance the probability of a multiphoton absorption, which is less probable compared with most one-photon transitions.⁶ Control of the delay time between the production of laser light, detected with a photodiode positioned inside the dye laser, and opening of the pulsed nozzle, is carried out using a digital delay generator (SRS DG535). By adjusting the delay, different regions of the free-jet expansion can be probed; the onset of the free-jet expansion contains the coldest species and by adjusting the delay, the effect of the internal temperature of the molecules on the spectra can be investigated.

2.3 Zero electron kinetic energy spectroscopy

Zero kinetic energy electron (ZEKE) spectroscopy can be used to give spectroscopic information on charged species. A schematic of the ZEKE process is shown in Figure 2(iv).

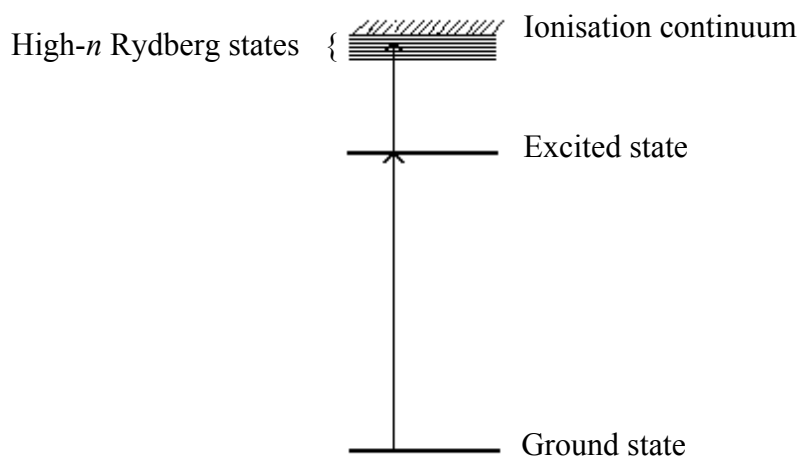


Figure 2(iv): *schematic of ZEKE spectroscopy. The high- n Rydberg states converge at an ionic eigenstate and are ionised by the application of a pulsed electric field.*

The system of interest is photoexcited to a high- n Rydberg state (where n is typically > 100)⁷ lying just below an ionisation limit⁸ via an excited state. Ionisation is achieved by the application of an electric field at some time (usually several microseconds) after photoexcitation, which lowers the ionisation energy by an amount proportional to the magnitude of the electric field. The onset of the pulsed field voltage for ionisation is delayed to allow electrons emitted with kinetic energy to move away from the ionisation region (these are *prompt* electrons and are emitted as the result of a multiphoton ionisation). The advantage of ZEKE spectroscopy over techniques such as photoelectron spectroscopy (PES) or threshold photoelectron spectroscopy (TPES) is the significantly improved resolution offered by the former (a resolution⁹ of 0.15

cm^{-1} is achievable, compared with conventional PES where a typical resolution⁸ is $> 80 \text{ cm}^{-1}$). The peak widths in a ZEKE spectrum reflect the energetic spread of the high- n Rydberg states ionised by the application of a pulsed electric field.

A related technique is mass-analysed threshold ionisation (MATI) spectroscopy, in which the ions produced as a result of pulsed field ionisation are detected rather than the electrons. This has the advantage of being mass selective. As the ions are much heavier than electrons, it is more difficult to separate them from ions produced by the initial laser pulse – prompt ions. A longer time delay between photoexcitation and pulsed field ionisation is necessary,¹⁰ as well as the presence of a small electric field in the ionising region, resulting in spatial separation between the MATI and prompt ions.

In the present work, two dye lasers are used: the first induces a transition to the first excited state (the S_1 state) of neutral $p\text{FT}$ via a one-photon absorption; the second laser energy is scanned over the vibrational levels in the electronic ground state of $p\text{FT}^+$. A ZEKE spectrum is obtained by measuring the yield of electrons produced by the delayed pulsed-field ionisation (PFI), as a function of the second photoexcitation laser energy and the line positions in the spectrum correspond to energy differences between the neutral intermediate state and the high- n Rydberg states located immediately below the energy levels of the ion.

The lifetimes of these high- n Rydberg states are crucial to the success of the ZEKE technique. If the states are not sufficiently stable, they may decay before the onset of the ionising pulsed electric field. The lifetimes of the high- n , low- l Rydberg states, to which the selection rules governing ZEKE spectroscopy allow transitions,¹¹ are found to be much higher than expected; this is a consequence of the conditions under which ZEKE spectroscopy is carried out. The presence of electric fields, and the high state density near the ionisation threshold, induces a mixing of orbital angular momentum, l

(mixing occurs between different l) and its projection m_l (mixing occurs between different m_l). Chupka¹² has treated this mixing in detail. There are two types of electric field responsible for this mixing: homogenous and inhomogeneous. Homogenous electric fields arise as a result of dc fields present in any ZEKE experiment and induce l -mixing. When the homogenous electric fields are minimised, inhomogeneous field components become more significant. These fields are the result of charged particles located near the Rydberg species and are responsible for m_l -mixing.

The experimental set-up used to carry out ZEKE spectroscopy is similar to that used for the REMPI experiments, as depicted in Figure 2(ii). Two dye lasers are used and each is focused into the ionisation chamber so that they intersect the free-jet expansion between the lower and middle extraction grids. The "pump" dye laser excites p FT from the electronic ground state (S_0) to the first electronically-excited state (S_1). The second dye laser photon energy is varied around the energy corresponding to the electronic ground state of the p FT cation (D_0). The dye laser beams and the nozzle and ionisation vacuum chambers are shown in Figure 2(v); a schematic representation of the vacuum chambers is given in Figure 2(ii).

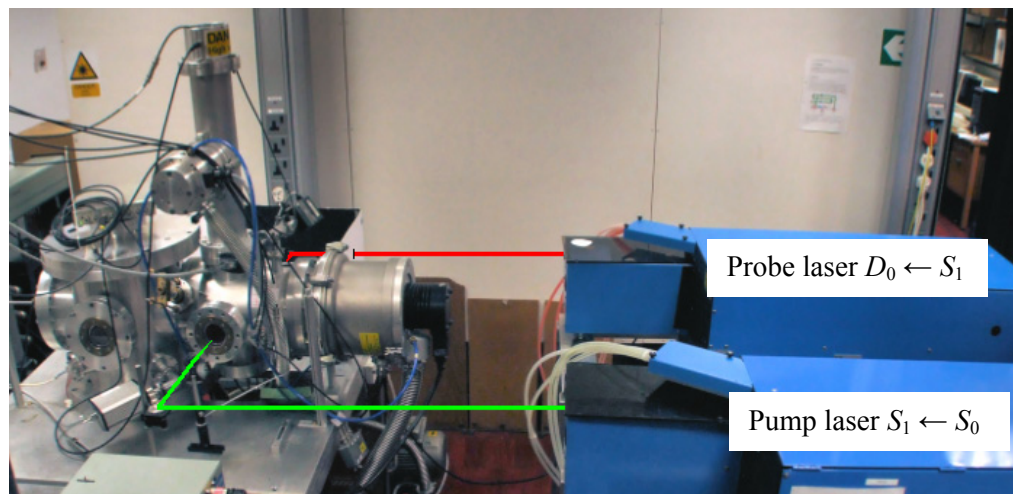


Figure 2(v): dye lasers and vacuum chambers used in the ZEKE experiment.

In the ZEKE experiment, the MCP detector positioned below the extraction grids is used to detect the electron signal. Application of a small, pulsed positive voltage onto the lower extraction grid proved to provide optimum ZEKE signal. The extraction grid configuration used to obtain the ZEKE signal is shown in Figure 2(vi).

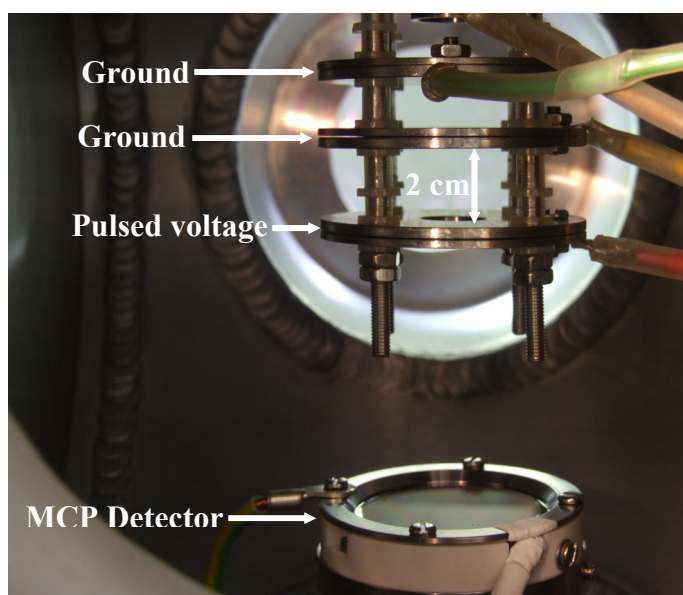


Figure 2(vi): *the voltages applied to the extraction grids and the MCP detector used in the ZEKE experiment.*

The work performed as part of the present thesis uses the high-resolution offered by ZEKE spectroscopy to investigate vibrational modes of the *para*-fluorotoluene cation at a level of precision that has not been achieved previously.

2.4 References

¹ J.M. Hollas, *Modern Spectroscopy 4th Edition*, John Wiley & Sons Ltd (2004) 452pp.

² L.A. Angel, D.Phil. Thesis, University of Sussex (1999).

- ³ P.W. Atkins, *Physical Chemistry, 6th Edition*, Oxford University Press (1998) 1014pp.
- ⁴ A. Ellis, M. Feher, T. Wright, *Electronic and Photoelectron Spectroscopy Fundamentals and Case Studies*, Cambridge University Press (2005) 286 pp.
- ⁵ S. Leutwyler, J. Bosiger, *Chem. Rev.* **90** (1990) 489-507.
- ⁶ M.N.R. Ashfold, S.G. Clement, J.D. Howe, C.M. Western, *J. Chem. Soc. Faraday Trans.* **89**(8) (1993) 1153-1171.
- ⁷ E.W. Schlag, *ZEKE Spectroscopy*, Cambridge University Press, (1998) 277pp.
- ⁸ C.E.H. Dessent, K. Müller-Dethlefs, *Chem. Rev.* **100** (2000) 3999-4021.
- ⁹ H. Dietrich, K. Müller-Dethlefs, *Phys. Rev. Lett.* **76**(19) (1996) 3530-3533.
- ¹⁰ R.C. Shiell, T.G. Wright, *Annu. Rep. Prog. Chem. Sect C*, **98** (2002) 375-419.
- ¹¹ C Sándorfy (Ed), *The Role of Rydberg States in Spectroscopy and Photochemistry*, Kluwer Academic Publishers, (1999) 512pp.
- ¹² W.A. Chupka, *J. Chem. Phys.* **98**(6) (1993) 4520-4530.

3 *Electronic spectroscopy of the 3dλ Rydberg states of NO–Rg (Rg = Ne, Ar, Kr, Xe)*
van der Waals complexes

3.1 *Introduction*

3.1.1 *3dλ States in nitric oxide*

Nitric oxide has the ground state electron configuration¹ $(1s\sigma)^2 (1s\sigma^*)^2 (2s\sigma)^2 (2s\sigma^*)^2 (2p\sigma)^2 (2p\pi)^4 (2p\pi^*)^1$ and represents the class of radicals with a singly occupied antibonding orbital. The states investigated here arise when the $2p\pi^*$ electron undergoes a transition to the unoccupied 3d Rydberg orbital and can be approximated by a single electron orbiting a singly-charged cationic (NO^+) core.¹ An electron transition in nitric oxide can result in the formation of one of two states: a Rydberg state, where the $2p\pi^*$ electron is promoted to an orbital with $n \geq 3$ where n is the principal quantum number; or a non-Rydberg (valence) state. The latter arises when electronic transitions are confined to the valence orbital, for example a π – π transition from $2p\pi$ to the partially filled $2p\pi^*$ orbital (the excited electron does not originate from the highest occupied molecular orbital – HOMO). The Rydberg and non-Rydberg states of nitric oxide with $n \leq 7$ are shown in Figure 3(i). This work is concerned with the Rydberg states arising when the $2p\pi^*$ electron has been promoted to the 3d orbital: the $\tilde{F}^2\Delta$, $\tilde{H}^2\Pi$ and $\tilde{H}^2\Sigma^+$ states.

3.1.2 *Energetic ordering of the 3dλ states*

The energetic ordering of the states relevant to the following discussion has been treated in detail previously.² Briefly, the ordering of the weakly-penetrating 3dλ states in NO is not as predicted by the long-range model used to describe $l \geq 3$ Rydberg

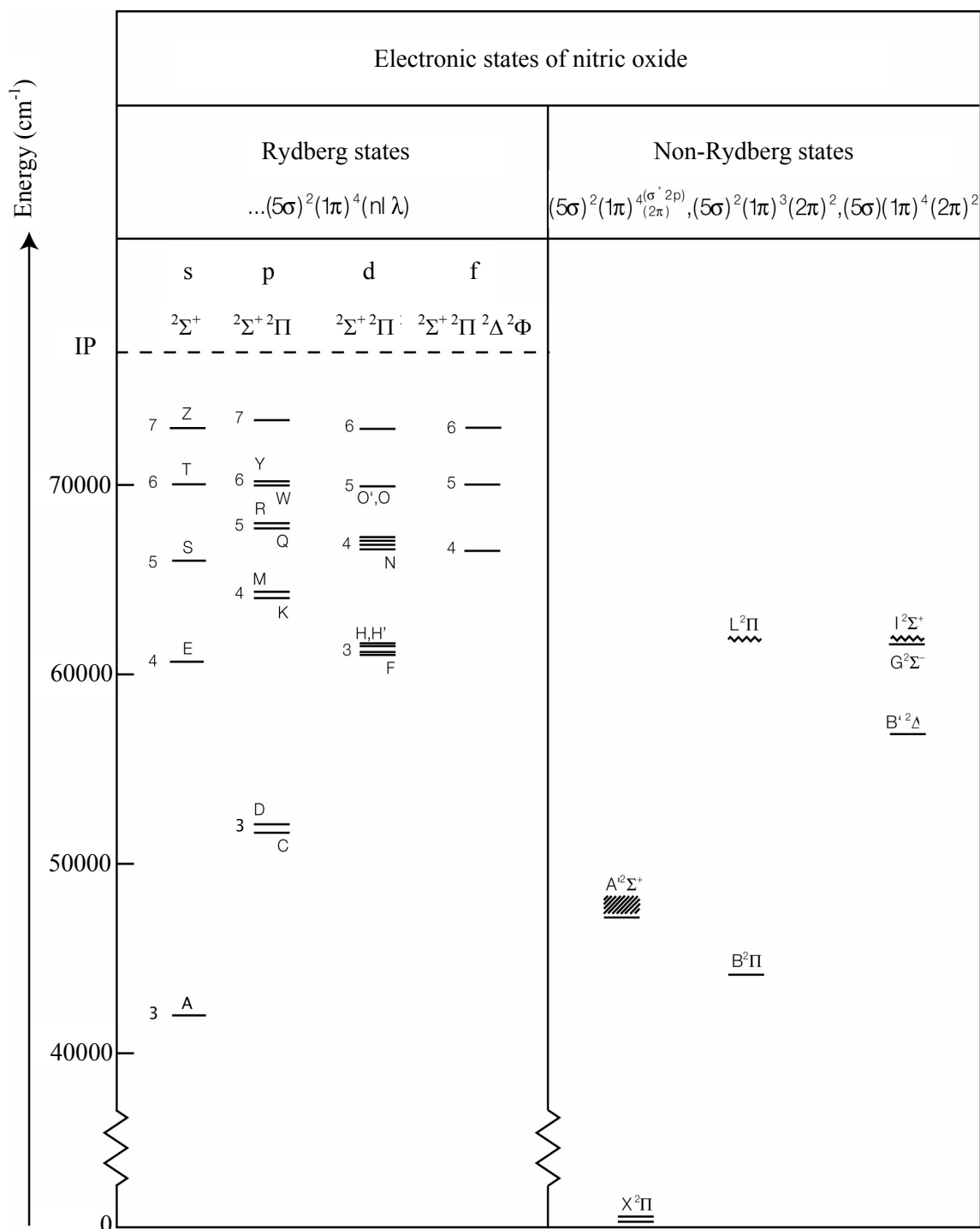


Figure 3(i): Rydberg states (shown in the column on the left) and non-Rydberg states (shown in the column on the right) of nitric oxide.

states. The atomic 3d orbital splits into molecular orbitals, which are characterised by the projection of the atomic orbital angular momentum l onto the molecular axis. This

projection is denoted by the quantum number λ . The expected energetic ordering, where the σ component lies lowest in energy and the δ component lies highest in energy, with the π component at an intermediate energy, is based upon the expected penetration of each type of electron. In fact, for the electronic states arising from the $3d$ occupancy, the energetic ordering observed is given by $\delta < \sigma < \pi$. This deviation in the expected energetic ordering of the λ components is due to the weak penetration of the $3d$ Rydberg electron, which is neglected by the long-range model, used to treat other non-penetrating orbitals successfully. The model corresponds to a singly charged core that, once the charge is activated, causes the $3d$ states to decrease in energy, whilst maintaining their degeneracy (the activation of this charge is represented by α in Figure 3(ii)). Since the charges in the core are not distributed spherically, a quadrupolar field is incorporated. Activating the quadrupolar field (denoted by θ in Figure 3(ii)), removes the degeneracy of the $3d$ states and results in the energetic ordering $\sigma < \pi < \delta$. The ordering of these levels is shown in Figure 3(ii) and is denoted by T^* .

Even though the $3d$ Rydberg electron is only weakly-penetrating, it is still able to interact with the many-electron NO^+ core, which requires a more sophisticated treatment. It is this overlap between the Rydberg electron and the NO^+ core, and subsequent interactions neglected in the long-range model, which gives rise to the observed energetic ordering. The states under consideration here are perturbed by interactions between the Rydberg electron and the NO core orbitals, which arise as a consequence of $3d$ electron penetration; the long-range model has been modified by Jungen² to take these penetration effects into account. These interactions have been considered more thoroughly elsewhere² and only a brief summary will be given here.

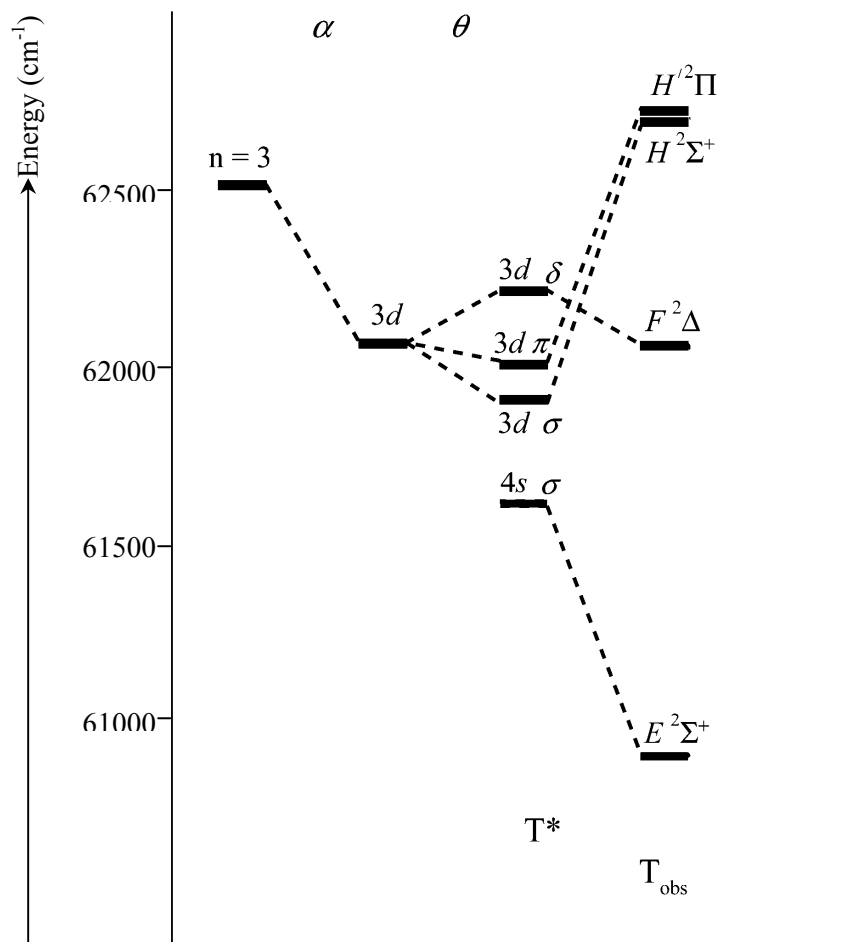


Figure 3(ii): *observed ordering (T_{obs}) of the $3d\lambda$ and $4s\sigma$ Rydberg states of NO. Ordering predicted by the long-range model, which neglects penetration of the $3d$ electron is shown by T^* .*

Exchange effects between the Rydberg electron and the core electrons, and the increased nuclear attraction felt by the $3d$ Rydberg electron upon penetration, are the predominant cause for the decrease in energy observed for the $3d\delta$ component. For the $3d\pi$ component, overlap between the Rydberg orbital and core orbitals of the same symmetry lead to an increase in energy from the unperturbed position. Finally, the non-spherical distribution of charges within the core leads to a mixing of Rydberg orbitals with the same symmetry: the $nd\sigma$ orbitals of NO are strongly mixed with the

orbitals $(n + 1) s\sigma$. This mixing is responsible for the $3d\sigma$ component moving up in energy. The energetic ordering observed for the $3d$ states in NO is given by T_{obs} in Figure 3(ii).

3.1.3 Previous work on the lower Rydberg states

Complexes involving nitric oxide are prototypes of chemically active systems involving open-shell atoms and molecules. The electronic spectroscopy of open-shell NO, complexed with closed-shell atoms and molecules, has been the subject of a number of studies. The simplest examples of closed-shell complexing partners are the rare gases (Rg), and the NO–Rg complexes have been extensively studied, with Rydberg states arising from occupation of the $3s$ ($\tilde{A}^2\Sigma^+$);^{3,4,5,6,7,8,9,10} $3p$ ($\tilde{C}^2\Pi$ and $\tilde{D}^2\Sigma^+$);^{6,10,11,12,13,14,15} $3d$ ($\tilde{F}^2\Delta$, $\tilde{H}^2\Pi$)^{1,14} and $4s$ ($\tilde{E}^2\Sigma^+$)^{13,14} orbitals investigated.

Of the low-lying Rydberg states, the $\tilde{A}^2\Sigma^+$ state is found to be the most weakly bound; for the NO–Ar complex for example, a dissociation energy of 44 cm^{-1} has been derived by Tsuji *et al.*⁹ compared to a value of 414 cm^{-1} for the $3p$ ($\tilde{C}^2\Pi$) state.⁹ The weak binding in the $\tilde{A}^2\Sigma^+$ state is consistent with the radius of the $3s$ orbit (2.86 \AA)⁶ being too small to allow a Rg atom to reside within: the $\tilde{A}^2\Sigma^+$ state comprises an NO^+ core, which is more effectively shielded from the Rg atom by the orbiting $3s$ Rydberg electron.^{3,4} Unlike the higher Rydberg states, where only the spectral region located near the origin is observed, it is possible to observe the energy levels of the $\tilde{A}^2\Sigma^+$ state in their entirety – from the vibration-less origin to the dissociation limit. In an investigation by Bush *et al.*⁴ and in a later study of Lozeille *et al.*⁸ the $(1 + 1)$ REMPI (resonance-enhanced multiphoton ionisation) spectrum of the $\tilde{A}^2\Sigma^+$ state of NO–Ar was interpreted in terms of an intermolecular stretch progression, together with an angular motion of the NO subunit. The geometry of the complex was found to be

linear near the origin, whereas when the intermolecular stretch is excited, the geometry approaches a skewed T-shape.^{4,8} This state has been investigated as part of the present thesis and is discussed in more detail in Chapter 6.

Excitation of the $2p\pi^*$ electron into the $3p$ Rydberg orbital results in the formation of σ and π components upon interaction with Rg: the $\tilde{D}^2\Sigma^+$ and $\tilde{C}^2\Pi$ states respectively. The majority of the studies carried out have focused on the $3p\pi$ $\tilde{C}^2\Pi$ state, using (2 + 1) resonance-enhanced multiphoton ionisation spectroscopy, where the complexes NO–Kr and NO–Xe,¹¹ NO–Ar¹³ and NO–Ne¹⁴ have been studied. The structure in the $\tilde{C}^2\Pi$ state spectra across the Rg series is similar: a dominant progression is assigned to the van der Waals intermolecular stretching mode, which is consistent with a vibrationally-averaged T-shaped geometry similar to that in the electronic ground state.¹ The $\tilde{D}^2\Sigma^+$ state of NO–Ar, which again is dominated by a long progression in the intermolecular stretch, has been probed by Miller *et al.*¹⁶ and Tsuji *et al.*¹⁷

3.1.4 Previous work on the $3d\lambda$ Rydberg states

The $3d\lambda$ Rydberg states have been investigated in a comparatively limited number of studies; the complexes NO–Ne¹⁴ and NO–Ar¹ have been probed using a one-colour (2 + 1) REMPI scheme. Both complexes have also been the focus of a study by Meyer and coworkers,¹ employing an IR-REMPI double resonance technique. This proved to be particularly useful for the NO–Ar complex, in which the $\tilde{F}^2\Delta$ and $\tilde{H}^2\Pi$ states were found to overlap, making an identification of the $\tilde{H}^2\Pi$ state origin problematic (see Section 3.3.2). In the initial excitation step, the NO chromophore is excited to the second vibrational level ($v'' = 2$) in the electronic ground state ($\tilde{X}^2\Pi$). The

vibrationally-excited complex is subsequently ionised, using a (2 + 1) REMPI scheme. Figure 3(iii), taken from Reference 1, shows the spectra obtained during the IR-REMPI experiment.

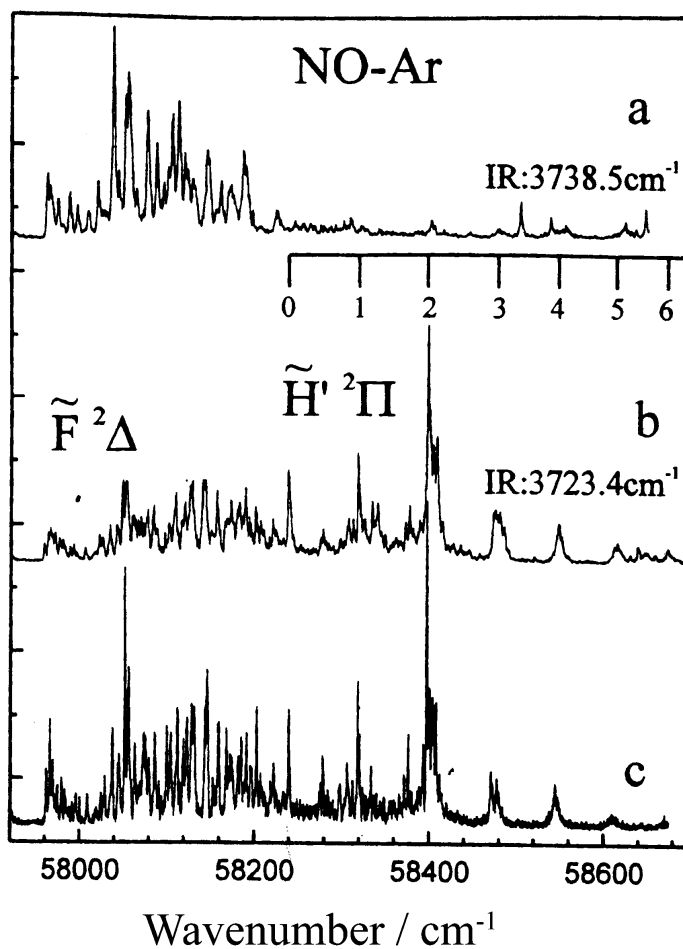


Figure 3(iii): taken from Reference 1 (a) IR-REMPI spectrum exciting NO $v'' = 2$ and one quantum of intermolecular bend; (b) IR-REMPI spectrum exciting NO $v'' = 2$ (at 3723.4 cm^{-1}); (c) (2 + 1) REMPI spectrum of NO-Ar, shifted by 3724 cm^{-1} .

When the NO molecule is excited to $v'' = 2$ (spectrum *b* in Figure 3(iii)), the resulting IR-REMPI spectrum is largely similar to the one-colour (2 + 1) REMPI spectrum (spectrum *c* in Figure 3(iii)) – both the $\tilde{F}^2\Delta$ and $\tilde{H}'^2\Pi$ states are observed. Conversely, when ionising via a level with the intermolecular bending motion excited

(spectrum *a* in Figure 3(iii)), the resulting IR-REMPI spectrum is significantly different from the one-colour (2 + 1) REMPI spectrum – only the $\tilde{F}^2\Delta$ state component is accessed, the $\tilde{H}^2\Pi$ state is absent. The interpretation of this is that the Franck-Condon factors for a transition to the $\tilde{H}^2\Pi$ state from the first bending level are small.¹ The $\tilde{H}^2\Pi$ state geometry of NO–Ne is near T-shaped (a Jacobi angle of 60° has been determined)¹ and it is reasonable to assume that NO–Ar will have a similar geometry. Upon excitation from the $\tilde{X}^2\Pi$ state (with a vibrationally averaged T-shaped structure)¹ the most significant geometry change will be a shortening of the intermolecular bond. Change in the Jacobi angle is expected to be small, leading to the poor Franck-Condon factors along the bending coordinate and the non-observation of the $\tilde{H}^2\Pi$ state.

The appearance of the $\tilde{H}^2\Pi$ state spectrum is in stark contrast with that of the $\tilde{F}^2\Delta$ state. In both NO–Ne and NO–Ar, the $\tilde{H}^2\Pi$ state displays a clear progression, with sharp, intense peaks assigned as members of the intermolecular stretch vibration. However, in both NO–Ne and NO–Ar, the appearance of the $\tilde{F}^2\Delta$ state is far more complicated. Simulation of the spectra (carried out by H. Meyer)¹ was only possible using two separate geometries for the $\tilde{F}^2\Delta$ state: a T-shaped configuration, with an angle (θ) of 85° between the NO vector and the Rg atom; and a less bent configuration ($\theta = 30^\circ$). The reason for this is not yet fully understood, although one interpretation is that the $\tilde{F}^2\Delta$ state potential may possess a less well-defined geometry with two possible minima.¹ This hypothesis would be consistent with the results of the IR-REMPI experiment described above: Franck-Condon factors governing a transition to the $\tilde{F}^2\Delta$ state are favourable when exciting via one quantum of intermolecular bend (a motion which sees a variation in θ), as well as via a vibration-less ground state (a motion where the change in θ is minimal), providing further evidence that the

geometry of the $\tilde{F}^2\Delta$ state is less well defined. In previous work,^{1,14} and in the present study, the $3d\lambda$ states of NO–Rg (Rg = Ne, Ar, Kr) are accessed via a two-photon absorption, and the two-photon spectroscopy of the $H^1^2\Pi, H^2\Sigma^+ \leftarrow X^2\Pi$ transition of NO has been treated previously.¹² Briefly, a transition between two Π states *i.e.* a transition to the $\tilde{H}^1^2\Pi$ component, will be carried by a zeroth rank tensor and/or a second rank tensor, whereas a transition to the $\tilde{H}^2\Sigma^+$ state will be carried by a second rank tensor only. A zeroth rank tensor allows only Q branches to appear, as is seen by the comparatively simple structure of the $\tilde{H}^1^2\Pi$ state spectra observed to date.^{1,12,14} The $\tilde{H}^1^2\Pi \leftarrow \tilde{X}^2\Pi$ transition is dominated by a zeroth rank tensor, with a minor contribution (6 %)¹² from a second rank tensor.

Of the NO–Rg series, the $3d\lambda$ states of the complexes NO–Kr and NO–Xe have received little attention. In the present study, the bound levels of the NO–Kr and NO–Xe van der Waals complexes (as well as the complexes NO–Ne and NO–Ar) were investigated using REMPI spectroscopy, in the hope of gaining a more thorough understanding of the low-lying $3d$ Rydberg states (the $\tilde{F}^2\Delta$, $\tilde{H}^2\Sigma^+$ and $\tilde{H}^1^2\Pi$ states).

3.2 Experiment

3.2.1 Experimental set-up

The apparatus used to carry out REMPI spectroscopy has been described in detail in Chapter 2. To form NO–Ar and NO–Ne, mixtures of ~5% NO (Messer; 99.5%) in the rare gas were used. NO–Kr and NO–Xe were formed using mixtures of ~2.5% NO and ~5% Rg (Kr, Xe: BOC; 99.9+%) seeded in either Ar (BOC; 99.9+%) or Ne (Spectra Gases; 99.9+%). The gas mixtures were held at pressure (~5 bar when Ar was the backing gas and ~9 bar when Ne was used) before expansion into vacuum through

a General Valve pulsed nozzle (750 μm , 10 Hz, opening time 230 μs). The resulting unskimmed supersonic expansion passes through a thin gate valve, into the extraction region of a time-of-flight mass spectrometer.

Ionisation is achieved in a (2 + 1) REMPI scheme using the focused, frequency doubled output of a Sirah Cobra Stretch dye laser (1800 lines/mm grating), pumped by the second harmonic (532 nm, 10 Hz) of a Surelite III Nd:YAG laser. The laser dye solution used is DCM (4-Dicyanomethylene-2-methyl-6-p-dimethylaminostyryl-4H-pyran,¹⁸ Sirah; SDL-550; 0.3 g) in DMSO (dimethyl sulphoxide, Merck; $\geq 99\%$; 1 l), with an emission peak at 651 nm.

All spectra are obtained in the parent ion mass channel, except for NO–Xe where features thought to be attributable to the complex are seen in the Xe^+ fragment channel (see Section 3.3.3). A mass gate (see Chapter 2) is used to avoid saturation of the detector (and subsequent baseline disturbances) by uncomplexed NO. Spectra are calibrated to the NO resonances ($E^2\Sigma^+$ and $H'^2\Pi$) located in the spectral range under investigation.

3.2.2 Calibration

Calibration was achieved by applying a constant offset in wavenumber units, to experimental data. The offset value was derived by comparing peak energies from a (2 + 1) REMPI spectrum of either the $E^2\Sigma^+$ state, or the $H'^2\Pi$ state of uncomplexed NO with their known energies; the state closest in energy to the spectral range probed is used for calibration. The following illustrates how the calibration procedure was carried out, using the $E^2\Sigma^+$ state of uncomplexed NO¹⁹ (an $E^2\Sigma^+$ state spectrum of NO is shown in Figure 3(v)). The energy of the $E^2\Sigma^+$ state origin transition ($v'' = 0, J''$

$= 1/2$ to $v' = 0, J' = 1/2$), is known from previous work.¹ However, this transition (identified as the Q₁₁ line) is not visible as a peak in the NO $E^2\Sigma^+$ state REMPI spectrum. The energy of an observable transition must be calculated, which requires knowledge of the rotational energy of the ground state and of the excited state, as well as the allowed transitions between these states. For the NO molecule, the rotational energy of the electronic ground state can be approximated by Hund's coupling case (a) (where the orbital angular momentum and the electron spin are both strongly coupled to the internuclear axis), and is given by Equation 3(a).

$$E_{J,\Omega} = B_0[J(J+1) - \Omega^2] \quad 3(a)$$

Ω is the projection of the angular momentum along the molecular axis (for a $^2\Pi$ state this can take values of $\Lambda + \Sigma = 3/2$ or $\Lambda - \Sigma = 1/2$, although for NO the state with $\Omega = 1/2$ lies lowest in energy) and J is the rotational quantum number. The rotational constant is typically given as B_e , which corresponds to the value at the equilibrium internuclear separation (r_e). However, due to anharmonicity, the equilibrium internuclear distance will increase as the molecule vibrates, hence the rotational constant will decrease. The rotational constant can be written more generally as B_v and can be calculated from B_e using:²⁰

$$B_v = B_e - \alpha_e(v + 1/2) + \dots \quad 3(b)$$

α_e is small compared to B_e since the vibration leads to a small change in internuclear separation (higher terms are smaller still and have therefore been neglected). The free-jet expansion used in the present work, along with careful control of the laser/pulsed nozzle delay time, ensures that higher vibrational levels in NO are minimally populated *i.e.* transitions are originating from the vibrational ground state. Using

Equation 3(b), with $B_e = 1.67 \text{ cm}^{-1}$ and $\alpha_e = 0.0171 \text{ cm}^{-1}$ (taken from Reference 21) gives $B_0 = 1.66 \text{ cm}^{-1}$ for the $X^2\Pi \nu'' = 0$ state. Using equation 3(a), with $\Omega = 1/2$ and $B_0 = 1.66 \text{ cm}^{-1}$ gives an energy of 0.83 cm^{-1} for the $J'' = 1/2$ rotational level, relative to the hypothetical $J'' = 0$ level of the ground state. The very low rotational temperature calculated for NO in the $X^2\Pi$ state in Section 3.2.3 below strongly suggests that transitions originate from the $J'' = 1/2$ rotational level.

The rotational energy of the $E^2\Sigma^+$ state, which can be described by Hund's coupling case (b), where the predominant coupling is that between the orbital angular momentum and rotation of the nuclear axis, can be calculated using equation 3(c).²⁰

$$E_N = B_0[N(N + 1)] \quad 3(c)$$

B is the rotational constant (in cm^{-1}) and N is the total angular momentum excluding electron spin. The levels of N are split by the electron spin S , to give $J = (N + S) \dots (N - S)$, although this effect is weak and cannot be resolved in the current experiment. Using $B_0 = 1.90 \text{ cm}^{-1}$, calculated using equation 3(b) with $B_e = 1.9863 \text{ cm}^{-1}$ and $\alpha_e = 0.182 \text{ cm}^{-1}$ (from Reference 21), gives energies of 0 cm^{-1} , 3.79 cm^{-1} , 11.37 cm^{-1} and 22.74 cm^{-1} for the levels $N = 0, 1, 2$ and 3 (relative to the level $N = 0$). Figure 3(iv) shows the rotational levels of the $X^2\Pi$ ground state and the levels $N = 0, 1, 2$ and 3 of the $E^2\Sigma^+$ state, together with some allowed transitions (transitions with $\Delta J = 0, \pm 1, \pm 2$ are allowed, since this is a two-photon transition).

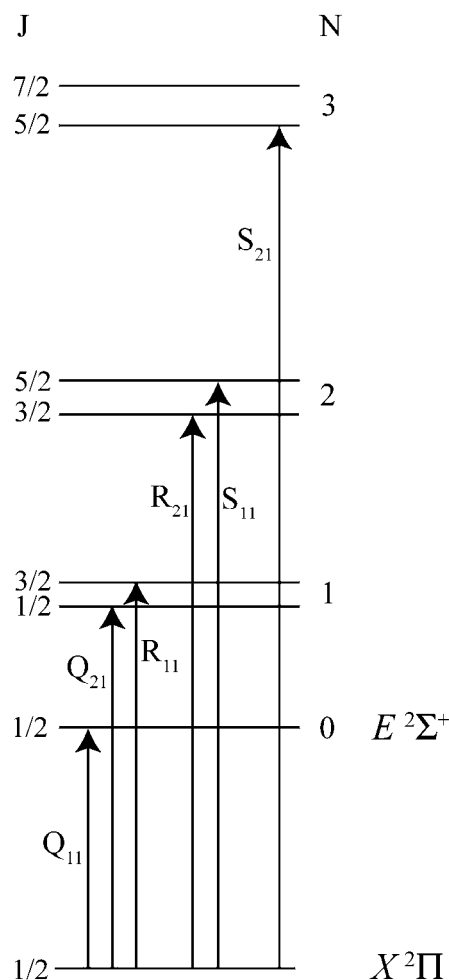


Figure 3(iv): rotational energy levels of the $X^2\Pi$ and $E^2\Sigma^+$ states of NO, corresponding to Hund's coupling cases (a) and (b) respectively. Also shown are allowed transitions with $\Delta J = 0, 1$ and 2 . Adapted from Reference 19.

Figure 3(iv) suggests that four features should be observable in the $E^2\Sigma^+$ state ($2 + 1$) REMPI spectrum, labelled as Q_{11} , the unresolved pair $Q_{21} + R_{11}$, the unresolved pair $R_{21} + S_{11}$ and S_{21} , where Q, R and S describe the change in J ($\Delta J = 0, 1$ and 2 respectively). Since the Q_{11} transition is not observed however, the spectrum consists of three features, the energies of which can be calculated from the origin (ν_{00}) transition energy (60863.8 cm^{-1} , this band origin refers to $N' = 0$ in the excited state and to the hypothetical level $J'' = 0$ of the $X^2\Pi$ ground state)²¹ and the rotational

energies of the $E^2\Sigma^+$ and $X^2\Pi$ states. The energies of the visible transitions are: $60863.8 - 0.83 + 3.79 = 60866.76 \text{ cm}^{-1}$; $60863.8 - 0.83 + 11.37 = 60874.34 \text{ cm}^{-1}$; $60863.8 - 0.83 + 22.74 = 60885.71 \text{ cm}^{-1}$. Intensities with a ratio of 2:2:1 are expected since the first two visible peaks ($Q_{21} + R_{11}$ and $R_{21} + S_{11}$) consist of two contributions, and the final peak just one (S_{21}). These calculated peak positions can be compared with their experimentally observed energies to give a calibration offset, which is to be applied to all experimental data. A calibration offset value of $24.4 \pm 0.5 \text{ cm}^{-1}$ is derived using this method. An $E^2\Sigma^+$ state spectrum of NO is shown in Figure 3(v). The three visible peaks are labelled with their calculated energies, their experimentally observed energies and the corresponding calibration offset.

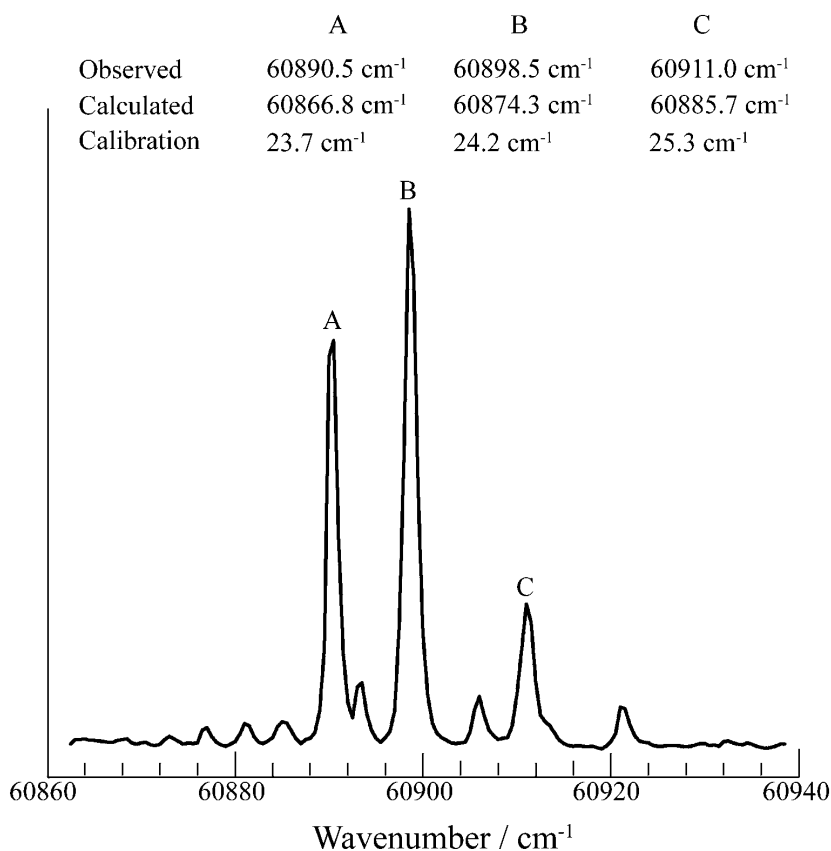


Figure 3(v): $(2 + 1)$ REMPI spectrum of the $E^2\Sigma^+$ state of NO used to calibrate data in the present work. Adapted from Reference 19.

3.2.3 Rotational temperatures

The efficiency of the supersonic expansion at cooling the van der Waals dimers can be estimated from the appearance of the spectra (the prominence of hotbands for example), although it is difficult to determine an exact temperature. It is useful to derive a rotational temperature for uncomplexed NO however since the rotational cooling is more efficient in a free-jet expansion experiment (rotational levels are more closely spaced than vibrational levels, hence fewer collisions are required to quench excess rotational energy). The thermal distribution of the rotational levels, *i.e.* the relative populations of the rotational levels, is given by:²⁰

$$N_j \propto (2J + 1)e^{-BJ(J+1)hc/kT} \quad 3(d)$$

The rotational level at which the population is at a maximum is given by J_{max} , where T is given in K and B is given in cm^{-1} .²⁰

$$J_{max} = \sqrt{\frac{kT}{2Bhc}} - \frac{1}{2} = 0.5896\sqrt{\frac{T}{B}} - \frac{1}{2} \quad 3(e)$$

The $E^2\Sigma^+$ state spectrum shown in Figure 3(v) can be used to give an estimate of the rotational temperature of NO. The spectrum contains three peaks, which correspond to transitions from the lowest rotational level in the $X^2\Pi$ state, $J'' = 1/2$. Although there are additional features in the spectrum, which are most likely transitions from the next rotational level in $X^2\Pi$, $J'' = 3/2$, they are very weak, implying that $J'' = 1/2$ is J_{max} . Using $B_0 = 1.66 \text{ cm}^{-1}$ derived using Equation 3(b), and substituting $J_{max} = 1/2$ into Equation 3(e), gives a rotational temperature $T = 4.78 \text{ K}$. At this calculated rotational temperature, the thermal distribution given in Equation 3(d) requires significant

population in $J'' = 3/2$ (for $J'' = 1/2$, the relative population N_J is 5.00, for $J'' = 3/2$ the relative population is similar, 4.98). From the spectrum, it is clear that this is not the case. Contributions from $J'' = 3/2$ are very weak and the relative populations of $J'' = 1/2$ and $J'' = 3/2$ are certainly not as similar as suggested by the values of N_J calculated above. The rotational temperature of 4.78 K is therefore an upper limit.

Spectra of the van der Waals dimers were collected using similar delays to those used for NO *i.e.* both NO and NO–Rg complexes were probed in a similar region of the supersonic expansion. Although it is difficult to determine the rotational temperature of the NO–Rg complexes, the appearance of the spectra (the lack of contributions from $J'' = 3/2$ – this is particularly apparent in the $\tilde{H}^2\Pi$ state) and the narrow linewidths, allows an estimation of rotational temperature, which does not exceed 5 K (as for uncomplexed NO).

3.3 Results

A contemporaneous investigation was carried out by H. Meyer and coworkers at the University of Georgia, which produced high quality data comparable with that presented here. The majority of the analysis presented in the following is based upon the data derived in the present work. Although when necessary, the results of H. Meyer were considered in combination with the data obtained during the present study. It will be clearly stated when both sets of data are considered.

(2 + 1) REMPI spectra of NO, NO–Ne, NO–Ar and NO–Kr are shown in Figure 3(vi). The spectral region shown includes the $3d$ states under consideration, as well as the $4s$ ($\tilde{E}^2\Sigma^+ v_{\text{NO}} = 0, 1$) state. The $3p$ ($\tilde{C}^2\Pi$) Rydberg state, with four quanta of NO stretch can be seen in the REMPI spectra of both bare NO and NO–Ne. A weak feature, at

61900 cm^{-1} in the NO–Ne complex spectrum and centred around 61500 cm^{-1} in the NO–Ar complex spectrum has been tentatively assigned as the $\tilde{D}^2\Sigma^+$ state, again with four quanta of intramolecular stretch. The 4s Rydberg state, and complexes with vibrationally excited NO are discussed in detail elsewhere (see Chapter 5).

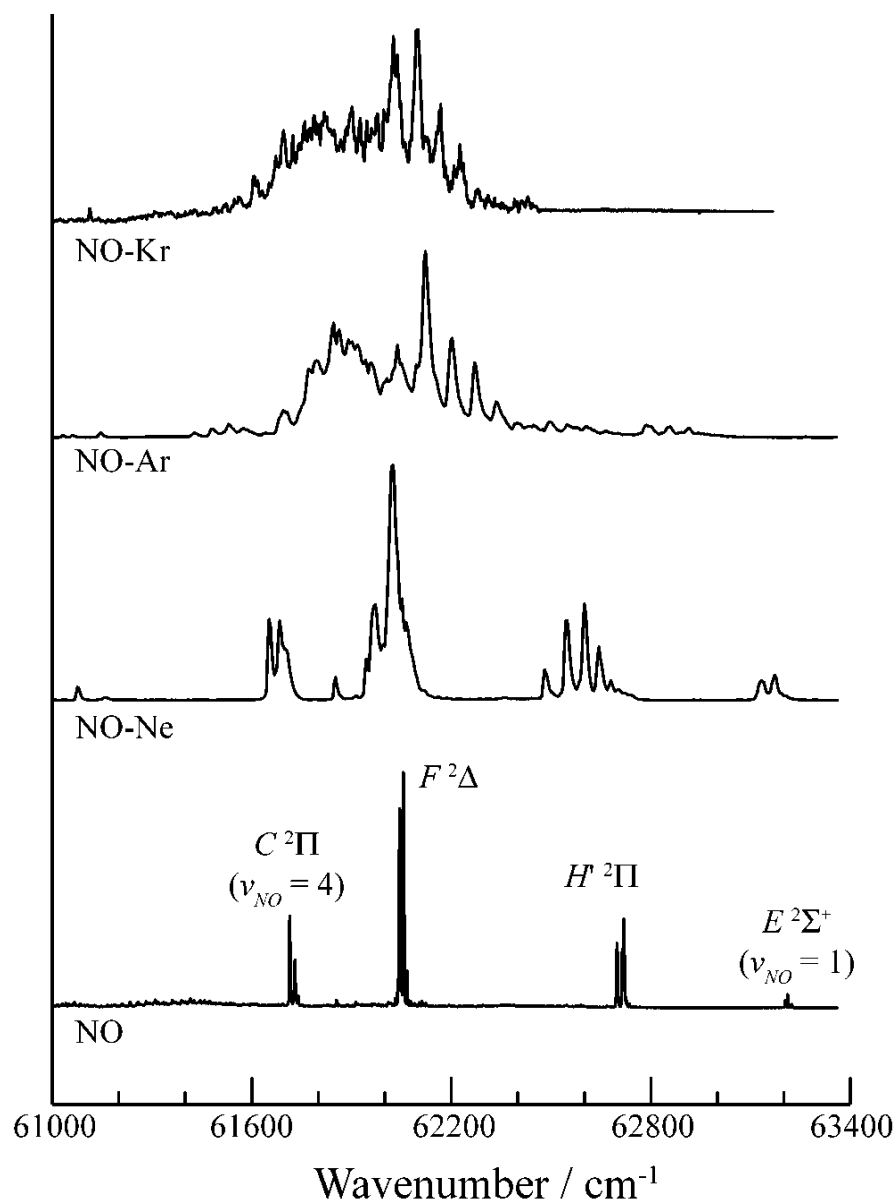


Figure 3(vi): $(2 + 1)$ REMPI spectra of NO and NO–Rg (Rg = Ne, Ar, Kr) showing the 3d and 4s Rydberg states. The $\tilde{C}^2\Pi$ state, with four quanta of intramolecular stretch, is also observed.

The absence of the $\tilde{H}^2\Sigma^+$ component can be explained in terms of the interaction that occurs between Rydberg states of the same symmetry. This has been discussed previously by Jungen.² Briefly, the $4s\sigma$ and $3d\sigma$ states interact, causing the $4s\sigma$ state to move down in energy and the $3d\sigma$ state to move up in energy. This interaction ($s\sim d$ mixing) results in the cancellation of the $\tilde{H}^2\Sigma^+ \leftarrow \tilde{X}^2\Pi$ transition moment (the intensity of the transition is weakened), while the $\tilde{E}^2\Sigma^+ \leftarrow \tilde{X}^2\Pi$ transition intensity is simultaneously enhanced.

3.3.1 Spectral redshift

The spectral redshift of each state relative to that in uncomplexed NO, as the rare gas complexing partner increases in size, is evident. The increased magnitude of the interaction between NO and the Rg atom in the excited states, relative to the ground state leads to a greater increase in the binding energy of the excited state than in the ground state, resulting in the observed spectral redshift. Of the $3d\lambda$ Rydberg states observed the $\tilde{F}^2\Delta$ state has the smallest radius at 5.28 Å, although this diameter is large enough to allow a Kr atom (with a van der Waals radius of 2.02 Å²²) to reside within. As a consequence, the $3d$ electron is less able to shield the Rg atom from the NO⁺ core, increasing the magnitude of the interaction in the excited state. In the ground state the Rg atom is more effectively shielded from the NO⁺ core and the intermolecular interaction is weaker as a result. That the spectral redshift increases with rare gas size, is due to the increasing polarisability as the rare gas group is descended. This is not a linear relationship however. As the Rg polarisability increases, the magnitude of the interaction between the Rg and the NO⁺ core will increase. However, the magnitude of the repulsive interaction between the electrons on the Rg atom and the $3d$ Rydberg electron will also increase. There are two competing factors that describe the NO/Rg interaction. The redshift indicates that the

attractive interaction dominates, although the redshift is expected to lessen as the Rg size increases further and the magnitude of the repulsive interaction increases. These competing interactions are more evident in the smallest $\tilde{A}^2\Sigma^+$ Rydberg state, which is discussed in Chapter 6.

3.3.2 Convergence of the $\tilde{F}^2\Delta$ and $\tilde{H}^1\Pi$ states.

Another notable feature of the NO–Rg spectra is that the $\tilde{F}^2\Delta$ and $\tilde{H}^1\Pi$ states for NO–Ar lie very close in energy, and these states show a significant overlap in NO–Kr. This can be seen in Figure 3(vii) where the $\tilde{F}^2\Delta$ and $\tilde{H}^1\Pi$ states are shown in more detail. This overlap hinders assignment of the origin in the $\tilde{H}^1\Pi$ Rydberg state, although by employing IR-REMPI (see Section 3.1.2), assignment of the origin and members of the vibrational progression was possible for NO–Ar;¹ the most intense member of the vibrational stretch progression has been assigned as $v' = 2$.¹

The laser power used to investigate the excited states has a distinct effect on the appearance of the spectral features observed. This can be seen by comparing spectra taken at low laser power [~ 2 mJ per pulse, recorded by H. Meyer and shown in the upper traces in Figure 3(vii)] and spectra recorded at a higher laser power [~ 5 mJ per pulse, recorded at Nottingham, the lower traces in Figure 3(vii)]. This is discussed in more detail in Section 3.4.2. The $\tilde{H}^1\Pi$ state has a comparatively simple structure – the features are sharp and well defined. The $\tilde{F}^2\Delta$ state is much more complicated however and as a result, identifying the origin feature is problematic (see Section 3.4.1.1).

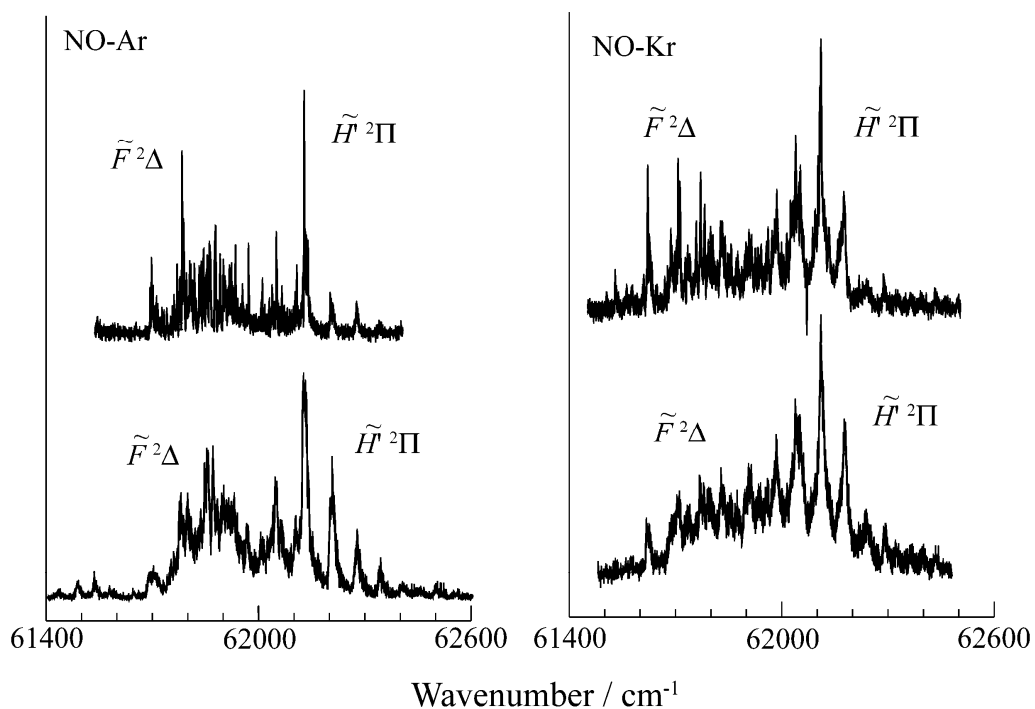
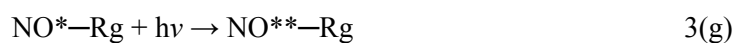


Figure 3(vii): $\tilde{F}^2\Delta$ and $\tilde{H}^2\Pi$ states of NO–Ar and NO–Kr recorded at low laser power (upper traces – recorded by H. Meyer) and high laser power (lower traces).

3.3.3 NO–Xe

Parent ions arising from the NO–Xe complex were not observed in the mass spectrum, unlike the other NO–Rg complexes; however, weak features that may be attributable to NO–Xe were seen in the REMPI spectra recorded via the Xe^+ mass channel. Initial excitation of the NO chromophore can lead to Rg^+ via the following series of steps:



This mechanism has been formulated by Miller.^{11,23} In step 3(g), the electron is excited (by the absorption of three photons) to a high-lying Rydberg orbital to form superexcited NO^{**}-Rg, and this excitation switches to NO-Rg* in 3(h) above. This will only be efficient if an excited state of the rare gas atom is energetically accessible. There are several atomic Xe transitions in the spectral region of interest, which require absorption of three photons, and only transitions that obey the three-photon transition rules are seen (the appropriate selection rules are given in Chapter 5, Section 5.2.2). These transitions are shown with an asterisk in Figure 3(viii). It is also possible for the excited complex NO-Rg* to absorb an additional photon, giving NO and Rg⁺ via dissociative photoionisation.

Also shown in Figure 3(viii) are several weak features, located in the energetic region centred around 62200 cm⁻¹, which are tentatively assigned as arising from the NO-Xe complex. The atomic Xe transitions have been used to calibrate the laser in later work and the assignment of the observed transitions is given in Chapter 5 (Section 5.2.2).

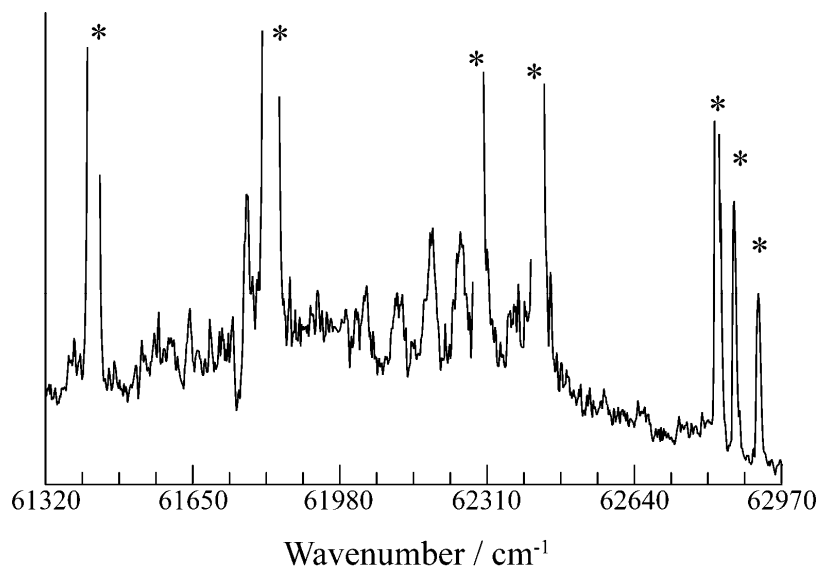


Figure 3(viii): REMPI spectrum recorded in the Xe⁺ mass channel. Features marked with an asterisk are atomic Xe resonances. See text for details.

3.4 Discussion

3.4.1 $\tilde{F}^2\Delta$ and $\tilde{H}^1\Pi$ state origins and vibrational constant determination

In a vibrational progression it is not always straightforward to identify the origin transition (a transition from $v'' = 0$ to $v' = 0$); this is pertinent to the $\tilde{F}^2\Delta$ state, although difficulties also arose in identifying the ν_{00} feature in the $\tilde{H}^1\Pi$ state. Once the origin feature has been assigned, however, the derived energy can be used to determine excited state dissociation energies, thus allowing a comparison of the interaction in each state. The following details how the $\tilde{F}^2\Delta$ and $\tilde{H}^1\Pi$ state origins have been determined.

3.4.1.1 $\tilde{F}^2\Delta$ state origin determination

The $\tilde{F}^2\Delta$ state spectrum is much more complicated than that of other low-lying Rydberg states and as a result it is more difficult to identify a progression in either an intermolecular stretch or bend, and hence to identify an origin feature. An initial identification of the $\tilde{F}^2\Delta$ state origin in NO–Ar was carried out in this work (see Figure 3(ix)). However, a further examination of the spectra obtained in this work, and a comparison with the spectra of H. Meyer and coworkers, has led to a reassignment of the origin feature. A (2 + 1) REMPI spectrum of NO–Ar, which includes the $\tilde{F}^2\Delta$ and $\tilde{H}^1\Pi$ states under consideration is shown in Figure 3(ix). The feature originally identified as the $\tilde{F}^2\Delta$ state origin is the peak labelled *a*; the ν_{00} transition energy was taken to be the onset of this feature at 61645 cm⁻¹. Also labelled are members of the $\tilde{H}^1\Pi$ state intermolecular stretch vibration (ν_σ), including the origin peak ($\nu = 0$).

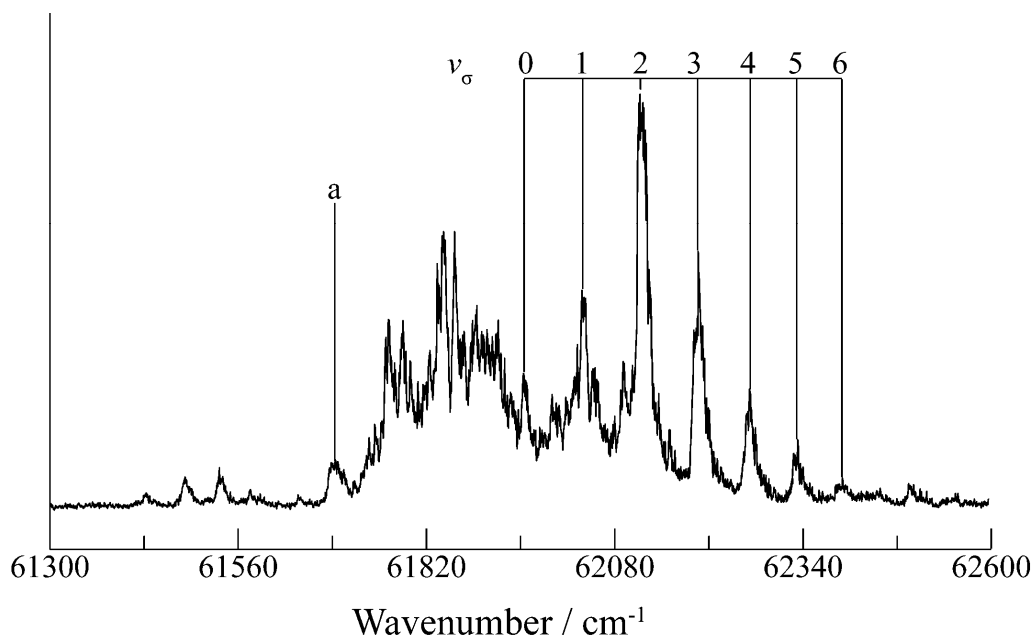


Figure 3(ix): $(2 + 1)$ REMPI spectrum of NO-Ar showing the $\tilde{F}^2\Delta$ and $\tilde{H}^{12}\Pi$ states: (a) original $\tilde{F}^2\Delta$ state origin; (v_g) $\tilde{H}^{12}\Pi$ vibrational progression.

A series of peaks can be seen to lower energy than the $\tilde{F}^2\Delta$ state, as shown in more detail in Figure 3(x). This progression contains four clearly discernable members and was found to have a spacing of $\sim 54 \text{ cm}^{-1}$ between the first and second peaks. These features have been tentatively assigned to the $\tilde{D}^2\Sigma^+$ ($v_{\text{NO}} = 4$) state.

An additional feature is identifiable at 61645 cm^{-1} , $\sim 69 \text{ cm}^{-1}$ to higher energy of the fourth peak of the progression. Since this spacing does not correspond to that of the progression, it has been attributed to the $\tilde{F}^2\Delta$ state and is, in fact, believed to be the $\tilde{F}^2\Delta$ state origin. There is the possibility that this peak may correspond to a hotband *i.e.* a transition from a vibrationally excited ground state, although if this were the case, then the peak would be expected to increase in intensity as warmer parts of the molecular beam are probed (as the population of higher vibrational levels in the ground state increases). The consistency of the appearance of the spectra from this

work and that of H. Meyer and coworkers, suggests that there is little interference from hotbands in this case.

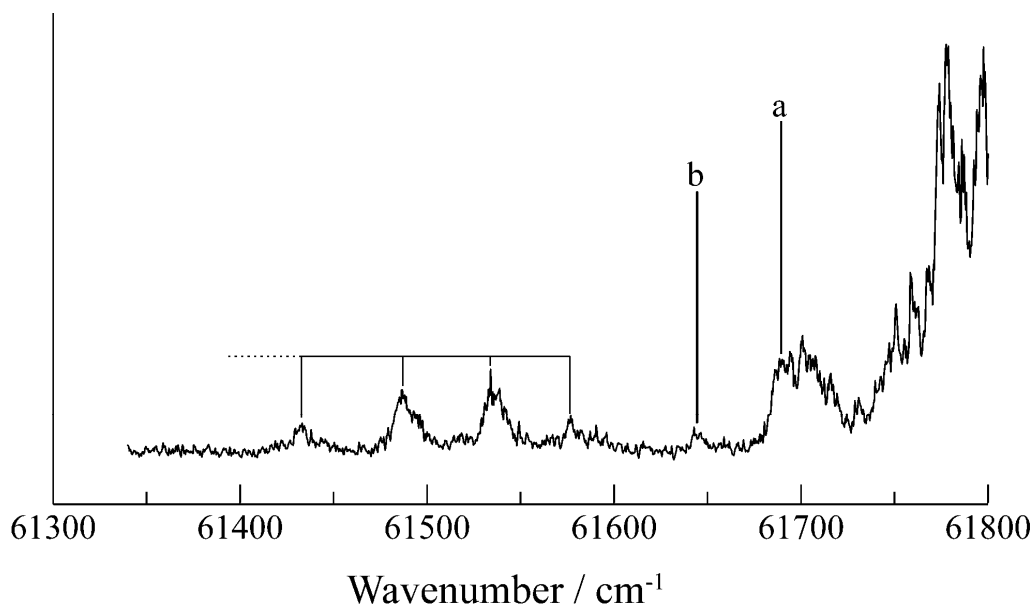


Figure 3(x): an expanded view of the (2 + 1) REMPI spectrum of NO-Ar shown in Figure 3(ix): (a) original $\tilde{F}^2\Delta$ state origin assignment; the "combed" peaks show members of the $\tilde{D}^2\Sigma^+$ ($v_{\text{NO}} = 4$) state; (b) reassigned $\tilde{F}^2\Delta$ state origin.

The $\tilde{F}^2\Delta$ state origin in NO-Kr has been assigned by comparing the spectra obtained in this work with those of H. Meyer and coworkers. The $\tilde{D}^2\Sigma^+$ ($v_{\text{NO}} = 4$) state does not appear in the NO-Kr spectra recorded in this work or that of H. Meyer, so the $\tilde{F}^2\Delta$ state origin has been attributed to the first clearly discernible band at 61501 cm^{-1} . The $\tilde{F}^2\Delta$ state of NO-Kr is shown in the (2 + 1) REMPI spectrum of H. Meyer in Figure 3(xi). The band labelled *a* has been assigned as the origin (v_{00} transition).

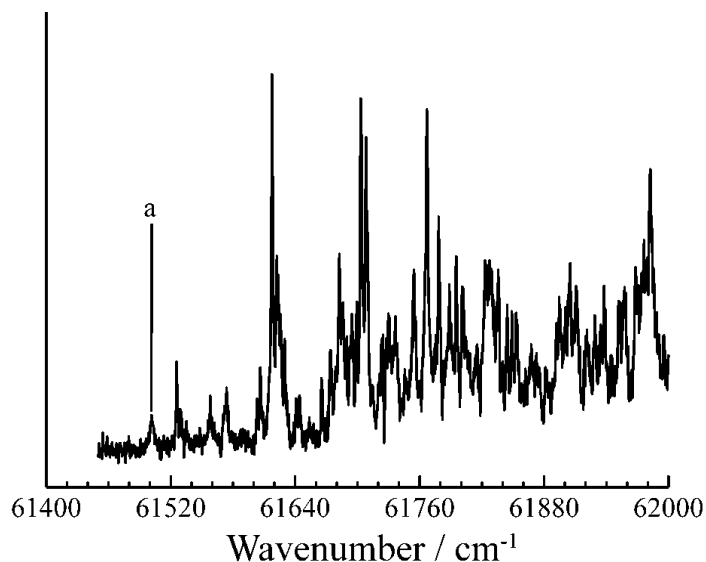


Figure 3(xi): $(2 + 1)$ REMPI spectrum of the $\tilde{F}^2\Delta$ state of NO–Kr, from the contemporaneous study of H. Meyer et al. The band labelled a is the $\tilde{F}^2\Delta$ state origin.

3.4.1.2 $\tilde{H}^2\Pi$ state origin determination

The ν_{00} transition in the $\tilde{H}^2\Pi$ state of NO–Ar is relatively straightforward to identify: an assignment of the $\tilde{H}^2\Pi$ state origin and higher members of the vibrational progression has been carried out in the IR-REMPI work of H. Meyer.¹ In NO–Kr, the $\tilde{F}^2\Delta$ and $\tilde{H}^2\Pi$ states overlap to a greater extent than in NO–Ar, making identification of the NO–Kr $\tilde{H}^2\Pi$ state origin more difficult. Assuming that the Franck-Condon factors for NO–Kr are similar to those for NO–Ar (*i.e.* that there is a similar geometry change during the transition in both cases), a thorough visual analysis of the $(2 + 1)$ REMPI spectrum obtained in this work, and comparison with the high quality spectrum of H. Meyer, leads to a tentative assignment of the band at 61836 cm^{-1} as the origin of the $\tilde{H}^2\Pi$ state. The NO–Kr $\tilde{F}^2\Delta$ and $\tilde{H}^2\Pi$ states are shown in the $(2 + 1)$ REMPI spectrum obtained in this work in Figure 3(xii); the vibrational numbering of the progression in the $\tilde{H}^2\Pi$ state is indicated.

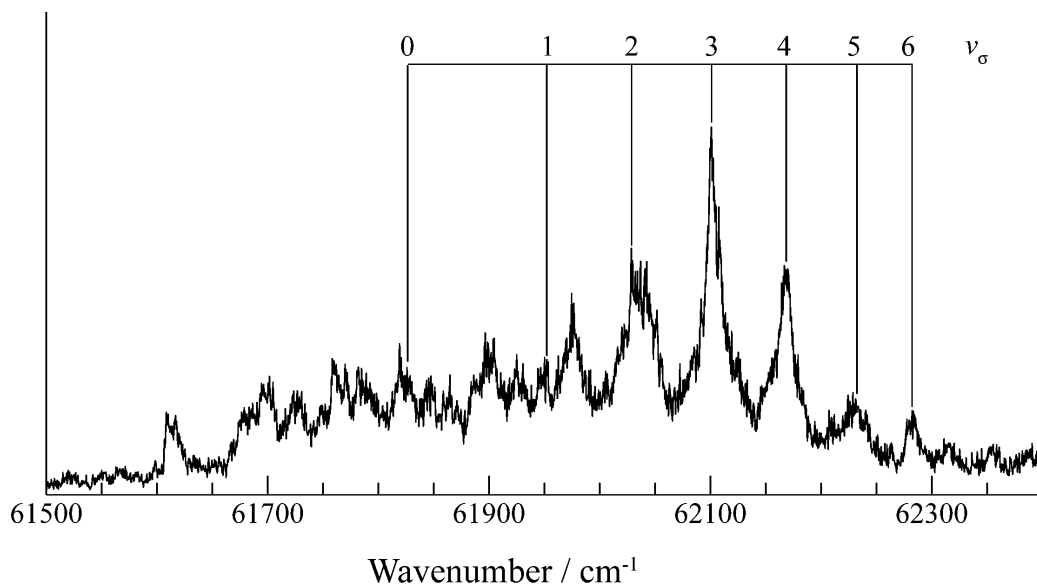


Figure 3(xii): $(2 + 1)$ REMPI spectrum of the $\tilde{F}^2\Delta$ and $\tilde{H}^12\Pi$ states of NO–Kr obtained in this work. The $\tilde{H}^12\Pi$ state vibrational progression is identified.

Higher members of the vibrational stretch progression are comparatively easy to identify and energies have been derived with confidence. Assignment of the origin has allowed an assignment of the vibrational numbering, where the most intense feature is then assigned as $\nu = 3$. Even though the $\tilde{H}^12\Pi$ state origin assignment is not certain, it should be noted that the 0–1 spacing is much larger than the spacing between higher levels would suggest. This may arise because of interactions between the significantly overlapped $\tilde{F}^2\Delta$ and $\tilde{H}^12\Pi$ states.

3.4.1.3 $\tilde{H}^12\Pi$ state vibrational constant determination

The $\tilde{H}^12\Pi$ state harmonic vibrational frequencies and anharmonicity constants were derived using a Birge-Sponer extrapolation, which assumes that the decrease in vibrational spacing, as the vibrational "ladder" is ascended, is linear. Whilst this is approximately the case for lower members of a vibrational progression, at high ν the

spacing can deviate from linearity, due to the effect of long-range forces acting at large intermolecular separations.²⁴ A Birge-Sponer extrapolation requires the observed levels to be fitted to a Morse potential, where the vibrational energy levels can be fitted to an equation of the form:

$$E_{\nu} = \omega_e (\nu + 1/2) - \omega_e x_e (\nu + 1/2)^2 \quad 3(k)$$

The energy spacing between vibrational levels ν and $\nu + 1$ is given by:

$$\Delta E_{(\nu+1,\nu)} = [\omega_e (\nu + 3/2) - \omega_e x_e (\nu + 3/2)^2] - [\omega_e (\nu + 1/2) - \omega_e x_e (\nu + 1/2)^2] \quad 3(l)$$

This can be simplified to give:

$$\Delta E_{(\nu+1,\nu)} = \omega_e - 2\omega_e x_e (\nu + 1) \quad 3(m)$$

A plot of the energy difference between a vibrational level ν and $\nu + 1$, against $\nu + 1$, yields a straight line with a gradient of $-2\omega_e x_e$ and an intercept of ω_e . A Birge-Sponer extrapolation, constructed to determine the vibrational constants of the $\tilde{H}^{12}\Pi$ state of NO–Kr, is shown in Figure 3(xiii).

A linear fit gives $\omega_e = 90.4 \text{ cm}^{-1}$ and $\omega_e x_e = 3.0 \text{ cm}^{-1}$. The vibrational constants of the NO–Ne and NO–Ar $\tilde{H}^{12}\Pi$ states were also derived in this way. The positions of the peaks, used to construct the plot shown above, are those indicated in Figure 3(xii). The $\tilde{F}^2\Delta$ and $\tilde{H}^{12}\Pi$ state origins and vibrational constants of NO–Kr (derived in this work) and NO–Ar (derived in this work and in a similar study by H. Meyer) are

shown in Table 3(I). $\tilde{F}^2\Delta$ and $\tilde{H}^2\Pi$ state origins and vibrational constants of NO–Ne¹ are shown for comparison.

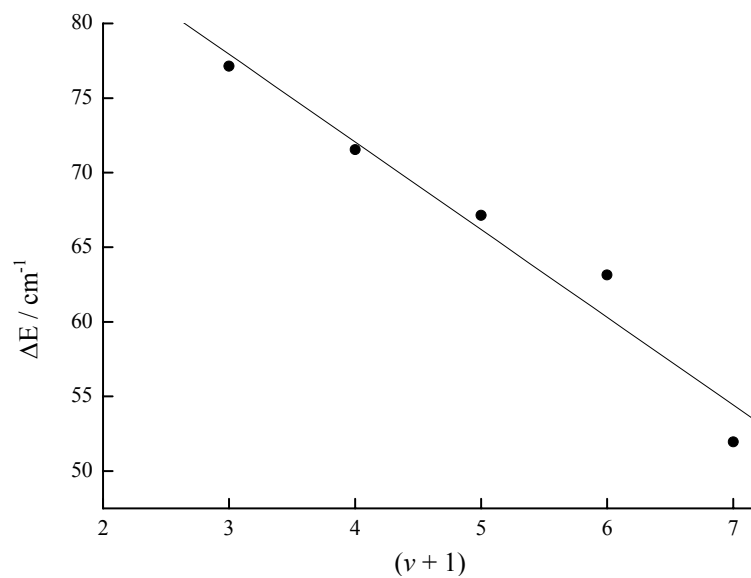


Figure 3(xiii): *Birge-Sponer extrapolation to determine ω_e and $\omega_e x_e$ for the NO–Kr $\tilde{H}^2\Pi$ state.*

NO–Ne	ν_{00}	ω_e	$\omega_e x_e$
$\tilde{F}^2\Delta$	61957 ^a	—	—
$\tilde{H}^1\Pi$	62482 ^a	72 ^b	9 ^b
Cation	—	82 ^c	—
NO–Ar	ν_{00}	ω_e	$\omega_e x_e$
$\tilde{F}^2\Delta$	61645 ^b	51 ^a	—
$\tilde{H}^1\Pi$	61940 ^a	88 ^b	4 ^b
Cation	73869 ^d	100 ^d	7.1 ^d
NO–Kr	ν_{00}	ω_e	$\omega_e x_e$
$\tilde{F}^2\Delta$	61501 ^b	—	—
$\tilde{H}^1\Pi$	61836 ^b	90 ^b	5 ^b
Cation	—	138 ^c	—
NO	$\tilde{F}^2\Delta$	$\tilde{H}^1\Pi$	Cation
ν_{00}	62044 ^a	62717 ^a	74721 ^e

Table 3(I): all values given in cm^{-1} (a) Reference 1; (b) this work. $\tilde{H}^1\Pi$ state constants were obtained from a Birge-Sponer extrapolation (see text for details); (c) Reference 25 (d) Reference 26; (e) Reference 27.

3.4.2 $\tilde{F}^2\Delta$ and $\tilde{H}^1\Pi$ states.

In Figure 3(vi) it can be seen that the $\tilde{F}^2\Delta$ and $\tilde{H}^1\Pi$ states converge in energy, as the rare gas complexing partner increases in atomic weight. Similarly, a comparison of the NO–Ar and NO–Kr spectra shown in Figure 3(vii) reveals a greater overlap of the states as the Ar atom is replaced with Kr. This convergence is also apparent in the

energy difference between these states, which can be determined by comparing the $\tilde{F}^2\Delta$ and $\tilde{H}^2\Pi$ state origins derived above. In NO–Ne, these states are separated by 525 cm^{-1} ; in NO–Ar this difference has reduced to 295 cm^{-1} . Note that for NO–Kr, these states are separated by 335 cm^{-1} , although this value is tentative due to a greater degree of uncertainty in the $\tilde{F}^2\Delta$ and $\tilde{H}^2\Pi$ state transition energies in NO–Kr (see Sections 3.4.1.1 and 3.4.1.2).

As discussed previously in Section 3.1.2, the difference in energy between these two states in uncomplexed NO is due to penetration effects. If penetration of the $3d$ electron is hindered by the presence of a Rg atom, the energy difference between these states is lessened and the states converge as observed. This is shown in Figure 3(xiv).

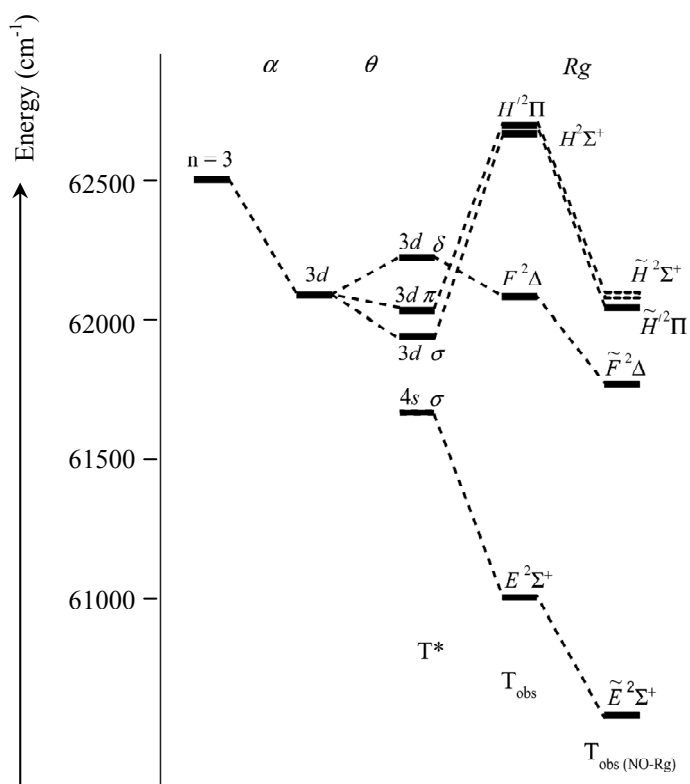


Figure 3(xiv): the observed relative energies (T_{obs}) of the $3d\lambda$ and $4s\sigma$ Rydberg states of uncomplexed NO. The change in energy of each state upon addition of a rare gas atom to the NO chromophore is shown ($T_{obs(NO-Rg)}$).

The relative energies of the $\tilde{F}^2\Delta$ and $\tilde{H}^1\Pi$ states in bare NO are represented by T_{obs} . Once a complexing partner (in this case a rare gas atom) is introduced, the energy difference between these two states is lessened and the states converge in energy as is seen in the spectra shown in Figure 3(vi) – this is represented by $T_{obs(NO-Rg)}$.

Based on the convergence in energy of the $\tilde{F}^2\Delta$ and $\tilde{H}^1\Pi$ states seen in NO–Kr, it seems that the Rydberg orbit is large enough for even a Kr atom to reside within. This leads to interactions between the electrons on the rare gas atom and the Rydberg electron and results in hindered penetration of the Rydberg electron. Penetration effects are responsible for the relative difference in the $\tilde{F}^2\Delta$ and $\tilde{H}^1\Pi$ state energies seen in uncomplexed NO. When these penetration effects are lessened by the presence of a Rg atom, the energetic ordering of the $\tilde{F}^2\Delta$ and $\tilde{H}^1\Pi$ states returns to that expected in the absence of penetration. From the appearance of the NO–Ar and NO–Kr spectra shown in Figure 3(vii), the convergence appears to have increased from NO–Ar to NO–Kr, suggesting that a larger Kr atom will hinder penetration of the $3d$ Rydberg electron to a greater extent than for Ar.

The $3d\pi$ component (the $\tilde{H}^1\Pi$ state) is shown to decrease in energy to a much greater extent than the $3d\delta$ component (the $\tilde{F}^2\Delta$ state). This can also be seen by comparing the transition energies derived in Section 3.4.1 and shown in Table 3(I). For the $\tilde{F}^2\Delta$ state the ν_{00} transition energy decreases from 62044 cm^{-1} in uncomplexed NO¹ to 61501 cm^{-1} in NO–Kr (a redshift of 543 cm^{-1}). In the $\tilde{H}^1\Pi$ state, the uncomplexed NO $H^1\Pi \leftarrow X^2\Pi$ transition energy¹ lies at 62717 cm^{-1} and this falls to 61836 cm^{-1} in NO–Kr (a redshift of 881 cm^{-1}).

3.4.3 Predissociation of the $\tilde{H}^{\prime 2}\Pi$ state.

Previous work¹ has demonstrated that the $\tilde{H}^{\prime 2}\Pi$ state of the NO–Ar complex undergoes predissociation via the continuum of the $\tilde{F}^{\prime 2}\Delta$ state when $\nu' \geq 2$ (two quanta in the intermolecular stretch vibration). The $3d\pi$ and $3d\delta$ states of NO–Ar are shown in the (2 + 1) REMPI spectrum in Figure 3(xv), recorded using a lower laser power by the group of H. Meyer.

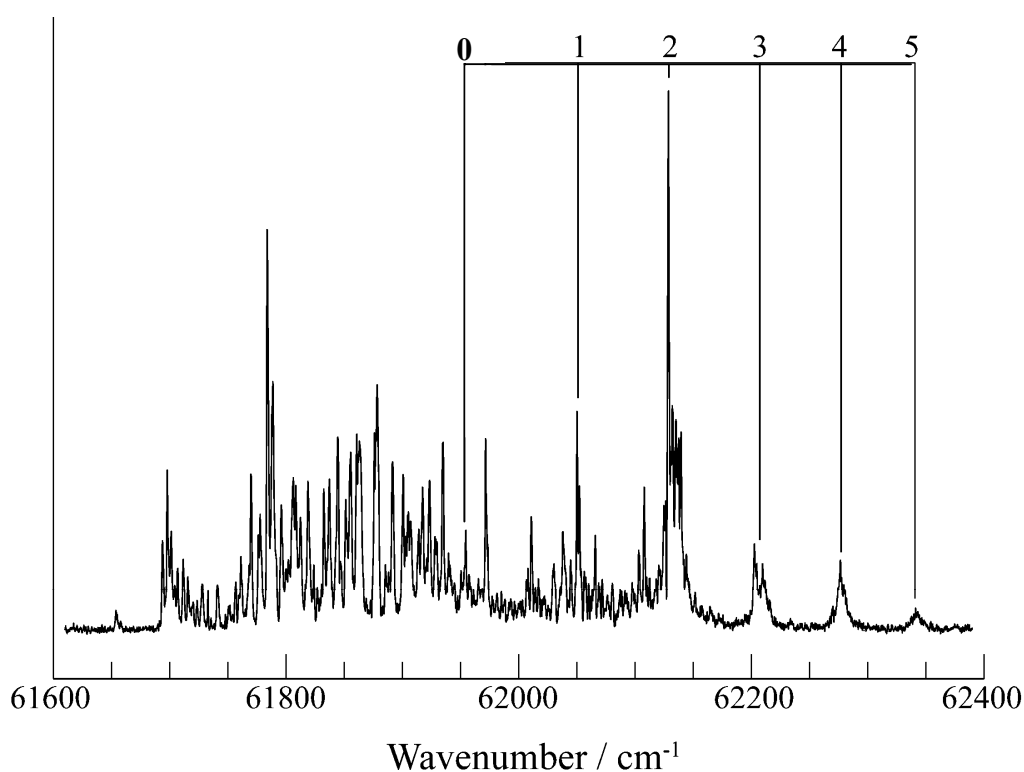


Figure 3(xv): (2 + 1) REMPI spectrum of NO–Ar showing the $\tilde{F}^{\prime 2}\Delta$ and $\tilde{H}^{\prime 2}\Pi$ states, recorded using 2 mJ/pulse (low laser power) by H. Meyer.

Predissociation of the $\tilde{H}^{\prime 2}\Pi$ state is indicated by a sharp drop in peak intensity at $\nu' = 2$ and a broadening of the features to higher energy (the broadening is indicative of the short lifetime of such levels). In fact, the peak corresponding to $\nu' = 2$ is dominated by

a sharp, intense feature at low energy, followed by a weak, much broader contribution to higher energy. This broad feature, centred around $62129 \pm 3 \text{ cm}^{-1}$, is identified as the onset of predissociation, and an expanded view of this peak is shown in the inset in Figure 3(xvi). Using a higher laser power results in power broadening – this can be seen in Figure 3(vii), where spectra were recorded using both high and low laser power. This power broadening obscures the structure in this band and hinders identification of the onset of predissociation.

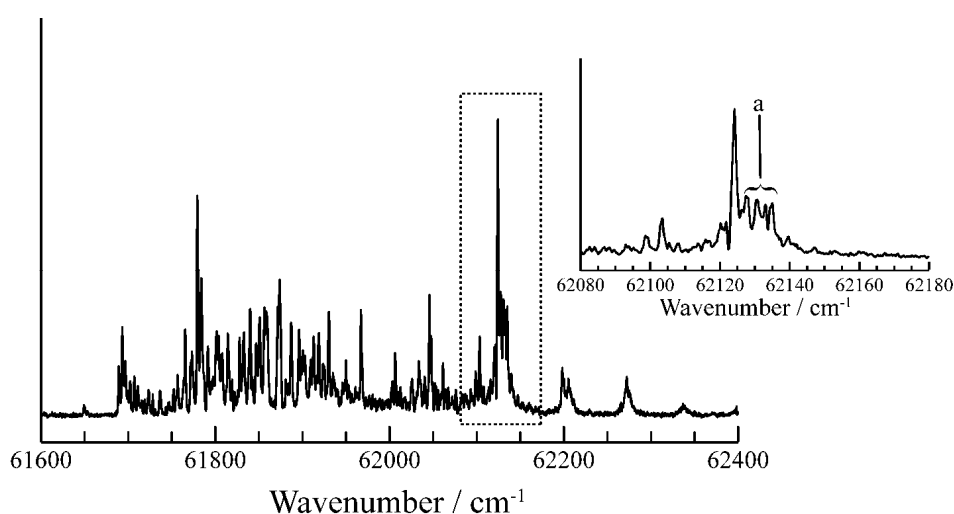


Figure 3(xvi): $(2 + 1)$ REMPI spectrum of NO–Ar showing the $\tilde{F}^2\Delta$ and $\tilde{H}^{12}\Pi$ states, recorded using a low laser power by H. Meyer and coworkers. The feature identified as the onset of predissociation is shown in the inset.

As for NO–Ar, predissociation of the NO–Kr $\tilde{H}^{12}\Pi$ state through the $\tilde{F}^2\Delta$ state can be more clearly seen when using a lower laser power. The $(2 + 1)$ REMPI spectrum of NO–Kr, recorded at a lower laser power by H. Meyer and coworkers, is shown in Figure 3(xvii). The feature at $\sim 62170 \text{ cm}^{-1}$ can be tentatively assigned as $\nu' = 4$, based upon the assignment of the band origin as discussed in Section 3.4.1.2. This feature appears to contain a sharp drop-off in intensity to high energy, and this is believed to

be due to predissociation through the $\tilde{F}^2\Delta$ state. An expanded view of the feature identified as the onset of predissociation, is shown in the inset in Figure 3(xvii).

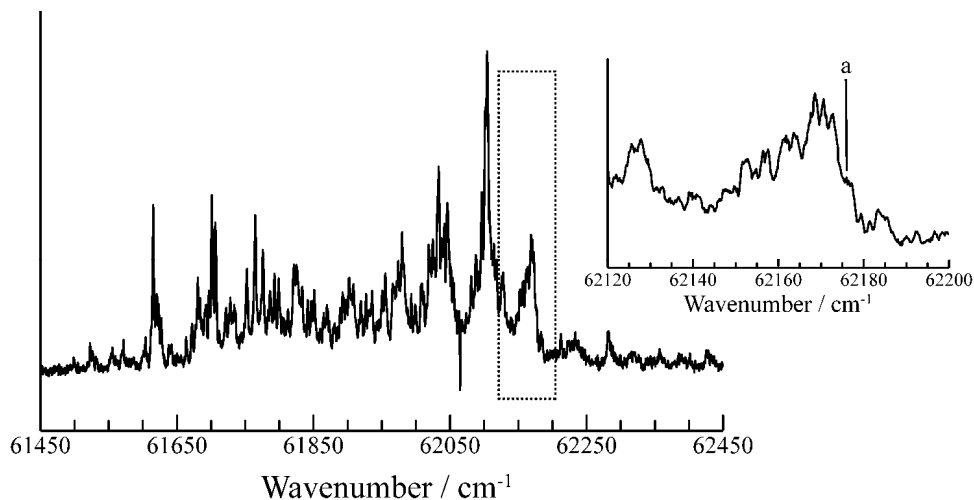


Figure 3(xvii): $(2 + 1)$ REMPI spectrum of NO–Kr showing the $\tilde{F}^2\Delta$ and $\tilde{H}^2\Pi$ states, recorded using a low laser power by H. Meyer and coworkers. The inset shows an expanded view of the onset of predissociation.

A comparison of spectra taken with low and high laser power for each species, as shown in Figure 3(vii), reveals that higher members of the vibrational progression are more apparent in spectra obtained with a higher laser power. Employing a higher laser power (~ 5 mJ per pulse) increases the probability of ionisation occurring before higher vibrational components of the $\tilde{H}^2\Pi$ state predissociate, leading to a competition between ionisation and predissociation. While this allows the higher vibrational components to be assigned with more certainty, it also causes such components to become broadened and can obscure the onset of predissociation. This is particularly evident in the NO–Kr traces, where the *low* power traces reveal a more obvious predissociation onset.

3.4.4 Dissociation energies.

The sharp drop in intensity observed in the feature that has been tentatively assigned as corresponding to $\nu' = 4$ for NO–Kr, and the broad feature within the peak corresponding to $\nu' = 2$ for NO–Ar, gives an estimate for the dissociation energy of the $\tilde{F}^2\Delta$ state relative to the ground state as $62177 \pm 5 \text{ cm}^{-1}$ and $62129 \pm 3 \text{ cm}^{-1}$ for NO–Kr and NO–Ar respectively. Combining these values with the $F^2\Delta \leftarrow X^2\Pi$ transition energy for NO (62044 cm^{-1} from Table 3(I)), gives the ground state dissociation energy (D_0'') of NO–Kr as $133 \pm 5 \text{ cm}^{-1}$ and NO–Ar as $85 \pm 5 \text{ cm}^{-1}$.

For NO–Kr, a determination of 105 cm^{-1} has been reported previously⁷; this was calculated from the $\tilde{A}^2\Sigma^+ \leftarrow \tilde{X}^2\Pi$ transition and was derived from the drop-off in intensity, taken as representing the dissociation of the $\tilde{A}^2\Sigma^+$ state. This value is significantly lower than the value determined in this work. It is possible that the D_0' value derived in the previous study⁷ could be affected by poor Franck-Condon factors; in other words, the drop-off in intensity may not correspond to dissociation of the NO–Kr complex. This seems unlikely however, based upon the appearance of the spectrum presented in the study of Gamblin *et al.*⁷ where there is a sharp drop in intensity to high energy. Additionally, the value of 105 cm^{-1} derived in that work is in good agreement with the value of 112 cm^{-1} calculated recently by Kłos.²⁸ Another possibility is that there is a barrier to dissociation in the $\tilde{F}^2\Delta$ state. Tsuji *et al.*⁹ have determined a barrier of 24 cm^{-1} for the $\tilde{A}^2\Sigma^+$ state of NO–Ar. In that work, a comparison of the average $\tilde{A}^2\Sigma^+$ state radius (4.75 \AA),²⁹ with the experimentally determined internuclear distance of NO–Ar in the $\tilde{A}^2\Sigma^+$ state (4.6 \AA), reveals that the Ar atom is located within the Rydberg orbit. Upon dissociation, when the internuclear separation increases, the Ar atom passes through the $3s\sigma$ Rydberg orbit radius. This is the region where a repulsive interaction between the Rydberg electron and the

electrons on the Ar atom will be most effective, and hence where a potential barrier to dissociation exists.⁹ It is possible that a similar barrier exists in the $\tilde{F}^2\Delta$ state of NO–Kr; for the experimental value of 105 cm^{-1} ,⁷ to be consistent with the present observations, a barrier of $28 \pm 5\text{ cm}^{-1}$ would have to be present. For NO–Ar, no barrier is required since the experimentally derived value of $85 \pm 5\text{ cm}^{-1}$ is in good agreement with the established value⁴⁷ of 88 cm^{-1} .

Derivation of the origins of the $\tilde{F}^2\Delta$ and $\tilde{H}^2\Pi$ states allows a determination of the dissociation energies of these excited states (D_0') if the ground state dissociation energy D_0'' is known. The excited state NO–Rg origin – $\nu_{00}(\text{NO–Rg})$ – a transition from $\nu'' = 0$ in $\tilde{X}^2\Pi$ to $\nu' = 0$ in $\tilde{F}^2\Delta$ or $\tilde{H}^2\Pi$, can be combined with the ground state dissociation energy D_0'' of the complex and the excited state NO origin ($\nu_{00}(\text{NO})$) to give the excited state dissociation energy using Equation 3(n).

$$D_0' = \nu_{00}(\text{NO}) + D_0'' - \nu_{00}(\text{NO–Rg}) \quad 3(\text{n})$$

The calculated dissociation energies of the excited states of NO–Ne, NO–Ar and NO–Kr are shown in Table 3(II). Ground state dissociation energies of 35 cm^{-1} , 88 cm^{-1} and 105 cm^{-1} are used for the complexes NO–Ne,¹ NO–Ar⁹ and NO–Kr⁷ respectively.

The dissociation energy of the $3d\pi$ and $3d\delta$ states increases as the Rg group is descended. This is not surprising given the polarisabilities of the rare gas atoms: Ne, Ar and Kr have polarisabilities of 0.396 \AA^3 , 1.64 \AA^3 and 2.48 \AA^3 respectively. In the $\tilde{F}^2\Delta$ and $\tilde{H}^2\Pi$ states, the Rg atom resides within the Rydberg orbit and experiences an interaction, which is dominated by the ion/induced-dipole term. The magnitude of this interaction will increase as the Rg atom electron-count and polarisability increases.

	$\tilde{F}^2\Delta$	$\tilde{H}^1\Pi$	Cation
NO–Ne	119 ^a	270 ^a	284 ± 10 ^d
NO–Ar	487 ^b	865 ^a	941 ^c
NO–Kr	648 ^b	986 ^b	1200 ± 30 ^d

Table 3(II): *all values given in cm⁻¹ (a) Reference 1; (b) this work; (c) derived using Equation 3(n) with ν_{00} (NO), D_0'' and ν_{00} (NO–Ar) from References 27, 9 and 26 respectively; (d) D_0' derived from D_e' , $\omega_{(s)}$ and $\omega_{(b)}$ given in Reference 25, using $D_0 = D_e - 1/2(\omega_s + \omega_b)$.*

For NO–Ne and NO–Ar, the dissociation energy of the $3d\pi$ state is a large proportion of that of the cation (95% and 92% respectively, based upon the values given in Table 3(II)). For NO–Kr, the excited state dissociation energy falls to just 82% of that of the cation. This value is tentative, however, due to the difficulties encountered in identifying the origin of the $\tilde{H}^1\Pi$ state. This trend suggests that, for a larger Rg atom, repulsive effects between the $3d$ electron and the Rg atom become more important. The interaction becomes less cationic as the larger Rg atoms become more effectively shielded from the NO^+ core, by the repulsive effects of the Rydberg electron. If NO–Xe spectra could be observed (not possible due to the presence of strong atomic Xe resonances in the spectral region of interest – see Section 3.3.3), it would be possible to extend this trend to the larger Xe complexing partner. This conclusion, that the smaller Ne and Ar atoms are better able to see the cationic core, may also explain the trends seen in the vibrational frequencies of the $3d\pi$ state, as shown in Table 3(I). The $\tilde{H}^1\Pi$ state NO–Ne and NO–Ar vibrational frequencies are very close to the cationic values (both are 88% of the cationic value). For NO–Kr, the

$\tilde{H}^{12}\Pi$ state vibrational frequency is just 65% of the cationic value, suggesting that Kr may be prevented from seeing the NO^+ core due to the presence of the $3d\pi$ electron.

A comparison of the dissociation energies of the $\tilde{F}^2\Delta$ and $\tilde{H}^{12}\Pi$ states of NO–Ar and NO–Kr reveal that the $3d\delta$ component is less strongly bound than the $3d\pi$ component – the $3d\delta$ electron seems to be more effective at shielding the Rg atom from the ion core. In other words, the $\tilde{H}^{12}\Pi$ states for both complexes are more cationic than the $\tilde{F}^2\Delta$ states. This implies that penetration of the $3d$ electron has a greater effect on the $3d\delta$ state so the rare gas atom is more effectively shielded from the cationic core. Similarly, the stronger binding energy in the $3d\pi$ state suggests an interaction that can be approximated more closely by an ion/induced-dipole type interaction. The reason for this is not clear although orientation of the rare gas atom with respect to the NO d -orbitals may have an effect. These orientation effects have already been considered for the $3s$ and $3p$ Rydberg states of NO–Ar by Shafizadeh *et al.*¹⁰

3.4.5 Orientation effects

Since the $\tilde{H}^{12}\Pi$ state is known to have a vibrationally-averaged T-shaped geometry,¹ the rare gas atom can be considered as lying along the x -axis, where the z -axis defines the N–O molecular bond and the plane xz defines the molecular plane. The $3d\pi$ state arises from occupation of the d_{xz} and d_{yz} orbitals; one of these components (the d_{yz} orbital) will have lobes lying out of the molecular plane. In this case the Rg will have a view of the NO^+ core and the interaction will be attractive. The remaining component (resulting from occupation of the d_{xz} orbital) will experience a large repulsion with the Rg atom as shown in Figure 3(xviii). It seems likely that these components will have significantly different energies (in the $\tilde{C}^2\Pi$ state it was found that the two electronic components were split by 4000 cm^{-1}).¹⁰

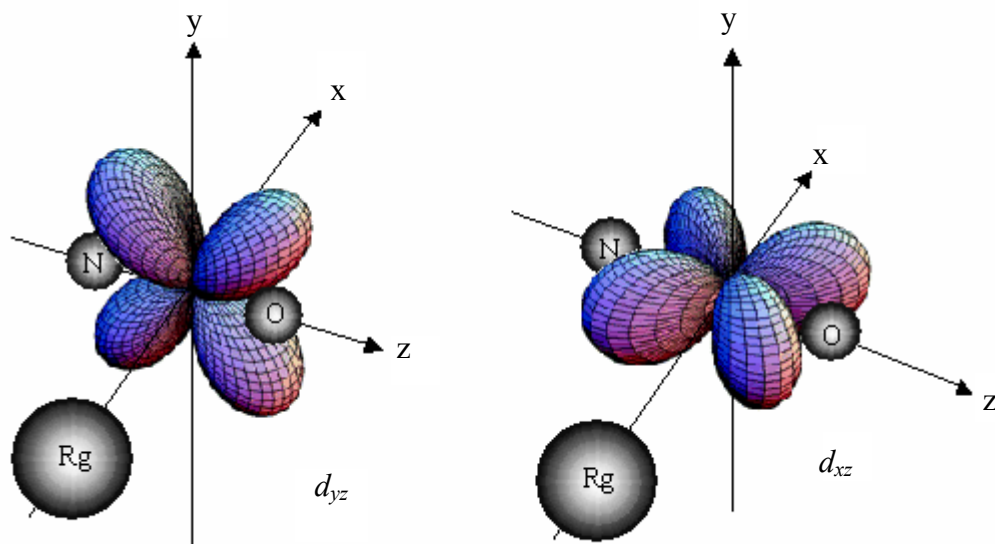


Figure 3(xviii): orientation of the d_{yz} (shown on the left) and d_{xz} orbitals (shown on the right), with respect to the Rg atom in the two $3d\pi$ components of the $\tilde{H}^2\Pi$ state.

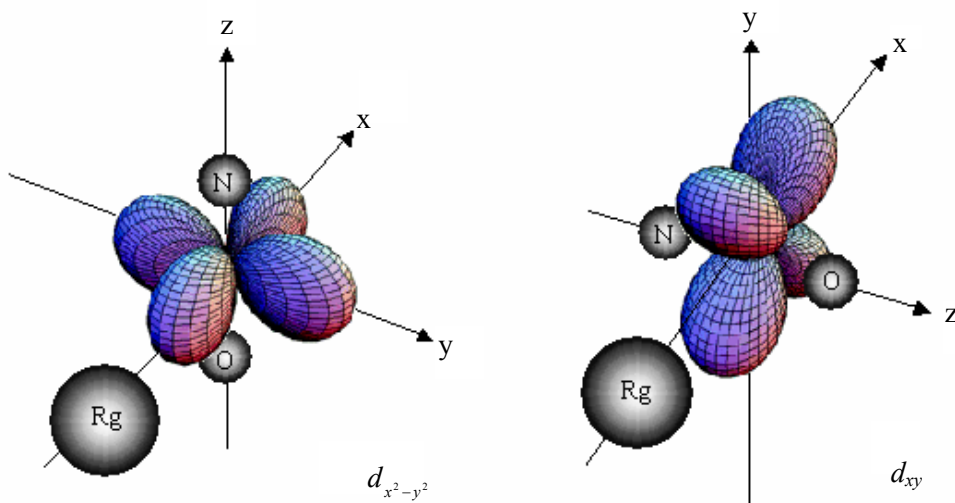


Figure 3(xix): orientation of the $d_{x^2-y^2}$ (shown on the left) and d_{xy} orbitals (shown on the right), with respect to the Rg atom in the two $3d\delta$ components of the $\tilde{F}^2\Delta$ state.

In the $3d\delta$ state, the occupied orbitals are $d_{x^2-y^2}$ and d_{xy} . Both components will have out-of-plane contributions, where electron density is directed out of the molecular

plane (along the y -axis). However, both components will direct electron density towards the Rg atom (along the x -axis), as with the d_{xz} component of the $\tilde{H}^1\Pi$ state: therefore, the dramatic energy difference expected for the two components of the $3d\pi$ state, based on the work of Shafizadeh *et al.*¹⁰ is not expected for the $3d\delta$ state, where the two components may lie closer in energy. The two $\tilde{F}^2\Delta$ state contributions are shown in Figure 3 (xix).

Such orientational considerations suggest that only one component of the $3d\pi$ state is observed, whilst the $3d\delta$ state may be composed of two components, with differing geometries. This corresponds with the fact that the $3d\delta$ state of NO–Ne could only be simulated with two contributions.^{1,14}

3.5 Conclusions

The $\tilde{F}^2\Delta$ and $\tilde{H}^1\Pi$ states of the NO–Rg complexes have been investigated using (2 + 1) REMPI spectroscopy, and new data for NO–Kr has been presented. Although attempts were made to record similar spectra of the NO–Xe complex, the presence of strong, three-photon atomic Xe absorptions in the spectral region of interest caused significant difficulties. (2 + 1) REMPI spectra of NO–Ne and NO–Ar have also been recorded in order to compare with the NO–Kr spectra obtained here.

Both electronic states are found to move to lower energy as the size of the complexing partner is increased: evidence that the excited states are more strongly bound than the ground state. This work has shown that the size of the Rydberg orbit is such that a Rg atom is able to reside within, and this is reflected in the spectra as the $\tilde{F}^2\Delta$ and $\tilde{H}^1\Pi$ states converge in energy. In uncomplexed NO, the energetic ordering of the $3d\lambda$ Rydberg states is determined by interactions between the weakly-penetrating Rydberg

electron and the NO^+ core. When penetration of the Rydberg electron is hindered by the presence of the Rg atom within the Rydberg orbit, these interactions are restricted and the energetic ordering of the states begins to return to that expected for a non-penetrating electron *i.e.* $\sigma < \pi < \delta$.

The convergence of the $\tilde{F}^2\Delta$ and $\tilde{H}^1\Pi$ states leads to predissociation of the $\tilde{H}^1\Pi$ state via the $\tilde{F}^2\Delta$ state. In the spectra this was seen as a sharp drop-off in intensity of the $\tilde{H}^1\Pi$ state features lying above the dissociation limit of the $\tilde{F}^2\Delta$ state. This was already known to be the case for NO-Ar ,¹ and this work has revealed that predissociation also occurs for NO-Kr . A comparison of the spectra obtained in this work with those of B. Wen and H. Meyer, reveals a competition between ionisation from the higher members of the $\tilde{H}^1\Pi$ state progression, and their predissociation via the $\tilde{F}^2\Delta$ state, at a high photon density. When using a high laser power, ionisation was favoured over predissociation, leading to higher members of the vibrational progression being more intense and easier to identify. However, the increased broadening of the features, associated with a higher photon density, was found to obscure the onset of predissociation. Using a lower laser power allowed the onset of predissociation, and hence the dissociation energy of the $\tilde{F}^2\Delta$ state, to be determined.

The ν_{00} transition of both the $\tilde{F}^2\Delta$ and $\tilde{H}^1\Pi$ states has been identified, although for NO-Kr , the overlap between these states makes identification of the latter more challenging. The $\tilde{F}^2\Delta$ state origin in NO-Ar was identified after a weak progression, attributed to the $\tilde{D}^2\Sigma^+$ ($\nu_{\text{NO}} = 4$) state was found in the (2 + 1) REMPI spectra recorded at the University of Nottingham. An additional feature, which did not belong to the $\tilde{D}^2\Sigma^+$ state progression, was then assigned as the $\tilde{F}^2\Delta$ state origin. These origin assignments have allowed the dissociation energy of the excited states to be

determined for NO–Kr in this work, and compared with values for NO–Ar and NO–Ne in order to examine trends across the series. Vibrational constants were calculated using a Birge-Sponer extrapolation, after identifying members of the vibrational stretch progression for the $\tilde{H}^1\Pi$ state. It was not possible to identify a progression in the intermolecular stretch in the $\tilde{F}^2\Delta$ state, due to the significantly more complicated appearance of the $\tilde{F}^2\Delta$ state spectra. Comparing the excited state dissociation energies with those of the cations revealed that the $\tilde{H}^1\Pi$ state became less cationic as the Rg atom increased in size. This has been attributed to the greater repulsive interaction between the electrons on the larger and more polarisable Rg atoms, and the Rydberg electron. As a result of this repulsive interaction, the larger Rg atoms are more effectively shielded from the NO^+ core.

The $\tilde{F}^2\Delta$ state spectrum was found to be considerably more complicated than that of the $\tilde{H}^1\Pi$ state. One possible explanation for this is the orientation of the Rg atom with respect to the NO d -orbitals that contribute to the two electronic states. The significant difference in energy between the two components (d_{yz} and d_{xz}) that make up the $3d\pi$ state suggests that only one component is seen in this work. In the $3d\delta$ state, both components are likely to have a similar energy and the spectrum observed may consist of two components, with differing geometries. This offers an explanation for the fact that simulation of the NO–Ne $\tilde{F}^2\Delta$ state was only possible using two geometries.

This work has shown that penetration of the $3d$ Rydberg electron is hindered by the presence of a Rg atom and that this leads to a convergence in energy of the $\tilde{F}^2\Delta$ and $\tilde{H}^1\Pi$ states. It was shown that, for NO–Kr, the $\tilde{H}^1\Pi$ state predissociates via the continuum of the $\tilde{F}^2\Delta$ state. This predissociation, and identification of the $\tilde{F}^2\Delta$ and

$\tilde{H}^{12}\Pi$ state origins has allowed the excited state dissociation energies to be determined. However, the $\tilde{H}^{12}\Pi$ state origin determination is hindered by overlap with the $\tilde{F}^{2}\Delta$ state. Performing an IR-REMPI experiment, similar to that carried out in previous work,¹ in which the $\tilde{H}^{12}\Pi \leftarrow \tilde{X}^{2}\Pi$ transition was removed by exciting via an N–O bending mode, would allow a less tentative assignment of the $\tilde{H}^{12}\Pi$ state vibrational origin.

3.6 References

¹ Y. Kim, H. Meyer, *Int. Rev. Phys. Chem.* **20**(3) (2001) 219-282.

² Ch. Jungen, *J. Chem. Phys.* **53**(11) (1970) 4168-4182.

³ A.M. Bush, J.M. Dyke, P. Mack, D.M. Smith, T.G. Wright, *J. Chem. Phys.* **105** (22) (1996) 9804.

⁴ A.M. Bush, J.M. Dyke, P. Mack, D.M. Smith, T.G. Wright, *J. Chem. Phys.* **108** (1998) 406.

⁵ P. Mack, J.M. Dyke, T.G. Wright, *J. Chem. Soc. Faraday Trans.* **94** (1998) 629-634.

⁶ J.D. Barr, J.M. Dyke, P. Mack, D.M. Smith, T.G. Wright, *J. Elec. Spect. Rel. Phen.* **97** (1998) 159-170.

⁷ S.D. Gamblin, S.E. Daire, J. Lozeille, T.G. Wright, *Chem. Phys. Lett.* **325** (2000) 232-240.

- ⁸ J. Lozeille, S.E. Daire, S.D. Gamblin, T.G. Wright, E.P.F. Lee, *J. Chem. Phys.* **113** (2000) 7224.
- ⁹ K. Tsuji, K. Shibuya, K. Obi, *J. Chem. Phys.* **100** (1994) 5441.
- ¹⁰ N. Shafizadeh, P. Bréchignac, M. Dyndgaard, J.H. Fillion, D. Gauyacq, B. Levy, J.C. Miller, T. Pino, M. Raoult, *J. Chem. Phys.* **108** (1998) 9313.
- ¹¹ J.C. Miller, *J. Chem. Phys.* **86** (6) (1987) 3166-3171.
- ¹² H. Meyer, *J. Chem. Phys.* **107** (19) (1997) 7721-7731.
- ¹³ H. Meyer, *J. Chem. Phys.* **107** (1997) 7732.
- ¹⁴ J. Fleniken, Y. Kim, H. Meyer, *J. Chem. Phys.* **109** (20) (1998) 8940-8947.
- ¹⁵ P. Mack, J.M. Dyke, D.M. Smith, T.G. Wright, H. Meyer, *J. Chem. Phys.* **109**(11) (1998) 4361-4366.
- ¹⁶ J.C. Miller, W-C Cheng, *J. Chem. Phys.* **89** (1985) 1647-1653.
- ¹⁷ K. Tsuji, K. Aiuchi, K. Shibuya, K. Obi, *Chem. Phys.* **231**(2-3) (1998) 279-288.
- ¹⁸ S.S. Khohlova, N.G. Lebedev, S.L. Bondarev, V.N. Knyukshto, A.A. Turban, V.A. Mikhailova, A.I. Ivanov, *Int. J. Quan. Chem.* **104**(2) (2005) 189-196.
- ¹⁹ J.A.E. Silber, Final Year Report, University Of Nottingham, 2006.

²⁰ G. Herzberg, *Molecular Spectra and Molecular Structure I. Spectra of Diatomic Molecules*, D. Van Nostrand Company Inc. New York, 1950, pp 658.

²¹ <http://webbook.nist.gov/chemistry/form-ser.html>.

²² A. Bondi, *J. Phys. Chem.* **68**(3) (1968) 441.

²³ J.C. Miller, *J. Chem. Phys.* **90** (1989) 4031-4036.

²⁴ L. R. Brock, M. A. Duncan, *J. Chem. Phys.* **21** (1995) 9200-9211.

²⁵ E.P.F. Lee, P. Soldán, T.G. Wright, *J. Phys. Chem. A.* **102** (1998) 6858.

²⁶ M. Takahashi, *J. Chem. Phys.* **96** (1992) 2594.

²⁷ G. Reiser, W. Habenicht, K. Müller-Dethlefs, E.W. Schlag, *Chem. Phys. Lett.* **152** (1988) 119.

²⁸ J. Kłos, private communication.

²⁹ J. Goodman, L.E. Brus, *J. Chem. Phys.* **67** (1977) 933.

4 *Electronic spectroscopy of NO–Rg_x complexes (Rg = Ne, Ar) via the 4s and 3d*

Rydberg states

4.1 *Introduction*

The spectroscopy of nitric oxide-containing van der Waals complexes has been of significant interest, both in the gas phase and in the bulk. The van der Waals dimers of NO bound to a rare gas atom have been the most widely studied. A more detailed review of relevant work is given in Chapter 3, where the 3d Rydberg states of NO–Rg have been investigated.

4.1.1 *Previous work on NO in Ne and Ar matrices*

The spectroscopy of NO has been investigated in various rare gas matrices in a series of studies.^{1,2,3,4,5} In the Ne matrix studies¹ the 3s, 3p, 4s and 4p Rydberg states were observed, upon excitation from the ground state. The absence of the 3dλ states in the fluorescence excitation spectrum of NO in solid Ne was attributed to the 3dλ states being weak and broadened, and/or partly coupled to a non-fluorescing channel. In the Ar^{1,2} and Kr² matrix studies, only the 3s and 3p Rydberg states were seen. That only the $n = 3$ ($\tilde{A}^2\Sigma^+$, $\tilde{C}^2\Pi$, $\tilde{D}^2\Sigma^+$) and $n = 4$ ($\tilde{E}^2\Sigma^+$, $\tilde{K}^2\Pi$, $\tilde{M}^2\Sigma^+$) Rydberg series are seen in a Ne matrix, and only the $n = 3$ Rydberg series is seen in an Ar matrix was addressed in Reference 1: The electronic absorption of rare gas solids is widely interpreted in terms of Wannier excitons, which represent bound electron-hole pairs as a hydrogenic pair in a dielectric medium, with an energy described by the hydrogenic formula.¹ (The term "hole" is used to describe the vacant orbital from which the electronic transition was initiated.)

$$E_n^i = E_G^i - B^i / n^2 \quad \text{for } n \geq 2 \quad 4(a)$$

n is the principal quantum number of the exciton (where n is the principal quantum number of the orbital to which a transition takes place and "exciton" is an electron-hole pair). E_G^i is the ionisation potential of the dopant undergoing excitation in the solid. The constant B^i is an effective Rydberg constant and is essentially independent of the nature of the species undergoing an excitation. B^i takes account of the dielectric shielding due to the crystal (ϵ) and the effective mass of the electron in the conduction band of the solid (m^*) and is given by:¹

$$B^i = 13.6 m^* / \epsilon^2 \quad 4(b)$$

Values of E_G^i and B^i are given in energy units (eV); the quantity ϵ is dimensionless (in Reference 6 the value of m^* for NO in a Ne, Ar and Kr matrix is given as 1, although no units are assigned). This treatment is adequate for excitons with $n \geq 2$, however $n = 1$ excitons, with radii smaller than the unit cell of the matrix, are not described well by Equation 4(a). In order to describe all exciton states a later description^{7,8} of Equation 4(a) incorporates the quantum defect:¹

$$E_n^i = E_G^i - B^i / (n - \delta_n)^2 \quad 4(c)$$

This quantum defect model assumes that the electron-hole interaction in the matrix is the same as in the isolated atom, within a particular radius – beyond this radius, the electron-hole interaction is a screened Coulombic potential, where the excited electron lies at distances beyond the matrix cage radius. The quantum defect δ_n (the value of which is different in the matrix than that in the gas phase) together with B^i , includes the solid-state effects due to the surrounding atoms and the deviations from the

Coulombic potential, caused by an interaction between the excited electron and the positively charged dopant core. In order to rationalise the fact that the $n = 4$ Rydberg states are not observed in the Ar matrix, despite the quantum defect formula predicting these states at accessible energies, Chergui *et al.*¹ proposed that a more thorough description of the matrix-isolated NO Rydberg energies is needed. For example, a potential that incorporates the short-range core potential experienced by the electron, together with the long-range shielded Coulombic electron-hole interaction, and the purely Coulombic interaction at distances intermediate between the core and the matrix cage radius.

In matrices, the lower Rydberg states are found to be blueshifted. This blueshift arises from a strong repulsive interaction, as the Rydberg orbital overlaps with the closed shells of the surrounding Rg matrix atoms. The magnitude of the shift will depend on the interaction between the NO Rydberg electron wavefunctions and the nearest neighbours in the matrix. In Reference 1 it was shown that the overlap (and hence the magnitude of the repulsive interaction and the resultant blueshift) between the Rydberg state wavefunctions and the p wavefunctions of the Ne, Ar and Xe matrix atoms increased in the order $s\sigma < p\sigma < p\pi$. It was also shown that the wavefunction overlap increases as the size of the matrix atoms increases (from Ne to Xe).¹

The ionisation energy of NO in a rare gas matrix is found to be redshifted relative to the gas phase value of 9.26 eV.⁹ The magnitude of the redshift increases in the order Ar < Kr < Xe (for NO in an Ar matrix, the ionisation energy is 8.26 ± 0.15 eV).¹ The NO ionisation energy in the Ne matrix was found to be slightly blueshifted, although to a lesser extent than the lower Rydberg states. Zerza *et al.*³ investigated transitions between Rydberg states of NO in an Ar matrix, using fluorescence depletion spectroscopy. Transitions from the $3s$ ($\tilde{A}^2\Sigma^+$) Rydberg state to the $3p$ ($\tilde{C}^2\Pi$, $\tilde{D}^2\Sigma^+$),

$3d$ ($\tilde{H}^2\Sigma^+$, $\tilde{H}'^2\Pi$), $4s$ ($\tilde{E}^2\Sigma^+$) and $4p$ ($\tilde{K}^2\Pi$, $\tilde{M}^2\Sigma^+$) Rydberg states are observed. (Note that a transition to the $\tilde{F}^2\Delta$ state is forbidden because of the $\Delta\Lambda = 2$ selection rule, for a one-photon transition $\Delta\Lambda = 0, \pm 1$ only). Since the excitation is now from the $\tilde{A}^2\Sigma^+$ state (and not from the ground state as in the study of Chergui *et al.*¹), the Franck-Condon factors and line strengths are altered and allow the $n = 4$ Rydberg states to be observed. Despite Rydberg transitions from the ground state exhibiting strong blueshifts in the matrix relative to the gas phase, Zerza *et al.*³ found that the Rydberg-Rydberg transitions showed a redshift. This suggests a compression in energy of the Rydberg series, as expected from the redshift of the ionisation energy. Higher- n states were not observed when exciting from the $\tilde{A}^2\Sigma^+$ state or directly from the ground state. In Reference 3 this was attributed to these higher- n ($n \geq 5$) Rydberg states being compressed into a small energy range of ~ 0.3 eV below the ionisation energy of NO in the Ar matrix. This gives rise to a quasi-continuous absorption, just below the ionisation threshold.³

More recent work on electronically-excited NO in rare gas matrices has focused primarily on the dynamics of the structural relaxation that follows the optical excitation of a Rydberg state.^{4,5,10,11,12} In all cases, the effect of formation of the $3s\sigma$ ($\tilde{A}^2\Sigma^+$) Rydberg state of NO on the surrounding matrix was probed. The matrices investigated were Ne (solid phase)^{11,12} and Ar (solid^{4,5} and fluid¹⁰ phases), as well as H₂ and D₂ (both in the solid phase). In all cases, the formation of a Rydberg state leads to the formation of a "bubble" – a cavity surrounding the molecule – as the atoms in the solvent cage are pushed outwards by a repulsive interaction with the Rydberg electron.⁴ In the solid Ar matrix, Jeannin *et al.*¹³ found that the formation of the $\tilde{A}^2\Sigma^+$ Rydberg state results in an initial perturbation of the first solvation shell, which has a temporal width of ~ 180 fs. This initial perturbation was followed by low-frequency oscillatory motion of the solvent cage for up to ~ 2 ps.

4.1.2 Previous work on NO–Rg_x clusters

Between the much-studied NO–Rg van der Waals dimers (see Chapters 3, 5 and 6) and NO in a bulk matrix, lies the realm of clusters. NO radicals in Rg_x clusters have been investigated primarily via theory,^{14,15} and NO^{+/-}–Rg_x clusters have been studied mass spectrometrically.^{16,17,18} The lowest energy cluster structures for NO–Ar_x where $x \leq 25$ have been described in the recent theoretical work of Naumkin *et al.*^{14,15} The NO molecule was found to lie on the surface of the cluster, with the structure resembling that for the Ar_{x+1} cluster. The calculated geometries of the complexes NO–Ar_x ($x = 1–6$) are shown in Figure 4(i), taken from Reference 14.

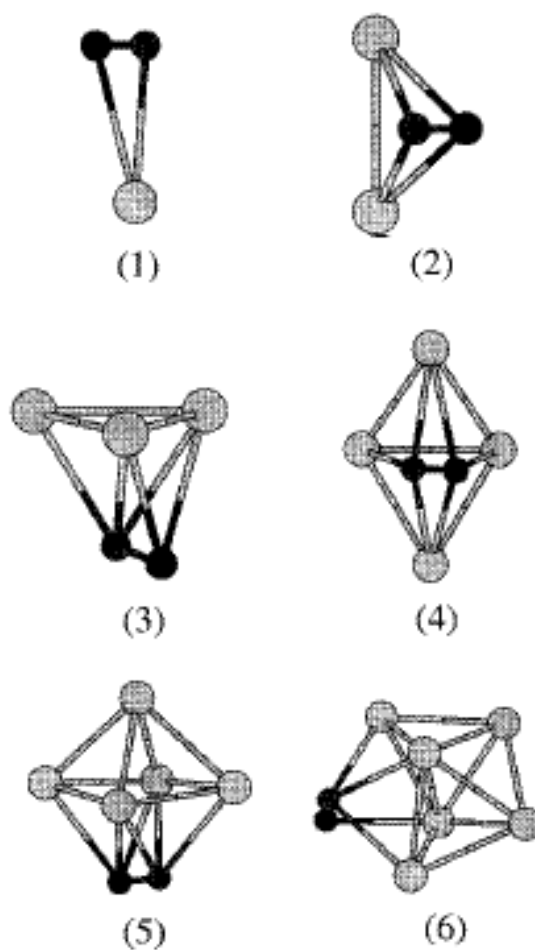


Figure 4(i): neutral NO–Ar_x ($x = 1–6$) geometries calculated by Naumkin *et al.*¹⁴

Magic numbers – structures with pronounced stability – were identified, which correspond to the complexes NO–Ar₁₂, NO–Ar₁₈, NO–Ar₂₂ and NO–Ar₂₅. These structures have also been identified as magic numbers in the mass spectrometric study of Desai *et al.*¹⁸ where they are attributed to the formation of very symmetric and hence stable icosahedral (and double icosahedral) structures. For NO^{+/-}–Ar_x charged complexes, a geometric perturbation is expected, and it has been postulated^{14,15,16} that the NO^{+/-} ion should take a central, solvated position in an Ar_x cluster. Hendricks *et al.*¹⁶ investigated NO⁻–Ar_x complexes via photoelectron spectroscopy, deriving stepwise solvation energies and noting that in addition to the expected icosahedral shell closing at $x = 12$, there was a local minimum at $x = 2$. The work presented here aims to extend the previous mass spectrometric studies on cations^{17,18} to the realm of spectroscopy.

A first attempt at exploring this regime spectroscopically is presented herein – a (2 + 1) resonance-enhanced multiphoton ionisation (REMPI) scheme has been used to study small NO–Rg_x clusters, focusing on higher energy states belonging to the 4s and 3d Rydberg levels. The 3d and 4s Rydberg states of nitric oxide/rare gas van der Waals dimers have also been investigated as part of the present thesis (see Chapters 3 and 5). The aim of the present work is to extend this to larger clusters, where the NO molecule is bound to more than one Rg atom. These states are of particular interest because the Rydberg orbital radius is of sufficient magnitude that a Rg atom may reside within the orbital. In Chapter 3 it was shown that the presence of a Rg atom at distances comparable to the radius of the Rydberg orbital leads to several interesting observations. For example, the 3d ($\tilde{F}^2\Delta$ and $\tilde{H}'^2\Pi$) states converge in energy. For larger clusters, such considerations are potentially complicated by the additional interactions present.

4.2 Experiment

The apparatus used to carry out REMPI spectroscopy has been described in detail elsewhere (see Chapter 2). To form NO–Ar_x and NO–Ne_x clusters, mixtures of ~6% NO (Messer; 99.5%) in the rare gas were used: Ar (BOC; 99.9+%) or Ne (Spectra Gases; 99.9+%). Pressures of ~5 bar Ar and ~7 bar Ne were sufficient to form the smaller clusters, although pressures of up to ~9 bar were used to form the larger species. The gas mixtures were held at pressure before expansion into vacuum through a General Valve pulsed nozzle (750 μm, 10 Hz, opening time 230 μs). The resulting unskimmed free-jet expansion passes through a thin gate valve, into the extraction region of a time-of-flight mass spectrometer.

Ionisation is achieved in a (2 + 1) REMPI scheme using the focused, frequency-doubled output of a Sirah Cobra Stretch dye laser (1800 lines/mm grating), pumped by the second harmonic (532 nm, 10 Hz) of a Surelite III Nd:YAG laser. The dye used is DCM (4-Dicyanomethylene-2-methyl-6-p-dimethylaminostyryl-4H-pyran,¹⁹ Sirah; SDL-550) in DMSO (dimethyl sulphoxide, Merck; ≥ 99%), with an emission peak at 651 nm. Control of the delay time between the production of laser light, detected with a photodiode positioned inside the dye laser, and opening of the pulsed nozzle, is carried out using a digital delay generator (SRS DG535). By adjusting the delay, the coldest spectra can be obtained by probing the onset, the coldest portion, of the free-jet expansion. All spectra are obtained in the parent ion mass channel. Photofragmentation of the larger complexes may cause contamination of the lower mass spectra, as fragmentation of a complex NO–Rg_{x+1} may lead to a spectrum appearing in the daughter fragment NO–Rg_x mass channel. (NO)_y clusters are an additional complication, since (NO)₃ has the same mass as NO–Ne₃ and NO–ArNe, and (NO)₅ has the same mass as NO–Ar₃. A mass gate (see Chapter 2) is used to avoid

saturation of the detector by uncomplexed NO or NO–Rg. Spectra are calibrated to the NO resonances ($E^2\Sigma^+$ and $H'^2\Pi$) located in the spectral range under investigation (see Section 3.2.2 for a description of the calibration procedure). Rotational temperatures are estimated to be less than 5 K (see Section 3.2.3 for the determination of rotational temperature).

4.3 Results

(2 + 1) REMPI spectra for the NO–Ar_x clusters ($x = 1-6$) are shown in Figure 4(ii). The $\tilde{E}^2\Sigma^+$ state, both with vibrationally cold NO and with one quantum of intramolecular stretch, the $\tilde{C}^2\Pi$ and $\tilde{D}^2\Sigma^+$ states, both with four quanta of intramolecular stretch excited ($\nu' = 4$), and the $\tilde{F}^2\Delta$ and $\tilde{H}'^2\Pi$ states are seen in the spectral range probed. The $\tilde{F}^2\Delta$ and $\tilde{H}'^2\Pi$ states have been discussed in Chapter 3 for the van der Waals dimers. The $\tilde{E}^2\Sigma^+$ state has been investigated for NO–Ne, NO–Ar and NO–Kr and this work is described in Chapter 5.

(2 + 1) REMPI spectra for the two NO–Ne_x species studied are shown in Figure 4(iii). Analogous to NO–Ar_x, the states observed correspond to the 4s and 3d Rydberg states, although there are also features associated with the $\nu' = 4$ vibrational level of the $\tilde{C}^2\Pi$ ($3p\pi$) state, and the first overtone for the $\tilde{E}^2\Sigma^+$ ($4s\sigma$) state. The $\nu' = 4$ level of the $\tilde{D}^2\Sigma^+$ state is also present as a sharp feature at $\sim 61550\text{ cm}^{-1}$ between the $\tilde{C}^2\Pi$ ($\nu' = 4$) and $\tilde{F}^2\Delta$ states. The redshift of the features for both NO–Ne and NO–Ar is the result of stronger intermolecular binding in the excited state than in the ground state.

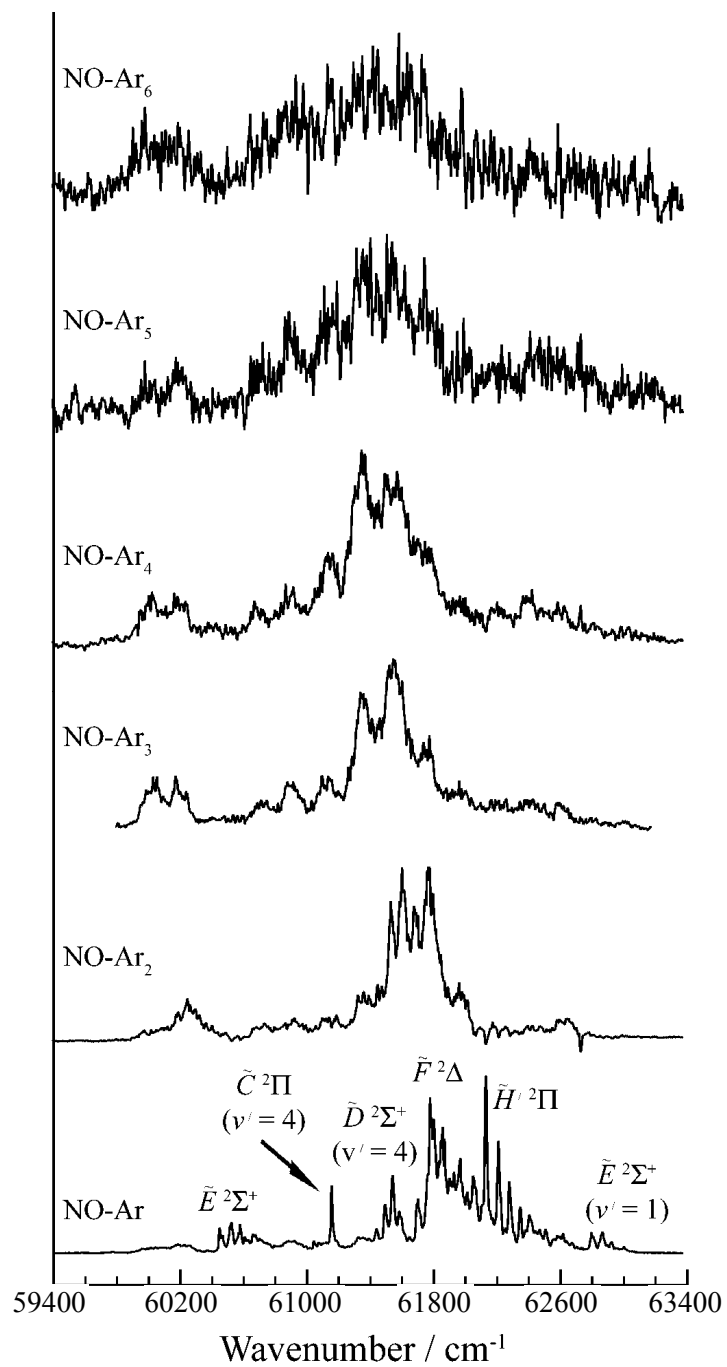


Figure 4(ii): $(2 + 1)$ REMPI spectra of the NO-Ar_x clusters ($x = 1-6$). The $\tilde{E}^2\Sigma^+$, $\tilde{F}^2\Delta$ and $\tilde{H}^2\Pi$ states are shown, as are the vibrationally-excited $\tilde{C}^2\Pi$, $\tilde{D}^2\Sigma^+$ and $\tilde{E}^2\Sigma^+$ states.

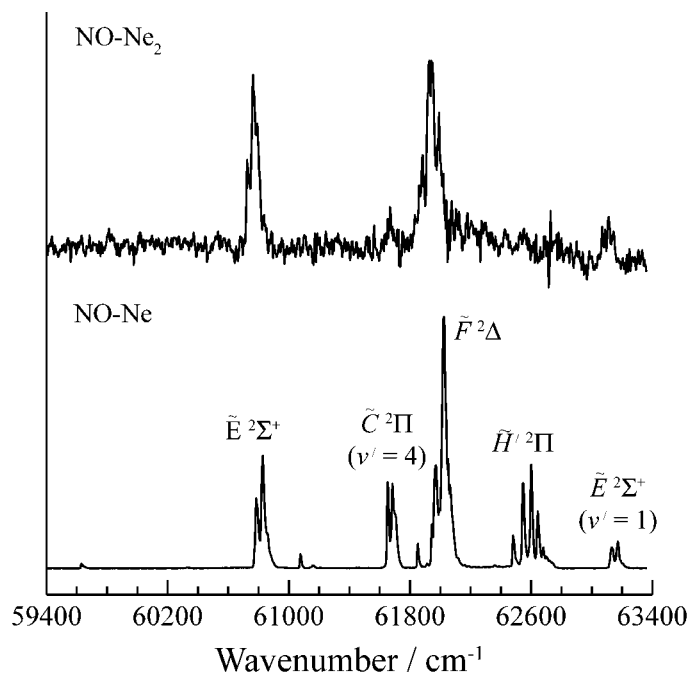


Figure 4(iii): $(2 + 1)$ REMPI spectra of the NO-Ne_x clusters ($x = 1-2$). The $\tilde{E}^2\Sigma^+$, $\tilde{F}^2\Delta$ and $\tilde{H}^2\Pi$ states are shown, as are the vibrationally-excited $\tilde{C}^2\Pi$ and $\tilde{E}^2\Sigma^+$ states.

As mentioned previously, fragmentation of higher-order clusters may lead to contamination of the spectra recorded through a lower mass channel. Fragmentation was seen to occur, although only at high laser powers. Weak spectra of the NO-Ar_{x+1} species were observed in the NO-Ar_x mass channel. A higher laser power could lead to the production of ions with a greater internal energy; a higher photon density increases the probability of absorption, so that instead of the three-photon absorption required to effect ionisation, additional photons may be absorbed to produce highly excited cationic species. Increased internal energy leads to a greater probability of fragmentation, hence the observed power dependence of photofragmentation. That fragmentation is only seen at higher laser powers suggests that the spectra shown in Figures 4(ii) and 4(iii) arise solely from the species indicated and not from species produced as a result of fragmentation. Although $(\text{NO})_2$ was seen in the mass spectrum,

it was weak and yielded an unstructured spectrum; higher-order clusters are weaker still and not expected to yield structured spectra. Given that the NO–Ar₂ and NO–Ar₃ (2 + 1) REMPI spectra are so similar, interference from (NO)₅ is unlikely (NO–Ar₃ and (NO)₅ share the same mass).

4.4 Discussion

4.4.1 Electronic structure NO–Ar_x ($x = 1-6$)

From the NO–Ar_x cluster spectra shown in Figure 4(ii), it can be seen that the greatest change in the appearance of the spectra occurs between the van der Waals dimer ($x = 1$) and NO–Ar₂. In the NO–Ar spectrum, the states are well-resolved and with an excellent signal-to-noise ratio. In NO–Ar₂, the features appear broadened and the $\tilde{F}^2\Delta$ and $\tilde{H}'^2\Pi$ states appear to have converged (these states overlap considerably in the dimer, due to hindered penetration of the 3d Rydberg electron – see Chapter 3). The appearance of the spectra changes little from NO–Ar₂ to NO–Ar₃, except for a broadening of the features present. This broadening continues as the cluster size increases and the signal-to-noise becomes increasingly poor as the intensities of the species decrease at higher mass.

The fact that the appearance of the spectra changes little from $x = 2$ and beyond (except for broadening of all spectral features and worsening signal-to-noise) implies that the electronic spectroscopy arises from an Ar₂ moiety, interacting with the NO⁺ core. Any additional Ar atoms are more weakly-bound and interact less strongly with the NO⁺ core. In Chapter 3, it was shown that a Rg atom was able to reside within the orbit of a 3d Rydberg state: the interaction between the weakly-penetrating 3d Rydberg electron and the NO⁺ core was hindered by the presence of the Rg atom and

as a result, the $\tilde{F}^2\Delta$ and $\tilde{H}'^2\Pi$ states moved closer in energy. In this work, it appears that two Ar atoms are able to reside "inside" the $3d$ and $4s$ Rydberg orbits, since the NO–Ar₂ spectrum bares a remarkable similarity to the spectra of the higher-order clusters. Since Ne is smaller than Ar, it is reasonable to assume that this is also the case for Ne, although as NO–Ne₂ is the largest cluster observed in this work, it is not possible to comment on whether the spectroscopy "converges" at NO–Ne₂. It is useful to define exactly what is meant by "inside" the Rydberg orbit: the Rydberg electron is partially shielded from the NO⁺ core by the Rg atom. Additional Ar atoms located "outside" the Rydberg orbit are shielded from NO⁺ by the Rydberg electron and are therefore more weakly-bound. This conclusion can be justified by considering the relevant dimensions: the $\tilde{F}^2\Delta$ state has the smallest Rydberg radius of the states under consideration at 5.28 Å; the Ne₂ and Ar₂ dimers have equilibrium bond distances of ~3 and ~4 Å respectively²⁰ and Ne and Ar have van der Waals radii of 1.54 and 1.88 Å respectively.²¹ Based upon the above dimensions, there are three plausible geometries for the NO–Rg₂ complexes, the first of which is where the Rg atoms occupy equivalent sites, one above and one below the N–O vector. The second possible geometry is a cross geometry, which is found to be the lowest energy configuration for the NO⁺–Rg₂ complexes – as shown in Figure 4(v). In this conformation, both Rg atoms sit on the same side of NO, with the Rg₂ vector and the N–O vector in perpendicular planes. In fact even in a linear geometry, where a Rg atom sits at each end of NO, it is likely that "most" of the electron density would reside within the Rydberg orbit.

Based on the preceding discussion it seems likely that no more than two Ar atoms are able to fit within the Rydberg orbital. Since any additional Ar atoms will lie beyond the Rydberg orbit, they will be more fully screened from the NO⁺ core and will be more loosely-bound. Higher Rydberg states, with a larger Rydberg orbit radius may

allow more than two Rg atoms to reside within and this would be seen as a convergence in the appearance of the spectra at larger x . It is not possible to comment on the convergence in the appearance of the NO–Ne $_x$ spectra, since only the two smallest clusters are observed, although it would be of interest to attempt to see the higher clusters.

In the ground state, the cationic core is fully screened from any complexed Ar atoms: the Ar atoms will be only weakly-bound and are expected to have a poorly defined separation from the NO $^+$ core. The ground state vibrational wavefunction is expected to extend over a wide range of geometries. Conversely, in the Rydberg state, the cationic core is now less effectively screened and Ar atoms located within the Rydberg orbit will be much more tightly-bound. The geometry of the Rydberg state is more constrained than for the weakly-bound ground state. The tighter-bound Rydberg state will govern the Franck-Condon factors; the region of the overlap with the ground state, centred about the geometry of the Rydberg state, will be observed. Since an Ar $_2$ moiety is able to reside within the Rydberg orbit, the strong interaction between Ar $_2$ and the NO $^+$ core governs the geometry of the complex and this is where the Rydberg vibrational wavefunction will be localised. This is reflected in Figure 4(ii), where the spectra with $x \geq 2$ bear a remarkable similarity to each other. In Figure 4(ii), the spectra for NO–Ar $_3$ and larger clusters appear broadened. This may be due to power broadening – a higher photon density was required to observe spectra of the larger complexes. Furthermore, larger complexes were only observed when probing a warmer portion of the free-jet expansion. Since this is where cooling becomes less efficient, it is probable that the observed broadening may be due, in part, to excited vibrational and rotational motions in the complex. There are two other possible causes for the spectral broadness, both of which are due to the presence of weakly-bound Ar atoms lying beyond the Rydberg orbit: (i) dissociation of these weakly-bound Ar atoms leads to lifetime broadening; or (ii) the Ar atoms contribute very low frequency

vibrations to the spectrum, in addition to the structure arising from excitation of the NO–Ar₂ "core".

As well as the broadening of the features seen as x increases from $x = 2$ to 6, the initially well-resolved structure in the NO–Ar spectrum evolves into broad features, comprising a progression of $\sim 200\text{ cm}^{-1}$: this structure is evident in all bands. This spacing is too large for a stretching frequency to be responsible for the progression (the frequencies of NO⁺–Ar₂ are in the range 18–99 cm^{-1} , see Section 4.4.4), although the structure is clearly related to the growth of the Ar _{x} cluster. The structure appears in all electronic states observed, suggesting that there is a common cause for the observed progression.

In the experimental work of Chergui *et al.*^{4,10,13} and in the molecular dynamics simulations of Jeannin *et al.*,¹³ the effect of formation of a Rydberg state (the $\tilde{A}^2\Sigma^+$ state) in NO trapped in an Ar matrix is investigated. The studies revealed the formation of a bubble, which forms quickly and can induce motion in different shells of matrix atoms. In the molecular dynamics simulations of Jeannin *et al.*¹³, the first shell trajectory was found to have a temporal width of 180 fs. This corresponds to a frequency of 185 cm^{-1} . This suggests that the progression of frequency $\sim 200\text{ cm}^{-1}$ seen in the present work may arise from the response of the Ar cluster to the sudden formation of a Rydberg state. From the work of Naumkin and Wales^{14,15} the NO molecule is known to occupy a surface site, so the sudden formation of a Rydberg state will create a dimple in the surface of the Ar _{x} cluster, and this dimple may be responsible for the broad progression seen in the spectra for the larger NO–Ar clusters shown in Figure 4(ii).

4.4.2 Electronic structure NO–Ne_x (x = 1–2)

The strong $\tilde{H}'^2\Pi$ state progression seen in the NO–Ar spectrum is not apparent in the spectra of the higher-order complexes. From previous work on the NO–Rg van der Waals dimers described in Chapter 3, it was concluded that penetration of the 3d electron was hindered by the presence of the Rg atom lying within the Rydberg orbit. This led to the convergence of the $\tilde{F}^2\Delta$ and $\tilde{H}'^2\Pi$ states. The addition of another Ar atom, within the Rydberg orbit, could therefore be expected to lead to a further reduction in penetration of the 3d electron, and so to an almost complete convergence of the $\tilde{F}^2\Delta$ and $\tilde{H}'^2\Pi$ states. However, an examination of the NO–Ne and NO–Ne₂ spectra suggests otherwise. In the NO–Ne spectrum, the $\tilde{E}^2\Sigma^+$, $\tilde{F}^2\Delta$ and $\tilde{H}'^2\Pi$ states are observed, as are the $\tilde{C}^2\Pi$ and $\tilde{E}^2\Sigma^+$ states with four and one quantum of intramolecular (N–O) stretch excited respectively. The $\tilde{D}^2\Sigma^+$ state, with four quanta of intramolecular stretch is also seen, as a sharp feature located at $\sim 61550\text{ cm}^{-1}$ between the $\tilde{C}^2\Pi$ ($\nu' = 4$) and $\tilde{F}^2\Delta$ states. However, in NO–Ne₂, while the $\tilde{E}^2\Sigma^+$ ($\nu' = 0$; $\nu' = 1$), $\tilde{D}^2\Sigma^+$ ($\nu' = 4$) and $\tilde{F}^2\Delta$ states remain, the $\tilde{C}^2\Pi$ ($\nu' = 4$) and $\tilde{H}'^2\Pi$ states have disappeared. That is, the two $^2\Pi$ states are absent from the NO–Ne₂ spectrum, when they are strong features in the NO–Ne spectrum. Additionally, the relative intensities of the $\tilde{E}^2\Sigma^+$ ($\nu' = 0$ and $\nu' = 1$) components are very similar for NO–Ne₂ and NO–Ar₂, confirming that the intensity loss is localised to the $\tilde{C}^2\Pi$ ($\nu' = 4$) and $\tilde{H}'^2\Pi$ states. Given the above, it seems likely that the $\tilde{C}^2\Pi$ ($\nu' = 4$) and $\tilde{H}'^2\Pi$ states are also absent from the NO–Ar₂ spectrum. The disappearance of the $\tilde{C}^2\Pi$ ($\nu' = 4$) and $\tilde{H}'^2\Pi$ bands will be discussed in more detail in Section 4.4.5.

4.4.3 Vibrational structure NO-Ne_x (x = 1-2)

Figure 4(iv) shows a comparison of the NO-Ne and NO-Ne₂ $\tilde{E}^2\Sigma^+$ ($v' = 0$) state spectra. The NO-Ne₂ spectrum has been shifted by ~ 59 cm⁻¹ to higher energy, so that its first intense band is aligned with that of NO-Ne. The first band corresponds to one quantum of intermolecular stretch, $\nu_\sigma = 1$ (this assignment was made in work by Fleniken *et al.*²² and is considered tentative); the origin band is not observed (this can be attributed to poor Franck-Condon factors resulting from a shortening of the NO-Ne separation upon excitation).

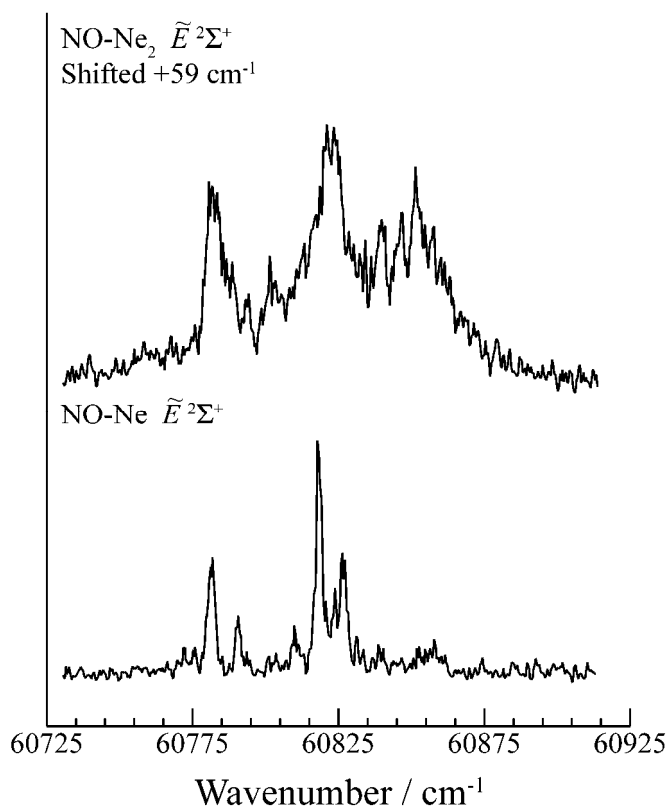


Figure 4(iv): (2 + 1) REMPI spectra of the $\tilde{E}^2\Sigma^+$ state of NO-Ne and NO-Ne₂. The latter has been shifted by 59 cm⁻¹, so that its first intense band (corresponding to one quantum of intermolecular stretch) is aligned with that of NO-Ne.

The features associated with the intermolecular stretch in NO–Ne are very similar to those in the NO–Ne₂ spectrum. The fact that the features in the larger cluster spectrum (upper trace) are broader than those in NO–Ne may be due to the NO–Ne₂ cluster being rotationally warmer, or to excitation of other intermolecular vibrations (including vibrational hotbands). This broadening of the spectrum makes it difficult to determine exactly how much the intermolecular stretching frequency is affected by the presence of an additional Ne atom, although from the spectra it appears that the values are very similar. In a previous study of Meyer and coworkers²² a 0–1 vibrational stretching frequency of 50 cm⁻¹ was derived for NO–Ne in the $\tilde{E}^2\Sigma^+$ state; the spacing between the $\nu = 1$ and $\nu = 2$ levels of the vibrational stretch was 36 cm⁻¹. In the present work, the 1–2 vibrational frequency is also 36 cm⁻¹. Despite the increased broadness of the features in the NO–Ne₂ $\tilde{E}^2\Sigma^+$ state spectrum, a value of 40 ± 3 cm⁻¹ is derived for the 1–2 vibrational stretching frequency. Given that the 1–2 vibrational stretching frequencies are so similar, it is likely that the 0–1 spacing for NO–Ne and NO–Ne₂ are also similar. This suggests that both Ne atoms interact with NO in the same manner and that the degree of Ne–Ne interaction is small, since any significant interaction between the Ne atoms will affect their interaction with the NO⁺ core. The dissociation energy of Ne₂ has been calculated²³ as 16.3 cm⁻¹, further evidence of a weak Ne–Ne interaction.

In order to understand the observations in more detail, the structures and vibrational frequencies of the cationic species NO⁺–Ne and NO⁺–Ne₂ have been calculated by T. G. Wright (MP2/6-311+G(2*d*)). The structure and vibrational frequencies of NO⁺–Ne have already been determined:²⁴ the complex has a skewed T-shaped geometry and the Ne atom lies closer to the N end of NO⁺. For NO⁺–Ne₂, the lowest energy geometry is a cross structure, as shown in Figure 4(v). The two Ne atoms lie on the same side of the NO⁺ moiety and the Ne–Ne and N–O vectors are perpendicular; the Ne atoms lie

significantly closer to N than to O. This geometry is very similar to that determined in Reference 14 for the neutral NO–Ar₂ complex.

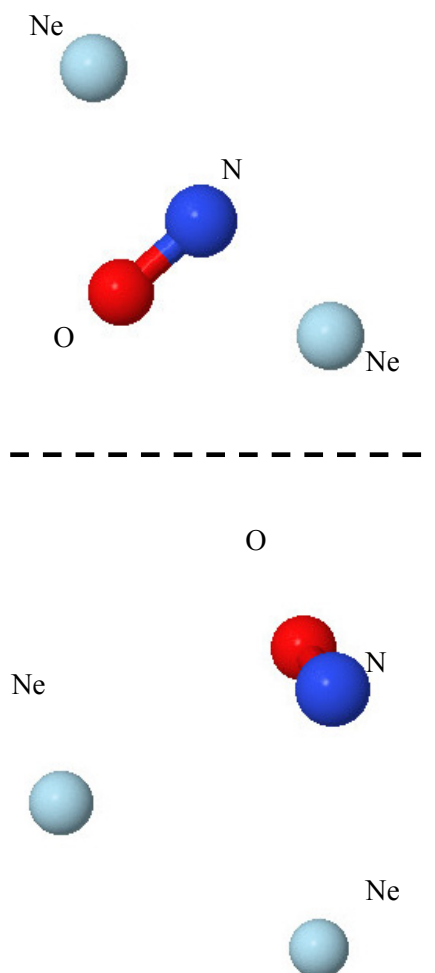


Figure 4(v): two views of the optimised geometry for the "cross" structure of NO⁺-Ne₂.

For NO⁺-Ne₂ the harmonic vibrational frequencies were calculated to be 21 cm⁻¹ for the Ne-Ne stretch, 31 and 32 cm⁻¹ for the bending modes and 70 cm⁻¹ for the asymmetric stretch. For the symmetric stretch a value of 84 cm⁻¹ has been calculated, which compares well with the intermolecular stretch frequency of 76 cm⁻¹ calculated for NO⁺-Ne. This suggests that each Ne atom vibrates along the intermolecular stretch coordinate (defined by the vector between the Ne atom and the centre of mass of NO)

essentially independently of the other, and so the frequency is very similar to that of the $\text{NO}^+\text{-Ne}$ intermolecular stretch. For the Rydberg states, the actual frequencies will be affected by the presence of the Rydberg electron – the 0–1 spacing is 50 cm^{-1} for both NO-Ne and NO-Ne_2 (see above). These lower frequencies indicate that the magnitude of the interaction between the Ne atoms and the NO^+ core in the Rydberg states, is less than in the cationic species, due to shielding of the NO^+ core by the $4s$ Rydberg electron. The main vibrational progressions in NO-Ne and NO-Ne_2 are expected to have a similar spacing to each other, as in the cationic species, and this is reflected in the similarity of the NO-Ne and NO-Ne_2 spectra.

A thorough analysis of the vibrational structure present in the NO-Ne_2 spectrum has not been carried out, although the Ne–Ne stretch and an intermolecular bend are expected to be present. Due to shielding of the NO^+ core by the Rydberg electron, these are expected to have lower frequencies than for the cation and should only be seen in combination with the dominant symmetric intermolecular stretch. The asymmetric stretch is not seen, due to the expected geometry change upon ionisation: in the cationic cluster, the Ne_2 vector lies significantly closer to the N end of the NO^+ moiety than in the neutral cluster, whose geometry is expected to be similar to that determined for NO-Ar_2 by Naumkin and Wales.¹⁴ The qualitative geometry change expected upon ionisation is shown in the schematic in Figure 4(vi), adapted from Reference 14.

A comparison between the NO-Ne and $\text{NO-Ne}_2 \tilde{E}^2\Sigma^+$ state spectra reveals that there is significantly more intensity to the high wavenumber end of the NO-Ne_2 spectrum than for NO-Ne , suggesting that the Franck-Condon factors are larger; there may be a more pronounced geometry change associated with the formation of the $\tilde{E}^2\Sigma^+$ state in the larger cluster. There is also a change in the Franck-Condon factors for the $\tilde{F}^2\Delta$

state, particularly in the case of NO-Ar_x , where the band profile changes as x increases from 1 to 2, and then settles to a similar profile thereafter.

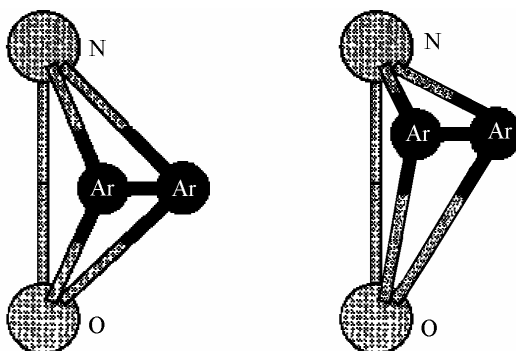


Figure 4(vi): *neutral NO-Ar_2 (left) and cationic NO^+-Ar_2 (right) geometries, adapted from Reference 14 to show the qualitative geometry change upon ionisation.*

4.4.4 Vibrational structure NO-Ar_x ($x = 1-6$)

Figure 4(vii) shows the $\tilde{E}^2\Sigma^+$ state spectra for NO-Ar_2 (upper trace) shifted by 139 cm^{-1} to higher energy to align the features with those of NO-Ar (lower trace). As for NO-Ne_x ($x = 1-2$), there is increased intensity to higher wavenumber in the NO-Ar_2 spectrum compared to NO-Ar . The similarity between the two spectra makes it possible to estimate the vibrational spacing. A comparison between the NO-Ar spectrum obtained in this work and that of Meyer,²⁵ suggests that the first strong feature corresponds to a single quantum of intermolecular stretch. Hence, the 1–2 vibrational spacing can be determined: 68 cm^{-1} for NO-Ar which reduces to 63.5 cm^{-1} for NO-Ar_2 . This compares well with the 1–2 vibrational spacing of 69 cm^{-1} derived for NO-Ar by Meyer.²⁵ That the vibrational spacing decreases for NO-Ar_2 , whereas no such decrease was seen for NO-Ne_2 , can be attributed to the increased repulsion between the two Ar atoms, as a consequence of their increased size.

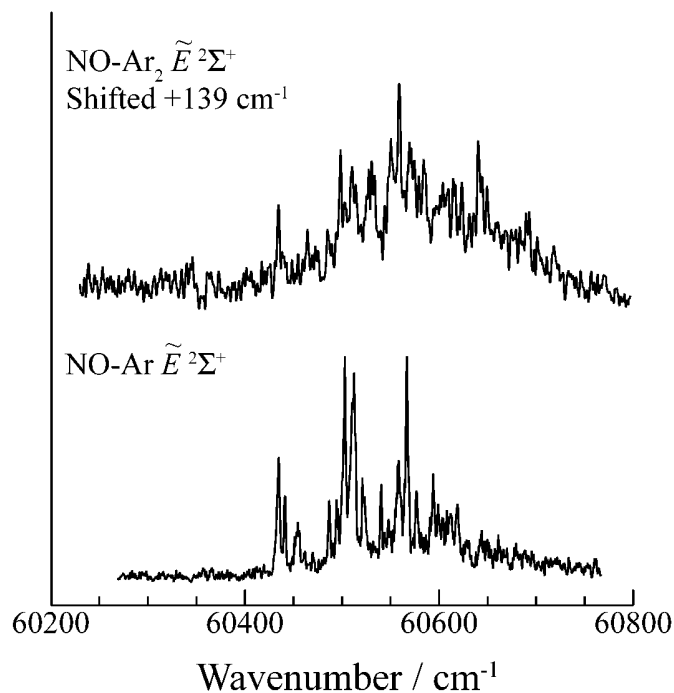


Figure 4(vii): $(2 + 1)$ REMPI spectra of the NO-Ar_x ($x = 1-2$) $\tilde{E}^2\Sigma^+$ state. The NO-Ar_2 spectrum has been shifted by 139 cm^{-1} .

As for NO^+-Ne_2 , the calculated equilibrium geometry (T. G. Wright, MP2/6-311+G(2d)) is a cross structure, with the Ar atoms symmetrically placed either side of the NO^+ cation and the Ar_2 positioned significantly closer to the N end of the molecule. For NO^+-Ar_2 the calculated harmonic vibrational frequencies were 18 cm^{-1} (Ar-Ar stretch), 69 and 78 cm^{-1} (bending modes), 97 cm^{-1} (asymmetric stretch) and 99 cm^{-1} (symmetric stretch). Comparing the symmetric stretch frequency of NO^+-Ar_2 with that calculated for NO^+-Ar (99 cm^{-1} compared with 101 cm^{-1}) reveals that, as in the case of NO^+-Ne_2 , the two Ar atoms are behaving almost independently as they vibrate along the vector between the centre of mass of NO and each Ar atom. Again, as for the NO-Ne_x clusters, the intermolecular stretch frequencies calculated for the cationic species, differ from those determined from the spectra for the Rydberg states. The Rydberg electron interacts with the Ar atoms, shielding them from the NO^+ core, resulting in a

decrease in the intermolecular stretch frequency. The spectra obtained in this work are highly structured, presumably due to excitations of bends and the Ar–Ar stretch.

4.4.5 Disappearance of the $\tilde{C}^2\Pi$ ($v' = 4$) and $\tilde{H}'^2\Pi$ bands.

One of the most striking observations of the present work is the disappearance of the $\tilde{C}^2\Pi$ ($v' = 4$) and $\tilde{H}'^2\Pi$ electronic bands in the spectrum of NO–Ne₂, and the likely disappearance of these bands from the NO–Ar₂ spectrum. The $\tilde{H}'^2\Pi$ state was also seen to disappear in the IR-REMPI work of Meyer and coworkers.²⁶ This has been discussed in more detail in Section 3.1.4 in Chapter 3. Briefly, when exciting via the intermolecular bend of ground state NO–Ar, the $\tilde{F}^2\Delta$ state persisted, whilst the $\tilde{H}'^2\Pi$ state feature was no longer observed. When the intermolecular bend was not excited, both states appeared with comparable intensity. This was attributed to a change in the Franck-Condon factor along the angular coordinate and indicates that the observed intensities in the NO–Rg_x systems can be extremely sensitive to geometry changes between the ground and excited electronic states.

Comparison of the calculated geometries of NO⁺–Ar₂ (this work) and NO–Ar₂ (Reference 14) shows that there is a significant change in geometry upon ionisation, as shown in Figure 4(vi). A similar geometric perturbation is expected for NO–Ne₂. The Rg₂ moiety will move from close to the centre of the N–O vector, to the N end, with a shortening of the distance between the Ne₂ vector and the N–O vector. In the Rydberg states, the Rydberg electron in the $\tilde{F}^2\Delta$ and $\tilde{H}'^2\Pi$ states is in an extended orbital, which will affect the orientation of Rg₂. It is plausible that the changes in Franck-Condon factors are such that both the $\tilde{C}^2\Pi$ ($v' = 4$) and $\tilde{H}'^2\Pi$ states essentially vanish from the spectrum, while the $\tilde{F}^2\Delta$ and $\tilde{E}^2\Sigma^+$ ($v' = 0$ and $v' = 1$) states remain.

4.4.6 Implications of the present results for bulk studies

The present work, and some of the previous work on NO–Rg complexes, described in Chapter 3, has implications for matrix studies. The $n = 3$ and $n = 4$ NO absorption peaks seen in previous matrix studies¹⁻⁵ are lifetime broadened, due to an interaction between the matrix atoms and the NO⁺ core. Upon excitation, a Pauli repulsion between the Rydberg electron and the surrounding matrix atoms creates a bubble around the NO⁺ core. In order for the matrix atoms to interact with NO⁺, giving rise to the broad absorption peaks, some matrix atoms must end up inside this bubble (gas phase results described in Chapter 3 indicate that at least one Rg atom can fit inside the Rydberg orbit and interact with the NO⁺ core). The above is supported by the fact that the ionisation energy of NO is lowered by ~ 1 eV in matrices from the gas phase value – an interaction between the Rg atoms and the NO⁺ core will shield the Rydberg electron from the core charge, resulting in a lowering of the ionisation energy as observed in matrix studies. The absorption energies of lower Rydberg states are blueshifted in matrices from their gas phase values (the Rydberg electron experiences a Pauli repulsion with the solvent cage). Since the ionisation energy is redshifted in the matrix, the implication is that Rg atoms must, at some point, penetrate the Rydberg orbital. Otherwise, the ionisation energy and higher electronic states would be expected to be blueshifted to an increasing extent, as the Rg atoms in the matrix are repelled further.

This work is also relevant to the study of the dynamical response of the matrix atoms to the rapid formation of a Rydberg state. In Reference 13, the formation of the $\tilde{A}^2\Sigma^+$ Rydberg state of NO, in a solid Ar matrix, led to a response in the first coordination shell. The motion of the first shell was found to have an effective vibrational frequency of 185 cm^{-1} . The fact that a similar spacing has been observed in this work

suggests that the first coordination shell in the matrices is represented reasonably well by the small clusters formed here.

4.5 Conclusions

(2 + 1) REMPI spectra have been recorded for NO–Ar_x ($x = 1-6$) and NO–Ne_x ($x = 1-2$) complexes. The spectra are successively redshifted, due to the increased magnitude of the intermolecular binding in the excited state relative to that in the ground state. The spectra were found to converge in appearance beyond NO–Ar₂. This led to the conclusion that two Ar atoms are able to fit within the Rydberg orbit and interact with the NO⁺ core. The NO–Ar₂ "core" dictates the appearance of the spectrum, with additional Ar atoms located beyond the Rydberg orbit. They are more efficiently shielded from the NO⁺ core and are therefore more weakly-bound. The fact that two Ar atoms are able to reside within the Rydberg orbit in the present work offers an explanation for the redshift of the ionisation energy of NO, as seen in matrices. It seems likely that a small number of Rg matrix atoms will be "inside" the Rydberg orbital *i.e.* they will be able to interact with the NO⁺ core. These Rg atoms will partially shield the Rydberg electron from the NO⁺ core charge and will therefore lessen the energy required to ionise. For the NO–Rg dimers discussed in Chapter 3 it was shown that the presence of the Rg atom within the 3*d* Rydberg orbit led to hindered penetration of the 3*d* Rydberg electron. As a result, the interaction between the weakly-penetrating 3*d* Rydberg electron and the NO⁺ core was lessened and this was seen in the spectra as the $\tilde{F}^2\Delta$ and $\tilde{H}'^2\Pi$ states converging in energy, approaching the energetic ordering expected for the 3*d* λ states in the absence of penetration. In the work described herein, the 3*d* Rydberg electron weakens the NO/Rg interaction. This is reflected in the intermolecular stretch frequencies for the NO–Rg and NO–Rg₂ complexes in the Rydberg states, which are lower than those

calculated for the corresponding cationic complexes. The shielding effect of the Rydberg electron is also apparent for the Ar atoms in the larger NO–Ar_x clusters (where $x \geq 3$), which are much more weakly-bound than the two Ar atoms that reside within the Rydberg orbit. These two effects: hindered penetration of the 3d Rydberg electron, which results in a reduced interaction with the NO⁺ core and is caused by the presence of a rare gas atom within the Rydberg orbit, and shielding of the NO⁺ core from the complexed Rg atom by the Rydberg electron counteract each other, and are responsible for the spectroscopic observations in this work, and those described in Chapter 3.

The vibrational structure in the $\tilde{E}^2\Sigma^+$ state spectra is very similar for the NO–Rg and NO–Rg₂ complexes. Values for the 1–2 vibrational spacings were similar for both Ne and Ar complexes and compared well with previous work (see References 22 and 25 respectively). *Ab initio* calculations on the cations, performed by T. G. Wright reveal a cross geometry, although in the excited states, the Rydberg electron is expected to have a significant effect on the equilibrium geometries. The calculations also indicate that the observed vibration for the NO–Rg dimers corresponds to the intermolecular (NO–Rg) stretch in both cases; the symmetric stretch is observed for the NO–Rg₂ species. That the NO–Rg and NO–Rg₂ vibrational frequencies are so similar is evidence that the two Rg atoms are essentially independent during this vibration.

The repeating structure, present in all bands, which becomes more evident as the size of the NO–Ar_x cluster increases, has been attributed to the response of the Ar_x cluster, provoked by formation of the Rydberg states. In the Ar matrix,¹³ sudden formation of the $\tilde{A}^2\Sigma^+$ Rydberg state resulted in a response from the first solvation shell which had an effective vibrational frequency of 185 cm⁻¹. The broad progression seen in the present work has a vibrational frequency of ~200 cm⁻¹, and has been attributed to the

formation of a "dimple" in the surface of the Ar cluster. This phenomenon suggests that the first coordination shell in the bulk matrix is represented relatively successfully by the NO–Ar_x van der Waals clusters investigated in the present work.

Finally, both the $\tilde{C}^2\Pi$ ($\nu' = 4$) and $\tilde{H}'^2\Pi$ states are absent from the spectra of the NO–Rg_x species for $x \geq 2$. These bands appear to be extremely sensitive to changes in angular Franck-Condon factors, caused by interactions between the NO⁺ core, the Rydberg electrons, and the two Rg atoms.

4.6 References

¹ M. Chergui, N. Schwentner, W. Böhmer, *J. Chem. Phys.* **85** (1986) 2472.

² E. Morikawa, A.M. Köhler, R. Reininger, V. Saile, P.Laporte, *J. Chem. Phys.* **89** (1988) 2729.

³ G. Zerza, F. Vigliotti, A. Sassara, M. Chergui, V. Stepanenko, *Chem. Phys. Lett.* **256** (1996) 63.

⁴ M.T. Portella-Orbeli, C. Jeannin, M. Chergui, *Chem. Phys. Lett.* **259** (1996) 475.

⁵ S. Jimenez, M. Chergui, G. Rojas-Lorenzo, J. Rubayo-Soneira, *J. Chem. Phys.* **114** (2001) 5264.

⁶ F. Vigliotti, M. Chergui, *Eur. Phys. J. D*, **10** (2000) 379-390.

⁷ K. Dressler, *Extrait des mémoires de las Société Royale des Sciences de Liège* (Liège, 1970), Vol. XX, p.357.

- ⁸ L. Resca, S. Rodriguez, *Phys. Rev. B*, **17** (1978) 3334 ; R. Resta, *Phys. Status Solidi* **86** (1978) 627 ; L. Resca, R. Resta, S. Rodriguez, *Phys. Rev. B*, **18** (1978) 702.
- ⁹ G. Reiser, W. Habenicht, K. Müller-Dethlefs, E.W. Schlag, *Chem. Phys. Lett.* **152** (1988) 119.
- ¹⁰ P. Larrégaray, A. Cavina, M. Chergui, *Chem. Phys.* **308** (2005) 13-25.
- ¹¹ F. Vigliotti, L. Bonacina, M. Chergui, *Phys. Rev. B*, **67** (2003) 115118; G. Rojas-Lorenzo, J. Rubayo-Soneira, F. Vigliotti, M. Chergui, *Phys. Rev. B*, **67** (2003) 115119.
- ¹² M. Chergui, *C. R. Acad. Sci. Paris, t. 2, Série IV* (2001) 1453-1467.
- ¹³ C. Jeannin, M. T. Portella-Oberli, S. Jiminez, F. Vigliotti, B. Lang, M. Chergui, *Chem. Phys. Lett.* **316** (2000) 51-59.
- ¹⁴ F.Y. Naumkin, D.J. Wales, *Mol. Phys.* **98** (2000) 219.
- ¹⁵ F.Y. Naumkin, D.J. Wales, *Comput. Phys. Commun.* **145** (2002) 141.
- ¹⁶ H.H. Hendricks, H.L. de Clercq, C.B. Friedhoff, S.T. Arnold, J.G. Eaton, C. Fancher, S.A. Lyapustina, J.T. Snodgrass, K.H. Bowen, *J. Chem. Phys.* **116** (2002) 7926.
- ¹⁷ J.C. Miller, W.-C. Cheng, *J. Phys. Chem.* **89** (1985) 1647.
- ¹⁸ S.R. Desai, C.S. Feigerle, J.C. Miller, *J. Chem. Phys.* **97** (1992) 1793.

- ¹⁹ S.S. Khohlova, N.G. Lebedev, S.L. Bondarev, V.N. Knyukshto, A.A. Turban, V.A. Mikhailova, A.I. Ivanov, *Int. J. Quan. Chem.* **104**(2) (2005) 189-196.
- ²⁰ E. F. Laschuk, M. M. Martins, S. Evangelisti, *Int. J. Quantum Chem.* **95** (2003) 303.
- ²¹ A. Bondi, *J. Phys. Chem.* **68**(3) (1968) 441.
- ²² J. Fleniken, Y. Kim, H. Meyer, *J. Chem. Phys.* **109** (1998) 8940.
- ²³ R.J. LeRoy, M.L. Klein, I.J. McGee, *Mol. Phys.* **28** (1974) 587.
- ²⁴ E.P.F. Lee, P. Soldán, T.G. Wright, *J. Phys. Chem. A*, **102** (1998) 6858.
- ²⁵ H. Meyer, *J. Chem. Phys.* **107** (1997) 7732.
- ²⁶ Y. Kim, H. Meyer, *Int. Rev. Phys. Chem.* **20**(3) (2001) 219-282.

*5 Electronic spectroscopy of the $\tilde{E}^2\Sigma^+ \leftarrow \tilde{X}^2\Pi$ transition of NO–Kr and
shielding/penetration effects in Rydberg states of NO–Rg complexes*

5.1 Introduction

Exciting NO–Rg complexes to Rydberg states allows the cation–Rg–electron interaction to be studied, by measuring intermolecular vibrational frequencies and dissociation energies. In Chapter 3 it was shown that for the $3d\lambda$ Rydberg states along the NO–Rg series (Rg = Ne–Kr) the Rg atom resides within the Rydberg orbit. This led to hindered penetration of the Rydberg electron, which was reflected in the spectra by the $\tilde{F}^2\Delta$ and $\tilde{H}^2\Pi$ states converging in energy. A three-way interaction between the Rydberg electron, the NO^+ core and the Rg atom led to the energetic ordering of the $3d\lambda$ states observed. When the Rg atom interacts with the cationic core, electron density will be donated into the $2p\pi^*$ orbital, leading to a change in the NO intermolecular stretch frequency, however, the weakly-penetrating Rydberg electron can shield the Rg atom from the NO^+ core. These interactions can be investigated from an examination of the fundamental NO-stretch frequency, which has been measured for each of the $4s$ and $3d$ Rydberg states, across the Rg = Ne–Kr series.

When probing the $3d\lambda$ Rydberg states, the $\tilde{H}^2\Sigma^+$ component was not observed. This has been discussed previously by Jungen.¹ Briefly, the $nd\sigma$ orbitals of NO are strongly mixed with the orbitals $(n + 1)s\sigma$, that is, the $\tilde{H}^2\Sigma^+$ and $\tilde{E}^2\Sigma^+$ states interact. As well as causing the $4s\sigma$ state to move down in energy and the $3d\sigma$ state to move up in energy, this interaction results in the cancellation of the $\tilde{H}^2\Sigma^+ \leftarrow \tilde{X}^2\Pi$ transition moment, while the $\tilde{E}^2\Sigma^+ \leftarrow \tilde{X}^2\Pi$ transition intensity is simultaneously enhanced.

5.1.1 Previous work on the $\tilde{E}^2\Sigma^+$ state of NO–Ne and NO–Ar

The $\tilde{E}^2\Sigma^+$ state of NO–Ne and NO–Ar has been investigated previously, both experimentally using a (2 + 1) resonance-enhanced multiphoton ionisation (REMPI) scheme, and by simulation.^{2,3} The experimental and simulated spectra for the complexes NO–Ne and NO–Ar, taken from References 2 and 3 are shown in Figures 5(i) and 5(ii) respectively. Both complexes were found to have a geometry which deviated from T-shaped, for NO–Ar this deviation was around 20°–25°.³

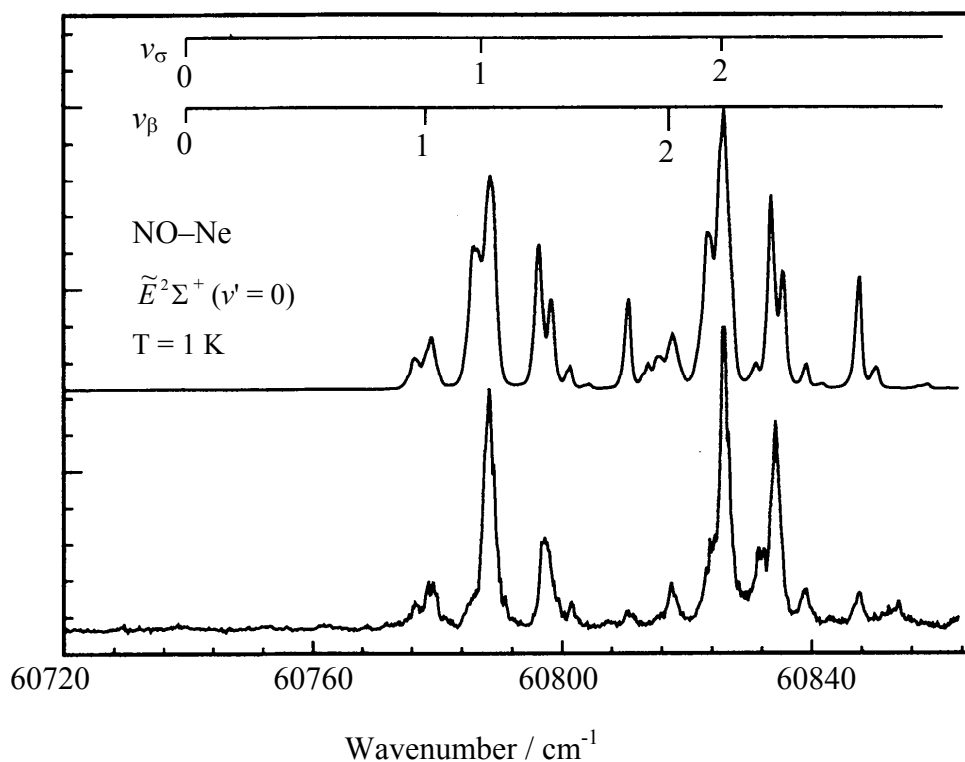


Figure 5(i): (2 + 1) REMPI spectrum of the $\tilde{E}^2\Sigma^+$ state of NO–Ne. The top spectrum represents the simulation of the two-photon spectrum, adapted from Reference 2.

In the case of NO–Ne, the spectrum was dominated by two bands, which were identified as members of the intermolecular stretch vibration. The weak bands

(satellite bands) seen to the red of these features have been attributed to the intermolecular bending mode. The measured dissociation energy and the intermolecular vibrational stretch and bend frequencies were found to be significantly increased compared to those of the $\tilde{C}^2\Pi$ state, which was also investigated in Reference 2. This increased interaction energy can be rationalised by the relevant Rydberg orbit radii,³ 3.6 Å and 6.1 Å for the $\tilde{C}^2\Pi$ and $\tilde{E}^2\Sigma^+$ states respectively. In previous work,^{2,3} it has been shown that the large Rydberg radius of the $\tilde{E}^2\Sigma^+$ state will allow a Rg atom to reside within it, leading to an interaction with the NO^+ core and an increased binding energy. This effect will be countered by the increased penetration of the 4s electron, which has a greater probability of being found in the core region, thus partially shielding the NO^+ charge.² In the present study, the $\tilde{E}^2\Sigma^+$ state of a heavier member of the NO–Rg series, NO–Kr is investigated. The Kr atom has more electrons than Ne and Ar, and so there should be a greater Pauli repulsion for NO–Kr, between the electrons on Kr and the 4s Rydberg electron. This increased repulsive interaction should be reflected in the binding energies of the excited state complexes, which are expected to become less cationic along the NO–Rg series (Rg = Ne–Kr), as was the case for the $3d\lambda$ Rydberg states (as discussed in Chapter 3).

The structure seen in the NO–Ar $\tilde{E}^2\Sigma^+$ state spectrum is more complicated than for NO–Ne. As for NO–Ne, the dominant features have been attributed to a progression in the NO–Ar stretch vibration. Again, red satellite bands can be seen accompanying the members of the stretch vibration, which have been identified as members of the intermolecular bending vibration, in combination with one or two quanta of intermolecular stretch.³

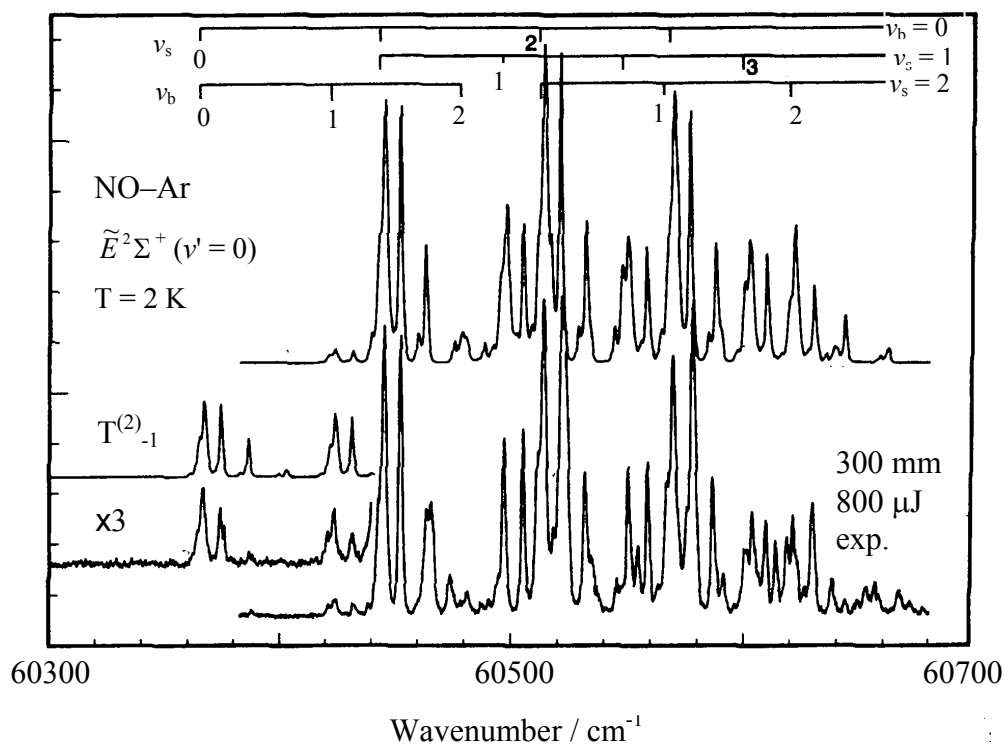


Figure 5(ii): $(2 + 1)$ REMPI spectrum of the $\tilde{E}^2\Sigma^+$ state of NO–Ar. The top spectrum represents the simulation of the two-photon spectrum, adapted from Reference 3.

The aims of the present work are to extend the previous $(2 + 1)$ REMPI studies on the $4s$ Rydberg state of NO–Ne² and NO–Ar,³ to the heavier NO–Kr van der Waals complex, so that trends along the $4s$ NO–Rg series can be examined. An assignment of the two-photon absorption spectrum is presented, based on a simulation performed by Meyer and coworkers in a contemporaneous investigation. In addition, the $\nu_{\text{NO}} = 1$ levels of the $\tilde{E}^2\Sigma^+$, $\tilde{F}^2\Delta$ and $\tilde{H}^2\Pi$ states, where one quantum of N–O stretch vibration is excited, have been observed. The fundamental NO vibrational frequency, which reflects the interactions in the complex, can be determined and compared to the stretching frequencies of NO⁺.

5.2 Experiment

5.2.1 Experimental set-up

The experimental set-up has been described previously (see Chapter 2). NO–Kr was generated using mixtures of ~2.5% NO and ~5% Kr seeded in Ar. The gas mixtures were expanded into vacuum using a pulsed nozzle. The resulting expansion travelled to the extraction region of a time-of-flight mass spectrometer. Ionisation is achieved in a (2 + 1) REMPI process using the frequency-doubled output of a dye laser operating with the dye DCM (DSL-550, Sirah Cobra Stretch, 1800 lines/mm grating), which is pumped by a Nd:YAG (yttrium-aluminium-garnet) laser.

5.2.2 Calibration

As noted in Chapter 3, it was not possible to record an NO–Xe $\tilde{E}^2\Sigma^+$ state spectrum in the NO⁺–Xe mass channel (all the spectra of the lighter NO–Rg complexes presented herein were collected in the parent ion mass channel). The reasons for this have been discussed in detail in Chapter 3 (see Section 3.3.3). Briefly, the initial excitation of the NO chromophore leads to the formation of a super excited NO^{**}–Xe complex. This can then form NO–Xe* and subsequently Xe⁺, so that features attributable to the NO–Xe complex appear in the Xe⁺ mass channel. This process is made more efficient by the presence of strong Xe atomic resonances at the three-photon level. These strong absorptions led to detector-overload problems (from strong Xe⁺ signals). As a result the NO–Xe spectra (recorded in either the NO⁺–Xe or Xe⁺ mass channels) were dominated by strong atomic resonances, which obscured any features that could be attributed to the NO–Xe complex. These strong (3 + 1) atomic Xe resonances were useful for calibration purposes however. A total of nine atomic

Xe resonances are observed, whose energies can be compared with their well-known literature values.⁴ Note that there are a number of transitions in the spectral range probed although only nine are allowed. For a three photon transition the following selection rules are appropriate: $\Delta\lambda = \pm 1, \pm 3$ and $\Delta J = 0, \pm 1, \pm 2, \pm 3$ (except $J'' = 0 \leftrightarrow J' = 0, 1, 2$ and $J'' = 1 \leftrightarrow J' = 1$). Table 5(I) shows the observed energies of the (3 + 1) atomic Xe transitions, together with the excited state electron configuration, excited state total angular momentum J , and the actual transition energies.

Configuration	Term	J	E/cm ⁻¹	E/cm ⁻¹
			literature value ^a	observed
5p ⁵ .(² P _{3/2} ^o).8s	² [3/2] ^o	1	90932.4	90932.4
5p ⁵ .(² P _{1/2} ^o).5d	² [5/2] ^o	3	91746.6	91746.0
5p ⁵ .(² P _{3/2} ^o).7d	² [1/2] ^o	1	92128.3	92128.5
5p ⁵ .(² P _{3/2} ^o).7d	² [3/2] ^o	1	92714.0	92715.3
5p ⁵ .(² P _{3/2} ^o).9s	² [3/2] ^o	1	93422.1	93424.5
5p ⁵ .(² P _{1/2} ^o).5d	² [3/2] ^o	1	93618.2	93622.5
5p ⁵ .(² P _{3/2} ^o).8d	² [1/2] ^o	1	94228.0	94234.5
5p ⁵ .(² P _{3/2} ^o).8d	² [7/2] ^o	3	94290.2	94296.6
5p ⁵ .(² P _{3/2} ^o).8d	² [5/2] ^o	3	94370.0	94401.0

Table 5(I): *atomic (3 + 1) Xe transitions used to calibrate the spectra in the present work: (a) Reference 4.*

A least squares fit of a plot of the observed peak energies against their actual energies gives a linear equation, which can be used to calibrate the spectra collected in the present work. A spectrum of the atomic Xe resonances used to calibrate the laser is shown in Figure 5(iii).

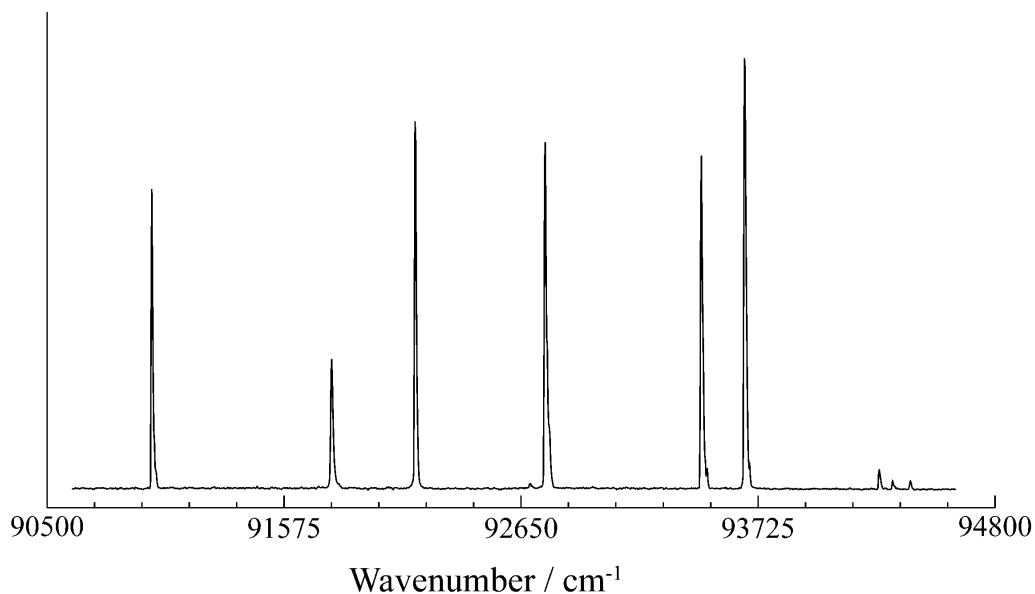


Figure 5(iii): $(3 + 1)$ REMPI spectrum recorded in the Xe^+ mass channel. The three-photon energies of the peaks are shown and have been used for calibration.

5.3 Results and discussion

5.3.1 NO–Kr $\tilde{E}^2\Sigma^+$ state

The $(2 + 1)$ REMPI spectra of the $\tilde{E}^2\Sigma^+$ state of NO–Ne, NO–Ar and NO–Kr, recorded in the present work in the region of $\nu_{NO} = 0$, are shown in Figure 5(iv). These spectra were collected at Nottingham and are consistent with those collected by Meyer and coworkers at the University of Georgia in a contemporaneous study. The structure seen in the NO–Kr spectrum is similar to that found for NO–Ne and NO–Ar, with all spectra showing a complicated series of structured bands. The $4s$ Rydberg state lies lower in energy than the $3d\lambda$ Rydberg states, owing to the increased penetration of the s electron compared with the d electron. The $3d\lambda$ Rydberg states have been discussed in detail for the NO–Rg van der Waals dimers in Chapter 3 (Rg = Ne–Kr), and for the larger NO–Rg_x clusters in Chapter 4 (Rg = Ne; $x = 1-2$ and Rg = Ar; $x = 1-6$). The

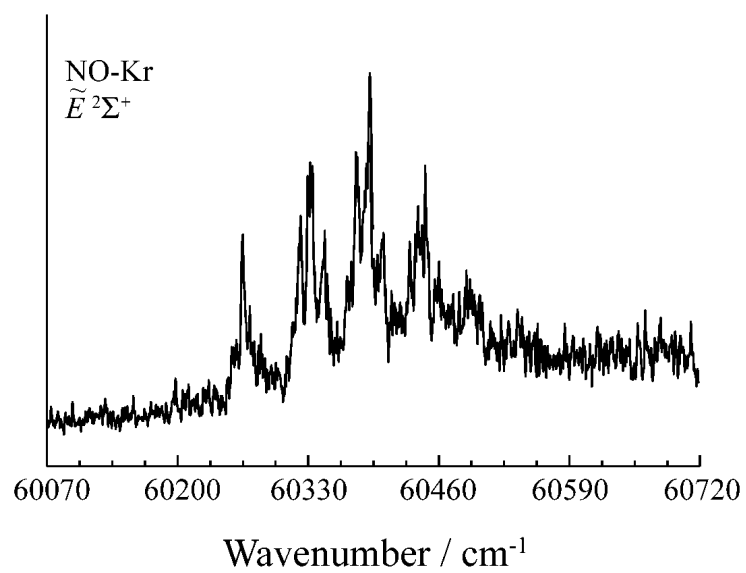
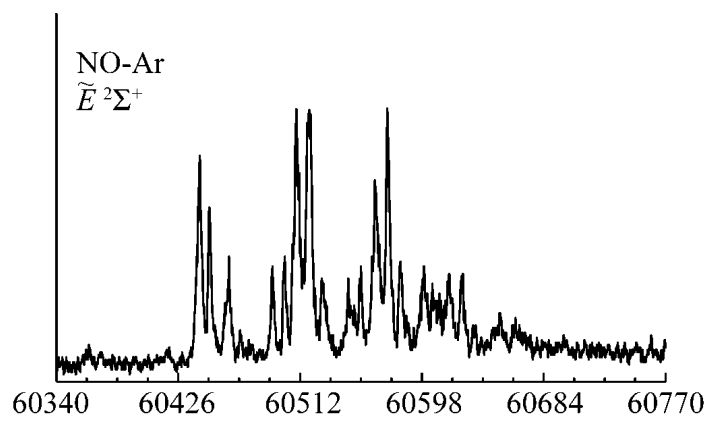
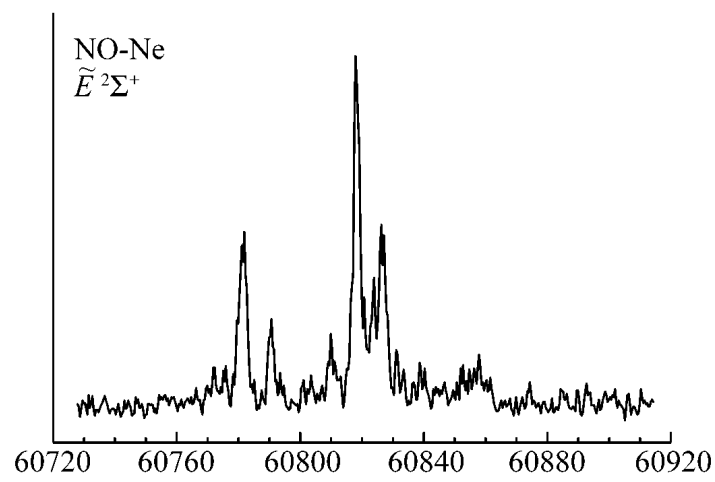


Figure 5(iv): $(2 + 1)$ REMPI spectra of the $\tilde{E}^2\Sigma^+$ state of NO-Ne, NO-Ar and NO-Kr with $v_{\text{NO}} = 0$.

first spectral features are seen to shift further to the red as the size and polarisability of the Rg atom increases, and reflect the increased magnitude of the interaction in the excited state relative to the ground state.

In Figure 5(v) is shown the $\tilde{E}^2\Sigma^+$ state spectrum of NO–Kr recorded at the University of Nottingham, together with that collected by Meyer *et al.*

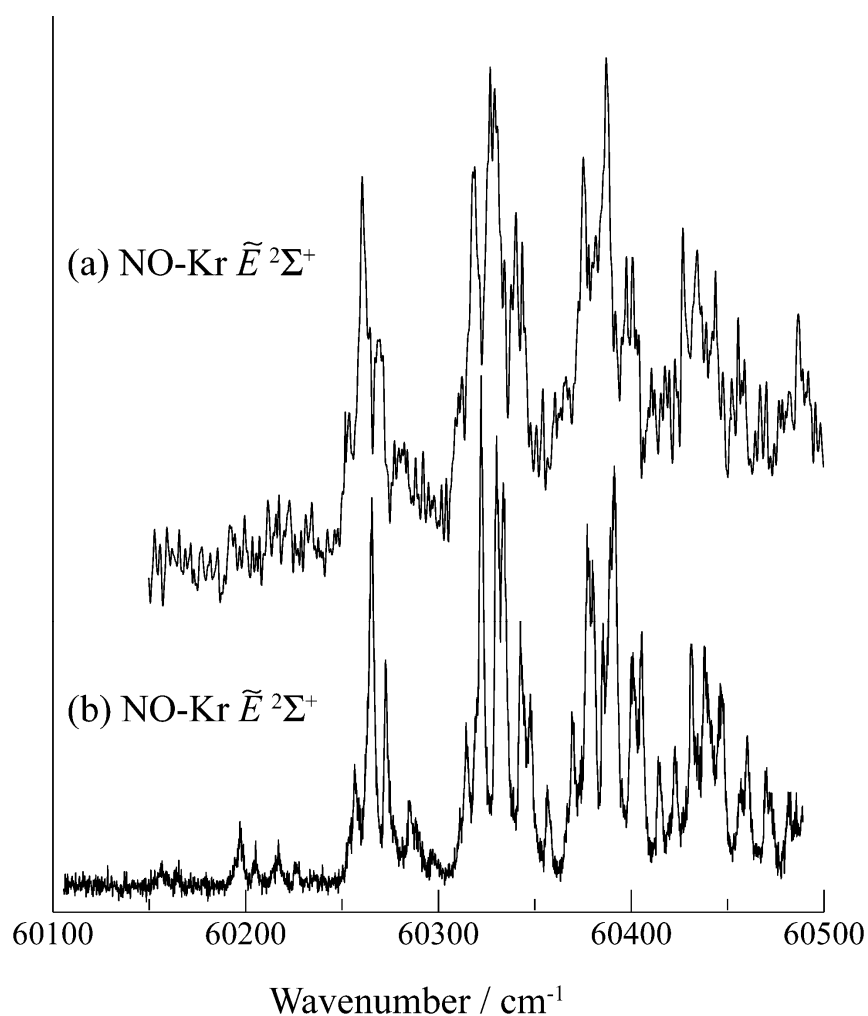


Figure 5(v): $(2 + 1)$ REMPI spectrum of the $\tilde{E}^2\Sigma^+$ state of NO–Kr recorded in the present work (top trace), and a comparable spectrum collected by Meyer and coworkers (lower trace).

An assignment of the features seen in the NO–Kr $\tilde{E}^2\Sigma^+$ state spectrum will be based on the experimental spectrum and simulation of Meyer *et al.* shown in Figure 5(vi). The simulated spectrum is based on a rotational temperature of 1.5 K (only the ground vibrational level is assumed to be populated). This temperature is consistent with that for previous work on the NO–Rg $3d\lambda$ Rydberg states as discussed in Chapter 3, where a rotational temperature of less than 5 K has been derived.

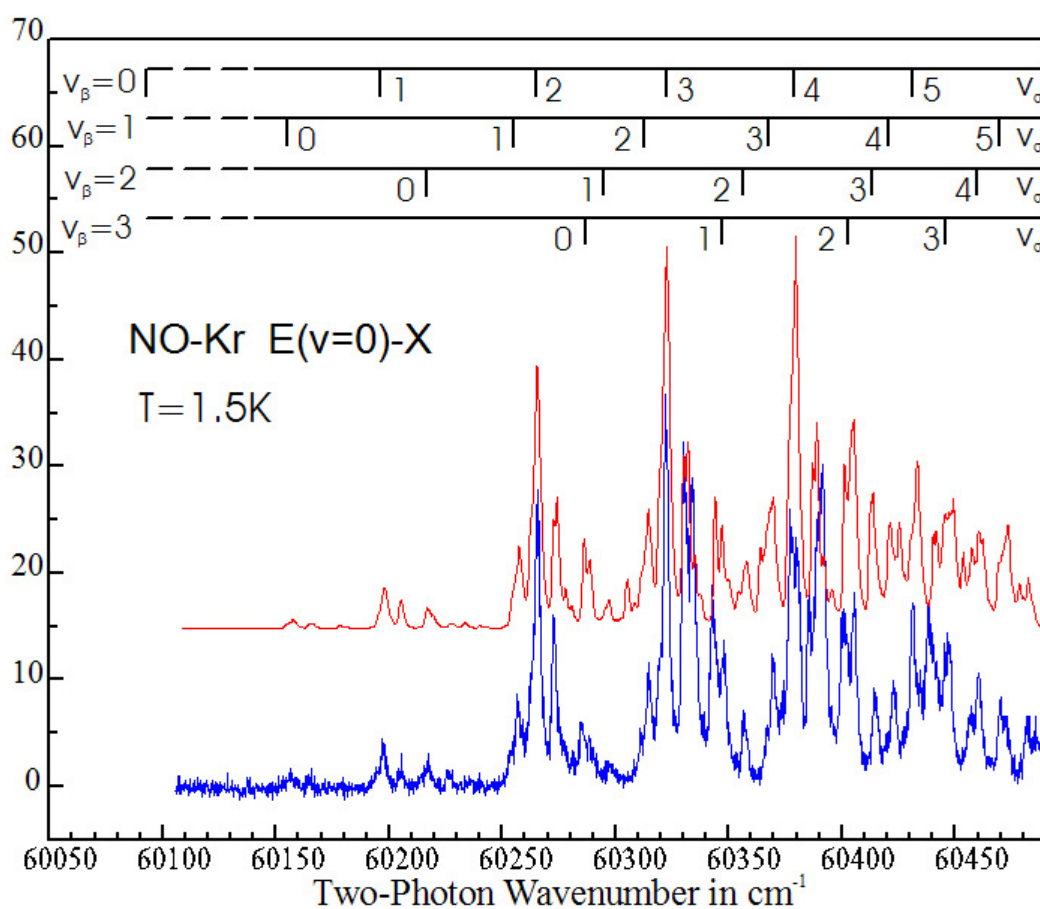


Figure 5(vi): *simulated (top trace) and experimental (bottom trace) (2 + 1) REMPI spectra of the $\tilde{E}^2\Sigma^+ (v_{\text{NO}} = 0) \leftarrow \tilde{X}^2\Pi$ transition in NO–Kr, recorded by Meyer and coworkers in a contemporaneous study.*

In the (2 + 1) REMPI spectrum of the $\tilde{E}^2\Sigma^+ (v_{\text{NO}} = 0) \leftarrow \tilde{X}^2\Pi$ transition in NO–Kr, collected by Meyer and coworkers, shown in the lower trace of Figures 5(v) and 5(vi), the first discernible band is located at $\sim 60150 \text{ cm}^{-1}$ and is comprised of at least three very weak sub-bands. This feature is followed by a series of several strong peaks located around 60200 cm^{-1} , 60264 cm^{-1} , 60323 cm^{-1} , 60382 cm^{-1} and 60433 cm^{-1} . The main feature of each band is accompanied by two others shifted towards higher wavenumber, with a weaker feature, shifted to lower wavenumber. At higher wavenumber, the spectrum becomes more complicated as different vibrational bands overlap.

An analysis of the NO–Ar $\tilde{E}^2\Sigma^+$ state has been carried out previously.^{3,5} The dominant progression in the NO–Ar spectrum was assigned as the intermolecular stretch vibration. This is due to the change in the intermolecular bond distance upon excitation: the excited state is more strongly bound compared with the ground state. This large geometry change is responsible for the absence of the origin (v_{00} transition) since it leads to poor Franck-Condon factors. In the present work, the intermolecular stretch vibration is expected to be dominant. Similarly, the origin feature is expected to be weak, as was the case for NO–Ar; this is found to be the case for NO–Kr.

The intensity of the pure bending progression is dependent upon the value of the overlap integral; the overlap between the ground and excited state wavefunctions, with no intermolecular stretch excited, $\langle v_{\sigma'} = 0 | v_{\sigma''} = 0 \rangle$. The overlap is expected to be small, again due to the large change in the intermolecular bond distance upon excitation, therefore, the pure bending progression is expected to be very weak (at least the lowest-energy members). Thus, bending modes are only expected to appear in combination with the intermolecular stretch. A careful inspection of the spectrum shown in the lower trace of Figure 5(vi) reveals an increased complexity from low to

high wavenumber. For example, the first bands at 60150 cm^{-1} and 60200 cm^{-1} are very simple, the next one at 60260 cm^{-1} is comprised of two bands, while the subsequent one at 60330 cm^{-1} is expected to contain overtones of the stretch and bending modes plus a combination band. All seem to contribute to the spectrum with similar intensities. The main progression is therefore assigned to the intermolecular stretch vibration, with secondary progressions arising from the stretching combination with at least one quantum of the bending vibration. This assignment (performed by H. Meyer *et al.*) is labelled in Figure 5(vi). A simulation of the two-photon transition to the $\tilde{E}^2\Sigma^+$ state performed by Meyer, has found that the intensity of the vibrational bands is governed by the Franck-Condon factors for the NO vibration, as well as the overlap integral for the intermolecular vibrations.

The structure seen in the NO–Kr $\tilde{E}^2\Sigma^+$ state spectra shown in Figure 5(v) (recorded in this work, and by Meyer and coworkers) has also been seen in the $\tilde{C}^2\Pi$ state for NO–Ar, NO–Kr and NO–Xe.^{3,6} The assignment of the $\tilde{C}^2\Pi$ and $\tilde{E}^2\Sigma^+$ state spectra was based upon simulations of the two-photon electronic transition, carried out by Meyer (the simulation performed to enable assignment of the NO–Kr spectrum recorded in the present work will be discussed further below). As for the $\tilde{E}^2\Sigma^+$ state, the main spectral progressions seen in the $\tilde{C}^2\Pi$ state were assigned as intermolecular stretches, bends and combinations of the two. Each member of the vibrational progressions observed was found to contain a reproducible pattern of more closely spaced features. This structure was attributed to rotation of the molecule around the a inertial axis. Owing to the T-shaped geometry of the $\tilde{C}^2\Pi$ state, the a -axis is almost coincident with the intermolecular vector between the Rg atom and the centre of mass of NO. Therefore this a -rotational structure is largely due to rotation of the NO moiety. The near T-shaped geometry of the $\tilde{E}^2\Sigma^+$ state complex also gives rise to a -rotational structure, which is partially resolved in this work.

The appearance of the progressions is indicative of the change in geometry between the ground and excited states (for example, the absence of the $\tilde{E}^2\Sigma^+$ state origin transition arises because of a shortening of the intermolecular bond), but this geometry change is also manifested in the spacings of the a -rotational lines, since the angle of NO to the intermolecular vector affects the A rotational constant. Hence, a successful simulation of the a -rotational structure within each feature can be used to derive a value for the Jacobi angle (see below) in the excited state. This may be compared to the ground state angular geometry, and combined with the known $\text{NO}^+\text{-Rg}$ cationic geometries,⁷ to gain some insight into how "cationic" the Rydberg states are.

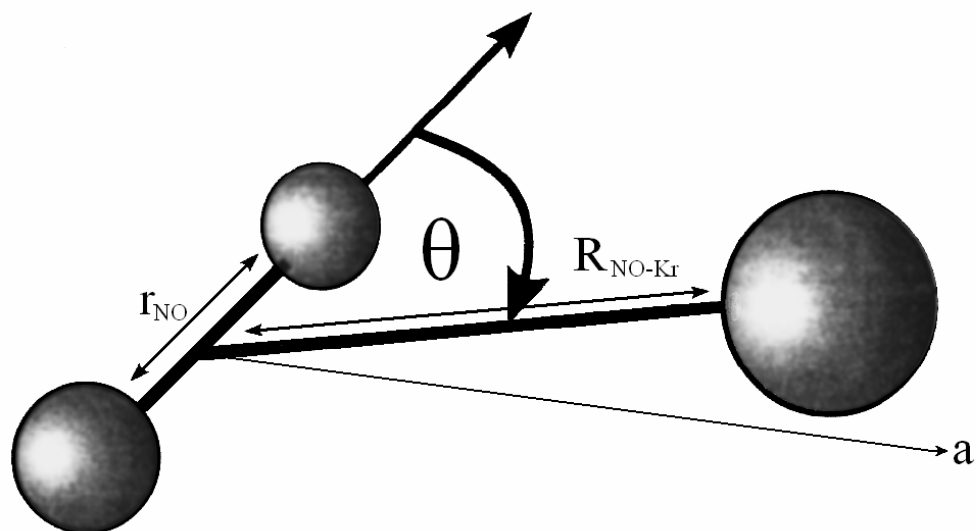


Figure 5(vii): the dimensions r_{NO} , $R_{\text{NO-Kr}}$, and the Jacobi angle θ , together with the a inertial axis for NO-Kr , used to simulate the $\tilde{E}^2\Sigma^+$ state $(2 + 1)$ REMPI spectrum.

Meyer has carried out a simulation of the rotational structure within each individual vibrational band and the simulated spectrum presented in Figure 5(vi) was obtained by summing the contributions for each individual vibrational band. Briefly, a ground state geometry with $r_{\text{NO}}'' = 1.16 \text{ \AA}$, $R_{\text{NO-Kr}}'' = 3.7 \text{ \AA}$ and a Jacobi angle $\theta = 88^\circ$ was used.

(The Jacobi coordinates are defined relative to the centre of mass of the diatom and the Jacobi angle defines the angle between the N–O molecular bond and the vector between the Rg atom and the centre of mass of NO). For the electronically-excited state, $r_{NO}' = 1.07 \text{ \AA}$ and $R_{NO-Kr}' = 3.07 \text{ \AA}$.⁶ The Jacobi angle was treated as an adjustable parameter. The dimensions r_{NO} , R_{NO-Kr} , and θ , together with the a inertial axis are shown in Figure 5 (vii).

The Jacobi angle found for the vibrational levels of NO–Kr in the $\tilde{E}^2\Sigma^+$ state is in the range $\theta = 50^\circ$ (for the feature corresponding to three quanta in both the intermolecular stretch and bend) to $\theta = 65^\circ$ (for the features with one quantum of intermolecular stretch, and with one quantum of stretch in combination with three quanta of intermolecular bend), where the Kr atom is positioned closer to the nitrogen end of NO. The Jacobi angle calculated for the cationic complex is $\theta = 81^\circ$.⁷ This similarity suggests that along the bending coordinate, the $\tilde{E}^2\Sigma^+$ state potential closely resembles that of the cation.

Once the $\tilde{E}^2\Sigma^+$ state dissociation energy is known, trends in the excited state binding energies for the complexes NO–Rg (Rg = Ne–Kr) can be investigated. In order to determine the excited state dissociation energy (D_0') the energy of the origin (ν_{00}) transition is needed. As discussed above, the large change in the intermolecular bond distance upon excitation leads to poor Franck-Condon factors, and the origin transition is not observed. An origin position has been estimated by extrapolating each of the assigned progressions (shown in Figure 5(vi)), to give a value of $60093 \pm 10 \text{ cm}^{-1}$. The ν_{00} energy of the complex ($\nu_{00}(NO-Rg)$) can be combined with the ground state dissociation energy D_0'' and the excited state NO origin ($\nu_{00}(NO)$) to give the excited state dissociation energy using Equation 5(a).

$$D_0' = \nu_{00}(\text{NO}) + D_0'' - \nu_{00}(\text{NO-Rg}) \quad 5(\text{a})$$

The excited state dissociation energies for NO–Ne, NO–Ar and NO–Kr are given in Table 5(II), along with the corresponding cationic values. The assignment of the vibrational bands in Figure 5(vi) allows estimates to be made of the vibrational spacings $\nu_\sigma = 66 \text{ cm}^{-1}$ and $\nu_\beta = 62 \text{ cm}^{-1}$ for the stretch and bend frequencies, respectively. In both cases, this is the 1–2 separation, owing to the fact that the origin was not observed. These values are given in Table 5(II) together with the 0–1 spacings for the intermolecular stretch and bend, for NO–Ne² and NO–Ar.³ Also shown are the harmonic stretch and bend frequencies for the cationic complexes NO⁺–Rg (Rg = Ne–Kr).

	NO–Ne	NO ⁺ –Ne	NO–Ar	NO ⁺ –Ar	NO–Kr	NO ⁺ –Kr
D_0'	161 ^{a‡} (57%)	284 ^{b†}	579 ^c (62%)	941 ^d	877 ^f (73%)	1200 ^{b†}
0–1 (σ)	50 ^a (61%)		79 ^c (79%)		66 ^{f*} (48%)	
0–1 (β)	39 ^a (95%)		57 ^c (71%)		62 ^{f*} (77%)	
ω_e (σ)		82 ^b		100 ^e		138 ^b
ω_e (β)		41 ^b		80 ^e		81 ^b

Table 5(II): *all values given in cm⁻¹; σ = intermolecular stretch; β = intermolecular bend; (a) Reference 2; (b) Reference 7; (c) Reference 3; (d) Reference 8; (e) Reference 9; (f) this work; (‡) Reference 10; (†) calculated from data presented in Reference 7; (*) this is the 1–2 spacing. Excited state values as a percentage of the corresponding cationic values are shown in parentheses.*

Using Equation 5(a) with an NO–Kr ground state dissociation energy¹¹ of 105 cm⁻¹, and an $E^2\Sigma^+$ state NO origin¹² (ν_{00}) of 60864 cm⁻¹, gives a dissociation energy for the $\tilde{E}^2\Sigma^+$ state of NO–Kr of 877 ± 10 cm⁻¹, which is only 73% of the value found for the cationic complex. Similar variations between the binding energies for the neutral and the cationic complexes are found for the other rare gas complexes: 62% for NO–Ar and 57% for NO–Ne. The relative increase of the binding energy is in line with the Rydberg electron being less able to penetrate into the cationic core for the heavier complexes. The heavier Rg atoms will be less effectively shielded from the NO⁺ core charge as penetration of the 4s Rydberg electron becomes increasingly hindered. Within the rare gas series, there is a trend for the stretch frequencies to decrease as a percentage of the corresponding cationic harmonic values, as the size and polarisability of the Rg atom increases, although this is not uniform across the series. For NO–Ne, the 0–1 spacing is 61% of the cationic value. This increases to 79% for NO–Ar, before decreasing for NO–Kr, where the 1–2 spacing is only 48% of the cationic value. The corresponding ratio for the bending frequencies does not show such a trend. The decrease in the stretch frequency as a percentage of the cationic value, between NO–Ne and NO–Kr may arise from a repulsive interaction between the Rydberg electron and the electrons on the Rg, which will be greatest for the (heaviest) Kr atom.

5.3.2 4s and 3d Rydberg states with $\nu_{\text{NO}} = 1$

During recording of the NO–Rg $\tilde{E}^2\Sigma^+$ state spectra at Nottingham, and the NO–Rg $\tilde{F}^2\Delta$ and $\tilde{H}^1\Pi$ states (Rg = Ne, Ar, Kr) discussed in Chapter 3, the $\nu_{\text{NO}} = 1$ band of the $\tilde{E}^2\Sigma^+$ state was observed. Corresponding spectra for the $\nu_{\text{NO}} = 1$ features of the $\tilde{F}^2\Delta$ and $\tilde{H}^1\Pi$ states were subsequently searched for and recorded. The NO–Kr $\tilde{E}^2\Sigma^+$ state spectra, with $\nu_{\text{NO}} = 1$ and $\nu_{\text{NO}} = 0$ are shown in Figure 5(viii). The

vibrationally-excited NO–Ar $\tilde{F}^2\Delta$ and $\tilde{H}^1\Pi$ state spectrum, and NO–Ne $\tilde{E}^2\Sigma^+$ state spectrum, are shown in Figures 5(ix) and 5(x) respectively. All are shown with $\nu_{\text{NO}} = 0$ for comparison and the $\nu_{\text{NO}} = 1$ spectra have been shifted to align the features with those in the corresponding $\nu_{\text{NO}} = 0$ spectra. Features in the vibrationally-excited spectra are broadened, due to the increased laser power required to collect the spectra. The band positions and peak intensities are comparable for each state with $\nu_{\text{NO}} = 0$ and $\nu_{\text{NO}} = 1$.

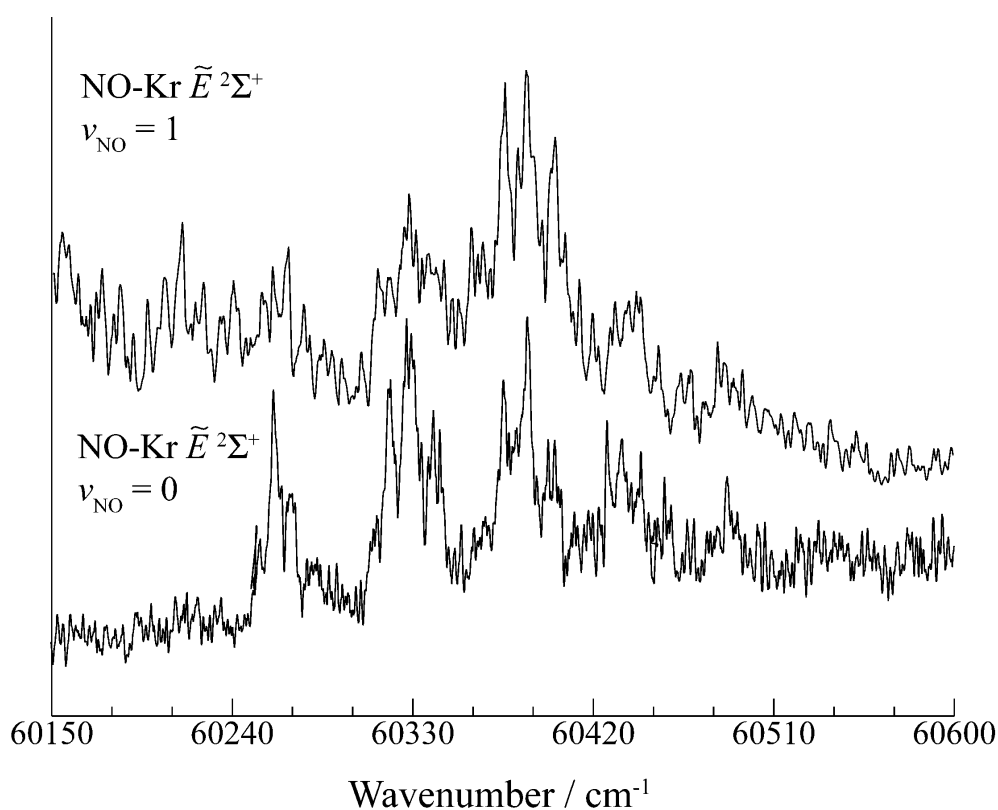


Figure 5 (viii): $(2 + 1)$ REMPI spectra of the NO–Kr $\tilde{E}^2\Sigma^+$ state, with $\nu_{\text{NO}} = 0$ (lower trace) and $\nu_{\text{NO}} = 1$ (upper trace). The vibrationally-excited spectrum has been shifted to lower energy by 2346.8 cm^{-1} .

To align the $\nu_{\text{NO}} = 0$ and $\nu_{\text{NO}} = 1$ spectra for NO–Ar presented in Figure 5(ix), the $\nu_{\text{NO}} = 1$ spectrum was shifted to lower energy by 2332 cm^{-1} . In order to align the $\tilde{F}^2\Delta$

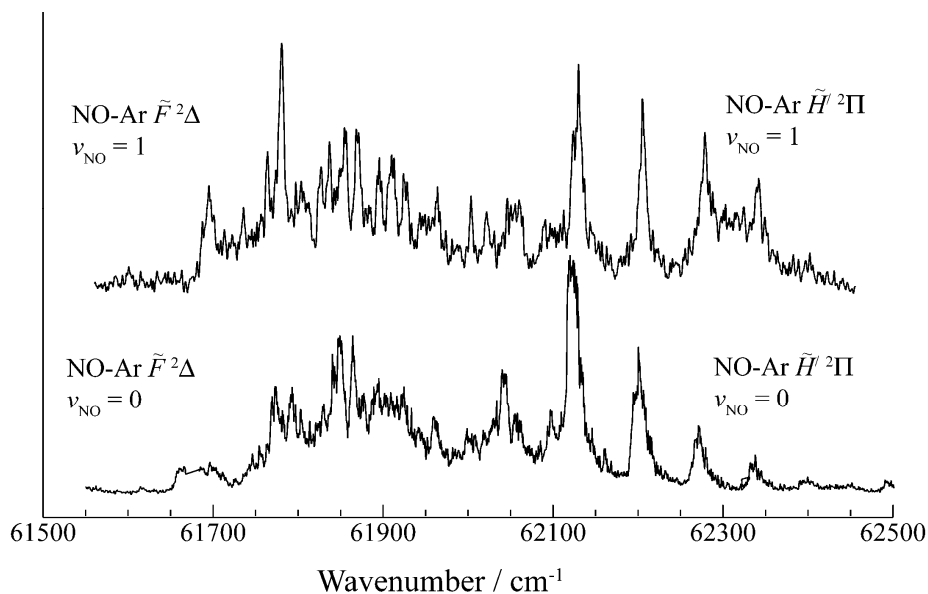


Figure 5(ix): $(2 + 1)$ REMPI spectra of the NO-Ar $\tilde{F}^2\Delta$ and $\tilde{H}'^2\Pi$ states, with $v_{\text{NO}} = 0$ (lower trace) and $v_{\text{NO}} = 1$ (upper trace). The vibrationally-excited spectrum has been shifted by 2332 cm^{-1} to lower energy. See text for details.

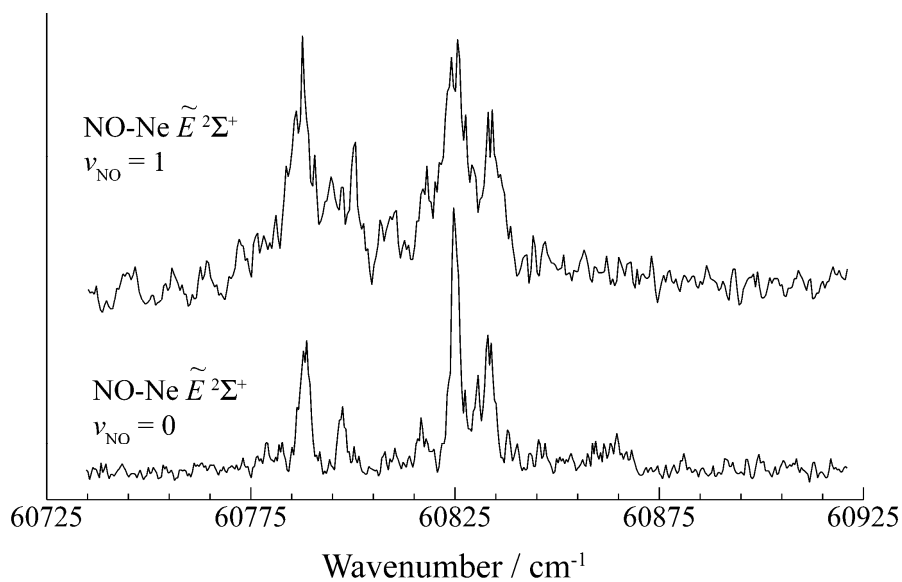


Figure 5(x): $(2 + 1)$ REMPI spectra of the NO-Ne $\tilde{E}^2\Sigma^+$ state, with $v_{\text{NO}} = 0$ (lower trace) and $v_{\text{NO}} = 1$ (upper trace). The $v_{\text{NO}} = 1$ spectrum is shifted by 2344.8 cm^{-1} to lower energy.

state features between the two spectra, a shift of 2333 cm^{-1} was found to provide the best alignment. For the $\tilde{H}^2\Pi$ state, a shift of 2331 cm^{-1} resulted in the best "visual" alignment of the $\nu_{\text{NO}} = 0$ and $\nu_{\text{NO}} = 1$ spectra. The shift of 2332 cm^{-1} presented in Figure 5(ix) is an average and was chosen to reflect the overall change in the appearance of the spectrum upon excitation of a single quantum of N–O intermolecular stretch and not the change in appearance of one particular state.

It was shown in Chapter 3 that in the $3d$ states, the Rg atom lies mostly inside the Rydberg orbital. Consequently, there is a competition for the NO^+ core between the Rg atom and the Rydberg electron. Each of these interactions can affect the observed NO vibrational frequency via the amount of penetration of the Rydberg electron, and the possibility of electron density transfer from Rg to NO^+ . The effect of complexation on the NO stretch frequency can be investigated quantitatively, since the NO 0–1 vibrational spacing for the NO–Rg complexes can be determined for the $4s$ and $3d$ Rydberg states, by comparing the $\nu_{\text{NO}} = 0$ and $\nu_{\text{NO}} = 1$ spectra. The energy of an intense feature in each of the corresponding spectra is used to calculate the NO 0–1 vibrational spacing. For example, in the $\tilde{E}^2\Sigma^+$ state of NO–Ne, the energy of the most intense feature in the $\nu_{\text{NO}} = 0$ spectrum, shown in the lower trace of Figure 5(x), was subtracted from the energy of the corresponding feature in the $\nu_{\text{NO}} = 1$ spectrum. These peak energies give an NO 0–1 vibrational spacing of 2345.8 cm^{-1} . The observed 0–1 vibrational spacings for NO and the NO–Rg complexes for the three states under consideration are shown in Table 5(III). For comparison, the corresponding calculated harmonic frequency for the uncomplexed cation (there being no experimental 0–1 spacings available for the complexed cations) is also shown.⁷

Experimental values for ω_e and $\omega_e x_e$ for the NO Rydberg states are well known and are available on the NIST website.⁴ These values can be used to calculate the 0–1 spacing, since the 0–1 spacing is given by:

$$\omega_e - 2\omega_e x_e \quad 5(b)$$

The 0–1 spacings for the $E^2\Sigma^+$ and $H^2\Pi$ states of uncomplexed NO measured in this work are seen to be consistent with their corresponding calculated values (the 0–1 spacings are calculated as 2342.5 and 2339.0 cm^{-1} using Equation 5(b) for the $E^2\Sigma^+$

State	NO	NO–Ne	NO–Ar	NO–Kr
$\tilde{E}^2\Sigma$	2342.2	2345.8	2340.0	2346.6
$\tilde{F}^2\Delta$	2318.2	2322.2	2334.2	2340.1
$\tilde{H}^2\Pi$	2341.2	2343.2	2330.2	2334.2
Cation	2343.9	—	—	—

Table 5(III): measured NO 0–1 vibrational spacings for the 4s and 3d Rydberg states of NO and NO–Rg, with errors of $\pm 1.5 \text{ cm}^{-1}$.

and $H^2\Pi$ states respectively). The $F^2\Delta$ state is more complicated, since it interacts with the valence $B^2\Delta$ state.^{13,14} The $F^2\Delta$ ($v' = 0$) level interacts with the $B^2\Delta$ ($v' = 2$) level, and the $F^2\Delta$ ($v' = 1$) level interacts with the $B^2\Delta$ ($v' = 4$) level. These interactions are different, leading to a change in the measured separation of the $F^2\Delta$ state vibrational levels. Indeed, the calculated, unperturbed separation is 2353.6 cm^{-1} , employing the vibrational constants⁴ using Equation 5(b), whereas the measured separation is 2318.2 cm^{-1} .

For the NO–Rg complexes in the $\tilde{E}^2\Sigma^+$ state, there is a very slight increase in the 0–1 spacing for NO–Ne and NO–Kr, relative to that in uncomplexed NO, but an extremely slight decrease for NO–Ar. The fact that the 0–1 spacing changes little upon complexation suggests that the interaction between the Rg atom and the NO^+ core is small in the $\tilde{E}^2\Sigma^+$ states. Additionally, the 0–1 spacing for the $\tilde{E}^2\Sigma^+$ state in uncomplexed NO, and the spacings across the NO–Rg series, are similar to that of the cation. This is also the case for the $\tilde{H}^2\Pi$ state of NO–Ne, where the measured 0–1 spacing is comparable to that of the cation and that of uncomplexed NO. Across the NO–Rg series however, the vibrational spacing decreases, dropping by 11 cm^{-1} and 7 cm^{-1} from the uncomplexed NO spacing for NO–Ar and NO–Kr respectively. The dissociation energy of the $\tilde{H}^2\Pi$ state was found to be very close to that of the cation (see Chapter 3). This was attributed to a strong interaction between the NO^+ core and the Rg atom, which resides within the Rydberg orbit and is poorly shielded from the NO^+ core charge by the $3d$ Rydberg electron. This interaction between the Rg atom and the NO^+ core can be viewed as a donation of electron density from the Rg atom into the now vacant $2p\pi^*$ orbital of NO. This will weaken the N–O bond, therefore leading to a reduction in the fundamental vibrational frequency. In the absence of other factors, this effect would be expected to result in a decrease in the vibrational frequency as the Rg atom increases in size. However there is not a uniform decrease in the vibrational stretch frequency as the Rg group is descended in the present work: the 0–1 vibrational spacing *increases* from 2330.2 cm^{-1} for NO–Ar, to 2334.2 cm^{-1} for NO–Kr, suggesting that other factors play a role. One possibility may be the requirement for electron density to be donated into the $2p\pi^*$ orbital: since this has lobes at the N and O ends of the molecule, the overlap between the Rg outermost s orbital and the $2p\pi^*$ orbital will be more efficient at geometries that deviate from T-shaped.

The variation in the $\tilde{F}^2\Delta$ state fundamental vibrational frequencies across the NO–Rg series is remarkable and cannot be attributable solely to interaction between the Rg atom and the NO⁺ core. As noted above, the $F^2\Delta$ state $v' = 0$ and $v' = 1$ levels of NO have been shown^{13,14} to interact with the $v' = 2$ and $v' = 4$ levels of the $B^2\Delta$ state. The interaction between these states is responsible for the perturbation of the 0–1 spacing seen in uncomplexed NO (2318.2 cm⁻¹), relative to the spacing calculated using ω_e and $\omega_e x_e$ available elsewhere⁴ (2353.6 cm⁻¹). The magnitude of the perturbation will lessen as the energy difference between the interacting states increases. Complexation lowers the $\tilde{F}^2\Delta$ state energy (note the spectral redshift of the $\tilde{F}^2\Delta$ state in the NO–Rg complexes, relative to the $F^2\Delta$ state in uncomplexed NO) and the vibrational spacing increases (towards the unperturbed value) across the Rg series. This suggests that the larger Rg atoms are reducing the interaction between the $\tilde{F}^2\Delta$ and $\tilde{B}^2\Delta$ vibrational levels, so that the vibrational spacing approaches the unperturbed value.

5.4 Conclusions

New spectra for the NO–Kr $\tilde{E}^2\Sigma^+ \leftarrow \tilde{X}^2\Pi$ transition have been presented and compared with those of NO–Ne and NO–Ar. The quality of the spectra obtained in the present work was comparable with the high quality spectra recorded in a contemporaneous study of H. Meyer and coworkers. A simulation of the two-photon NO–Kr absorption spectrum was performed at the University of Georgia by the group of H. Meyer. This led to an assignment of the $\tilde{E}^2\Sigma^+$ spectrum in terms of progressions of intermolecular stretches, and combinations of stretches and bends. Each member of the progressions has a -axis rotational structure, which is essentially rotation of the NO moiety, since the a inertial axis is almost coincident with the intermolecular vector. The end-over-end rotation of the molecule is not resolvable with the present laser system, in either this work or that of Meyer *et al.*

During the present study, the $\tilde{E}^2\Sigma^+$ state with $\nu_{\text{NO}} = 1$ was observed. This led to the observation of the $\tilde{F}^2\Delta$ and $\tilde{H}^1\Pi$ states, both with $\nu_{\text{NO}} = 1$. By comparing the energies of equivalent peaks in the $3d$ and $4s$ Rydberg state $\nu_{\text{NO}} = 0$ and $\nu_{\text{NO}} = 1$ spectra (collected at the University of Nottingham), the fundamental vibrational spacing for the NO moiety in the NO–Rg complexes was determined. An examination of the fundamental NO stretching frequency reveals that there is very little interaction between the Rg and the NO^+ core in the $\tilde{E}^2\Sigma^+$ state, consistent with the dissociation energies, which are found to be less cationic than for the previously studied $3d\lambda$ Rydberg states. For the $\tilde{H}^1\Pi$ state, there is no obvious shift in the vibrational spacing for NO–Ne, but there are significant decreases in frequency for NO–Ar and NO–Kr, suggesting that there is an interaction between the Rg atom and the NO^+ core. This interaction has been defined as electron donation into the $2p\pi^*$ orbital of NO from the larger Rg atoms, weakening the N–O bond and lowering the NO stretching frequency.

The $\tilde{F}^2\Delta$ state has anomalously large shifts, which cannot solely be due to the interaction between NO^+ and the Rg atom. This has been interpreted in terms of the relative positions of the valence $\tilde{B}^2\Delta$ state and the $\tilde{F}^2\Delta$ state, vibrational levels of which are known to interact with each other in uncomplexed NO. Complexation lowers the energy of the $\tilde{F}^2\Delta$ state, moving the vibrational levels apart, so decreasing the interaction, and leading to a return of the NO fundamental frequency to a value close to that of the cation. These complicated interactions obscure the overall picture for the $3d\delta$ states: in previous work on the $3d\lambda$ Rydberg states of NO–Kr (see Chapter 3) and in previous work reported by Kim and Meyer,⁵ the unexpectedly low dissociation energy of the $\tilde{F}^2\Delta$ state, compared with the $\tilde{H}^1\Pi$ state and the cation, the low intermolecular frequencies, and the complicated appearance of the $\tilde{F}^2\Delta$ state

spectra have led to the suggestion that there are subtle angular effects caused by the interaction of the $3d\delta$ electron density and that of the Rg atoms. Work carried out on NO–Rg_v complexes (see Chapter 4) has shown that there are interesting effects seen as the excited electron interacts with the surrounding Rg atoms. The approach described herein, using the changes in fundamental vibrational frequencies as a measure of intermolecular electron shielding/penetration, will enable a more detailed understanding of these and other complex systems.

5.5 References

¹ Ch. Jungen, *J. Chem. Phys.* **53**(11) (1970) 4168-4182.

² J. Fleniken, Y. Kim, H. Meyer, *J. Chem. Phys.* **109** (1998) 8940.

³ H. Meyer, *J. Chem. Phys.* **107** (1997) 7732.

⁴ http://physics.nist.gov/cgi-bin/AtData/levels_form.

⁵ Y. Kim, H. Meyer, *Int. Rev. Phys. Chem.* **20** (2001) 220.

⁶ P. Mack, J.M. Dyke, D.M. Smith, T.G. Wright, H. Meyer, *J. Chem. Phys.* **109** (1998) 4361.

⁷ E.P.F. Lee, P. Soldán, T.G. Wright, *J. Phys. Chem. A*, **102** (1998) 6858.

⁸ D_0' calculated using $D_0' = v_{00}(NO) + D_0'' - v_{00}(NO-Ar)$, where D_0'' of NO–Ar is given in K. Tsuji, K. Shibuya, K. Obi, *J. Chem. Phys.* **100** (1994) 5441; $v_{00}(NO)$ is given in G. Reiser, W. Habenicht, K. Müller-Dethlefs, E.W. Schlag, *Chem. Phys. Lett.* **152** (1988) 119 and $v_{00}(NO-Ar)$ is given in M. Takahashi, *J. Chem. Phys.* **96** (1992) 2594.

⁹ M. Takahashi, *J. Chem. Phys.* **96** (1992) 2594.

¹⁰ D_0' calculated using $D_0' = v_{00}(NO) + D_0'' - v_{00}(NO-Ne)$, where D_0'' of NO–Ne is given in M.H. Alexander, P. Soldán, T.G. Wright, Y. Kim, H. Meyer, P.J. Dagdigian, E.P.F. Lee, *J. Chem. Phys.* **114** (2001) 5588 and $v_{00}(NO) - v_{00}(NO-Ne)$ is given in J. Fleniken, Y. Kim, H. Meyer, *J. Chem. Phys.* **109** (1998) 8940.

¹¹ S.D. Gamblin, S.E. Daire, J. Lozeille, T.G. Wright, *Chem. Phys. Lett.* **325** (2000) 232-240.

¹² Y. Kim, H. Meyer, *Int. Rev. Phys. Chem.* **20**(3) (2001) 219-282.

¹³ M. Huber, *Helv. Phys. Acta.* **37** (1964) 329.

¹⁴ C. Jungen, *Can. J. Phys.* **44** (1966) 3197.

6 The $3s\sigma \tilde{A}^2\Sigma^+$ Rydberg state of NO–Rg (Rg = Ne–Xe)

6.1 Introduction

The electronic spectroscopy of NO-containing van der Waals complexes has formed the basis of several studies,^{1,2,3,4,5,6,7,8,9} where the complexing partner is a closed-shell species. The simplest examples of such systems are the NO–Rg (Rg = Ne, Ar, Kr, Xe) series and a review by Kim and Meyer¹ summarizes the work up to 2001. The $3d\lambda$ Rydberg states of NO–Rg (Rg = Ne–Xe) and NO–Rg_x (Rg = Ne, $x = 1-2$; Rg = Ar, $x = 1-6$), have been discussed in detail in Chapters 3 and 4 respectively. The $4s\sigma$ Rydberg state of NO–Rg (Rg = Ne–Kr) has been discussed in Chapter 5. The $\tilde{A}^2\Sigma^+ \leftarrow \tilde{X}^2\Pi$ transition in NO–Ar,² NO–Kr and NO–Xe has been observed previously,^{3,4,5} employing resonance-enhanced multiphoton ionisation (REMPI) spectroscopy. Despite considerable effort at the time the corresponding spectra of NO–Ne were not obtained, although electronic spectra of this species have been recorded via several different electronic states (see Chapters 3, 4 and 5). Similar failure to observe a structured spectrum had also been reported by Meyer and coworkers,⁶ Miller and Cheng⁷ (using REMPI) and Levy and coworkers⁸ (using laser-induced fluorescence). In the present work, a further attempt is made to record the $\tilde{A}^2\Sigma^+ \leftarrow \tilde{X}^2\Pi$ transition in NO–Ne.

6.1.1 Previous work on the $\tilde{A}^2\Sigma^+$ state of NO–Rg (Rg = Ar–Xe)

Of the low-lying Rydberg states, the $\tilde{A}^2\Sigma^+$ state is found to be the most weakly-bound; for the NO–Ar complex for example, a dissociation energy of 44 cm^{-1} has been derived by Tsuji *et al.*⁹ compared with their value of 414 cm^{-1} for the $3p\pi$ ($\tilde{C}^2\Pi$) state. In NO, the $A^2\Sigma^+$ state is Rydberg-like in character: the spectroscopic constants

and molecular parameters are similar to those of the NO^+ core. However, for each vibrational level of the $\tilde{A}^2\Sigma^+$ state in the complex, the van der Waals bond length is longer than that calculated for the ion and the $\tilde{A}^2\Sigma$ state dissociation energy is lower than that for the $\tilde{X}^2\Pi$ state¹⁰ (44 cm^{-1} in the excited state compared to 88 cm^{-1} in the ground state).¹ The weak binding in the $\tilde{A}^2\Sigma^+$ state is consistent with the radius of the 3s orbit (2.86 Å)¹¹ being too small to allow a Rg atom to reside within and the NO^+ core being more effectively shielded from the Rg atom by the orbiting 3s Rydberg electron.^{3,10} Unlike the higher Rydberg states, where only the spectral region located near the origin is observed, it is possible to observe the energy levels of the $\tilde{A}^2\Sigma^+$ state in their entirety – from the vibration-less origin to the dissociation limit.

The $\tilde{A}^2\Sigma^+$ state of NO-Ar has been observed in a number of studies using (1 + 1) resonance-enhanced multiphoton ionisation (REMPI)^{2,9,10} and laser-induced fluorescence.¹² The well-resolved (1 + 1) REMPI spectrum of Lozeille and coworkers² shown in Figure 6(i) is comparable to the spectra of Tsuji *et al.*⁹ and Bush *et al.*¹⁰ All contain three strong peaks, at 44242 cm^{-1} , 44273 cm^{-1} and 44276 cm^{-1} , labelled *A*, *B* and *C*. The analysis of Tsuji and coworkers⁹ gave an intermolecular bond distance of 4.6 Å for band *A*. This was shorter than the intermolecular distances (5.3 Å, 5.4 Å) derived from analysis of bands *B* and *C*. The longer bond lengths derived from bands *B* and *C* indicate a contribution from the stretch mode to these two bands. Band *A* has been identified as the origin, bands *B* and *C* have been assigned to rovibrational transitions involving the first excited stretching vibrational level. The weak feature labelled *b* has been tentatively attributed to the first excited bending level since it was found to be visible even under cold conditions.

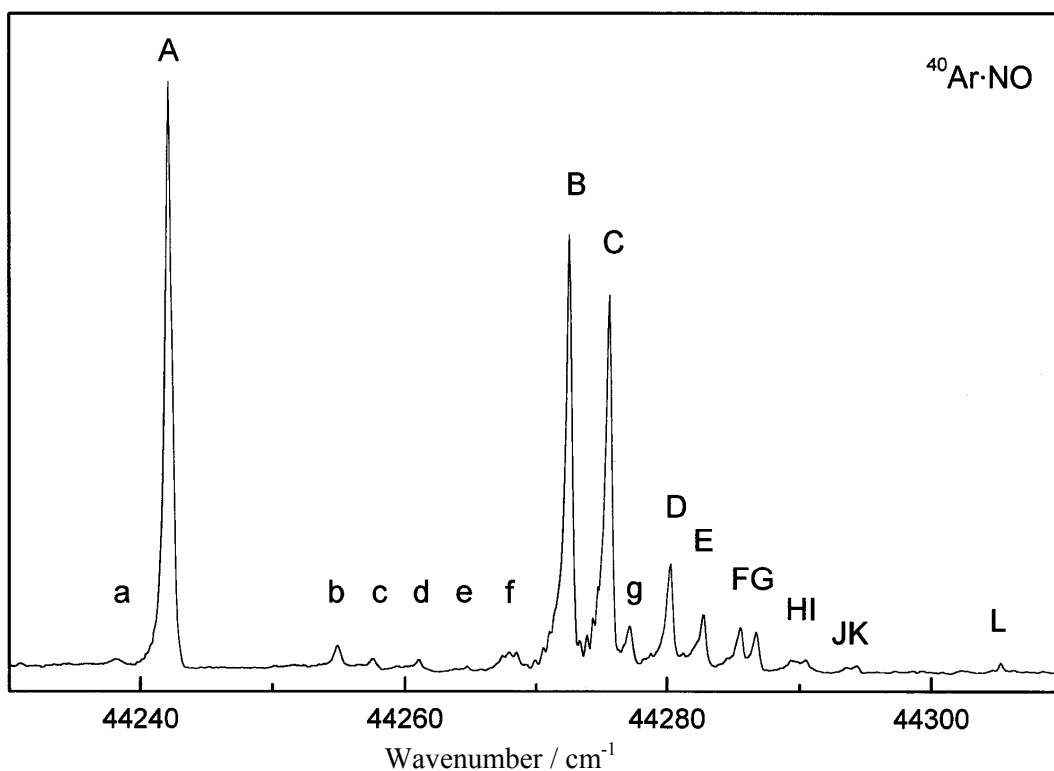


Figure 6(i): $(1 + 1)$ REMPI $\tilde{A}^2\Sigma^+$ state spectrum of NO–Ar taken from Reference 2. The features A–L and a–g have been interpreted in terms of the intermolecular stretch and bend vibrations, together with rotation of the NO moiety.

The main structure seen in the spectrum shown in Figure 6(i) has been interpreted in terms of an intermolecular stretch progression, onto which rotational motion of the NO subunit is superimposed. The form of the origin band was found to be consistent with a complex with a linear or near-linear geometry. If the complex were T-shaped the origin band would contain additional structure due to rotation of the complex about the a inertial axis (this rotational motion has been seen in the $\tilde{E}^2\Sigma^+$ of NO–Kr discussed in Chapter 5). Much of the structure observed in the higher wavenumber region of the spectrum is due to transitions to different rotational levels of the same upper vibrational state. Rotation of the complex becomes more significant as the intermolecular stretch vibration is excited: the average bond length increases and the

Ar atom will have less effect on the NO moiety, which will begin to behave more like a free rotor. The geometry of the complex was found to approach a skewed T-shape as the intermolecular stretch was excited.^{2,10}

The $\tilde{A}^2\Sigma^+$ state spectrum of NO–Kr is significantly more complicated than that of NO–Ar shown in Figure 6(i). The spectrum of Gamblin and coworkers⁵ is shown in Figure 6(ii) and offers better resolution than the earlier spectrum of Bush *et al.*³

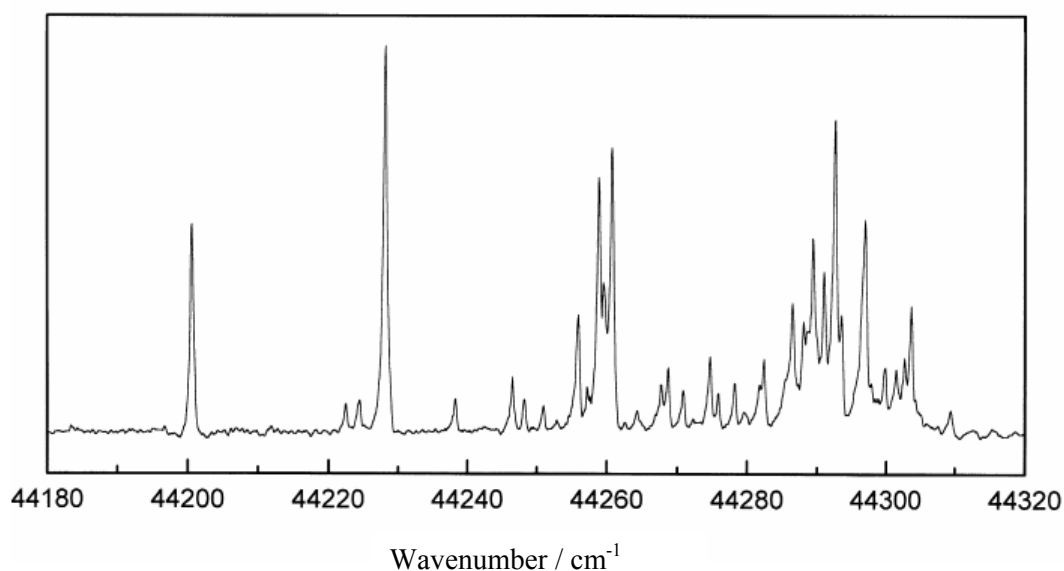


Figure 6(ii): $(1 + 1)$ REMPI $\tilde{A}^2\Sigma^+$ state spectrum of NO–Kr taken from Reference 5.

The spectrum consists of four strong features, with a spacing of $\sim 30 \text{ cm}^{-1}$, which have been identified as a progression in the intermolecular stretch vibration.⁵ The first feature is a single band, consistent with a (near) linear $\tilde{A}^2\Sigma^+$ state geometry, as was seen for NO–Ar. The spectrum is seen to increase in complexity to higher energy: the NO–Kr interaction decreases as the internal energy of the complex increases *i.e.* as the intermolecular stretch vibration is excited and the average bond length increases. The increased spectral complexity is thought to arise from rotation of the complex around

the a inertial axis (defined relative to the centre of mass of the complex), which becomes more likely as the interaction between the NO moiety and the Kr atom decreases. The sharp drop-off in intensity, seen in the spectra of both NO–Ar and NO–Kr, suggests that the dissociation limit of the complex is reached.⁵ In the spectrum shown in Figure 6(ii), the dissociation limit has been identified as being the high-energy side of the last sharp peak at 44304 cm⁻¹. In Reference 5 the appearance of levels higher than the dissociation limit was taken to imply the presence of a barrier to dissociation and the existence of quasibound levels.

The origin band in the NO–Ar $3s\sigma$ state spectrum is blueshifted relative to the NO $A^2\Sigma^+$ state origin, evidence that the excited state is less strongly-bound than the $\tilde{X}^2\Pi$ ground state, and the origin band for NO–Kr is almost isoenergetic with the NO $A^2\Sigma^+$ state origin. This is contrary to the $3d\lambda$ and $4s\sigma$ Rydberg states investigated in Chapters 3 and 5 respectively, where the increased binding energy in the excited states was reflected in a redshift of the excited state features, relative to those of the ground state. The dissociation energy of the NO–Kr complex, determined by Gamblin *et al.*⁵ as 103.7 cm⁻¹, is much lower than for the cationic complex, which has a dissociation energy of 1200 ± 300 cm⁻¹.¹³ This is also the case for NO–Ar (see above). (Note that for the higher $3d\lambda$ Rydberg states discussed in Chapter 3, the $\tilde{F}^2\Delta$ and $\tilde{H}^2\Pi$ state dissociation energies are 54% and 82% of the cationic value.) The low dissociation energy determined for the NO–Kr $A^2\Sigma^+$ state can again be attributed to the small Rydberg orbit of the $3s$ electron, which leads to a repulsive interaction between the Rydberg electron and the Kr atom. The presence of a Kr (or Ar) atom outside the Rydberg orbit results in a weakly-bound complex, rather than the tightly-bound Rydberg complexes seen in the $3d\lambda$ and $4s\sigma$ Rydberg states.^{3,5,10}

(1 + 1) REMPI spectra of the $\tilde{A}^2\Sigma^+ \leftarrow \tilde{X}^2\Pi$ transition in NO–Xe have been recorded by Mack *et al.*⁴ and more recently by Gamblin *et al.*⁵ The spectrum from Reference 5 is shown in Figure 6(iii).

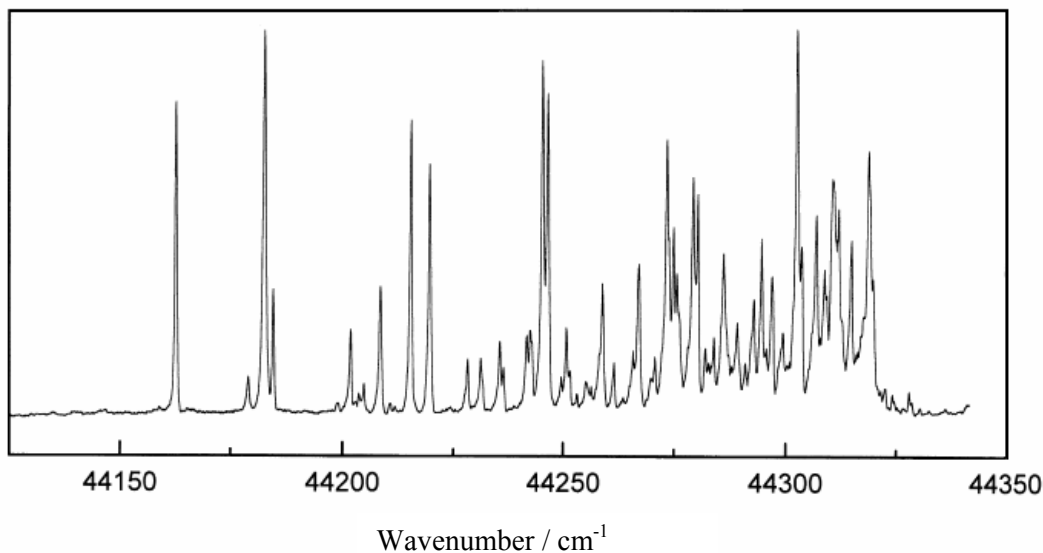


Figure 6(iii): (1 + 1) REMPI $\tilde{A}^2\Sigma^+$ state spectrum of NO–Xe taken from Reference 5.

The structure seen in the NO–Xe $\tilde{A}^2\Sigma^+$ state spectrum is much more complicated than for either NO–Ar or NO–Kr and it is not straightforward to identify a stretch progression.^{4,5} In Reference 4, the spectral complexity was partly attributed to angular momentum coupling effects, as the angular momentum of NO becomes coupled to the inertial axes of the complex. As for the NO–Ar and NO–Kr spectra shown in Figures 6(i) and 6(ii) respectively, the dissociation limit of the complex can be identified by a sharp drop-off in intensity of the spectral features to high wavenumber.

The NO–Kr and NO–Xe spectra shown in Figures 6(ii) and 6(iii) were recorded in the corresponding NO^+ –Rg mass channels. In both cases, spectra with identical structure were recorded in the corresponding Rg^+ mass channels, although the relative

intensities of some of the features differed between the two $\text{NO}^+\text{-Rg}$ and Rg spectra.^{4,5} A mechanism has been devised by Miller^{14,15} and is described in Chapter 3, Section 3.3.3. Briefly, the $\tilde{A}^2\Sigma^+$ state absorbs a second photon to form a superexcited species $\text{NO}^{**}\text{-Rg}$. If there is a reasonable amount of interaction between the NO moiety (where the initial excitation takes place) and the Rg atom, then a transfer of energy will occur to form a Rg^* excited atom. This can then absorb a third photon, leading to ionisation. A competition exists between the formation of the superexcited $\text{NO}^{**}\text{-Rg}$ species and direct ionisation to form $\text{NO}^+\text{-Rg}$ (not unlike the competition seen between ionisation and predissociation of the $\tilde{H}^1\Pi$ state via the continuum of the $\tilde{F}^2\Delta$ state, as discussed in Chapter 3), where the observed ratio of Rg^+ to $\text{NO}^+\text{-Rg}$ was dependent upon the proximity of the excited Rg^+ levels to the two-photon energy, and the laser power. Differences in the relative intensities of spectral features recorded in the Rg^+ mass channel were attributed to different couplings between the superexcited state and the ionisation continuum and/or the $\text{NO}^+\text{-Rg}$ manifold.⁵

Attempts were made by Mack *et al.*⁴ and Gamblin *et al.*⁵ to record a (1 + 1) REMPI spectrum of the $\tilde{A}^2\Sigma^+ \leftarrow \tilde{X}^2\Pi$ transition of NO-Ne although without success. In both cases this has been attributed to the repulsive interaction between the 3s Rydberg electron and the Ne atom. Recently, Pajón-Suárez *et al.*¹⁶ performed RCCSD(T)/aug-cc-pVTZ calculations to obtain the intermolecular potential energy surface (IPES) of the $\tilde{A}^2\Sigma^+$ state of NO-Ne . The interaction was found to be extremely weak, with $D_e = 4 \text{ cm}^{-1}$, and some agreement with a previously derived empirical potential¹⁷ was found. Since no rovibrational energy calculations were performed as part of that work, it is not possible to conclude whether or not the complex is bound and hence whether an electronic spectrum is expected to be observed. Success at recording other low-lying Rydberg states, such as the $3d\lambda$ and $4s\sigma$ states for both NO-Ne and the NO-Ne_2 cluster (see Chapters 3 and 4 respectively), together with the paper of Pajón-Suárez *et*

*al.*¹⁶ prompted another attempt at recording a (1 + 1) REMPI spectrum of the $\tilde{A}^2\Sigma^+ \leftarrow \tilde{X}^2\Pi$ transition of NO–Ne.

6.2 Experiment

6.2.1 Experimental set-up

The apparatus employed in the present investigation has been described in detail in Chapter 2 and only a brief overview will be provided here. To generate NO–Ar and NO–Ne, mixtures of ~5% NO (99.5%, Messer) in the rare gas are used, with pressures of ~6 bar and up to ~9 bar employed respectively. NO–Kr and NO–Xe are generated using mixtures of ~2.5% NO and ~5% Rg (Kr, Xe: 99.9+%, BOC) seeded in Ar (99.9+%, BOC). The gas mixtures are expanded into vacuum using a general valve pulsed nozzle (10 Hz, 750 μm orifice, ~200–250 μs opening time). The resulting unskimmed free-jet expansion travels to the extraction region of the time-of-flight mass spectrometer through a thin gate valve. Ionisation is achieved in a (1 + 1) REMPI process using the frequency-doubled output of a Sirah Cobra Stretch dye laser (1800 lines/mm grating, Coumarin 450), which is pumped by the third harmonic (355 nm, 10 Hz) output of a Surelite III Nd:YAG (yttrium aluminium garnet) laser. All spectra are collected in the parent ion mass channel. For NO–Kr and NO–Xe complexes, a number of different isotopomer channels could be sampled, and in addition, signals could be observed in the Kr^+ or Xe^+ mass channels, respectively, as discussed in Reference 5. In order to ensure that conditions remained optimal, spectra of NO–Kr, NO–Xe and NO–Ar were recorded at regular intervals around the attempted recording of NO–Ne spectra.

6.2.2 Calibration

Spectra are calibrated using rotational lines of the $A^2\Sigma^+ \leftarrow X^2\Pi$ transition of NO. A least squares fit of a plot of the observed peak energies against their calculated energies gives an equation of the form $y = mx + c$, which can be used to calibrate the spectra collected in the present work. A similar method of calibration has been used previously, during an investigation of the $4s\sigma$ Rydberg state of NO–Rg (Rg = Ne–Kr) discussed in Chapter 5.

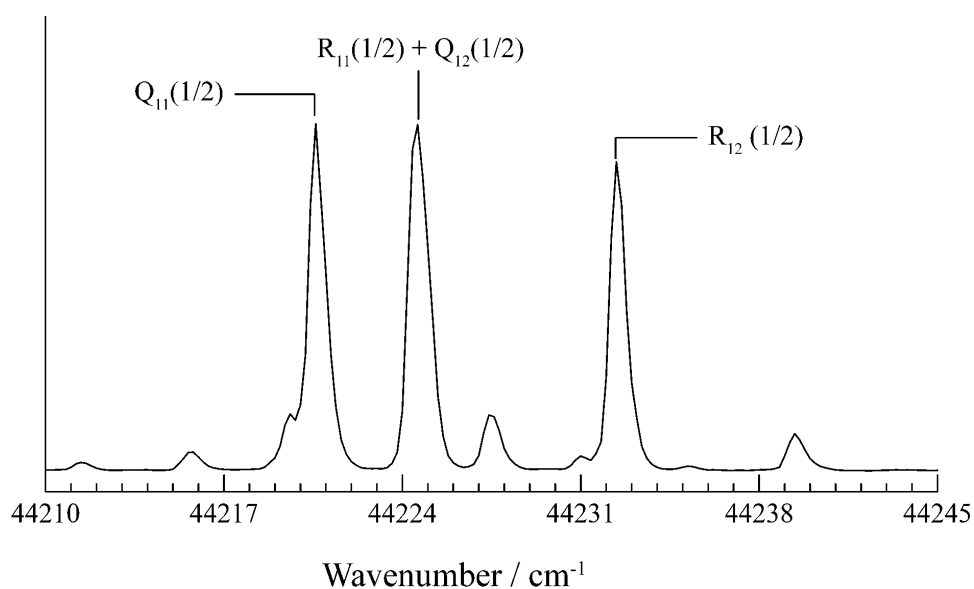


Figure 6(iv): $(I + 1)$ REMPI spectrum of the $A^2\Sigma^+$ state of NO. The rotational lines $Q_{11}(1/2)$, $Q_{21}(1/2) + R_{11}(1/2)$ and $R_{21}(1/2)$ used for calibration are labelled.

The rotational lines present in the $A^2\Sigma^+$ state spectrum of NO have been assigned previously² as the lines $Q_{11}(1/2)$, $Q_{21}(1/2) + R_{11}(1/2)$ and $R_{21}(1/2)$. These transitions between the ground state and a $^2\Sigma^+$ excited state are shown in Figure 3(iv) in Chapter 3. These peaks are labelled in the uncalibrated $A^2\Sigma^+$ spectrum of NO shown in Figure 6(iv).

The energies of these rotational lines are given in Reference 3 as 44198.8 cm^{-1} , 44202.8 cm^{-1} and 44210.7 cm^{-1} and these energies were used to calibrate the spectra presented herein. However, these energies were later found to be inaccurate, after recalculation by Gamblin *et al.*² using the spectroscopic constants presented in Reference 18. In order to calculate the energy of the rotational lines, the rotational energy of the ground state is required (0.83 cm^{-1} as calculated in Chapter 3, Section 3.2.2), as is the rotational energy of the excited state levels and the ν_{00} transition energy. The latter is given in Reference 18 as 44140.81 cm^{-1} and must be corrected for the spin-orbit splitting of the ground state (the electron spin angular momentum σ couples with the orbital angular momentum λ to give two states ${}^2\Pi_{3/2}$ and ${}^2\Pi_{1/2}$). The ${}^2\Pi_{1/2}$ state is lowered by an energy corresponding to $\sigma\lambda A_0$ where $\sigma = 1/2$, $\lambda = 1$ and $A_0 = 123.14 \text{ cm}^{-1}$,¹⁸ to give a transition energy of 44202.38 cm^{-1} . Rotational energy levels of the $E^2\Sigma^+ \leftarrow X^2\Pi$ state transition in uncomplexed NO were calculated and a detailed description of the procedure is given in Chapter 3, Section 3.2.2. A similar procedure is used to calculate the rotational transition energies of the $A^2\Sigma^+ \leftarrow X^2\Pi$ transition. Briefly, the excited state rotational level energies are calculated using:¹⁹

$$E_N = B_0[N(N+1)] \quad 6(a)$$

For the $A^2\Sigma^+$ state B_0 is 1.986 cm^{-1} (Reference 18), which gives energies of 0, 3.97 and 11.92 cm^{-1} for the $N = 0, 1$ and 2 levels of the $A^2\Sigma^+$ state. Combining these values with the $A^2\Sigma^+ \leftarrow X^2\Pi$ ν_{00} transition energy and the rotational energy of the ground state gives energies of $44202.38 - 0.83 + 0 = 44201.55 \text{ cm}^{-1}$, $44202.38 - 0.83 + 3.97 = 44205.52 \text{ cm}^{-1}$ and $44202.38 - 0.83 + 11.92 = 44213.47 \text{ cm}^{-1}$ for the $Q_{11}(1/2)$, $Q_{21}(1/2) + R_{11}(1/2)$ and $R_{21}(1/2)$ lines respectively. Note that unlike the spectrum of the $E^2\Sigma^+$ state of NO the S_{11} branch is not observed, since a transition to the $A^2\Sigma^+$ state requires a single photon and the selection rule $\Delta J = 0, \pm 1$ applies.

The recalculated values are in reasonable agreement with the original values, and are therefore expected to have only a minor quantitative effect on the spectra presented herein.

6.3 Results

The experimental work described in the current thesis has been carried out in collaboration with the theoretical work of Hernández-Lamonedá and coworkers; details of the theoretical work have been published elsewhere.²⁰ The $\tilde{A}^2\Sigma^+$ state spectra recorded in this work are shown in Figure 6(v). The complexes NO–Ar, NO–Kr and NO–Xe yield well-resolved spectra, which compare extremely well with those reported previously.³⁻⁵ A spectrum of the $A^2\Sigma^+ \leftarrow X^2\Pi$ transition of NO is also shown, together with a scan of the same spectral region obtained whilst gating over the expected time-of-flight of the NO–Ne complex.

A number of attempts were made to record the $\tilde{A}^2\Sigma^+$ state spectrum of NO–Ne, each time alternating with recording spectra of the heavier NO–Rg species. Given that the $\tilde{A}^2\Sigma^+$ state is so weakly-bound ($D_e = 4 \text{ cm}^{-1}$),¹⁶ and that the dissociation energy of the $\tilde{X}^2\Pi$ state is $< 35 \text{ cm}^{-1}$ (Reference 21), it is reasonable to expect the $\tilde{A}^2\Sigma^+$ state spectrum of NO–Ne to appear $\sim 30 \text{ cm}^{-1}$ to the blue of the origin of the $\tilde{A}^2\Sigma^+ \leftarrow \tilde{X}^2\Pi$ transition of uncomplexed NO. Even though much wider energetic regions were investigated the NO–Ne $\tilde{A}^2\Sigma^+$ state spectrum was not observed, in line with observations made previously by Miller and Cheng⁷ and others.⁶

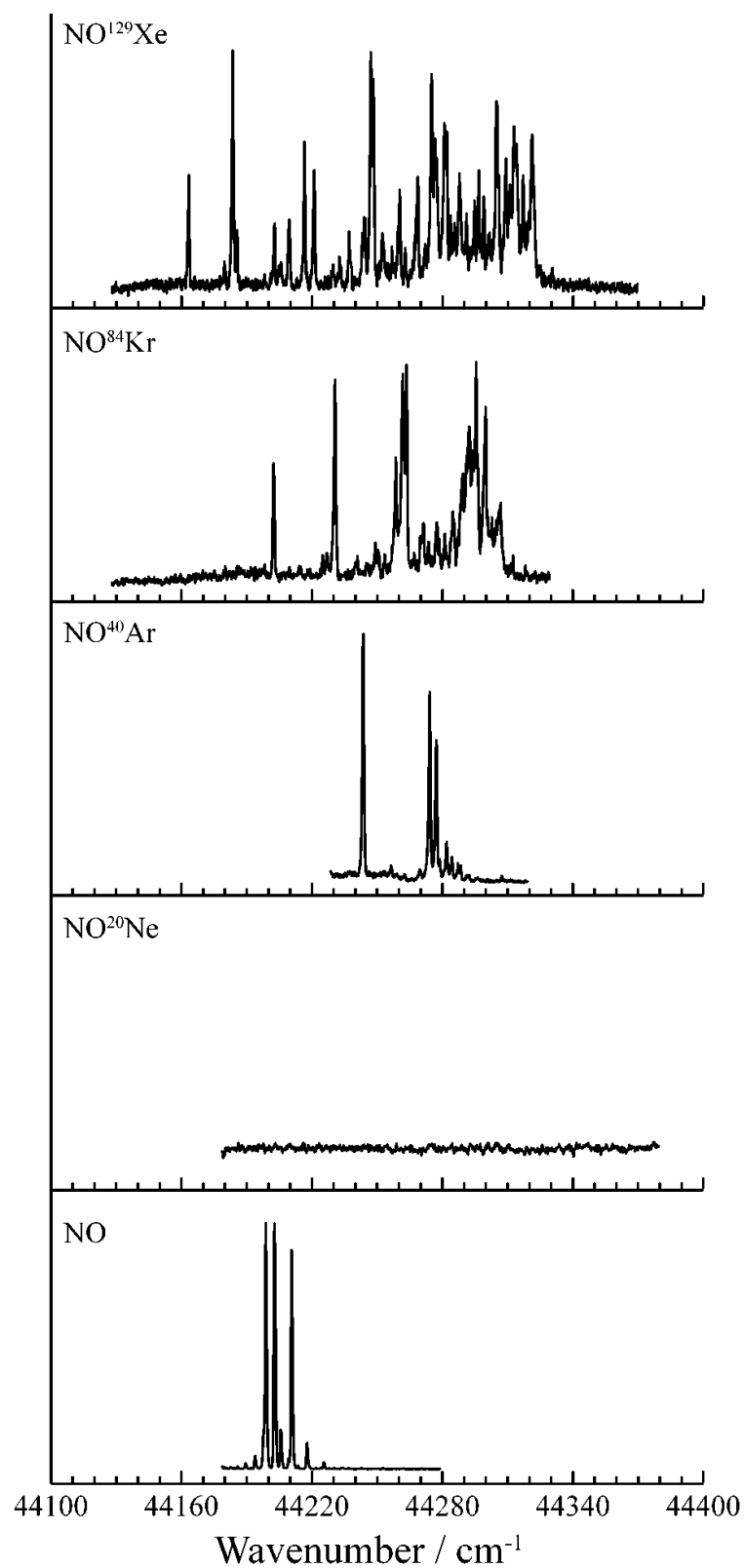


Figure 6(v): $(1 + 1)$ REMPI spectra of the $\tilde{A}^2\Sigma^+ \leftarrow \tilde{X}^2\Pi$ transition of NO and NO- R_g ($R_g = \text{Ar-Xe}$). The $\tilde{A}^2\Sigma^+$ state of NO-Ne is not observed.

The fact that strong, cold spectra of NO–Ar, NO–Kr and NO–Xe were successfully recorded, coupled with the successful recording of spectra of NO–Ne via the higher $3d\lambda$ and $4s\sigma$ Rydberg states, suggests that large numbers of NO–Ne complexes were being formed in the free-jet expansion. To facilitate complex formation a variety of backing pressures were employed, ranging from 1–9 bar, and various intervals of the free-jet expansion pulse were probed; in all cases without success. Given that NO–Ne has a weaker binding energy than NO–Ar might suggest that the expected number density for NO–Ne would be less than that for NO–Ar. This seems unlikely to be the cause for the non-observation of the NO–Ne complex however, given that in previous work on the $3d\lambda$ and $4s\sigma$ Rydberg states, the intensity of all electronic state spectra recorded were comparable for the NO–Ne and NO–Ar complexes.

The experimental results are consistent with there being either no bound $\tilde{A}^2\Sigma^+ \leftarrow \tilde{X}^2\Pi$ transitions for NO–Ne, or if there are any, the corresponding Franck–Condon factors are extremely small. These conclusions are completely in line with those reached previously in Reference 5 and are confirmed by the results of high-level *ab initio* calculations performed by J. Kłos and M. H. Alexander,²⁰ using the potential of Pajón-Suárez *et al.*¹⁶ in collaboration with the experimental work presented herein. A summary of the theoretical work is given in Section 6.5.

6.4 Discussion

The binding energy of the $\tilde{A}^2\Sigma^+$ state is found to be much lower than for the higher Rydberg states. The binding energy in the NO–Ar complex has been determined previously⁹ to be 44 cm^{-1} , compared with 487 cm^{-1} for the $\tilde{F}^2\Delta$ state (the most weakly-bound of the $3d\lambda$ Rydberg states investigated in Chapter 3). For NO–Kr and NO–Xe, it is possible to determine an excited state binding energy from the sharp drop

in intensity seen in the spectra obtained in this work, shown in Figure 6(v). The binding energy is given by the energy difference between the sharp drop in intensity, identified as the dissociation limit, and the origin feature. These values have already been determined⁵ as 103.7 cm⁻¹ for NO–Kr and 157.6 cm⁻¹ for NO–Xe.

The lower binding energy seen in the $\tilde{A}^2\Sigma^+$ state is due to the orbital radius of the 3s Rydberg electron (2.86 Å).¹¹ In higher states, where the Rydberg orbit is larger (the $\tilde{F}^2\Delta$ state has a radius of 5.28 Å for example), the Rg atom is more exposed to the NO⁺ core, as the Rydberg electron occupies a spatial region which is far removed from that of Rg. In the $\tilde{A}^2\Sigma^+$ state, the smaller Rydberg radius brings the Rg atom and the 3s Rydberg electron into direct spatial conflict, leading to a Pauli repulsion between the 3s electron and the electrons on the Rg atom. The overall binding in the $\tilde{A}^2\Sigma^+$ state will be governed both by the repulsive Pauli interaction, and by the attractive dipole/induced-dipole interaction.

In Figure 6(v) it can be seen that, for NO–Ar, the $\tilde{A}^2\Sigma^+$ state origin feature is blueshifted relative to that in uncomplexed NO. This indicates that the excited state is *less* strongly-bound than the ground state, despite the dipole of the $\tilde{A}^2\Sigma^+$ state being larger than that of the ground state (1.1 D vs. 0.2 D, References 22 and 23 respectively). The spectral blueshift suggests that the increase in the attractive term is outweighed by the increase in the repulsive interaction between the electrons on Ar and the 3s electron. For NO–Kr, the $\tilde{A}^2\Sigma^+$ origin feature is almost coincident with that of uncomplexed NO. Due to the increased polarisability of Kr, the magnitude of both the attractive and repulsive components of the interaction will increase. The increase in the attractive interaction is now greater than the change in the repulsive interaction and as result, the NO–Kr $\tilde{A}^2\Sigma^+$ state origin feature becomes almost isoelectronic with that of uncomplexed NO. The NO–Xe $\tilde{A}^2\Sigma^+$ state spectrum is

redshifted relative to that of uncomplexed NO. This indicates that although the repulsive interaction between the electrons on Xe and the Rydberg electron will increase, the change in the repulsive term will be much smaller than the increase in the attractive interaction, owing to the increased polarisability of the Xe atom. Given the above, it is likely that the repulsive interaction in the $\tilde{A}^2\Sigma^+$ state in the NO–Ne complex will increase to a greater extent than the attractive interaction, due to the much smaller polarisability of the Ne atom.

In Reference 9, it was noted that the spatial conflict between the 3s Rydberg electron and the complexed Rg atom led to two possible positions for the Rg to occupy. In the first, the Rydberg electron moves to a larger radius orbit where the Rg atom can interact with the NO^+ core forming a strongly-bound Rydberg complex (*i.e.* a Rydberg electron orbiting an NO^+ –Rg core). Conversely, the Rg atom can move outside the Rydberg orbital, forming a weakly-bound complex. There is also the possibility that both geometries can occur in the same electronic state: this has been observed in Hg–Ar complexes in the Hg 7s Rydberg state by Duval *et al.*²⁴ where a strongly-bound minimum exists at short bond lengths (where the Ar atom lies within the 7s Rydberg orbit), and a shallow minimum exists at longer bond lengths (the Ar atom lies outside the Rydberg orbit). The preceding discussion suggests that, in the $\tilde{A}^2\Sigma^+$ state, only one minimum exists, where the Rg atom resides outside of the 3s Rydberg orbit. This is in line with the intermolecular bond length of 4.6 Å calculated for NO–Ar in the $\tilde{A}^2\Sigma^+$ state by Tsuji *et al.*⁹ which is much larger than the radius of the Rydberg orbit (2.86 Å),¹¹ implying that the Ar atom lies outside the Rydberg orbit.

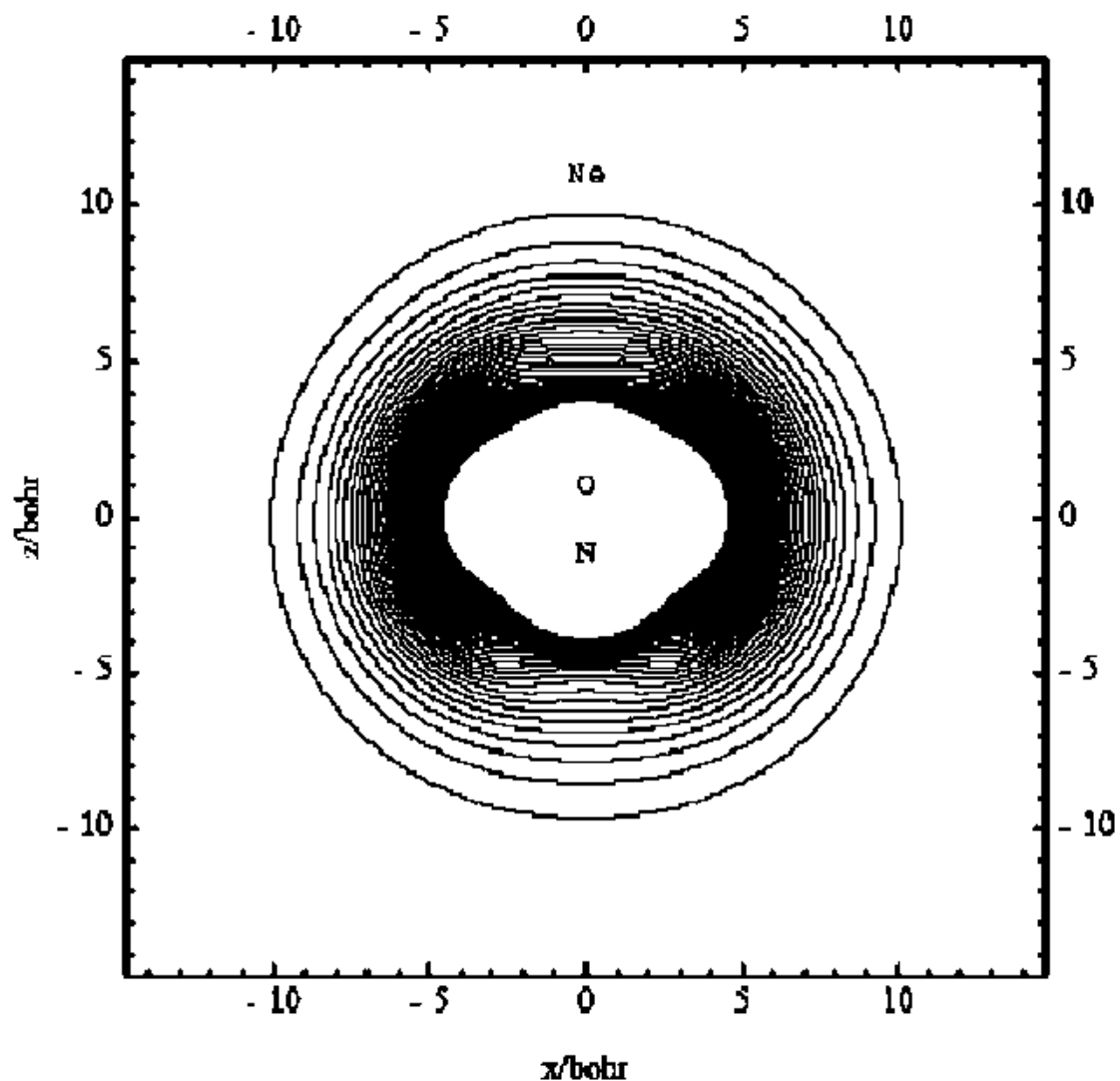


Figure 6(vi): *contour plot of the total electron density of the $A^2\Sigma^+$ state of NO (Hernández-Lamonedá et al.).²⁰*

The 3s Rydberg state has been shown to be highly extended – a contour plot (Hernández-Lamonedá *et al.*)²⁰ of the total electron density in the $A^2\Sigma^+$ state is shown in Figure 6(vi). The Ne atom is expected to lie outside the main 3s Rydberg electron density (at the equilibrium bond distance of ~12 bohr) and will therefore have little interaction with the NO^+ core, confirming the conclusions outlined above. Also shown, in Figure 6(vii), is the electron density for the $X^2\Pi$ state of NO (Hernández-

Lamoneda *et al.*),²⁰ which is much less radially extended thus allowing a closer approach of the Ne atom.

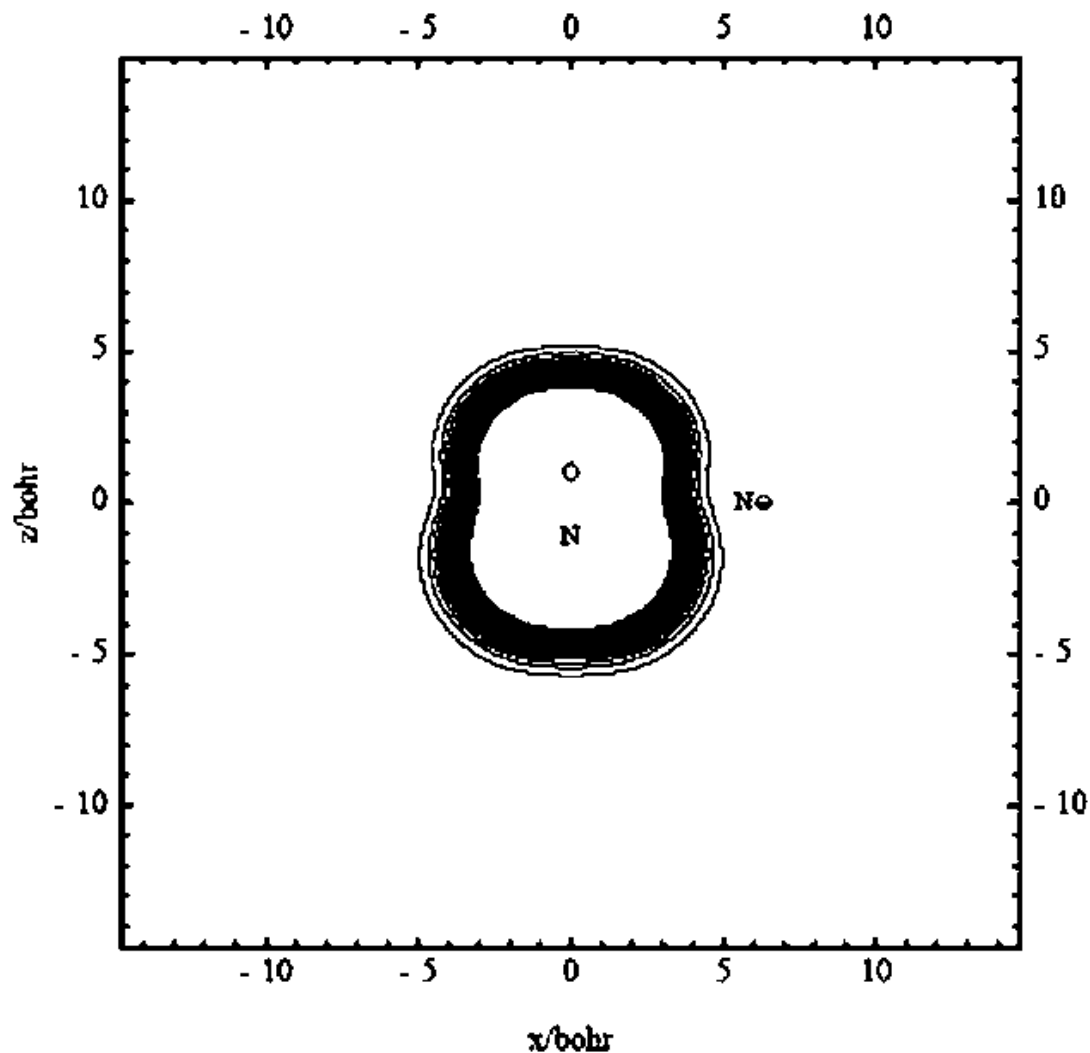


Figure 6(vii): *contour plot of the total electron density of the $X^2\Pi$ state of NO (Hernández-Lamoneda et al.).*²⁰

6.5 Theory

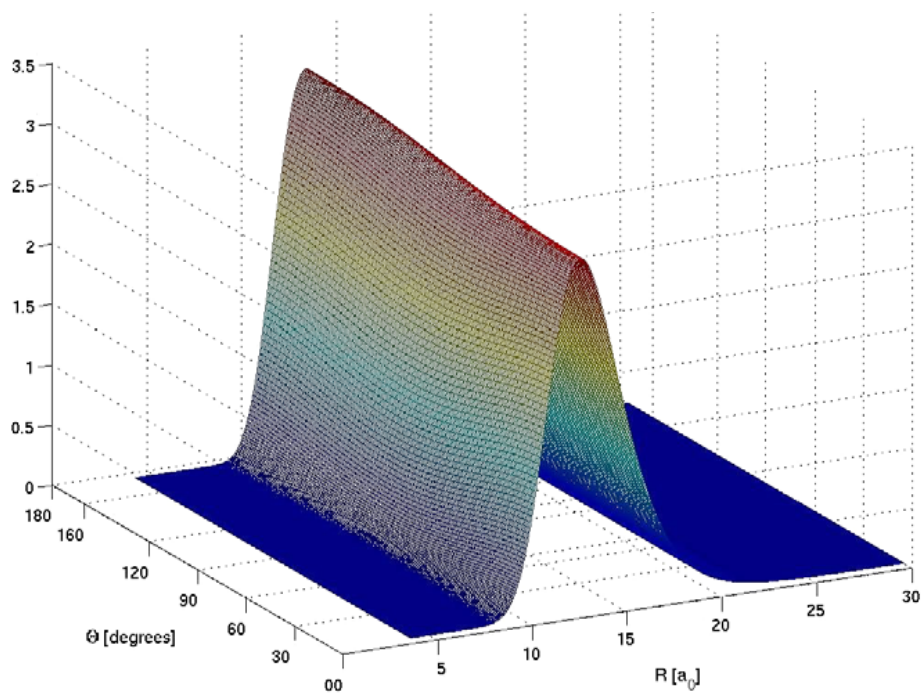
In addition to the experimental work described above, rovibrational energies were calculated for the $\tilde{A}^2\Sigma^+$ Rydberg state of the NO–Ne complex by J. Kłos and M.H.

Alexander, employing the intermolecular potential energy surface (IPES) calculated by Pajón-Suárez and coworkers.¹⁶ The results indicate that there are two vibrational energy levels, the wavefunctions of which show these vibrations to be the $\nu = 0$ and $\nu = 1$ levels of the intermolecular stretch. These wavefunctions are shown in Figure 6(viii).

Both of these energy levels are found to be very weakly-bound, with energies of 2.04 cm^{-1} and 0.32 cm^{-1} for $\nu = 0$ and $\nu = 1$ respectively. Additionally, the wavefunctions are spatially extended and have almost no angular dependence (suggesting that there are no bound bending levels). The lack of bending levels may lie in the (near) linear geometry of the complex (seen for the heavier NO–Rg complexes in the vibrational ground state). The dipole of NO will be orientated along the intermolecular axis, and in a linear geometry the dipole/induced-dipole interaction will be at a maximum. Any movement of the Ne atom off the intermolecular axis will lessen the magnitude of the attractive interaction, although not the repulsive interaction since the 3s Rydberg electron density is close to isotropic (see Figure 6(vi)). The linear conformation of the NO–Ne complex is confirmed in the work of Pajón-Suárez *et al.*¹⁶ where a collinear approach of Ne and NO is the lowest energy direction.

The difference in the binding energy (D_0) of the ground and excited states in NO–Ne is significantly larger than for NO–Ar, where the $\tilde{A}^2\Sigma^+ \leftarrow \tilde{X}^2\Pi$ transition has been successfully recorded. For NO–Ne the relevant energies are 35 cm^{-1} (from Reference 1) and 2.04 cm^{-1} for the ground and excited states respectively; for NO–Ar the relevant D_0 energies are 88 cm^{-1} and 44 cm^{-1} (from Reference 9 for the ground and excited states respectively). Given the magnitude of the change in binding energy upon excitation for NO–Ne, it is anticipated that there will be a large geometry change during the $\tilde{A}^2\Sigma^+ \leftarrow \tilde{X}^2\Pi$ transition, leading to poor Franck-Condon factors; or that a

NO-Ne $\tilde{A}^2\Sigma^+ J=1/2 v=0$ state $D_0 = -2 \text{ cm}^{-1}$



NO-Ne $\tilde{A}^2\Sigma^+ J=1/2 v=1$ state $D_0 = -0.3 \text{ cm}^{-1}$

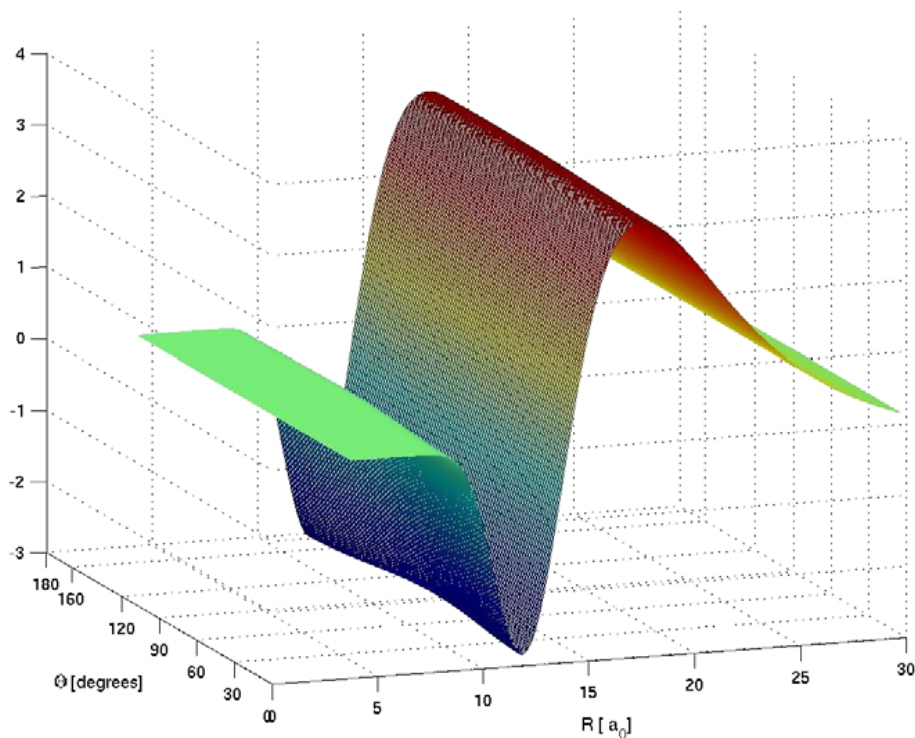


Figure 6(viii): calculated vibrational wavefunctions for the $\tilde{A}^2\Sigma^+$ state of NO-Ne.²⁰ These are the $v=0$ and $v=1$ levels of an intermolecular stretch.

vertical transition from the ground state will access the dissociative portion of the excited state potential. In Figure 6(ix) the wavefunctions for $\tilde{X}^2\Pi$ ($v = 0$) and $\tilde{A}^2\Sigma^+$ ($v = 0$) are compared.²⁰ The overlap between the wavefunctions is shown to be minimal, confirming that the Franck-Condon factors will be extremely small. This is also the case for the $\tilde{A}^2\Sigma^+$ ($v = 1$) level.

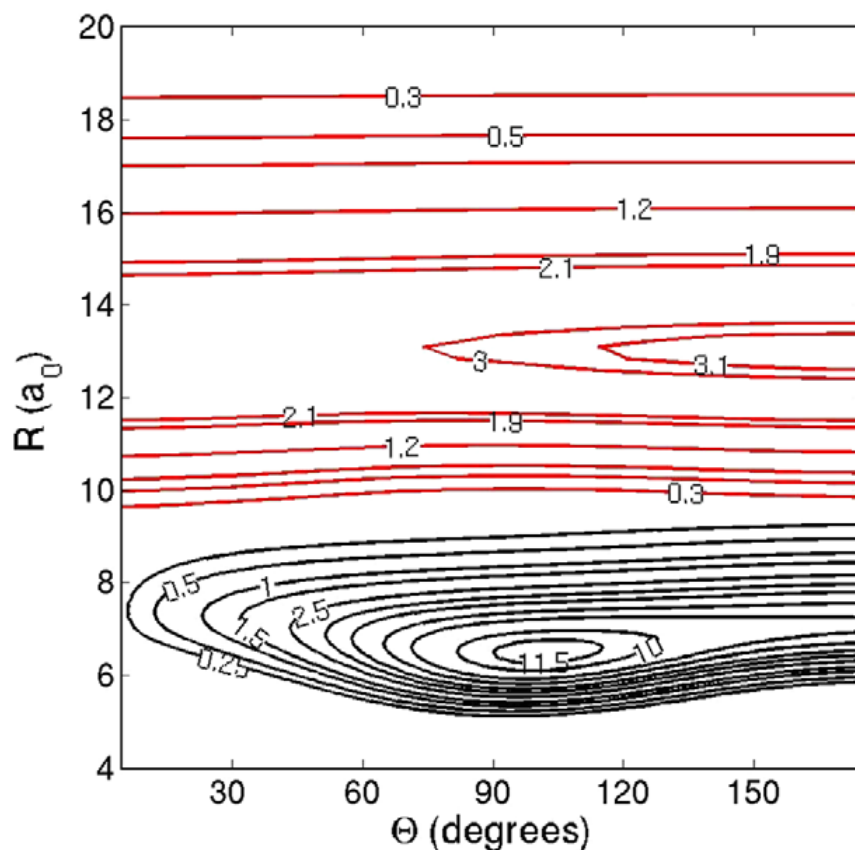


Figure 6(ix): contour map (cm^{-1}) of the $v = 0$ levels of the $\tilde{X}^2\Pi$ state (lower trace) and the $\tilde{A}^2\Sigma^+$ state (upper trace).²⁰

6.6 Conclusions

High-quality spectra of the $\tilde{A}^2\Sigma^+ \leftarrow \tilde{X}^2\Pi$ transition in the NO-Rg complexes (Rg = Ar–Xe) have been recorded successfully. The $\tilde{A}^2\Sigma^+$ state spectrum of NO–Ne was

not observed however, owing to the weak binding in the $3s\sigma$ state. This weak binding is a result of the small size of the $3s$ Rydberg orbit, which brings the $3s$ Rydberg electron and the Ne atom into direct spatial conflict. The presence of the $3s$ electron shields the Ne atom from the NO^+ core which, together with the low polarisability of Ne, results in a relatively weak attractive interaction. Additionally, there is a repulsive interaction between the electrons on Ne and the Rydberg electron. The attractive and repulsive interactions are of a similar magnitude and this is responsible for the weak binding in the $\tilde{A}^2\Sigma^+$ state of NO–Ne. For the heavier NO–Rg complexes, the magnitude of the increase in the attractive dipole/induced-dipole term is greater than the increase in the repulsive interaction. This is due to the increasing polarisability of the Rg atoms. This can be seen in the spectra by the origin band of the NO–Rg $\tilde{A}^2\Sigma^+$ state, which is blueshifted from the $A^2\Sigma^+ \leftarrow X^2\Pi$ transition in uncomplexed NO for NO–Ar and then shifts progressively to the red for NO–Kr (where the complex and monomer bands are almost isoelectronic) and NO–Xe. It is possible to eliminate experimental difficulties as the cause of the non-observation of the NO–Ne complex: spectra of the heavier NO–Rg complexes were successfully recorded at regular intervals during the search for NO–Ne, confirming that conditions for complex formation were optimal throughout. In addition, NO–Ne complexes have been successfully formed in previous work discussed in Chapters 3 and 4, where the higher $3d\lambda$ Rydberg states were investigated for NO–Ne and NO–Ne₂.

Theoretical studies carried out in collaboration with the experimental work presented herein, have revealed that there are only two bound vibrational levels in the NO–Ne $A^2\Sigma^+$ state complex, corresponding to $\nu = 0$ and $\nu = 1$ in the intermolecular stretch vibration. The vibrational wavefunctions of these levels are very extended, and the lack of angular dependence leads to an absence of bound bending levels. Additionally,

the overlap between these excited state levels and the $\tilde{X}^2\Pi$ $v = 0$ level has been shown to be very small, leading to poor Franck-Condon factors.

6.7 Conclusions from the study of NO–Rg Rydberg states

The work described thus far concerns the electronic spectroscopy of NO, bound to one or more Rg atoms in a van der Waals complex. Excitation of the NO chromophore to a number of low-lying Rydberg states allows some general comments to be made about the effects of the NO–Rg geometry, Rg atom polarisability, Rydberg orbit size and the degree of Rydberg electron penetration on the NO/Rg interaction.

The geometries of the NO–Rg complexes are known and have an effect on the rotational and vibrational structure observed in the REMPI spectra. The $\tilde{X}^2\Pi$, $\tilde{H}^2\Pi$ and $\tilde{E}^2\Sigma^+$ state NO–Rg complexes have a near T-shaped geometry (see Chapter 1, Reference 1 and Reference 25 respectively). Previous work^{2,5,10} on the $\tilde{A}^2\Sigma^+$ Rydberg state has revealed a near linear geometry at $v' = 0$ which approaches T-shaped as the vibrational stretch is excited. The $\tilde{F}^2\Delta$ state has a less well-defined geometry: two possible conformations were necessary to simulate the $\tilde{F}^2\Delta$ state spectrum of NO–Ne, one near T-shaped and one near linear).^{1,25} REMPI spectra of near T-shaped Rydberg states are dominated by the intermolecular stretch due to favourable Franck-Condon factors (the NO–Rg separation decreases upon excitation). If the Rydberg state complex deviates from T-shaped (for NO–Ar, the $\tilde{E}^2\Sigma^+$ state geometry deviates from T-shaped by 20–25°),²⁵ then rotation about the a -inertial axis (which for T-shaped configurations is coincident with the intermolecular axis) will increasingly contribute to the spectrum.

The effect of increasing Rg polarisability on the NO–Rg binding energies (D_0') can be seen in Table 6(I); for all the Rydberg states investigated, D_0' is seen to increase as the Rg atom becomes more polarisable.

Rg	α_{Rg} (\AA^3) ^a	D_0' (cm^{-1})				
		$\tilde{X}^2\Pi$	$\tilde{A}^2\Sigma^+$	$\tilde{F}^2\Delta$	$\tilde{H}^2\Pi$	$\tilde{E}^2\Sigma^+$
Ne	0.396	35 ^b	2.04 ^e	119 ^b	270 ^b	161 ^f
Ar	1.64	88 ^c	44 ^c	487 ^e	865 ^b	579 ^g
Kr	2.48	105 ^d	103.7 ^d	648 ^e	986 ^e	877 ^e
Xe	4.04	121.3 ^d	157.6 ^d	—	—	—

Table 6(I): Rydberg state binding energy (D_0') in cm^{-1} with respect to Rg dipole polarisability (α_{Rg}) in \AA^3 . (a) Reference 26; (b) Reference 1; (c) Reference 9; (d) Reference 5; (e) this work; (f) Reference 6; (g) Reference 25.

The size of the Rydberg orbit has an impact on the binding energy of the complexes as can be seen from the D_0' values shown in Table 6(II). When the Rydberg orbit is small, the shielding effects of the Rydberg electron result in a weakly-bound complex. As the size of the Rydberg orbit increases, the Rydberg electron is less able to shield the Rg atom from the NO^+ core charge and D_0' increases. The $\tilde{E}^2\Sigma^+$ state binding energies do not follow this trend however, the D_0' values are lower than those for the $\tilde{H}^2\Pi$ state, despite the increase in r . The $4s$ Rydberg electron is more penetrating than the $3d$ electron and is therefore more effective at shielding the NO^+ core charge from the Rg atom, resulting in the lower $\tilde{E}^2\Sigma^+$ state binding energies.

Rg	r (Å)	D_0' (cm ⁻¹)			
		Ne	Ar	Kr	Xe
$\tilde{A}^2\Sigma^+$	2.86 ^h	2.04 ^e	44 ^c	103.7 ^d	157.6 ^d
$\tilde{F}^2\Delta$	5.28 ^b	119 ^b	487 ^e	648 ^e	—
$\tilde{H}'^2\Pi$	5.65 ^b	270 ^b	865 ^b	986 ^e	—
$\tilde{E}^2\Sigma^+$	6.1 ^g	161 ^f	579 ^g	877 ^e	—

Table 6(II): Rydberg state binding energy (D_0') in cm⁻¹ with respect to the Rydberg orbit radius (r) in Å. (a–g) References given in Table 6(I); (h) Reference 11.

The measured NO vibrational frequency (Table 6(III)) gives an indication of the degree of NO⁺/Rg interaction. An increasing deviation of the measured values from the 0–1 spacing for NO⁺ implies an increasing degree of NO⁺/Rg interaction.

	NO	NO–Ne	NO–Ar	NO–Kr
$\tilde{E}^2\Sigma$	2342.2	2345.8	2340.0	2346.6
$\tilde{F}^2\Delta$	2318.2	2322.2	2334.2	2340.1
$\tilde{H}'^2\Pi$	2341.2	2343.2	2330.2	2334.2
Cation	2343.9	—	—	—

Table 6(III): NO 0–1 vibrational spacings for the 4s and 3dλ Rydberg states of NO and NO–Rg and NO⁺ (all values given in cm⁻¹).

The similarity of the $\tilde{E}^2\Sigma^+$ state NO 0–1 spacing between NO, NO⁺ and NO–Rg is indicative of a small interaction between Rg and the NO⁺ core. Penetration effects partly account for the variation in the NO 0–1 spacings of the $3d\lambda$ states (the $3d$ Rydberg electron is weakly penetrating), although factors such as orientation of the vacant $2p\pi^*$ orbital relative to the Rg atom and the presence of non-Rydberg states, which can interact with Rydberg states of the same symmetry (the $\tilde{B}^2\Delta$ and $\tilde{F}^2\Delta$ states) may play a role.

The work on NO–Rg complexes in the present thesis has shown that in order to rationalise the interaction in these complexes, it is necessary to consider not only the size of the Rydberg orbit, but also the penetration of the Rydberg electron and orientation of the Rydberg electron density with respect to the Rg atom.

6.8 References

¹ Y. Kim, H. Meyer, *Int. Rev. Phys. Chem.* **20** (2001) 219.

² J. Lozeille, S.D. Gamblin, S.E. Daire, T.G. Wright, D.M. Smith, *J. Chem. Phys.* **113** (2000) 7224.

³ A.M. Bush, J.M. Dyke, P. Mack, D.M. Smith, T.G. Wright, *J. Chem. Phys.* **105** (1996) 9804.

⁴ P. Mack, J.M. Dyke, T.G. Wright, *J. Chem. Soc., Faraday Trans.* **94** (1998) 629.

⁵ S.D. Gamblin, S.E. Daire, J. Lozeille, T.G. Wright, *Chem. Phys. Lett.* **325** (2000) 232.

- ⁶ J. Fleniken, Y. Kim, H. Meyer, *J. Chem. Phys.* **109** (1998) 8940.
- ⁷ J.C. Miller, W.-C. Cheng, *J. Phys. Chem.* **89** (1985) 1647.
- ⁸ M.E. Carrasquillo, P.R.R. Langridge-Smith, D.H. Levy, in: A.R.W. McKellar, T. Oka, B.P. Stoicheff (Eds.), *Laser Spectroscopy V*, Springer, Berlin, 1981, p. 333.
- ⁹ K. Tsuji, K. Shibuya, K. Obi, *J. Chem. Phys.* **100** (1994) 5441.
- ¹⁰ A.M. Bush, J.M. Dyke, P. Mack, D.M. Smith, T.G. Wright, *J. Chem. Phys.* **108** (1998) 406.
- ¹¹ J.D. Barr, J.M. Dyke, P. Mack, D.M. Smith, T.G. Wright, *J. Elec. Spect. Rel. Phen.* **97** (1998) 159-170.
- ¹² N. Shafizadeh, P. Bréchignac, M. Dyndgaard, J.H. Fillion, D. Gauyacq, B. Levy, J.C. Miller, T. Pino, M. Raoult, *J. Chem. Phys.* **108** (1998) 9313.
- ¹³ A.M. Bush, T.G. Wright, V. Špirko, M. Juřek, *J. Chem. Phys.* **106** (1997) 4531.
- ¹⁴ J.C. Miller, *J. Chem. Phys.* **86** (1987) 3166-3171.
- ¹⁵ J.C. Miller, *J. Chem. Phys.* **90** (1989) 4031-4036.
- ¹⁶ P. Pajón-Suárez, G. Rojas-Lorenzo, J. Rubayo-Soneira, R. Hernández-Lamoneda, *Chem. Phys. Lett.* **421** (2006) 389.

- ¹⁷ G. Rojas-Lorenzo, J. Rubayo-Soneira, F. Vigliotti, M. Chergui, *Phys. Rev. B*, **67** (2003) 115119.
- ¹⁸ J. Danielak, U. Domin, R. Kepa, M. Rytel, and M. Zachwieja, *J. Mol. Spec.* **181** (1997) 394.
- ¹⁹ G. Herzberg, *Molecular Spectra and Molecular Structure I. Spectra of Diatomic Molecules*, D. Van Nostrand Company Inc. New York, 1950, pp 658.
- ²⁰ V.L. Ayles, R.J. Plowright, M.J. Watkins, T.G. Wright, J. Kłos, M.H. Alexander, P. Pajón-Suárez, J. Rubayo-Soneira, R. Hernández-Lamoneda, *Chem. Phys. Lett.* **441** (2007) 181.
- ²¹ M.H. Alexander, P. Soldán, T.G. Wright, Y. Kim, H. Meyer, P.J. Dagdigian, E.P.F. Lee, *J. Chem. Phys.* **114** (2001) 5588.
- ²² E.D. Glendening, D. Feller, K.A. Peterson, E.A. McCullough Jr., R.J. Miller, *J. Chem. Phys.* **103** (1995) 3517.
- ²³ R.M. Neumann, *Astrophys. J.* **161** (1970) 779.
- ²⁴ M.-C. Duval, O.B. D'Azy, W.H. Breckenridge, C. Jouvét, B. Soep, *J. Chem. Phys.* **85** (1986) 6324.
- ²⁵ H. Meyer, *J. Chem. Phys.* **107** (1997) 7732.
- ²⁶ *Handbook of Chemistry and Physics*, 74th ed. D.R. Lide, (Ed). CRC Press, (1993).

7.1 Introduction

In the work described in this chapter a number of vibrational levels in the first electronically-excited (S_1) state of para-fluorotoluene (pFT) are excited in order to investigate vibrational levels in the electronic ground state of the pFT^+ cation. The vibrational modes relevant to the work described herein are shown in Figure 7(i).

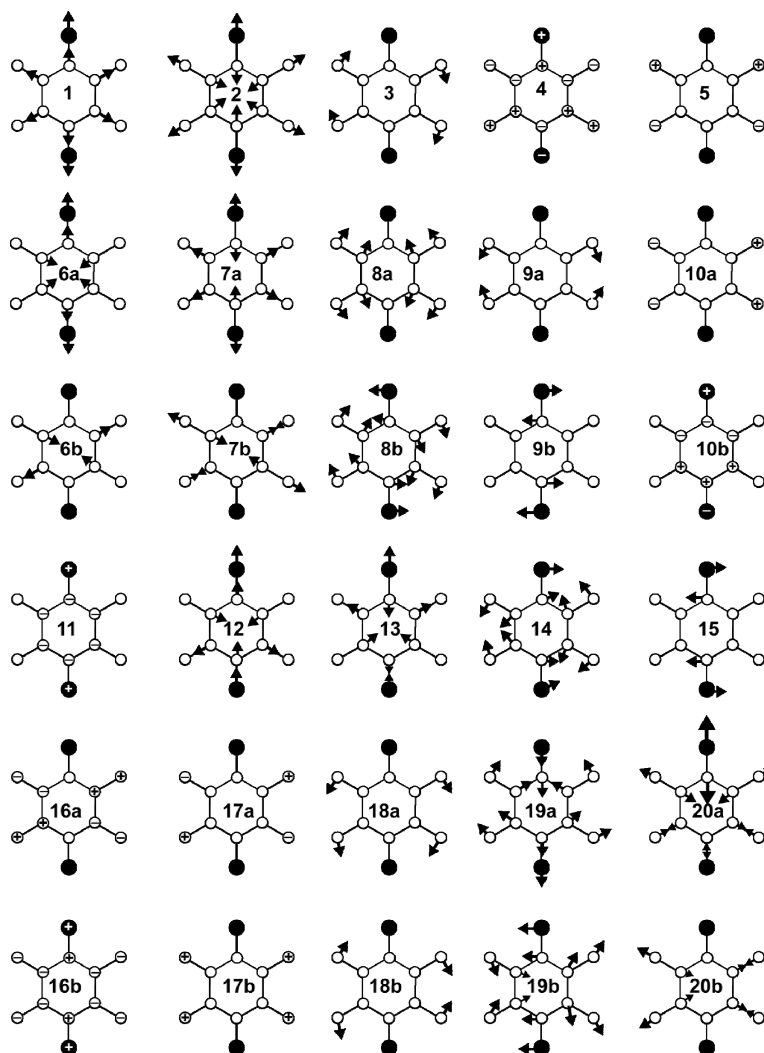


Figure 7(i): pictorial representations of the vibrational modes of a di-substituted benzene investigated during this work on para-fluorotoluene.

The electronic states of relevance here are the electronic ground state S_0 with 1A_1 symmetry, the first electronically-excited state S_1 , with 1B_2 symmetry and the electronic ground state of the cation (D_0), which has 2B_1 symmetry. Both the electronic symmetries and those of the vibrational modes shown in Figure 7(i) are derived by treating p FT as belonging to the C_{2v} point group.

7.1.1 Previous work on the S_1 state of *para*-fluorotoluene

The S_1 state of the *para*-fluorotoluene (p FT) molecule has been the subject of a number of studies.^{1,2,3,4,5,6,7,8,9,10,11} The majority of the previous studies have focused directly or indirectly upon the effect of the methyl group, which may act to accelerate the rate of intramolecular vibrational redistribution (IVR) in the S_1 state. The most comprehensive assignment of the vibrational levels observed in the S_1 state of p FT has been presented in a laser-induced fluorescence (LIF) spectroscopic study, by Okuyama *et al.*¹ The fluorescence excitation spectrum of the S_1 state of p FT of Okuyama *et al.* is shown in Figure 7(ii), with assignments for the main vibronic bands given in Wilson/Varsanyi notation¹² (p FT is treated as being of C_{2v} symmetry, both in the work of Okuyama *et al.*¹ and in the present study; previous work² suggests that the methyl group is largely a spectator to the excitation and ionisation processes, and if the methyl group is ignored then the molecule may be viewed as being of C_{2v} symmetry).

The assignment of the vibronic bands observed was based upon the analysis of (unreported) dispersed fluorescence spectra, which were obtained by exciting the individual vibronic bands. The ground state vibrational frequencies were well known from previous infrared and Raman studies¹³ and the frequencies observed in the dispersed fluorescence spectra, together with the observed intensity patterns allowed a definitive assignment of the features in the S_1 spectrum.

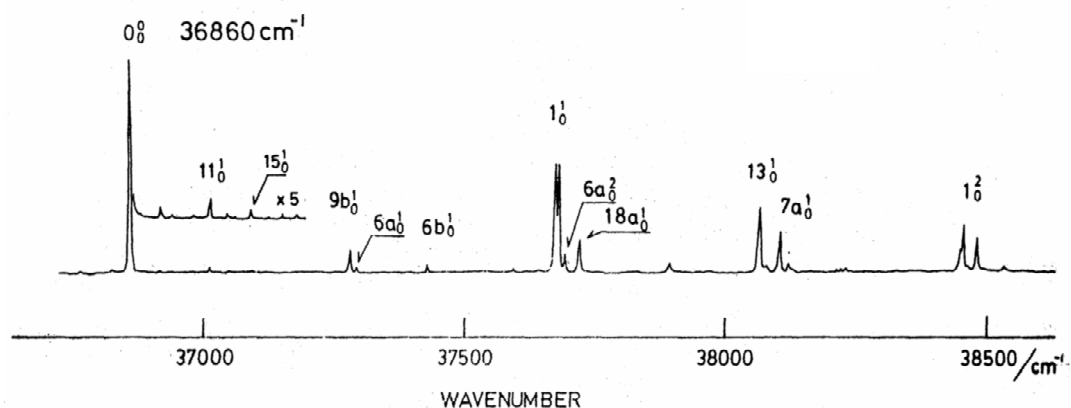


Figure 7(ii): fluorescence excitation spectrum of *pFT*, taken from Reference 1. The energy of the 0^0 origin band is shown.

As well as the LIF study of Ito and coworkers,¹ resonance-enhanced multiphoton ionisation (REMPI) spectra of *pFT* have been reported^{3,4} in relation to studies concentrating on the *pFT*-Ar van der Waals complex. The assignments presented in Reference 1 have been used in the REMPI studies. The two-colour REMPI spectrum of *pFT* of Georgiev *et al.*⁴ is shown in the lower trace of Figure 7(iii). The upper trace is the two-colour REMPI spectrum of the *pFT*-Ar van der Waals complex. Both spectra are shown on a relative excitation energy scale, where the energy of the 0^0 origin band has been set to equal zero.

The features in the *pFT* spectrum (lower trace) that are relevant to the present investigation are the vibronic bands 15^1 , $9b^1$ and $6a^1$. These features are labelled using Wilson/Varsanyi notation¹² where *pFT* is treated as belonging to the C_{2v} point group. Additional features to lower energy are attributed to internal rotational levels of the methyl substituent, assigned as $3a_1''$ and $5e_1''$ in References 1–4. As these features are associated with rotation of the methyl group only, they are labelled using the symmetries of the D_{3h} point group. The features labelled 1–5 in the upper trace of

Figure 7(iii) have been attributed to the bend and stretch vibration of an Ar atom relative to the *p*FT molecule, by Hu *et al.*³

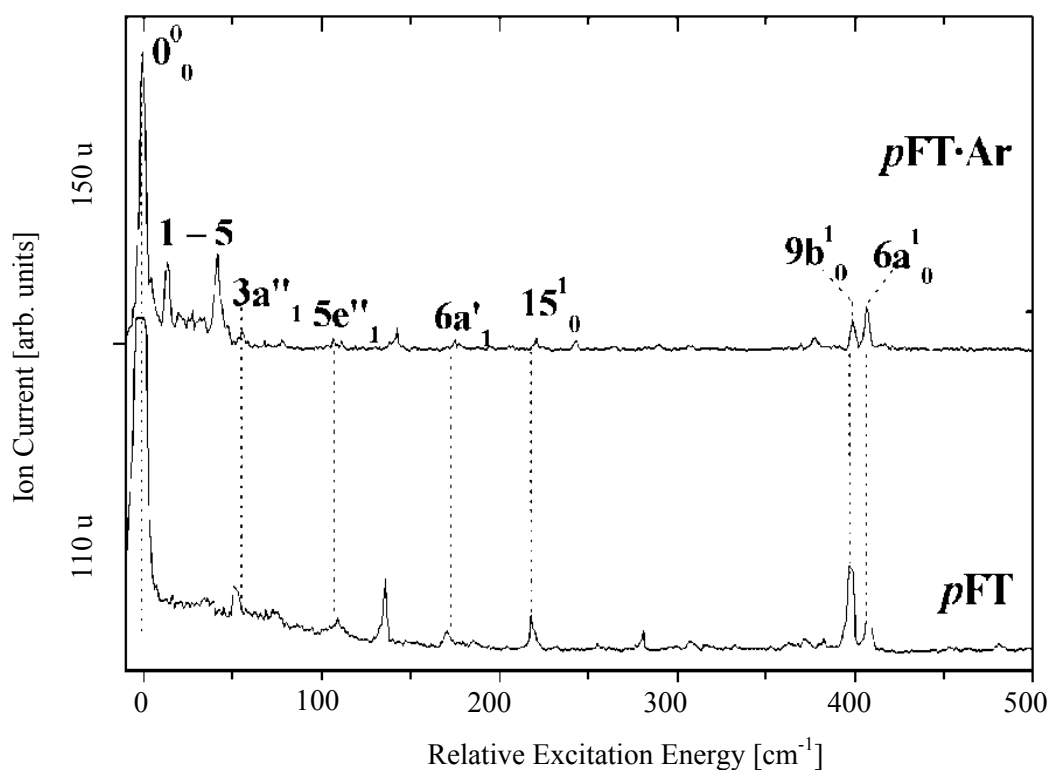


Figure 7(iii): two-colour REMPI spectra of the S_1 state of *p*FT (lower trace) and *p*FT–Ar (upper trace) adapted from Reference 4.

The present study is concerned with vibrational levels of pFT^+ which requires a definitive assignment of vibrational levels observed in the S_1 state of *p*FT; internal rotational levels of the methyl substituent, and stretch and bend vibrations of the *p*FT–Ar van der Waals complex will not be considered further in the present thesis.

7.1.2 Previous work on the *p*FT cation

Bellm *et al.*⁵ have assigned vibrational frequencies for twelve vibrational modes in the electronic ground state of the ion. Using a (1 + 1) REMPI ionisation scheme, a total of

ten vibronic $S_1 \leftarrow S_0$ transitions were excited prior to ionisation, and photoelectrons emitted as a result of ionisation were collected and their time-of-flight converted into ion internal energy (where zero energy corresponds to the electronic ground state of the cation – D_0 – with $v = 0$, *i.e.* the adiabatic ionisation energy). For the first eight vibrational modes excited (up to 845 cm^{-1} above the S_1 origin), nanosecond laser pulses were used and yielded vibrationally resolved photoelectron spectra. For the 13^1 and $7a^1$ levels, picosecond laser pulses were necessary to achieve vibrationally resolved spectra. This was due to a combination of the IVR dynamics exhibited by these states, which leads to a loss in the structure of the photoelectron spectra and the experimental resolution. From assignment of the photoelectron spectra, approximate vibrational frequencies have been deduced for twelve vibrational levels of the cation, with a cited error of $\pm 20 \text{ cm}^{-1}$.

ZEKE spectroscopy offers a much higher spectral resolution than traditional photoelectron spectroscopy (PES) and as such is ideally suited to the study of (ro)vibrational levels of a cation. ZEKE spectroscopy has been applied to a wide range of systems,^{2,14} including halogen-substituted benzenes and toluenes. *p*FT itself has been the subject of both a ZEKE spectroscopic study by Takazawa *et al.*¹⁵ and the sister technique of mass-analysed threshold ionisation (MATI) spectroscopy by Georgiev *et al.*⁴ The former used ZEKE spectroscopy to observe the internal rotational energy levels of the *p*FT cation in its electronic ground state (D_0).

The study of Georgiev *et al.*⁴ used MATI spectroscopy to determine the binding energies of the neutral and cationic *p*FT–Ar complex. During that study, Georgiev and coworkers recorded a MATI spectrum of *p*FT exciting via the $S_1(0^0)$ origin band, and by the feature assigned by them as $S_1(9b^1)$ – the assignment of the $9b^1$ feature in that work will be discussed further in Section 7.3. The MATI spectra are shown below in Figure 7(iv).

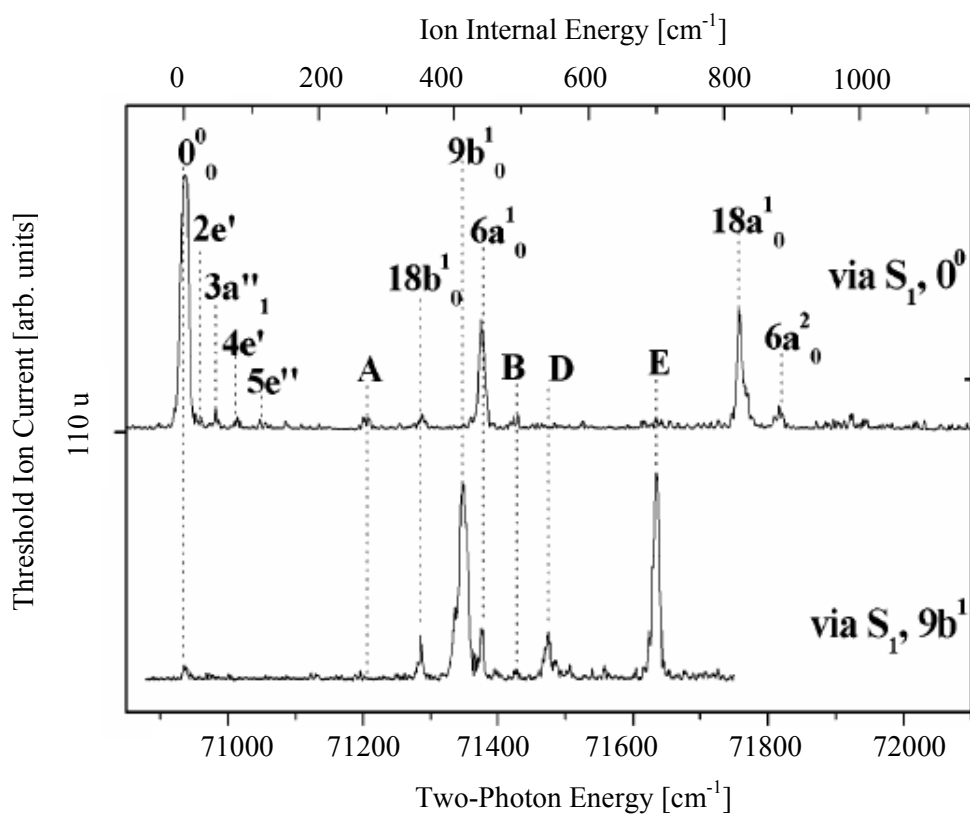


Figure 7(iv): adapted from Reference 4. MATI spectra of *pFT* via $S_1(0^0)$ (upper trace) and $S_1(9b^1)$ (lower trace).

The assignment of features in the MATI spectrum via the $S_1(0^0)$ origin band, as labelled in the upper trace of Figure 7(iv) will be discussed in Section 7.4.1. The lower trace in Figure 7(iv) shows the MATI spectrum obtained via the $S_1(9b^1)$ level. Vibrational levels are labelled using Wilson/Varsanyi notation¹² where *pFT* is treated as belonging to the C_{2v} point group; torsions are labelled using the symmetries of the D_{3h} point group.

There is comparatively little information known about the vibrations of pFT^+ (the REMPI-PES investigation of Bellm *et al.*⁵ is the most comprehensive study to date, although it is hindered by the limited resolution of the technique). The aims of the present work are to report ZEKE spectra recorded out of various vibrational levels of the S_1 state of *pFT*, and upon assignment of these spectra, to provide some

independent confirmation of the previously reported S_1 vibrational assignment and to derive cationic vibrational frequencies. The ZEKE experiments reported here achieve significantly improved resolution, revealing spectral details inaccessible in previous studies.

7.2 Experiment

7.2.1 Experimental set-up

The apparatus used in the present work has been described in detail in Chapter 2. Briefly, the second (532 nm) and third (355 nm) harmonics of a neodymium-doped yttrium aluminium garnet (Surelite III, 10 Hz) laser were used to pump two tuneable dye lasers (Sirah Cobra Stretch, 1800 lines/mm grating). p FT was seeded in ~ 5 bar Ar and passed through a General Valve pulsed nozzle (750 μm , 10 Hz, opening time of 230 μs) to create an unskimmed free-jet expansion. The frequency-doubled output of each dye laser was focused and directed coaxially and counter-propagating into a vacuum chamber. The laser beams intersected the supersonic expansion between two biased electric grids located in the extraction region of a time-of-flight mass spectrometer.

(1 + 1) REMPI spectroscopy was used to determine the required pump energy to excite vibrational modes in S_1 p FT selectively. The first (pump) dye laser was then fixed at the required energy. The second (ionisation) dye laser was tuned to an energy so that the two-colour (1 + 1') energy exceeded the adiabatic ionisation energy of the complex (given in Reference 4 as $70935 \pm 5 \text{ cm}^{-1}$), so that a good ion signal could be observed with a constant extraction voltage. By adjusting the alignment and the relative intensities of the two focused laser beams, a close to 100% two-colour ion signal could be obtained — checked for by recording a photoionisation efficiency

curve. A 100% two-colour ion is defined as a $p\text{FT}^+$ signal that arises solely due to a (1 + 1') REMPI process, where absorption of one photon from the pump laser and one photon from the probe laser results in ionisation. The intensity of the pump laser was minimised to limit the (1 + 1) REMPI process. At that point, the voltages on the elements of the ion lens were switched for ZEKE detection. Once a ZEKE feature had been identified, the overlap of the lasers and the voltages were re-optimised, and then a scan started to record a ZEKE spectrum. The most intense ZEKE signal was obtained by applying a pulsed positive potential (~ 16 V, SRS DG535 digital delay generator) to the grid nearest to the microchannel plate detectors, generating a field of ~ 8 V cm^{-1} . In order to maintain the optimum ZEKE signal intensity, the laser intensities and the focusing conditions were adjusted after each scan. The pump dye laser operated on Coumarin 153, although in order to access the higher vibrational levels ($7a^1$ and 13^1) the dye was mixed with Coumarin 503. In the probe laser, different dye solutions were used to explore a wide wavelength region: PM 597 with an emission peak at 582 nm, PM 580 with an emission peak at 557 nm, and to access the range between the output of PM 597 and PM 580, a 50/50 mixture of both laser dyes. Note that some spectral regions did not have good coverage with these dye solutions, and so remained largely inaccessible in these experiments. These regions correspond to the gaps in some of the spectra. A rotational temperature of ~ 5 K is estimated, with a laser bandwidth of 0.3 cm^{-1} and a ZEKE resolution (which results from pulsed field ionisation) of ~ 7 – 9 cm^{-1} . ZEKE spectra were converted to ion internal energy to aid assignment, with zero energy corresponding to the cationic electronic (and vibrational) ground state $D_0(0^0)$ origin band.

7.2.2 Calibration

In order to determine the adiabatic ionisation energy accurately, it was necessary to calibrate the pump dye laser, as well as the ionisation dye laser used to record the

ZEKE spectra. The pump dye laser was calibrated using strong atomic (3 + 1) Xe resonances (this calibration procedure has been used previously and is described in Chapter 5), and the origin of the (1 + 1) REMPI spectrum was calibrated to 36859.9 cm⁻¹, the literature value of the S_1 origin.¹ The ionisation laser was calibrated using the $E^2\Sigma^+$ state of NO. $E^2\Sigma^+$ state spectra of NO were recorded using a (2 + 1) REMPI scheme shortly before the present work was undertaken and the energy of three rotational lines seen in the spectra have been calculated previously (see Chapter 3). The one-photon energy of the three rotational lines (averaged from a total of eight $E^2\Sigma^+$ spectra) was compared with the one-photon energy of the rotational lines calculated previously (see Chapter 3), and a constant offset (in wavelength) determined, which could then be applied to the ZEKE spectra.

7.3 Results

A (1 + 1) REMPI spectrum of *p*FT is shown in Figure 7(v), indicating the assignment of the S_1 vibrational levels; many of which were used as resonances in the present work. The assignment of these features is based on the LIF work of Okuyama *et al.*¹ and will be discussed further in Section 7.4.5. The ZEKE spectra reported herein were recorded following excitation via a total of thirteen S_1 vibrational levels (in Wilson/Varsanyi notation):¹² 0^0 , 11^1 , 15^1 , the unresolved pair $16a^2$ and $9b^1$, $6a^1$, $6b^1$, 1^1 , $6a^2$, $18a^1$, 12^1 , 13^1 and $7a^1$. For clarity these vibrations are shown in Figure 7(i). As in previous work on substituted benzene molecules, levels with symmetries other than the totally symmetric a_1 symmetry are observed, transitions to which are formally forbidden from the totally symmetric vibration-less S_0 ground state, which has a_1 symmetry. A brief overview of the REMPI spectrum will be given below, and the main points of each ZEKE spectrum will be summarized; general trends in the ZEKE spectra will be addressed in the Discussion. ZEKE spectra recorded via the totally

symmetric features will be considered first, then the non-totally symmetric ones. There are a large number of weak bands, which have been tentatively assigned to combination bands, although given uncertainties in anharmonicities and the possible presence of torsional modes throughout the spectra, only the major features in the spectra will be discussed.

A. $(1 + 1)$ REMPI spectrum

The REMPI spectrum of S_1 *p*FT shown in Figure 7(v) compares favourably with the LIF spectrum of Okuyama *et al.*,¹ shown in Figure 7(ii), and with the limited-range REMPI spectrum of Georgiev *et al.*,⁴ shown in the lower trace of Figure 7(iii). Although the main peaks in the spectrum are due to totally symmetric a_1 vibrations, there are other non-totally symmetric vibrations present. These can be used to probe additional cationic vibrations in the ZEKE experiment, since non-totally symmetric vibrations in S_1 will have different Franck-Condon factors for the ionisation process than vibrations of a_1 symmetry. Note that the band assigned to 12^1 in this spectrum was not assigned in the work of Okuyama *et al.*¹ but has been assigned in the present work mainly on the basis of the ZEKE spectra and also employing density functional theory (DFT) calculations performed by C. J. Hammond and T. G. Wright.

B. ZEKE spectrum via $S_1(0^0)$

The vibration-less S_1 origin has a_1 symmetry, and thus a_1 vibrations are expected to dominate the spectrum. The ZEKE spectrum of *p*FT via the $S_1(0^0)$ origin band (shown in Figure 7(vi)) reveals this to be the case.

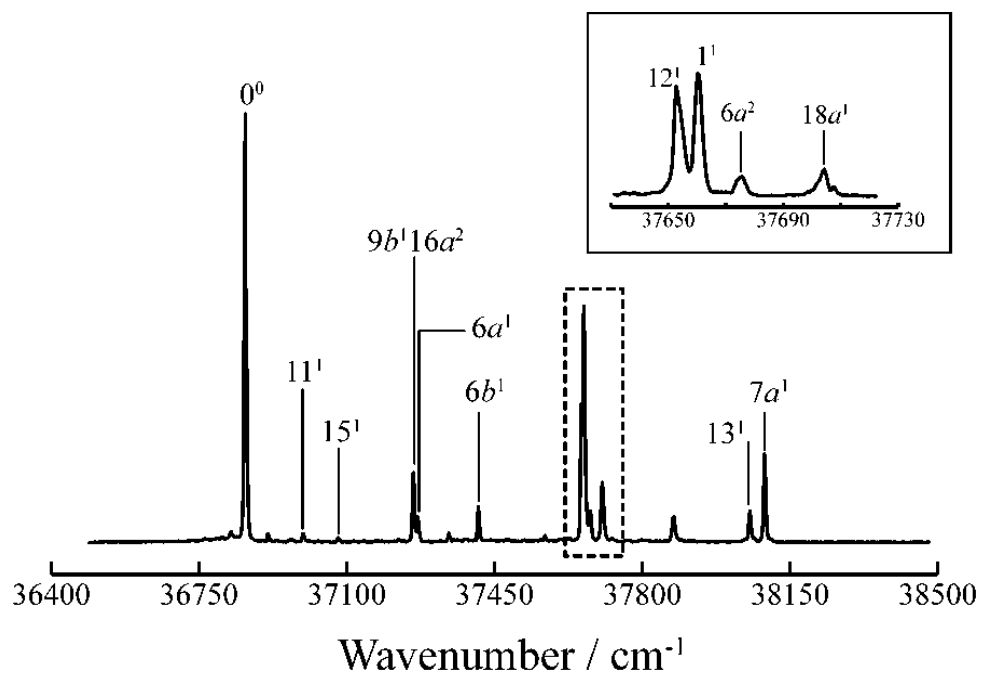


Figure 7(v): $(1 + 1)$ REMPI spectrum of *para*-fluorotoluene. Insert is a close-up of the ν_{12} and ν_1 regions.

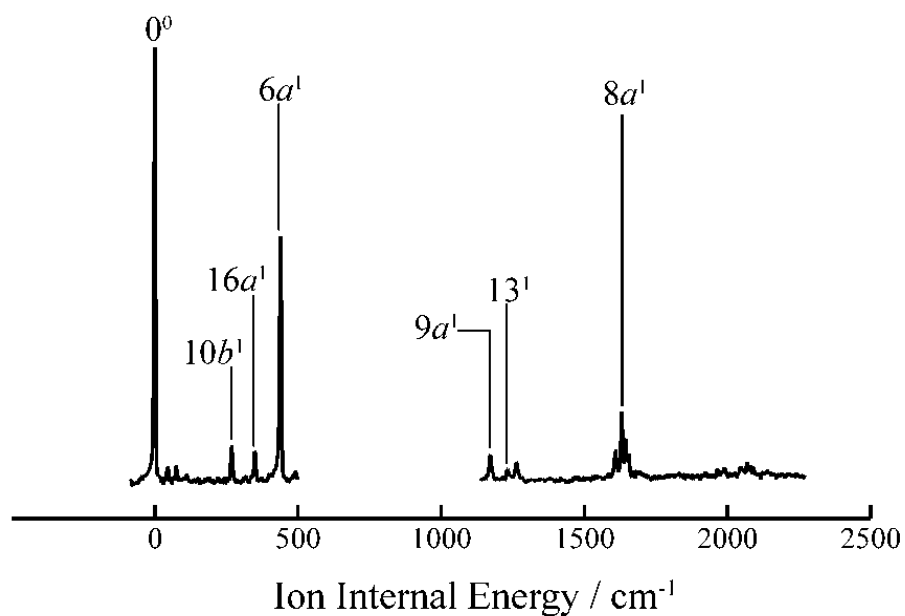


Figure 7(vi): ZEKE spectrum recorded using the $S_1(0^0)$ level as the intermediate resonance. UV intensity was poor in the blank region (see text for details).

The origin band is the most intense, suggesting that changes in geometry between the S_1 state and the cation are small. Interestingly, there are non-totally symmetric modes observed, such as the $10b^1(b_1)$, $11^1(b_1)$ and $15^1(b_2)$ levels, and the combination band $9b^116a^2(b_2)$. The gap in the spectrum, over the range 500–1150 cm^{-1} ion internal energy, corresponds to a region where there was insufficient photon intensity from the dyes used to observe a ZEKE spectrum. Georgiev *et al.*⁴ reported a MATI spectrum of *p*FT via the $S_1(0^0)$ level, over a fairly similar region to that shown in Figure 7(vi). They appear to have had reasonable UV intensity over the whole range, and hence observe the $18a$ vibration in the gap in this spectrum. Otherwise the spectra are fairly similar in appearance. The MATI spectrum of Georgiev *et al.*⁴ is shown in Figure 7(iv) and contains bands labelled A, B, D and E, for which a definite assignment was not presented. This will be discussed further below.

C. ZEKE spectrum via $S_1(6a^1)$ ($0^0 + 408 \text{ cm}^{-1}$)

This spectrum is given in Figure 7(vii), over a shorter range than the previous two spectra. The $6a^1$ feature is the most intense and forms part of a progression of 0^0 , $6a^1$, and $6a^2$. Some non-totally symmetric modes are observed, notably the $10b^1(b_2)$ vibration and the $6a^110b^1(b_1)$ combination band. The $6a^116a^1(a_2)$ combination band is also observed, although the fundamental $16a^1$ appears to be too weak to see.

D. ZEKE spectrum via $S_1(1^1)$ ($0^0 + 803 \text{ cm}^{-1}$)

This spectrum is shown in Figure 7(viii), and the appearance of the spectrum is quite different to that recorded via $S_1(0^0)$. The 1^1 feature is the most intense, again suggesting that geometry changes during the cation $\leftarrow S_1$ process are minimal. In this spectrum, the intense features are assignable only to totally symmetric vibrations, in contrast to the 0^0 spectrum, where the $10b^1(b_1)$ appears with reasonable intensity.

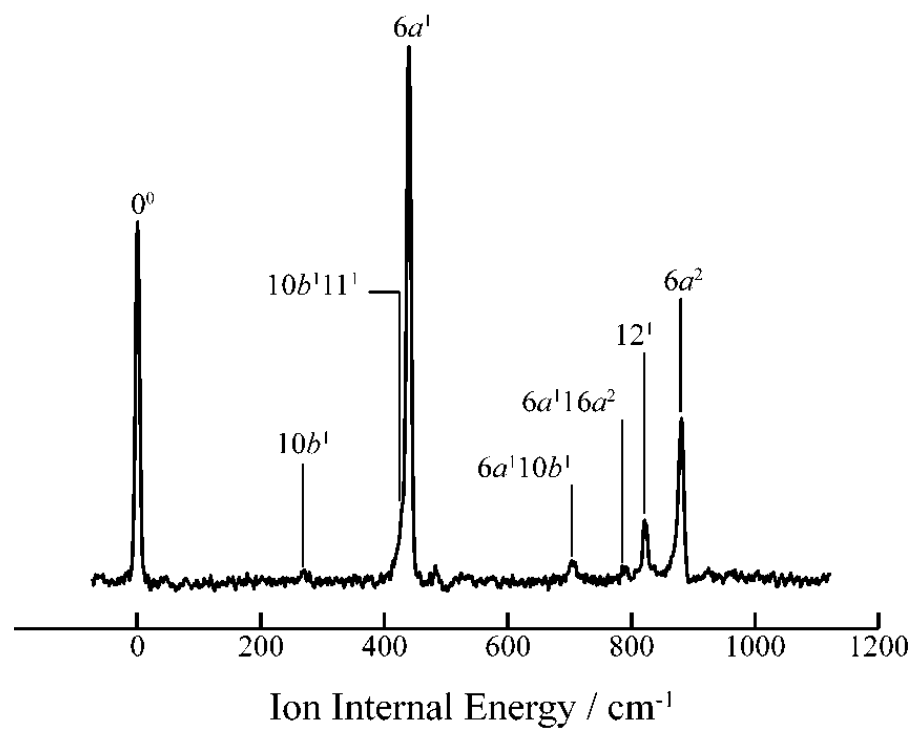


Figure 7(vii): ZEKE spectrum recorded using $S_1(6a^1)$ as the intermediate resonance.

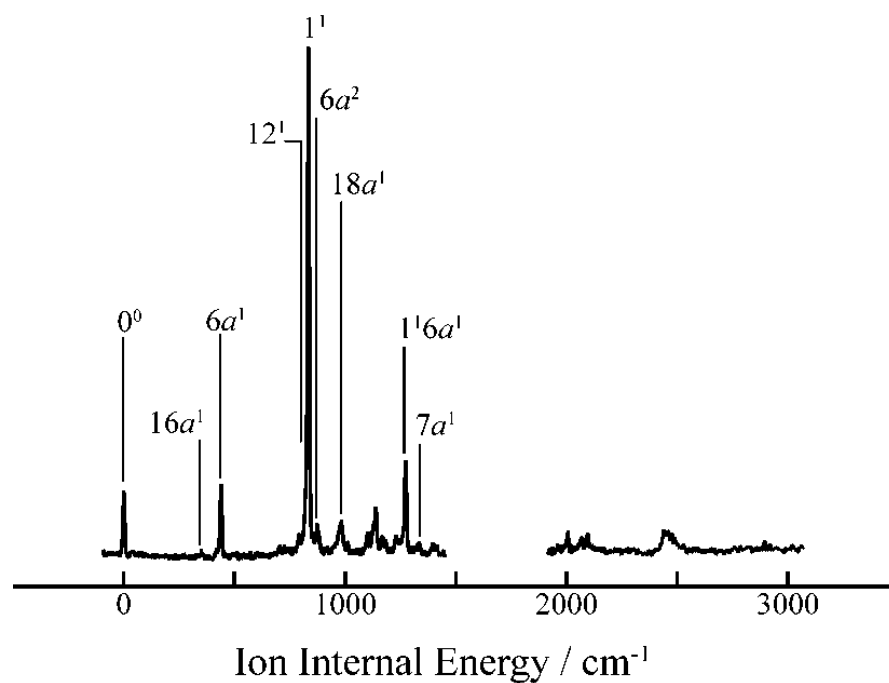


Figure 7(viii): ZEKE spectrum recorded using $S_1(1^1)$ as the intermediate resonance.

UV intensity was poor in the blank region (see text for details).

Again, there was a small region of the spectrum that was inaccessible owing to a lack of UV intensity from the ionisation laser.

E. ZEKE spectrum via $S_1(12^1)$ ($0^0 + 793 \text{ cm}^{-1}$)

The S_1 feature that was excited here is assigned to 12^1 on the basis of the observed ZEKE spectrum (see Section 7.4.5 below). It was not assigned in the work of Okuyama *et al.*¹ This spectrum, Figure 7(ix), is similar to that obtained when exciting through the 1^1 vibration, and again contains a wealth of features. Interestingly, the 1^1 feature is very intense, in contrast to the weaker 12^1 feature obtained when exciting through 1^1 . In addition, there are a number of non-totally symmetric vibrations observed: $10b^1(b_1)$, $16a^1(a_2)$ and $9b^1(b_2)$ with the possibility of other combination bands.

F. ZEKE spectrum via $S_1(6a^2)$ ($0^0 + 816 \text{ cm}^{-1}$)

Exciting via the overtone of the $6a$ vibration yielded the spectrum shown in Figure 7(x). This is the only ZEKE spectrum obtained where the " $\Delta v = 0$ " feature (see below) was not the most intense. As may be seen, both the $6a^1$ and $6a^3$ bands are more intense than the $6a^2$ one. This is discussed further in Section 7.4.3. The increased noise seen in this spectrum is a reflection of the weak intensity of this feature in the S_1 REMPI spectrum (Figure 7(v)).

G. ZEKE spectra via $S_1(18a^1)$ ($0^0 + 845 \text{ cm}^{-1}$)

This vibration is also of a_1 symmetry, and so again mainly a_1 vibrations are expected to be observed. This feature is quite weak, and so the signal-to-noise in the spectrum (Figure 7(xi)) is poorer than in the other spectra reported so far — this is also the case

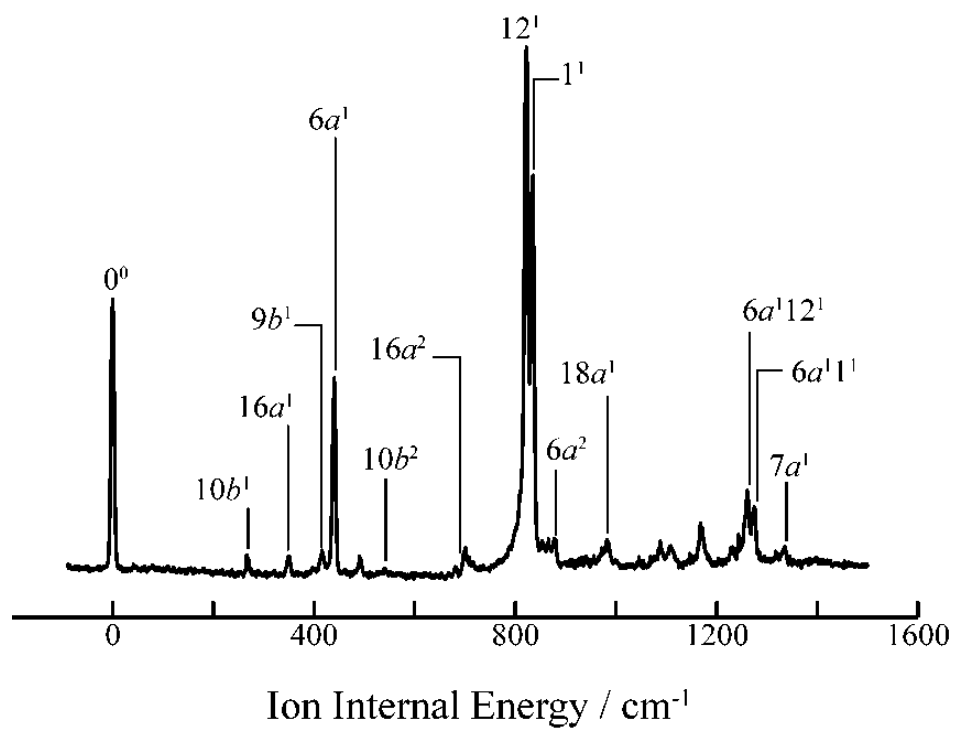


Figure 7(ix): ZEKE spectrum recorded using $S_1(12^1)$ as the intermediate resonance.

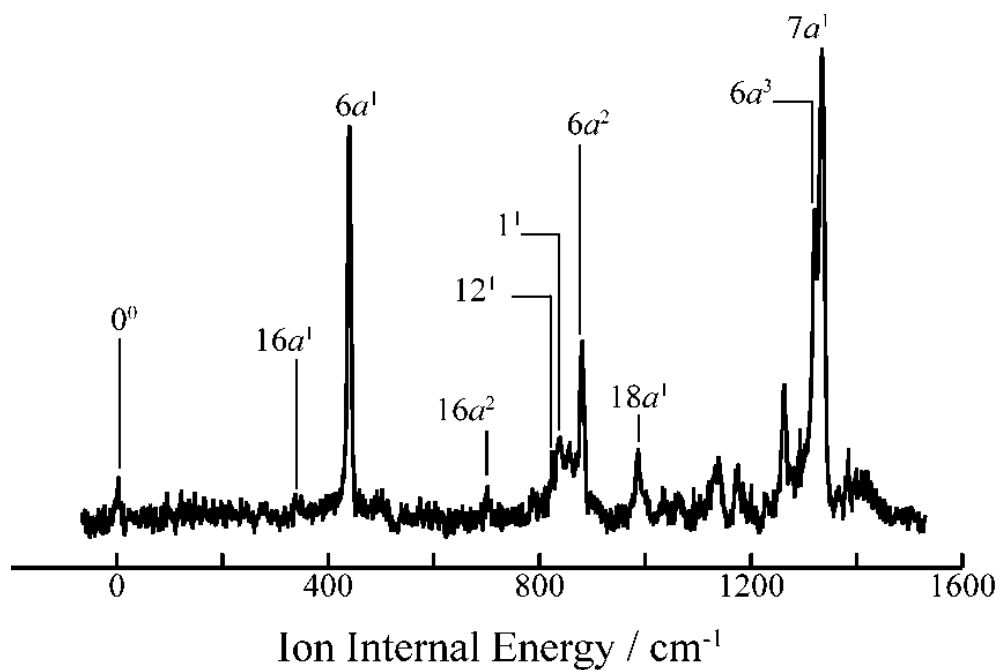


Figure 7(x): ZEKE spectrum recorded using $S_1(6a^2)$ as the intermediate resonance.

for the $S_1(6a^2)$ feature. In the ZEKE spectrum, the $18a^1$ feature is the most intense, with contributions from a number of a_1 vibrations. In addition, there are contributions from several non-totally symmetric ones, with the 11^1 and 11^116a^1 combination bands being seen to low energy (both of b_1 symmetry), and the 11^118a^1 and 15^118a^1 bands to higher energy (b_1 and b_2 symmetry respectively). The broad feature at $\sim 900\text{ cm}^{-1}$ is a composite of a number of features; one possible assignment for the sharp band to the low wavenumber end is the combination band $10b^111^115^2(a_1)$.

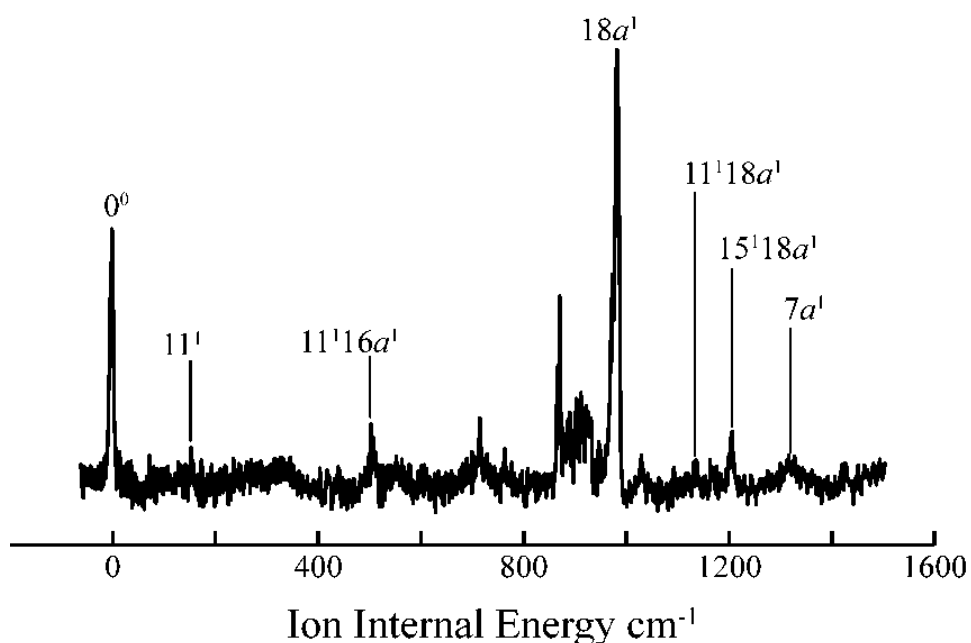


Figure 7(xi): ZEKE spectrum recorded using $S_1(18a^1)$ as the intermediate resonance.

H. ZEKE spectra via $S_1(13^1)$ and $S_1(7a^1)$ ($0^0 + 1194$; $0^0 + 1230\text{ cm}^{-1}$)

Both of these levels have a_1 symmetry, and so again mainly a_1 vibrations are expected in the ZEKE spectrum, Figure 7(xii), as observed. This would include the origin although the dye range was not sufficient to scan this far to the red in these cases. These two ZEKE spectra were published recently as part of a paper discussing IVR in $p\text{FT}$;¹⁶ this is not the focus of the present thesis however and only a brief outline of the

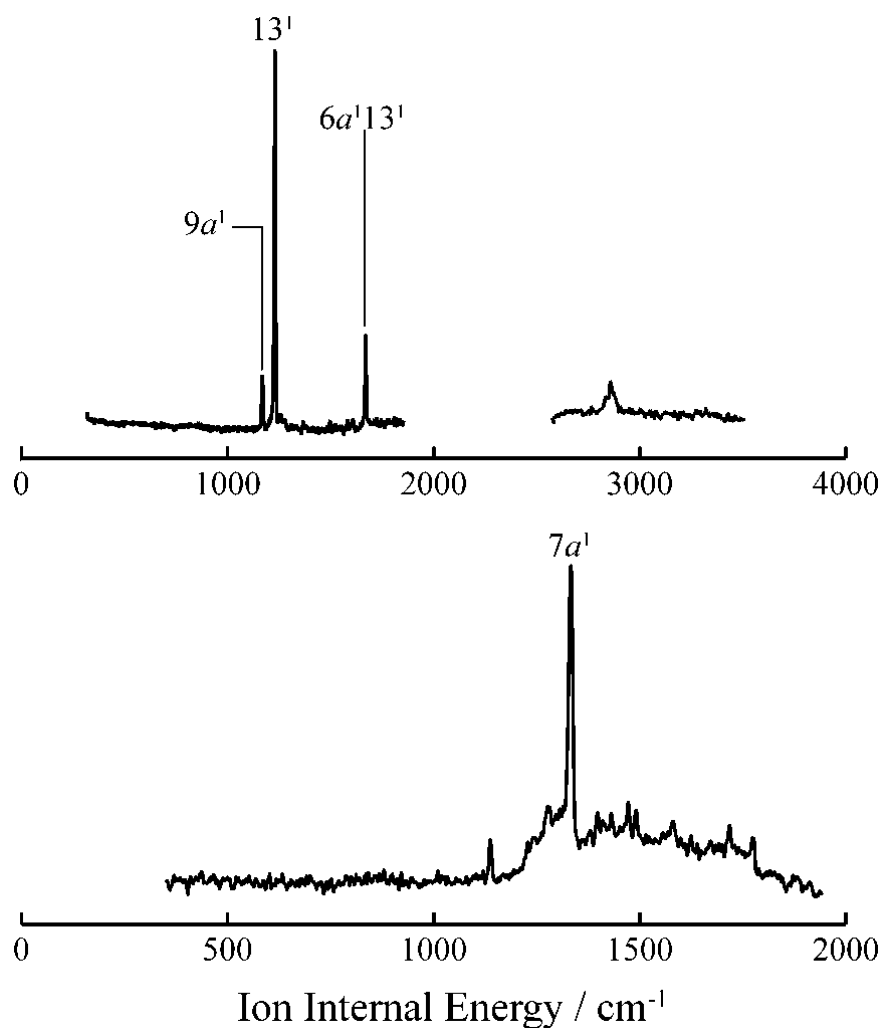


Figure 7(xii): ZEKE spectra recorded using S_1 (13^1 and $7a^1$) as the intermediate resonances. The IVR dynamics seen in these S_1 levels is responsible for the marked difference in their appearance and has been discussed elsewhere (see Reference 16).

dynamics will be given here. IVR arises as a consequence of the preparation of a superposition of molecular eigenstates, which can be described as a result of coupling of an optically accessible "bright" state to a number of optically inaccessible "dark" states. At zero time, the superposition is localised in the bright state, and evolves in time as a consequence of anharmonic or other couplings between the bright and dark states. IVR dynamics in the first excited state of p FT have been studied by a number of groups,⁶⁻¹¹ with most attention focusing on the 13^1 level at 1194 cm^{-1} and the $7a^1$

level at 1230 cm^{-1} , where mode 13 is a totally symmetric C–CH₃ stretch and mode $7a$ is a totally symmetric C–F stretch. The ZEKE experiment gives information on the projection of a time-averaged superposition of S_1 eigenstates onto ionic internal states. In other words, the ZEKE spectrum obtained from an S_1 level that undergoes IVR will be a convolution of ZEKE spectra, arising from the optically accessible bright state and from the inaccessible dark states to which the optically accessible bright state (either the 13^1 or $7a^1$ level) is coupled.

The ZEKE spectrum obtained following excitation of the $7a^1$ level shows evidence of extensive rovibronic coupling *i.e.* the spectrum is found to be extremely congested as a result of containing ZEKE spectra from one or more optically inaccessible bath states. In contrast, the ZEKE spectrum arising as a result of excitation of the 13^1 level does not appear to contain contributions from dark states, suggesting that (under the experimental conditions present) the $7a^1$ level undergoes IVR, whereas the 13^1 level does not. This has been presented in a recent publication¹⁶ and will not be discussed further herein. Both spectra are dominated by the $\Delta\nu = 0$ peak — the $7a^1$ feature is the most intense in the $S_1(7a^1)$ ZEKE spectrum (lower trace in Figure 7(xii)) and the 13^1 feature dominates the $S_1(13^1)$ ZEKE spectrum (upper trace in Figure 7(xii)). There are a number of possible assignments for the other sharp band in the $S_1(7a^1)$ ZEKE spectrum at $\sim 1139\text{ cm}^{-1}$, with $6b^2$ being favoured. The gap in the $S_1(13^1)$ ZEKE spectrum corresponds to a region where the UV intensity was not sufficient to observe a ZEKE signal.

I. ZEKE spectrum via $S_1(11^1)$ ($0^0 + 137\text{ cm}^{-1}$)

The $S_1 \leftarrow S_0$ transition leads to the observation of a number of non-totally symmetric modes. These can be employed to probe a range of additional cationic vibrational levels, which may not be accessible from the totally symmetric S_1 levels (since only a_1

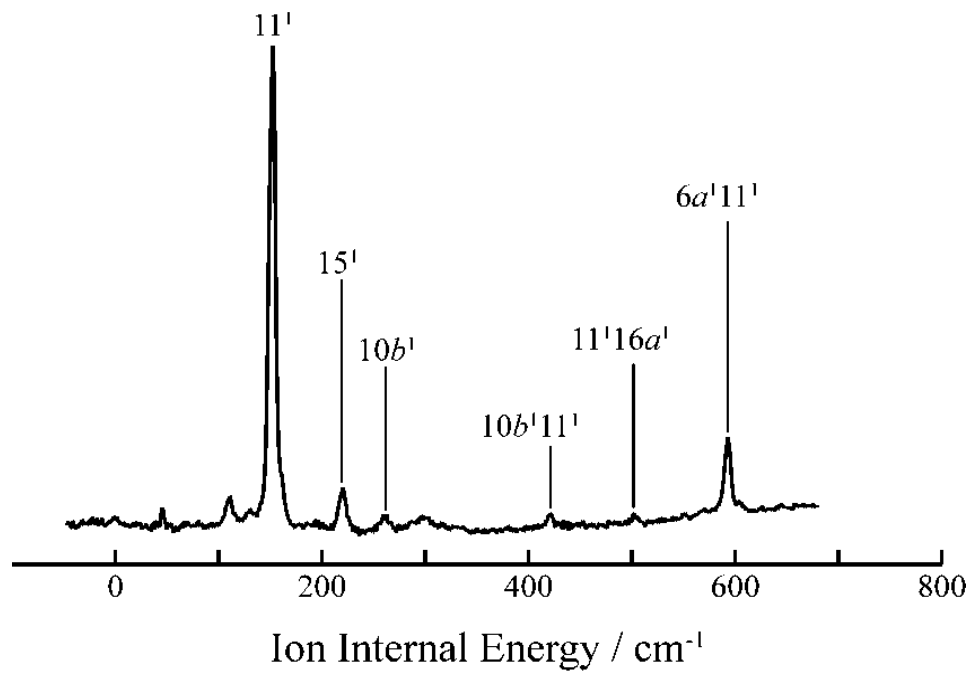


Figure 7(xiii): ZEKE spectrum recorded using $S_1(11^1)$ as the intermediate resonance.

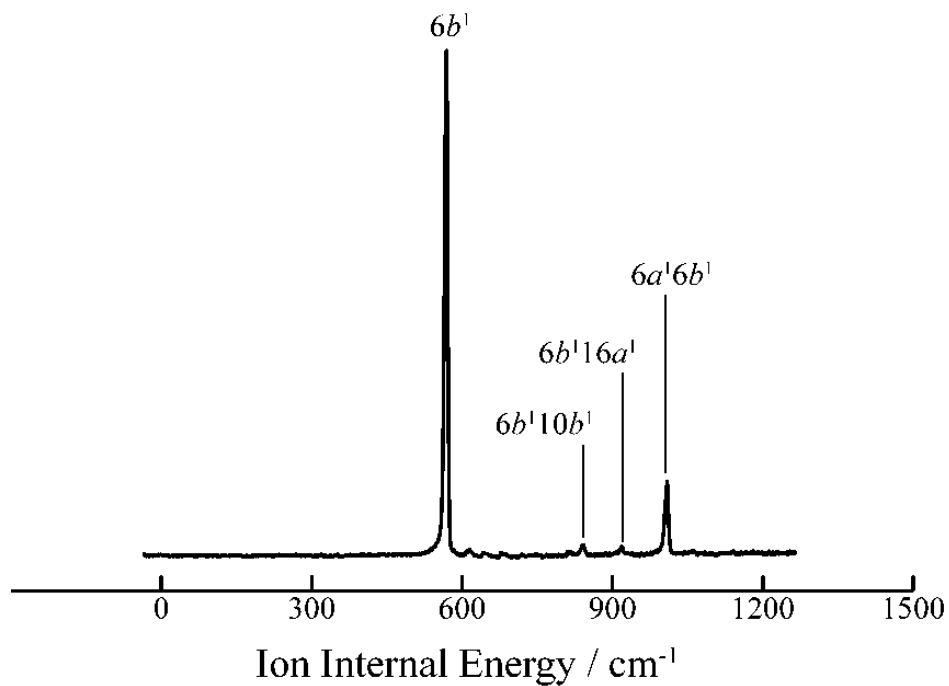


Figure 7(xiv): ZEKE spectrum recorded using $S_1(6b^1)$ as the intermediate resonance.

$\leftarrow a_1$ are formally allowed). The first such spectrum presented is that via $11^1(b_1)$, shown in Figure 7(xiii).

The 11^1 band is by far the most intense feature, with $6a^111^1$ being the next most intense. The origin is not observed in the spectrum, in line with its having a_1 symmetry, and so being symmetry-forbidden. However, other symmetry-forbidden bands (not of b_1 symmetry) are observed, such as $15^1(b_2)$, and combination bands, for example, $10b^111^1(a_1)$.

J. ZEKE spectrum via $S_1(6b^1)$ ($0^0 + 549\text{ cm}^{-1}$)

Excitation via $6b^1$ leads to the spectrum shown in Figure 7(xiv), which is also notable for the absence of the (symmetry-forbidden) origin peak; indeed, there is essentially no activity until the appearance of the strongest feature, $6b^1$. There then follow some weak features, which it is possible to assign to various combination bands, where the $6b^1$ feature is seen in combination with the bands $10b^1$, $16a^1$ and $6a^1$. This series of combination bands is also seen in the $S_1(6a^1)$ and $S_1(15^1)$ ZEKE spectra as shown in Figures 7(vii) and 7(xv) respectively.

K. ZEKE spectrum via $S_1(15^1)(b_2)$ ($0^0 + 219\text{ cm}^{-1}$)

The most intense band in this spectrum, shown in Figure 7(xv), is due to 15^1 , with the 15^16a^1 combination being the next most intense. The origin is again absent (the $a_1 \leftarrow b_2$ transition is forbidden), but there are other weak symmetry-forbidden bands, such as the combination bands $15^110b^1(a_2)$ and $15^116a^1(a_2)$ discussed above.

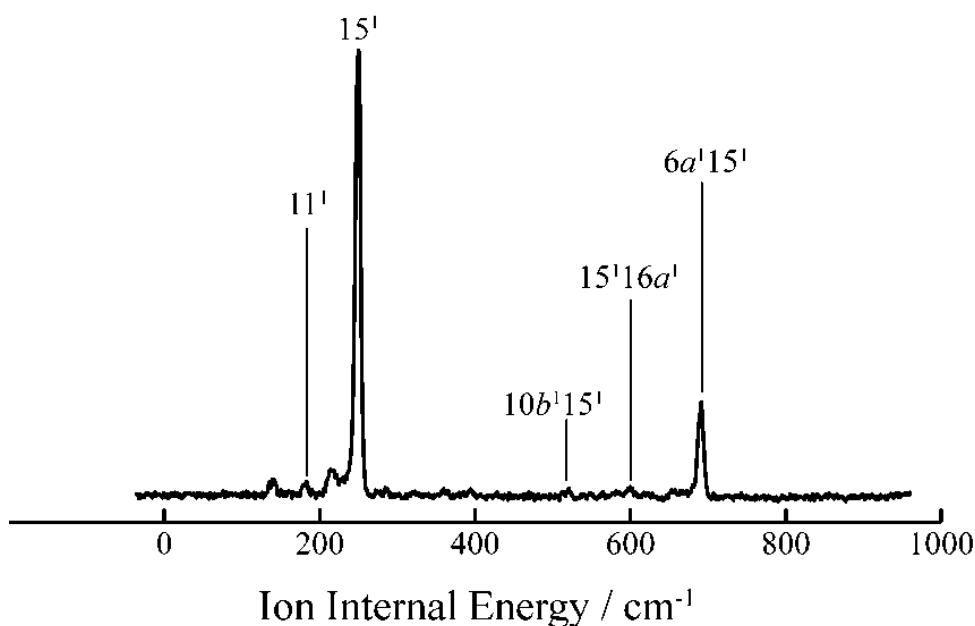


Figure 7(xv): ZEKE spectrum recorded using $S_1(15^1)$ as the intermediate resonance.

L. ZEKE spectra via the overlapped features $S_1(9b^1$ and $16a^2)$ ($0^0 + 399$ cm⁻¹)

These two features are highly overlapped in the $S_1 \leftarrow S_0$ spectrum, as may be seen in the top trace of Figure 7(xvi). ZEKE spectra were recorded at three different wavenumbers in this band: at the maximum, and to the red and blue of the maximum, marked III, II, and I, respectively. The appearance of the ZEKE spectra changed markedly, as may be seen from the lower three traces.

The ZEKE spectrum recorded through the low-energy side of the unresolved REMPI feature (central ZEKE spectrum, labelled II), is dominated by the $16a^2$ level. Based upon the dominance of the $\Delta v = 0$ feature seen in the majority of the ZEKE spectra already collected (see Section 7.4.1), this suggests that the red side of the REMPI feature is mainly due to the $16a^2$ vibration. Similarly, the ZEKE spectrum obtained using the high-energy side of the REMPI feature (lower ZEKE spectrum, labelled I) is

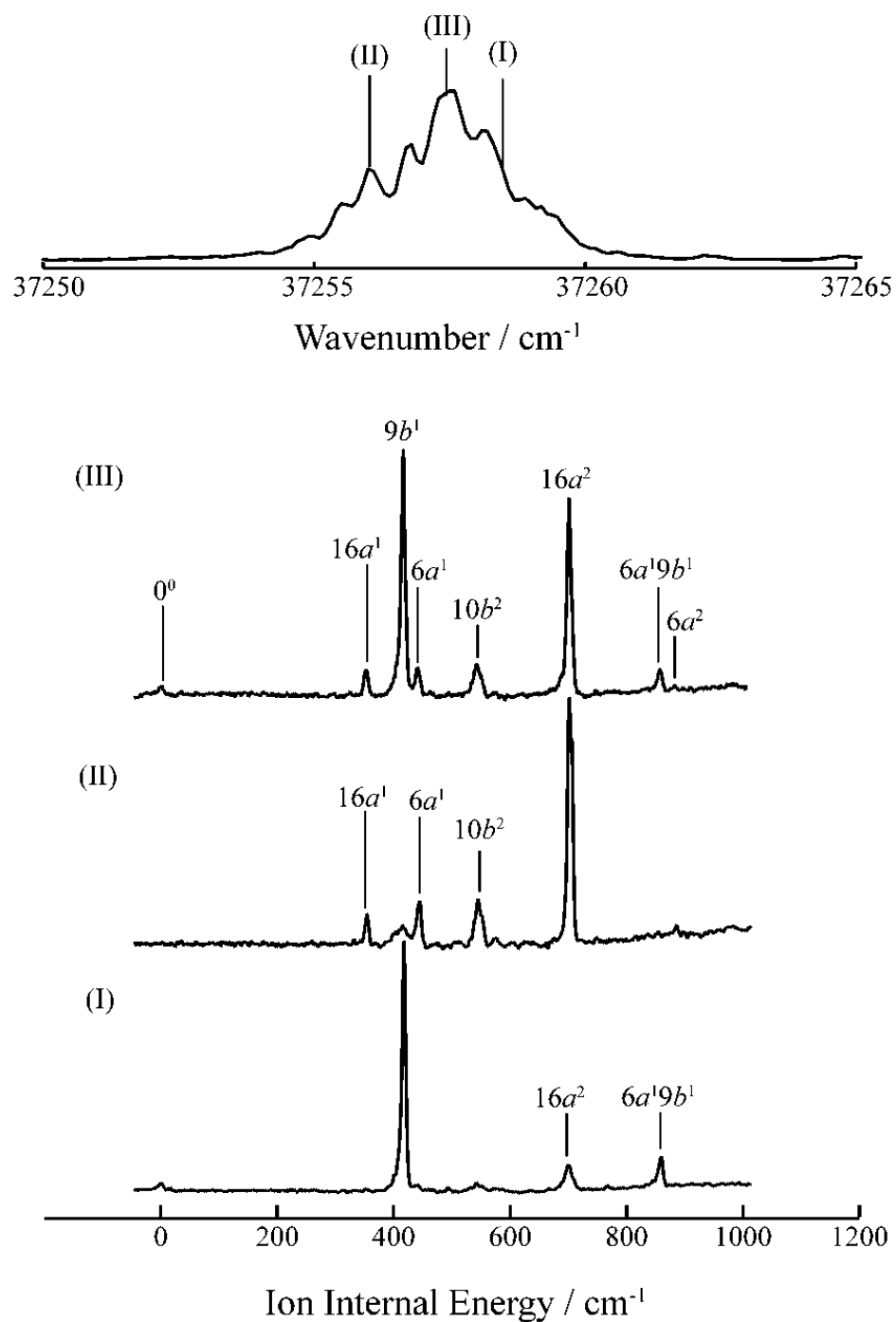


Figure 7(xvi): *Top trace: (1 + 1) REMPI spectrum of the overlapped $S_1(9b^1/16a^2)$ features showing three energetic regions of this band probed (labelled I, II and III). Bottom three traces: ZEKE spectra recorded using three different regions (I, II and III) of the overlapped $S_1(9b^1/16a^2)$ levels as the intermediate resonances. See text for details.*

dominated by the $9b^1$ level. Hence, the blue side of the REMPI feature is mainly due to the $9b^1$ vibration and there is a significant overlap between these two vibrations in the centre. As a result, the ZEKE spectrum obtained by exciting through the centre of the REMPI peak contains almost equal contributions from each of the two vibrations (upper ZEKE spectrum, labelled III).

Georgiev *et al.*⁴ also report a spectrum via an S_1 feature which they label as the $9b^1$ vibration. By comparing the spectrum of Georgiev and coworkers (shown in Figure 7(iv)), with those in Figure 7(xvi), it seems that they have excited through the centre of the S_1 feature, shown in the upper trace of Figure 7(xvi), and thus simultaneously excited both the $9b^1$ and $16a^2$ vibrations. This is confirmed by the work of Bellm *et al.*,⁵ who noted that their photoelectron spectrum obtained through (presumably the centre of) this unresolved feature had two distinct contributions. This example shows that it is possible to record "clean" ZEKE spectra from overlapped features, as long the overlap is not complete.

M. *The adiabatic ionisation energy*

From the calibrated $S_1(0^0)$ and $D_0(0^0)$ origin bands in the REMPI and ZEKE spectra, it is possible to derive an adiabatic ionisation energy. The value derived in the present work was $70946 \pm 4 \text{ cm}^{-1}$, where the ZEKE spectra were recorded with an electric field of $\sim 8 \text{ V cm}^{-1}$. The value from work by Takazawa *et al.*¹⁵ is 70940 cm^{-1} , although they applied a smaller ionising field ($\sim 1.0 \text{ V cm}^{-1}$) and the value from Georgiev *et al.*⁴ is $70935 \pm 5 \text{ cm}^{-1}$, recorded with a field of 1000 V cm^{-1} . The effect of an electric field on the ionisation energy is well documented.¹⁷ Briefly, the electric field lowers the ionisation energy (in cm^{-1}), by an amount proportional to the square root of the magnitude of the applied electric field (in V cm^{-1}) with a constant in the range 4–6.¹⁷ In principle therefore the measured values should be corrected upward. However, it is

well established that for larger polyatomic molecules, decay of the lower Rydberg states (for example, by predissociation) means that only the upper slice of Rydberg states is accessed in the ZEKE spectrum, and so the full correction is not required. It is assumed that many of the lower Rydberg states that would have been accessed have decayed and are not observed. This is supported by the width ($\sim 8 \text{ cm}^{-1}$) of the features in the ZEKE spectrum, which are not the whole expected $11\text{--}17 \text{ cm}^{-1}$. Georgiev *et al.*⁴ saw comparable peak widths in spite of the large electric field applied. All the ZEKE values are consistent with old measurements from Lias and Ausloos,¹⁸ who determined a value of $70928 \pm 65 \text{ cm}^{-1}$ from charge-transfer equilibrium measurements. Consistency is also present with even older measurements by Watanabe *et al.*¹⁹ who used the long wavelength limit of the ionisation continuum to derive a value for the adiabatic ionisation potential of $70900 \pm 80 \text{ cm}^{-1}$.

N. DFT calculations

As part of the present study, DFT calculations were performed by C. J. Hammond and T. G. Wright at the B3LYP level of theory using two basis sets: aug-cc-pVDZ and aug-cc-pVTZ. Minimum-energy geometries and harmonic vibrational frequencies were calculated. The assignment of the vibrations from the calculations was achieved by looking at the animated modes and comparing to the well-known motions of substituted benzene molecules. In a few cases, there was some ambiguity as to the identity of the band; in these cases a best attempt at the assignment is given. The main assignments made, together with a brief description of the vibrational modes, and their Wilson/Varsanyi labels are given in Table 7(I) – pictorial representations of the vibrational modes are shown in Figure 7(i). The cationic vibrational frequencies derived in previous work⁵ are also presented since these have been used to aid assignment in the present study (see below). Also presented are the unscaled B3LYP

Mode	Description	S_0^a	S_1^b	D_0^a	D_0^b	aVDZ ^c	aVTZ ^d
$8a^1 (a_1)$	Ring str.	1607	—	1637	1631	1678	1678
$7a^1 (a_1)$	CF str.	1223	1230	1344	1332	1337	1351
$13^1 (a_1)$	C-CH ₃ str.	1214	1194	1200	1230	1245	1248
$9a^1 (a_1)$	CH rock	1155	—	1122	1170	1182	1194
$18a^1 (a_1)$	Ring bend	1017	845	944	984	992	999
$1^1 (a_1)$	Ring br.	844	803	786	834	833	836
$12^1 (a_1)$	C-CH ₃ str.	728	793	—	822	724	731
$6a^1 (a_1)$	Ring br.	455	408	418	440	447	450
$6a^2 (a_1)$	Ring br.	—	816	—	879	—	—
$6a^3 (a_1)$	Ring br.	—	—	—	1316	—	—
$16a^1 (a_2)$	Ring twist	404	199	328	350	365	367
$16a^2 (a_1)$	Ring twist	—	—	—	699	—	—
$10b^1 (b_1)$	CH ₃ wag	340	255	—	269	275	274
$10b^2 (a_1)$	CH ₃ wag	—	—	—	540	—	—
$11^1 (b_1)$	Boat def.	157	137	150	156	114	113
$11^2 (a_1)$	Boat def.	—	—	—	305	—	—
$6b^1 (b_2)$	Ring bend	638	549	578	570	579	581
$9b^1 (b_2)$	CF rock	420	399	383	416	418	424
$15^1 (b_2)$	CH ₃ rock	312	219	222	224	318	322

Table 7(I): assigned modes given in Wilson/Varsanyi notation¹² (symmetry under C_{2v} point group given in parentheses). These modes are shown in Figure 7(i) for clarity: ^a Reference 5; ^b this work; ^c B3LYP/aug-cc-pVDZ harmonic vibrational frequencies (unscaled); ^dB3LYP/aug-cc-pVTZ harmonic vibrational frequencies (unscaled). Five overtones ($6a^2$, $6a^3$, $16a^2$, $10b^2$, 11^2) of pFT⁺ D_0 were identified in this ZEKE study. All values given in cm^{-1} .

harmonic vibrational frequencies, as calculated with the aug-cc-pVDZ and aug-ccpVTZ basis sets. The agreement of the calculated (unscaled harmonic) frequencies with the experimental fundamentals is for the most part extremely good, certainly sufficient to support the assignments made.

7.4 Discussion

7.4.1 Assignment of the spectra and the $\Delta v = 0$ propensity rule

The spectra were partially assigned on the basis of the vibrational frequencies reported in previous photoelectron work by Bellm *et al.*⁵ and also using the results of the B3LYP calculations in Table 7(I). This preliminary assignment provided confirmation that the $\Delta v = 0$ selection rule held for this species (this was previously noted by Bellm *et al.*⁵ and is seen to be the case for most substituted aromatics).²⁰ As a result of the $\Delta v = 0$ propensity rule, the most intense feature in almost every ZEKE spectrum corresponds to a transition from the S_1 neutral excited state to a cationic energy level where there is no change in the vibrational level excited in S_1 upon ionisation ($\Delta v = 0$). However, this is not the case for the ZEKE spectrum resulting from excitation via $S_1(6a^2)$ as can be seen in Figure 7(x). This will be discussed further below. The fact that the $\Delta v = 0$ propensity rule is evident in all but one of the ZEKE spectra implies that the geometries of the neutral S_1 and ionic D_0 states are fairly similar.

Weaker features in the ZEKE spectra were assigned by comparing their energies to assigned features in other ZEKE spectra and by considering their expected symmetries based upon the symmetry of the feature excited in S_1 (symmetry considerations are discussed in detail in Section 7.4.2 below). Confidence in the assignments comes from a comparison with the results of the B3LYP calculations and the consistency seen between the spectra.

Assignments in the present work are in contrast to those presented in the previous study of Georgiev *et al.*⁴ The $S_1(0^0)$ MATI spectrum of *p*FT is shown in the upper trace of Figure 7(iv) and the $S_1(9b^1)$ MATI spectrum is shown in the lower trace, although based on the present study, that spectrum is actually a result of excitation of the unresolved S_1 features $9b^1$ and $16a^2$. Disagreement is found between the assignments made in the present work and with some of the assignments presented in Reference 4. Alternative assignments are given here, as well as assignments for the previously unassigned bands labelled A, B, D and E in that work. A ZEKE feature at 356 cm^{-1} in that work has been previously assigned to ν_{18b} . The ν_{18b} band is expected to lie $> 1000\text{ cm}^{-1}$ (see Table 7(I)). This feature is in fact believed to be ν_{16a} , based upon its appearance in the $S_1(9b^1/16a^2)$ spectra (see Figure 7(xvi)) and on the results of the DFT calculations.

The band at 823 cm^{-1} was previously assigned⁴ as the ν_{18a} and is assigned here to ν_{12} . The assignment of the ν_{12} level is discussed in more detail in Section 7.4.5 below. In this work, the ν_{18a} is assigned to the feature at 984 cm^{-1} (seen in the 1^1 , 12^1 and $6a^2$ spectra in Figures 7(viii), 7(ix) and 7(x) respectively). This assignment is based upon the appearance of the ZEKE spectrum presented in Figure 7(xi) and is in good agreement with the calculations.

The features in the $S_1(9b^1/16a^2)$ MATI spectrum labelled D and E can be assigned as $D_0(10b^2)$ and $D_0(16a^2)$. The peak labelled A, seen in the $S_1(0^0)$ MATI spectrum of Georgiev *et al.* can be assigned as $10b^1$ and is seen in several of the ZEKE spectra presented here both as a single level, and in combination with the $\Delta\nu = 0$ feature. The feature labelled B lies at 491 cm^{-1} and this peak is seen in the present work in the 0^0 , 12^1 spectra, and extremely weakly in the $9b^1$ spectrum. This feature is tentatively assigned as $10b^115^1$.

7.4.2 Symmetry effects

The symmetry of the S_1 vibrational mode employed as the intermediate resonance largely determines the appearance of the resulting ZEKE spectrum. In the case of weak vibronic coupling, the electronic and vibrational contributions to the transition strength can be separated, allowing the vibrational part to be considered in isolation via the Franck-Condon factor (FCF) $\langle \psi_{v'} | \psi_{v''} \rangle^2$. For the FCF to be nonzero, the symmetry of both vibrations is required to be the same (for non-degenerate point groups), under the common point group of the two electronic states; such transitions are symmetry-allowed and others are symmetry-forbidden. In particular, the zero-point energy level is always totally symmetric, and so exciting from this level in the lower state leads to the expectation of only observing totally symmetric vibrations in the upper state. This argument applies both to the $S_1 \leftarrow S_0$ excitation, as well as to the ion $\leftarrow S_1$ ionisation step. It is clear that the $S_1 \leftarrow S_0$ REMPI spectrum, as well as the ZEKE spectra display symmetry-forbidden bands (non-totally symmetric vibrations). That these vibrations appear could be indicative of distortion of the molecule away from C_{2v} symmetry, or a breakdown of the Born–Oppenheimer approximation so that vibrational and electronic coupling cannot be completely ignored. A detailed examination of the origins of the symmetry-forbidden bands will not be given here, but note that they are commonplace in the spectra of substituted benzenes.

The presence of such features in the $S_1 \leftarrow S_0$ spectrum allows different symmetry vibrations to be employed to record the ZEKE spectra, thus enabling the observation of non-totally symmetric cationic vibrations. The ZEKE spectra presented herein reveal that the spectra recorded via totally symmetric (a_1) S_1 vibrations contain mostly totally symmetric vibrations. In particular, excitations via the a_1 symmetry vibrations 1, 6a, 12 and 18a all show strong origin bands, as well as the $\Delta v = 0$ features referred

to above. The intensity of symmetry-forbidden features are all fairly weak, suggesting that for *p*FT, the vibrational selection rule ($a_1 \leftarrow a_1$ only) under C_{2v} symmetry does appear to hold quite well. In addition, there is often more than one forbidden symmetry type observed, indicating the likely presence of more than one mechanism for relaxing the symmetry restraint in the ionisation step for this molecule. In the cases where non-totally symmetric intermediate vibrational states have been employed (11, 6*b*, 9*b*, and 15) then the symmetry-allowed features are now those that have the same symmetry as the intermediate level. As such, the strongest bands have this symmetry, with the $\Delta v = 0$ feature being the dominant one, as noted in the above. Of note is that in these spectra the (a_1) origin band is essentially absent, which is in line with its having a different symmetry.

7.4.3 *6a* dominance

There are three sets of spectra that are not quite in line with the above general comments. First, the spectrum recorded through the $6a^2$ overtone feature, as shown in Figure 7(x) does not behave quite as expected. This feature is totally symmetric, and hence was expected to have a relatively strong origin transition, but, in fact, this is rather weak. Secondly, the $\Delta v = 0$ propensity rule appears not to be obeyed here, since both the $6a^1$ feature and the second overtone ($6a^3$) are more intense than the first overtone. This observation could be explained by a geometry change along the ν_{6a} coordinate between the S_1 state and the cation, leading to a poor Franck-Condon overlap with the $6a^2$ level. In fact, the $7a^1$ feature is the most intense feature in the spectrum. This implies that there is a coupling between the ν_{6a} and ν_{7a} vibrations, which seems plausible given that the former involves elongation of the ring along the C_2 axis, and the latter is the C–F stretch. If the $7a^1$ level were seen with significant intensity in the $6a^1$ spectrum then this may be taken as further evidence of this coupling, although the high wavenumber region of the $6a^1$ ZEKE spectrum (where the

$7a^1$ feature is expected) was not probed in the current investigation. It was not possible to observe the levels $6a^1$, $6a^2$ or $6a^3$ when exciting through $7a^1$ since the presence of IVR appears to have disguised much of the structure seen in the spectrum – Figure 7(xii).

It is of interest to note the dominance of the ν_{6a} mode in the spectra. A transition to the $6a^1$ level is observed in several ZEKE spectra. Additionally, in all the ZEKE spectra collected, the $6a^1$ level is seen in combination with the S_1 vibrational mode from which excitation occurs (although the combination band $18a^16a^1$ is not immediately apparent in the $18a^1$ spectrum, a very weak feature located at $\sim 1422\text{ cm}^{-1}$ is a likely candidate). The first overtone of the ν_{6a} vibration is also present in a number of ZEKE spectra (resulting from excitation of the $6a^1$, $6a^2$, $9b^1$, 12^1 and 1^1 levels). Reiser *et al.*²¹ also observed the dominance of this mode in their study on *para*-difluorobenzene (*p*DFB) as did Kwon *et al.*²² in their VUV MATI study. Kwon *et al.*²² calculated the neutral and ground state geometries of *p*DFB, and evaluated the atomic displacements upon ionisation. The atomic displacements were compared with the eigenvector of ν_6 of the cation (Kwon *et al.* used Mulliken notation,²³ where the ring breathing mode $6a$ referred to herein using Wilson/Varsanyi notation is given by mode 6). This is shown in Figure 7(xvii), taken from Reference 22.

They found that the atomic displacement between the neutral and cationic states corresponds to the motion of the ν_{6a} vibration. The conclusion in the present work therefore, is that there is a displacement along the ν_{6a} coordinate (this is essentially a distortion along the C_2 axis) upon ionisation in *p*FT (in line with the conclusions based on the failure of the $\Delta\nu = 0$ propensity rule for the $6a^2$ ZEKE spectrum), thus accounting for the prevalence of the ν_{6a} mode seen in the ZEKE spectra presented herein.

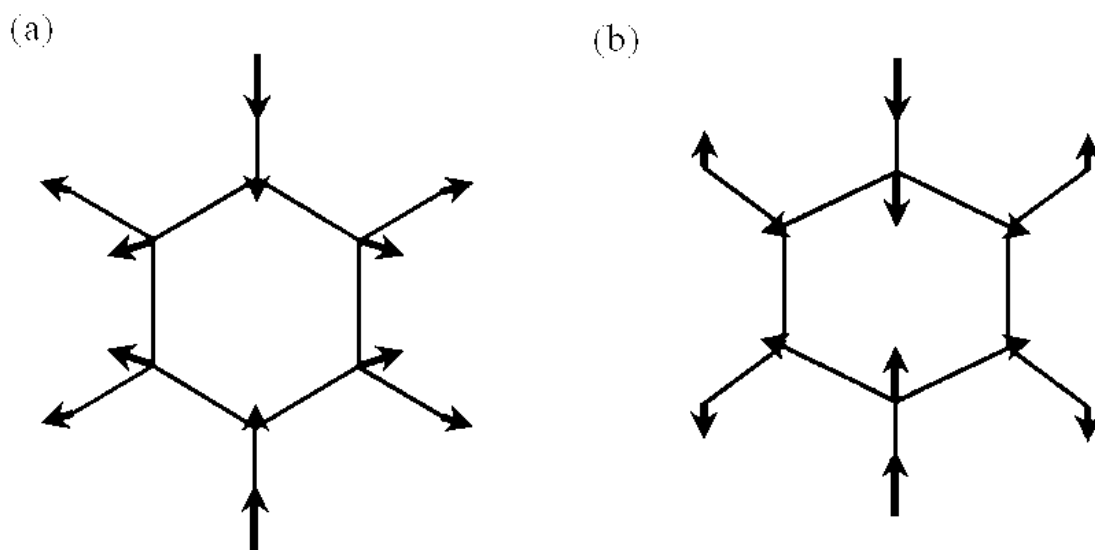


Figure 7(xvii): taken from Reference 22 (a) equilibrium geometry of neutral pDFB; arrows indicate atomic displacements upon ionisation magnified by 10 (b) equilibrium geometry of cationic pDFB; arrows indicate the eigenvector of ν_{6a} of the cation.

7.4.4 Unresolved $S_1(9b^1/16a^2)$ feature

A second set of spectra that requires some additional discussion are those recorded via the overlapped $9b^1/16a^2$ feature as shown in Figure 7(xvi). As noted above, ZEKE spectra were recorded at three positions within this feature: ZEKE spectra recorded through the low- and high-energy side of the unresolved band in S_1 were predominantly due to each of the separate vibrations; a spectrum recorded via the centre of the band was a combination of those two spectra. In the spectrum via $16a^2$ (trace II), the $\Delta\nu = 0$ band is the strongest. Contributions from other totally symmetric features, $16a^1$, $6a^1$, and $10b^2$ are present as expected although, interestingly, the origin is essentially absent from this spectrum. For the spectrum via $9b^1$ (trace I) the $\Delta\nu = 0$ feature is again the strongest, with the $9b^1 6a^1$ combination band also present. Somewhat unexpectedly, the totally symmetric contribution $16a^2$ (a ring twisting motion) is present in the $9b^1$ (C–F rock) spectrum, although other features associated

with excitation via $16a^2$ ($16a^1$, $6a^1$ and $10b^2$) are not. The latter are weak, even in the $16a^2$ spectrum so it is not surprising that they are not visible in the $9b^1$ spectrum. The appearance of the $16a^2$ peak in the $9b^1$ spectrum suggests that there is a small overlap between the S_1 $9b^1$ and $16a^2$ levels at position (I) in the overlapped feature. Even more unexpected was the fact that the weak origin seen in the spectrum recorded at (III) actually appears when exciting via $9b^1$ and not via the totally symmetric $16a^2$. It is not immediately clear why this should be, but is clearly another example of symmetry-forbidden features being observed.

7.4.5 Assignment of the 12^1 level

The third spectrum which requires further consideration is that recorded through $S_1(12^1)$, since this vibration has not been assigned previously (in the laser-induced fluorescence study of Okuyama *et al.*,¹ the ν_{12} vibrational energy is given in the ground state but not in the excited state). Assignments were made on the basis of the observation of dispersed fluorescence spectra, obtained by exciting the main vibronic bands. The dispersed fluorescence spectra were not presented in that work so it is not possible to explain why no assignment of the ν_{12} vibration in the S_1 state was made). In the REMPI spectrum, the band is seen at 793 cm^{-1} , with a comparable intensity to the close-lying ν_1 feature at 803 cm^{-1} . The intensity suggests that this feature has a_1 symmetry, since the a_1 symmetry of the vibration-less ground state dictates that totally symmetric S_1 features should dominate the REMPI spectrum. After considering a number of possible assignments, including combination bands and overtones, the symmetry requirements, and comparison with the calculated vibrational frequencies (see below), the S_1 feature at 793 cm^{-1} is assigned in this work as 12^1 .

ZEKE spectra were recorded though the 1^1 , 12^1 and $6a^2$ levels, which could be easily separated with the resolution of the current experiment – these levels are shown in the

insert in Figure 7(v). The ZEKE spectrum recorded through the $S_1(1^1)$ feature, contains a strong band at 834 cm^{-1} which is taken to be the $\Delta v = 0$ feature. For the 12^1 ZEKE spectrum shown in Figure 7(ix), two strong bands were observed, one with the same energy as the $\Delta v = 0$ feature in the 1^1 spectrum (the $D_0(1^1)$ level) and the other lying at lower energy, believed to be the $\Delta v = 0$ feature and therefore assigned as ν_{12} at 822 cm^{-1} . Based upon the calculated vibrational frequencies (see Table 7(I)), and on the spectra of other substituted benzenes (*p*-difluorobenzene^{5,21,22} and chlorobenzene²⁴) the ν_1 vibration lies to higher energy of the ν_{12} vibration and the assignment of the bands is consistent with this ordering. The symmetry of the ν_{12} vibration (a_1) is also consistent with the assignment of this band, since the ZEKE spectrum is dominated by totally symmetric bands. The S_1 features at 793 cm^{-1} and 803 cm^{-1} are therefore assigned to the ν_{12} and ν_1 vibrations respectively, with the corresponding cation vibrations at 822 cm^{-1} and 834 cm^{-1} .

The agreement between the experimentally-derived vibrational frequencies and the calculated ones is generally good, although there are two vibrations for which agreement is poor, one of which is ν_{12} (the experimental value is 822 cm^{-1} , the calculated values are 724 cm^{-1} and 731 cm^{-1}). This has been found to be the case in previous work on the substituted benzenes chlorobenzene²⁴ and *p*DFB,²¹ although no correlation can be found for the vibration for which the discrepancy arises. This assignment is considered to be reliable based upon the appearance of the ZEKE spectrum (the presence of the origin band suggests an S_1 level with a_1 symmetry) and the observation of the 1^1 and 12^1 levels in the spectra of other substituted benzenes. This is despite agreement with the calculated frequency being poor. This is believed to be the first time that the ν_{12} vibration has been assigned in the S_1 state.

7.5 Conclusions

Zero electron kinetic energy (ZEKE) spectroscopy has been employed to gain information on the vibrational energy levels of the *para*-fluorotoluene (*p*FT) cation. A total of thirteen vibrational levels in S_1 have been excited (these levels are 0^0 , 11^1 , 15^1 , the unresolved pair $16a^2$ and $9b^1$, $6a^1$, $6b^1$, 1^1 , $6a^2$, $18a^1$, 12^1 , 13^1 and $7a^1$), including non-totally symmetric levels, allowing the observation of a range of cationic vibrational frequencies. The assignment of these vibrational frequencies was achieved both from a knowledge of the S_1 vibrational states and also by comparison with density functional calculations. A total of fourteen fundamental vibrational frequencies in S_1 have been assigned with confidence, including the hitherto unassigned 12^1 level, as well as five overtone bands. The assignment of the ZEKE spectra confirm the assignments of the S_1 vibrations of Okuyama *et al.*¹ and most of the assignments made in this work are in agreement with those of Bellm *et al.*,⁵ although the precision is significantly better than the $\pm 20 \text{ cm}^{-1}$ error range cited in Reference 5. The assignments given herein were found to contradict those given in the MATI spectroscopic investigation of Georgiev *et al.*,⁴ and alternative assignments to those of Reference 4 are given, based upon the $\Delta v = 0$ rules and the theoretical results. The adiabatic ionisation energy of *p*FT was derived as $70946 \pm 4 \text{ cm}^{-1}$ and agrees well with previous work.

In the present work the dominance of the $6a$ mode was observed, the unresolved $9b^1$ and $16a^2$ levels in S_1 were probed, and the ν_{12} vibration was identified. The dominance of the $6a$ mode has been seen in previous work^{21,22} and can be rationalised by considering the overlap of the geometry change which occurs as a result of ionisation, with the motion associated with the $6a$ mode. During both ionisation and excitation of the $6a$ mode, the most significant geometry change is localised along the C_2 axis. The $\Delta v = 0$ propensity rule is evident in all but one of the ZEKE spectra presented herein.

In the $6a^2$ spectrum, the most intense feature is the $7a^1$ level. A progression in the $6a$ mode is seen, although the fundamental and the second overtone are both more intense than the $6a^2$ level. This may be due to distortion of the molecule along the $6a$ coordinate upon ionisation. The strength of the $7a^1$ feature implies that a coupling exists between the $6a$ and $7a$ modes, although the presence of IVR in the $S_1(7a^1)$ level and the fact that the $6a^1$ ZEKE spectrum did not extend to high enough energy to see the $7a^1$ feature means that this cannot be confirmed.

Owing to the high resolution of the ZEKE experiment, it was possible to unravel an overlapped feature ($9b^1/16a^2$) in S_1 by recording ZEKE spectra through different regions of the band in the REMPI spectrum. In the previous work of Georgiev *et al.*⁴ both vibrations were excited simultaneously, however the ZEKE spectrum was incorrectly attributed to just the $9b^1$ level. Additionally, in the REMPI-PES study of Bellm *et al.*⁵ it was not possible to excite these vibrations separately because of the limited resolution offered by the photoelectron spectroscopy experiment. By exciting through different energetic regions of the REMPI feature in the present work it was shown that the $16a^2$ vibration dominated the low-energy side of the REMPI feature and that the $9b^1$ vibration dominates the high-energy side. The central part of the REMPI peak contains contributions from both vibrations and the ZEKE spectrum is a convolution of the $16a^2$ and $9b^1$ ZEKE spectra.

In addition, the ν_{12} vibration has been identified for the first time in the ZEKE spectra and has therefore been assigned in the S_1 state. The intensity of the hitherto unassigned level in the S_1 state suggested that the feature had a_1 symmetry. The assignment was confirmed as 12^1 by an examination of the ZEKE spectrum obtained as a result of exciting this feature in the S_1 state. The ZEKE spectrum contained two strong bands, lying close in energy, one of which could be confidently assigned as $D_0(1^1)$. The remaining band (identified as the $\Delta\nu = 0$ peak) was assigned as 12^1 , based upon the

appearance of the 12^1 ZEKE spectrum and on the relative energies of the 1^1 and 12^1 bands seen in the S_0 and S_1 spectra of other substituted benzenes. This assignment is made with confidence, despite agreement between the calculated vibrational frequencies and the experimentally-derived values being poor.

7.6 References

- ¹ K. Okuyama, N. Mikami, M. Ito, *J. Phys. Chem.* **89** (1985) 5617.
- ² M.C.R. Cockett, K. Müller-Dethlefs, T.G. Wright, *Annu. Rep. Prog. Chem., Sect. C: Phys. Chem.* **94** (1998) 327.
- ³ Y. Hu, X. Wang, S. Yang, *Chem. Phys.* **290** (2003) 233.
- ⁴ S. Georgiev, T. Chakraborty, H.J. Neusser, *J. Phys. Chem. A*, **108** (2004) 3304.
- ⁵ S.M. Bellm, P.T. Whiteside, K.L. Reid, *J. Phys. Chem. A*, **107** (2003) 7373.
- ⁶ A.K. King, S.M. Bellm, C.J. Hammond, K.L. Reid, M. Towrie, P. Matousek, *Mol. Phys.* **103** (2005) 1821.
- ⁷ C.S. Parmenter, B.M. Stone, *J. Chem. Phys.* **84** (1986) 4710.
- ⁸ D.B. Moss, C.S. Parmenter, *J. Chem. Phys.* **98** (1993) 6897.
- ⁹ P.J. Timbers, C.S. Parmenter, D.B. Moss, *J. Chem. Phys.* **100** (1994) 1028.
- ¹⁰ Q. Ju, C.S. Parmenter, T.A. Stone, Z.-Q. Zhao, *Isr. J. Chem.* **37** (1997) 379.

- ¹¹ J.S. Baskin, T.S. Rose, A.H. Zewail, *J. Chem. Phys.* **88** (1988) 1458.
- ¹² G. Varsanyi, L. Lang, *Assignments for Vibrational Spectra of Seven Hundred Benzene Derivatives* (Wiley, New York, 1974), p. 668.
- ¹³ H. Thompson, R. Temple, *J. Chem. Soc.* (1948) 1432; K. Deb, *Indian J. Phys.* **36** (1962) 59; J. Green, *Spectrochim. Acta, Part A*, **26** (1970) 1503; E. Ferguson, R. Hudson, J. Nielsen, *J. Chem. Phys.* **21** (1953) 10; G. Joshi, N. Singh, *Spectrochim. Acta, Part A*, **23** (1967) 1341; J. Green, *Spectrochim. Acta, Part A*, **26** (1970) 1913.
- ¹⁴ R.C. Shiell, T.G. Wright, *Annu. Rep. Prog. Chem., Sect. C: Phys. Chem.* **98** (2002) 375.
- ¹⁵ K. Takazawa, M. Fujii, M. Ito, *J. Chem. Phys.* **99** (1993) 3205.
- ¹⁶ C.J. Hammond, V.L. Ayles, D.E. Bergeron, K.L. Reid, T.G. Wright, *J. Chem. Phys.* **125** (2006) 124308.
- ¹⁷ W.A. Chupka, *J. Chem. Phys.* **98** (1993) 4520.
- ¹⁸ S.G. Lias, P.J. Ausloos, *J. Am. Chem. Soc.* **100** (1978) 6027.
- ¹⁹ K. Watanabe, T. Nakayama, J. Mottl, *J. Quant. Spectrosc. Radiat. Transf.* **2** (1962) 369.
- ²⁰ X. Song, C.W. Wilkerson, J. Lucia, S. Pauls, J.P. Reilly, *Chem. Phys. Lett.* **174** (1990) 377.

²¹ G. Reiser, D. Rieger, T.G. Wright, K. Müller-Dethlefs, E.W. Schlag, *J. Phys. Chem.* **97** (1993) 4335.

²² C.H. Kwon, H.L. Kim, M.S. Kim, *J. Chem. Phys.* **118** (2003) 6327.

²³ R.S. Mulliken, *J. Chem. Phys.*, **23** (1955) 1997.

²⁴ T. G. Wright, S. I. Panov, T. A. Miller, *J. Chem. Phys.* **101** (1995) 4793.

8 *Electronic spectroscopy of para-fluorotoluene clusters*

8.1 *Introduction*

Non-covalent π - π interactions between two or more aromatic molecules play a prominent role that spans many areas of chemistry: from the relatively simple, *i.e.* the formation of non-covalently bound clusters in the gas phase; to the more complicated, for example, the interaction of neighbouring aromatic amino acids in a protein. Therefore, the characterisation of small non-covalently bound aromatic clusters is of interest to the wider chemical community.¹ For gas phase clusters, recent experimental and theoretical efforts have established that multiple conformers seem to be the norm.² The monomer, dimer and larger clusters of benzene have been extensively studied by both experiment^{3,4,5} and theory.^{6,7} The combined experimental and theoretical work to date suggests that the most favourable configurations are the perpendicular T-shaped and parallel-displaced (PD) geometries, with the eclipsed sandwich (S) configuration somewhat higher in energy. (These structures are shown in Figure 8(i) taken from Reference 6). The theoretical study of Sinnokrot *et al.*⁶ suggests that in a vacuum, the perpendicular T-shaped and parallel-displaced (PD) isomers are the most stable configurations of the benzene dimer, with the eclipsed sandwich structure being the least stable, although more recent work⁷ suggests that the parallel-displaced (PD) isomer is more stable than the T-shaped geometry. Controversy still surrounds the ground state minimum energy structure.

The ground state minimum energy structure⁸ of the toluene dimer^{1,9} is also still a matter of some debate. Spectroscopic measurements^{3,10} show that the toluene dimer consists of at least two isomers in the gas phase. The S_1 absorption spectrum of Schauer *et al.*³ was suggested¹¹ as being due to an isomer with a parallel structure (the lowest energy structure), two antiparallel structures (slightly higher in energy) and a

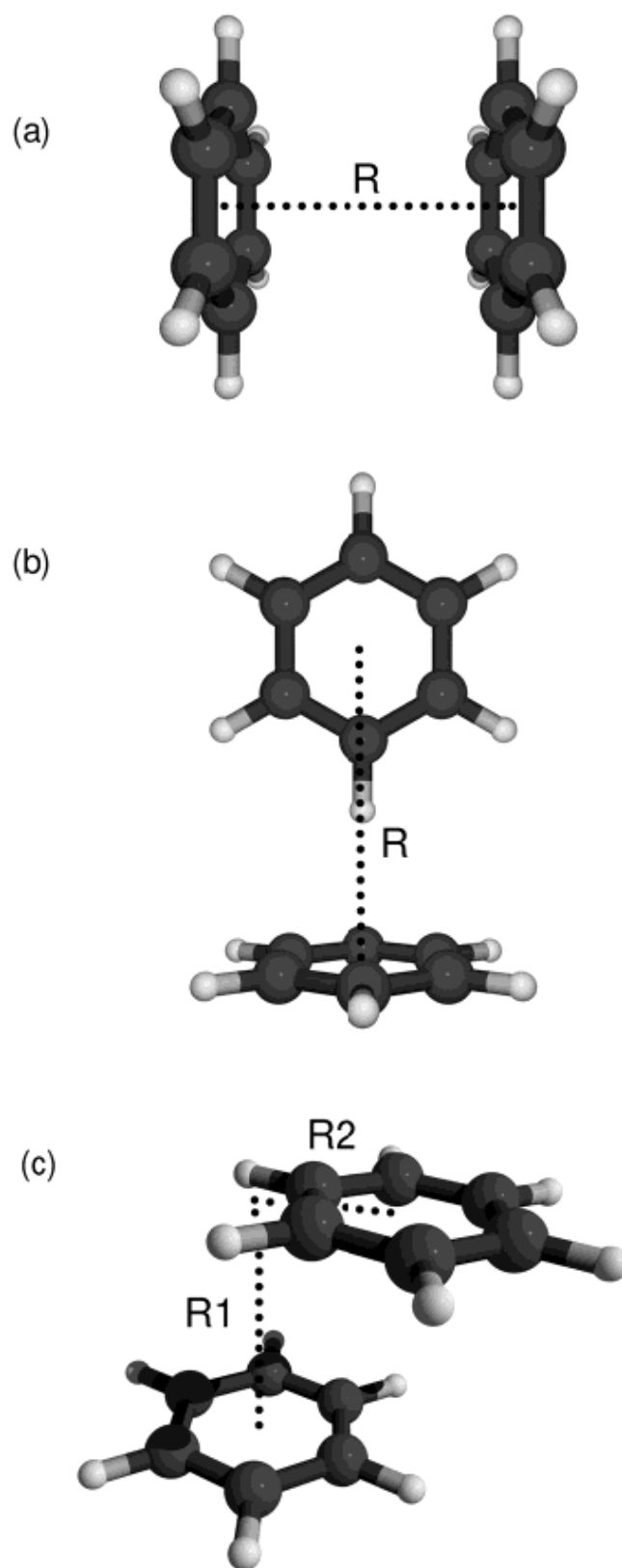


Figure 8(i) (a) sandwich; (b) T-shaped and (c) parallel-displaced configurations of the benzene dimer, taken from Reference 6.

T-shaped geometry (highest energy structure). The stability of the stacked isomers (parallel, antiparallel) over the T-shaped isomer was attributed to more favourable dispersion interactions in the former set and is in contrast to the energetic ordering of the isomers of the benzene dimer.

The controversy in determining the lowest energy structures of the benzene and toluene dimers persists in part due to the size of the molecules and in part because of a subtle balance between the different terms contributing to the interaction energy. For some substituted benzenes, the equilibrium structure is a compromise between the orientational demands of a hydrogen bond and the effects of π - π interactions (the phenol dimer is a good example of this).¹² Gas phase spectroscopic interrogation of (ro)vibronic structure remains an important avenue for structural and electronic characterization of aromatic dimers and larger clusters, giving the most detailed information and targets for high level *ab initio* calculations; in addition, such spectra are not complicated by the presence of solvent, hence providing information on the actual binding mechanism between the molecules within the complex. (It is possible to add in the effects of solvation later, and compare to the gas phase results to investigate the effect the solvent is having on energies of transitions, band intensities etc.)¹³ The understanding of excited states of clusters and complexes has ramifications in the design of organic dyes and molecular electronic components.

The first electronically-excited (S_1) state of the *para*-fluorotoluene (*p*FT) molecule has been the subject of a number of studies, the majority of which have focused directly or indirectly upon the methyl group, which may act to accelerate the rate of intramolecular vibrational redistribution (IVR) in the S_1 state.^{14,15,16,17} In the laser-induced fluorescence (LIF) spectroscopic study of Okuyama *et al.*¹⁸ assignments for the main vibronic bands were given. These assignments (see Chapter 7), together with the results of DFT calculations, were used to aid assignment of the (1 + 1) REMPI

spectrum of the S_1 state of *p*FT, shown in Figure 8(ii), obtained as part of the zero electron kinetic energy (ZEKE) study presented in Chapter 7.

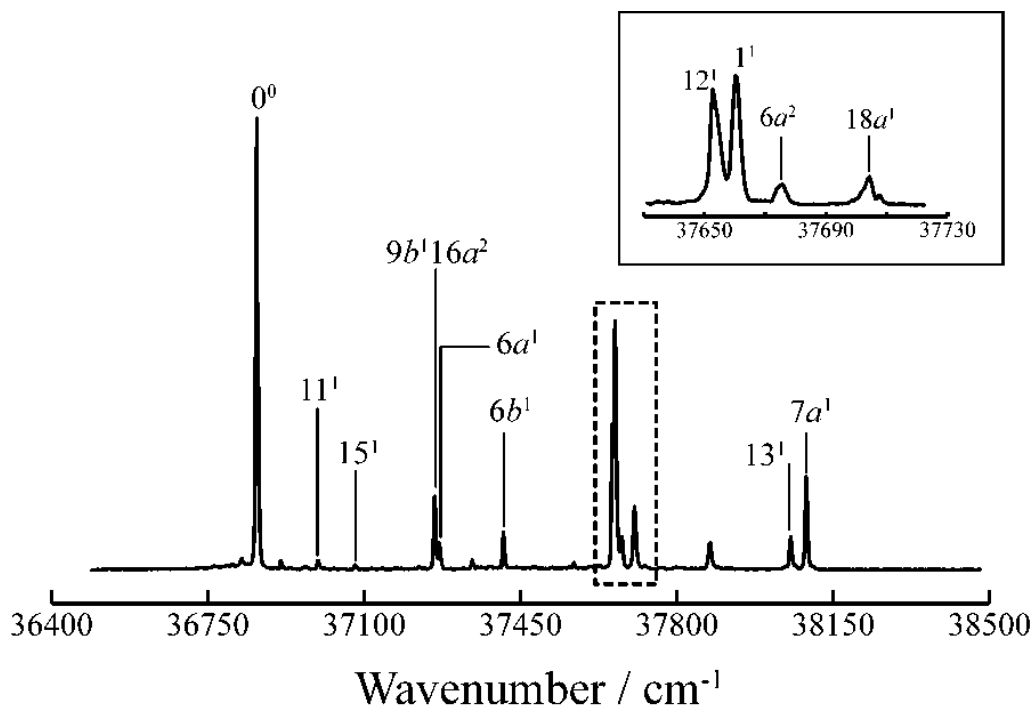


Figure 8(ii): $(1 + 1)$ REMPI spectrum of the S_1 state of *p*FT obtained during a previous study on the *p*FT cation (see Chapter 7). Assignments given in Wilson/Varsanyi notation.¹⁹

In this chapter, the first gas phase study of jet-cooled clusters of *para*-fluorotoluene in the S_1 state for the clusters $(p\text{FT})_n$ ($n = 1-11$) is presented. The appearance of the spectra as n increases is discussed, and the effects of fragmentation are addressed.

8.2 Experiment

The REMPI spectrometer has been described in detail in Chapter 2. For the experiment described herein, Ar held at ~ 5 bar was bubbled through a liquid sample of

p FT and the resultant mixture was expanded into a vacuum chamber via a pulsed valve. The resulting jet expansion was intersected in the extraction region of a time-of-flight mass spectrometer by the UV pulses from a frequency-doubled tuneable dye laser. The dye used was Coumarin 153, yielding a frequency-doubled emission peak at ~ 268 nm. Peaks in the mass spectrum were monitored on an oscilloscope and averaged with a boxcar integrator, before being sent to a PC for recording and analysis. No special efforts were required to achieve good clustering, and no significant attempts to control or alter the concentration of p FT in the expanding gas were necessary. For the smaller clusters, where the spectra were recorded towards the onset of the free-jet expansion, it is likely that the rotational temperature is < 5 K (consistent with previous work on NO); for the larger clusters, which were probed further back in the expansion, it is difficult to be precise about the temperature, but somewhere around 20 K would be representative, based on previous experience with the apparatus. Laser pulse energies were 1–3 mJ, with the higher values being used for the weaker spectra of the larger clusters.

8.3 *Results and discussion*

8.3.1 *Fragmentation*

The production of larger p FT_{*n*} clusters was found to be extremely sensitive to the delay between the pulsed valve and the laser pulse, and the intensity of the laser. Mass spectra recorded at varying delays and with a range of laser intensities are shown in Figures 8(iii) and 8(iv) respectively.

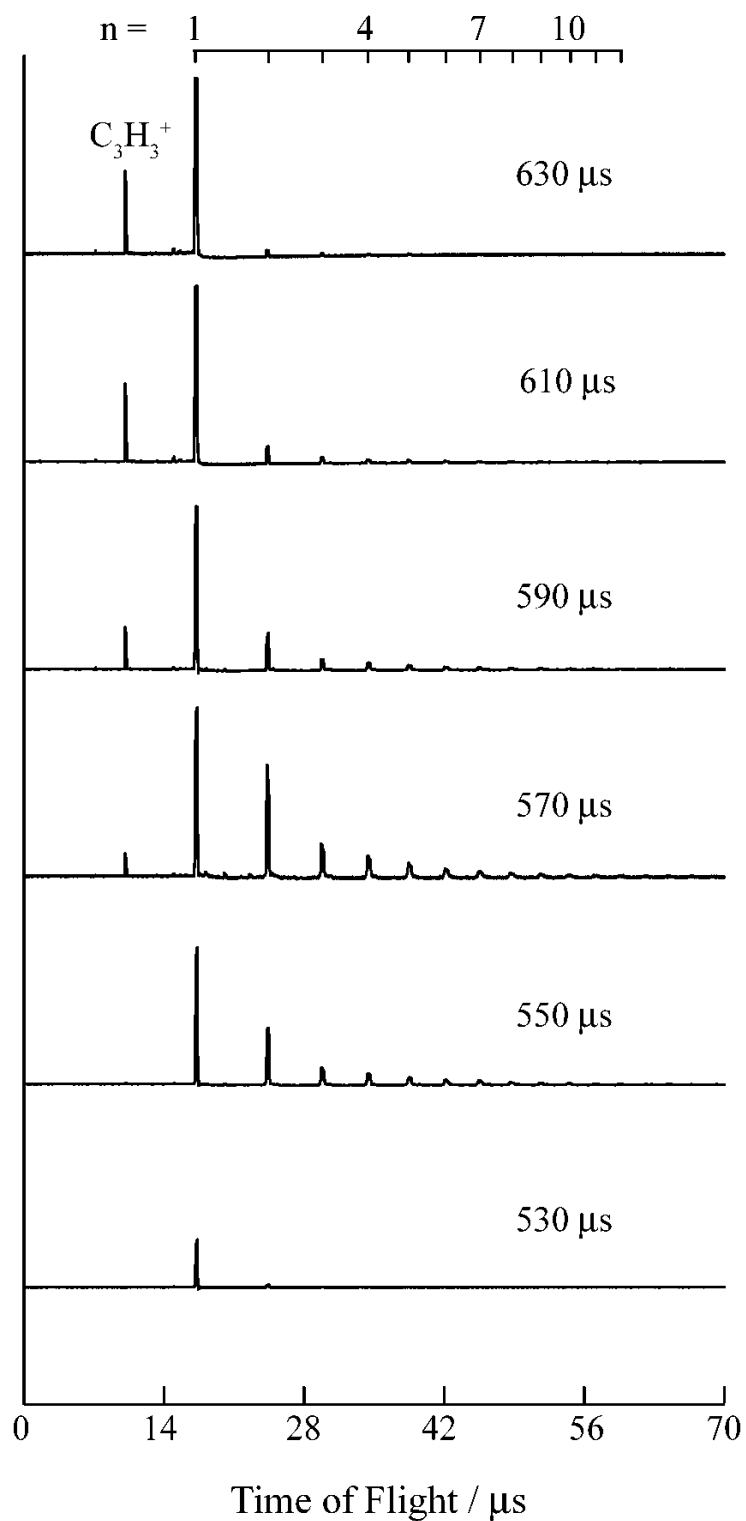


Figure 8(iii): mass spectra acquired at increasing delay between firing of the pulsed valve and firing of the laser (all other parameters remain constant). Optimal clustering conditions were found at a delay of 570 μs , where clusters up to pFT_{16} are observed (marked up to $n = 12$ in the comb).

As can be seen in Figure 8(iii), the formation of larger clusters becomes more favourable as the delay between opening of the pulsed valve and the production of laser light is increased *i.e.* as a warmer portion of the free-jet expansion is probed; (1 + 1) REMPI spectra of the larger clusters were collected by sampling a warmer part of the free-jet expansion than for the *p*FT monomer (this is discussed further in Section 8.3.2). To generate a free-jet expansion the pulsed valve was open for 230 μ s. If the collision rate varies during this time then different regions of the free-jet expansion will correspond to different internal molecular temperatures. By increasing the delay between opening the pulsed valve and firing the laser, a later portion of the expansion can be probed. Based on previous work on NO-Rg where an increased delay led to an increasing contribution from vibrational hotbands in the Rydberg state spectra, it is reasonable to conclude that at a longer delay (*i.e.* probing further into the expansion and not at the onset), the internal temperatures of the complexes are higher, resulting from a drop in the collision rate. At a delay of 570 μ s, the formation of larger clusters was favoured, with clusters of up to (*p*FT)₁₆ being observed. As the pulsed valve/laser pulse delay was increased further (up to a maximum of 630 μ s), larger clusters were no longer observed in the mass spectrum. As the delay is increased from 570 μ s to 630 μ s, and warmer parts of the free-jet expansion are probed, the relative intensity of the monomer:dimer signals changes; the monomer signal intensity increases relative to that of the dimer and larger clusters. The clusters sampled in a warmer part of the free-jet expansion will have an increased internal energy, owing to less efficient collisional cooling as they pass through (and just beyond) the nozzle aperture, thus increasing the probability of fragmentation. The relative increase of the monomer signal intensity suggests that this fragmentation involves the loss of a whole *p*FT molecule.

As well as less efficient collisional cooling, it is also possible that the absorption of multiple photons is increasing the internal energy of the clusters and leading to

fragmentation. The strong dependence of the $(pFT)_n$ cluster ion distribution on the laser intensity can be seen in Figure 8(iv)(a).

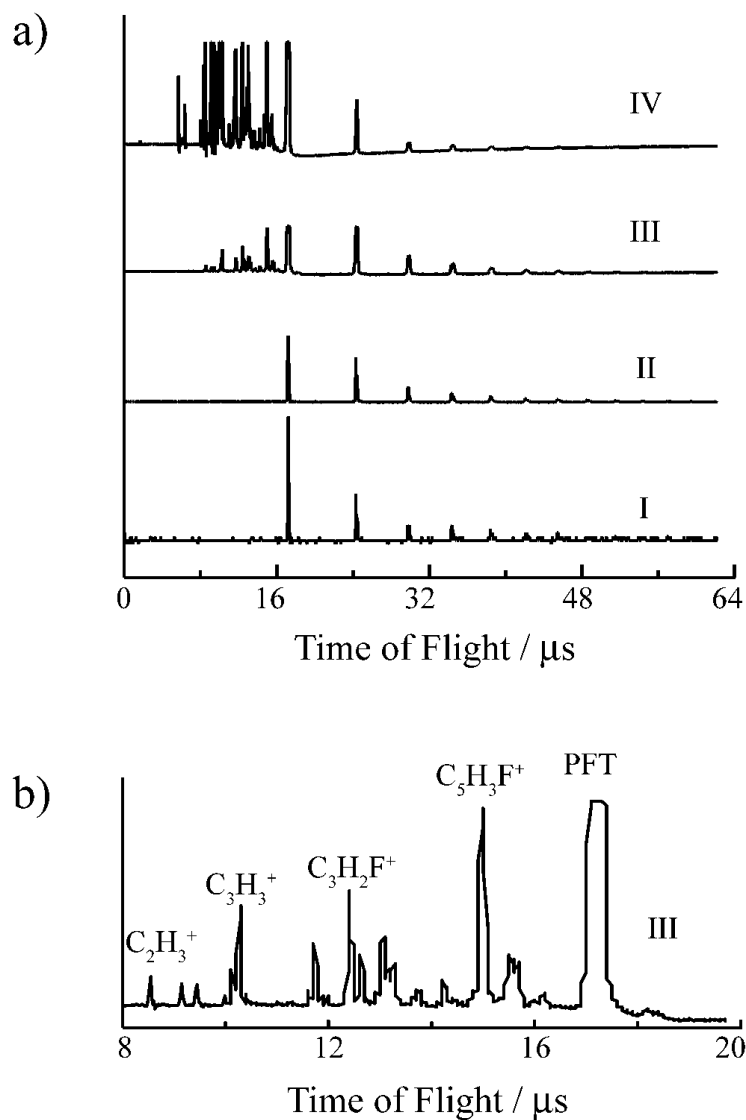


Figure 8(iv): (a) mass spectra collected at increasing laser power I–IV; each scan is normalised to the dimer signal and averaged over 100 shots – monomer and fragment ion peaks go off scale in traces III and IV. (b) fragmentation pattern in the low-mass region of trace III, showing main peaks arising from fragmentation of the monomer. The unusual shape of some peaks is due to the digitisation of these spectra.

The weaker signals from the clusters necessitates the use of higher laser powers and as can be seen in Figure 8(iv)(a), this leads rapidly to a competition between the appearance of the larger cluster ions and the appearance of fragment ions. The lowest laser power (trace I) was selected by minimising the cluster ion signals in the mass spectrum; the highest laser power (trace IV) was selected by observing the ion signal of the fragments – the ion signals were maximised whilst ensuring that the signals did not overload the detector. Traces II and III were recorded with two laser powers between these extremes. As the laser intensity is increased between traces I (lowest power), and II, there is a slight increase in signal intensity of the larger clusters. The signals from the larger clusters are then seen to decrease as the laser power is increased further. This is evidence of cluster fragmentation, arising from the higher internal energy of the $(pFT)_n$ complexes afforded by the increased photon density. In the low-mass region, fragments of the pFT monomer occur at the higher laser energies (traces III and IV): these are labelled in Figure 8(iv)(b), which is an expansion of trace III. At even higher laser powers (trace IV) the atomic ion, C^+ may be seen. The fragment $C_3H_3^+$ can be seen with increasing intensity as the laser power is increased (and also when the pulsed valve/laser delay was increased). Squire *et al.*²⁰ have also seen the formation of this fragment in work on toluene clusters. In that work, the origin of this fragment was attributed to the $C_7H_7^+$ cation. This ion exists in two forms of near equal energy, the six-membered ring tolyl (methylenebenzene) cation and the seven-membered ring (cycloheptatrienyl) cation, and the $C_3H_3^+$ fragment is considered to arise from the latter. Squire *et al.*²⁰ proposed that the $C_7H_7^+$ ion originates from fragmentation of the dimer, which first loses a hydrogen atom and then dissociates to give $C_7H_7^+$ and C_7H_8 . In the present work, this fragmentation becomes more probable as the laser power is increased and multiphoton absorption becomes more likely. The appearance of this fragment in the mass spectra collected whilst varying the pulsed valve/laser pulse delay suggests that the fragmentation pathway that leads to this daughter ion becomes more favourable as the delay (and hence the internal energy of

the clusters) increases. In the higher mass region, the spectra are simpler, with no obvious sign of fragment ions between n and $n + 1$, for $n \geq 1$ *i.e.* fragmentation channels in which a cluster loses only part of a *p*FT molecule are not observed. As the clusters are presumably bound primarily by van der Waals interactions, loss of an intact *p*FT molecule is expected to be the predominant fragmentation pathway, owing to the intermolecular bonds being the weakest. Squire and Bernstein²⁰ have described the fragmentation of small ($n = 1-4$) toluene clusters when subjected to multiphoton ionisation, and the fragmentation patterns observed in the present work agree well with theirs, with the exception of fluorine-containing ions appearing in the present study.

8.3.2 Spectroscopy

There have been a number of reports of electronic spectra of substituted benzene dimers and trimers,^{3,10,21,22,23,24} although analysis of such spectra has been brief owing to their complexity and the fact that much of the effort has revolved around identifying the presence of isomers. In the following, the spectrum of the van der Waals dimer is presented initially and an assignment of the features present is suggested. Additionally, the overall trends observed in the electronic spectra for the larger clusters are discussed.

8.3.2.1 Structure in the dimer spectrum

Fragmentation of the larger complexes, caused by increasing laser intensity has been discussed above. The fragmentation of larger clusters observed in the mass spectrum discussed previously would be expected to lead to the observation of the $(pFT)_{n+1}$ spectrum appearing in the spectrum recorded via the $(pFT)_n$ mass channel. Reasonable $(pFT)_2^+$ ion signals were obtained at laser intensities which were low enough to

prevent substantial fragmentation, and the (1 + 1) REMPI spectrum of the monomer, presented in the lower trace of Figure 8(v), is free of features attributable to the simultaneously-monitored dimer mass channel. Several attempts were made to record a dimer spectrum with resolved intermolecular structure, although the structure was not reproducible. Despite features being observed which were suggestive of vibrational modes associated with the dimer, their appearance was found to vary significantly from scan to scan. This variation may arise as a result of internal temperature changes (associated with probing different portions of the free-jet expansion), or with the dimer spectra containing contributions from the trimer as a result of photofragmentation, or from the presence of more than one isomer. It was not possible to record the intermolecular structure consistently, despite varying the pulsed valve/laser pulse delay and the laser intensity over a wide range of conditions (varying the pressure of Ar gas and the volume of *p*FT in the free-jet expansion, for example) therefore this structure will not be discussed here. The position and overall shape of the major bands in the dimer spectrum did not change with laser power, however. A spectrum of the (*p*FT)₂ complex obtained with a high laser power to give a good signal-to-noise ratio, although with reduced structure, is presented in the upper trace of Figure 8(v). Also shown in Figure 8(v) is the (1 + 1) REMPI spectrum of the *p*FT monomer. An expanded view of the higher energy region of both spectra is shown, together with the assignment of some of the features in the monomer spectrum.

The features seen in the monomer spectrum have been assigned in Figure 8(v) based upon the assignments of Okuyama *et al.*¹⁸ using the Wilson/Varsanyi¹⁹ nomenclature for the vibrational modes. The weak features lying to the red of the monomer origin (0^0) band are vibrational hotbands, which can be eliminated by further cooling *i.e.* probing a colder portion of the free-jet expansion. The vibrational levels seen in the (1 + 1) REMPI spectrum of *p*FT are discussed in detail in Chapter 7 and will not be discussed further herein. An assignment of the major bands in the dimer spectrum can

be achieved by comparing the $(pFT)_2$ spectrum (upper trace in Figure 8(v)) with that of the monomer (lower trace in Figure 8(v)).

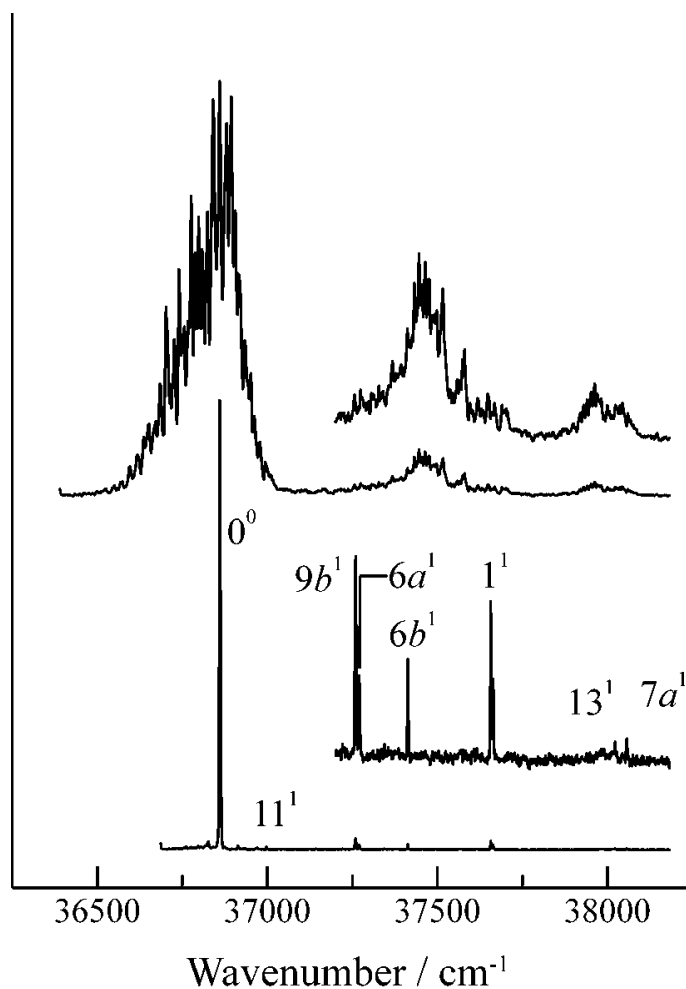


Figure 8(v): $(1 + 1)$ REMPI spectra of pFT and $(pFT)_2$ with expanded views of the higher energy regions – factors of $\times 3$ and $\times 5$ for pFT and $(pFT)_2$ respectively. Each spectrum has been normalised to the most intense feature.

The first band at ~ 36800 cm⁻¹ corresponds to the origin of the dimer and appears redshifted relative to the monomer origin band. The origin band in the dimer spectrum is also significantly broader than in the monomer spectrum and this broadening is more apparent on the low energy side of the peak. Assuming that the structure of the second band, at ~ 37400 cm⁻¹ will evolve in a similar fashion, then it is difficult to

determine which feature from the monomer spectrum might give rise to this band. The $9b^1$ level (CF rock) or the $6a^1$ level (symmetric ring-breathing mode) may correspond to this band, although these features would be significantly blueshifted; this blueshift may arise if these motions are sterically hindered in the dimer. This is not what is seen for the origin band, or indeed for all the assigned features in the toluene dimer spectrum²¹ where a redshift is observed. The most likely candidate in the monomer spectrum is the $6b^1$ peak (ring bend), which lies closest in energy and experiences a smaller blueshift upon complexation.

There is a weaker feature to the blue of this dimer band at $\sim 37600\text{ cm}^{-1}$ which is tentatively assigned to the redshifted 1^1 ring-breathing vibration. Additional features in this region may be attributable to intermolecular structure, or may be associated with $(pFT)_3$ and appear as a result of fragmentation of the trimer. Similarly, there are very weak features lying to the red of the $6b^1$ dimer band. These may be due to dramatically weakened $9b^1$ and $6a^1$ features. The two features lying at $\sim 38000\text{ cm}^{-1}$ are attributed to the 13^1 (C-CH₃ stretch) and $7a^1$ (C-F stretch) features, with the latter to higher energy.

8.3.2.2 Trends for pFT_n

(1 + 1) REMPI spectra collected in the mass channels corresponding to the $(pFT)_n$ ($n = 1-11$) series are shown in Figure 8(vi). As discussed previously, the pulsed valve/laser pulse delay and laser intensity can be optimised to give spectra where the intensity of vibrational hotbands and fragmentation effects are minimised. However, the comparatively weak ion signals seen for the larger clusters result in a poor signal-to-noise ratio. In addition, it is possible that the geometry change in the larger clusters as a result of ionisation is significant, leading to a poor overlap between the (neutral) S_1 and (ionic) D_0 wavefunctions and the higher laser powers are necessary to "force" a

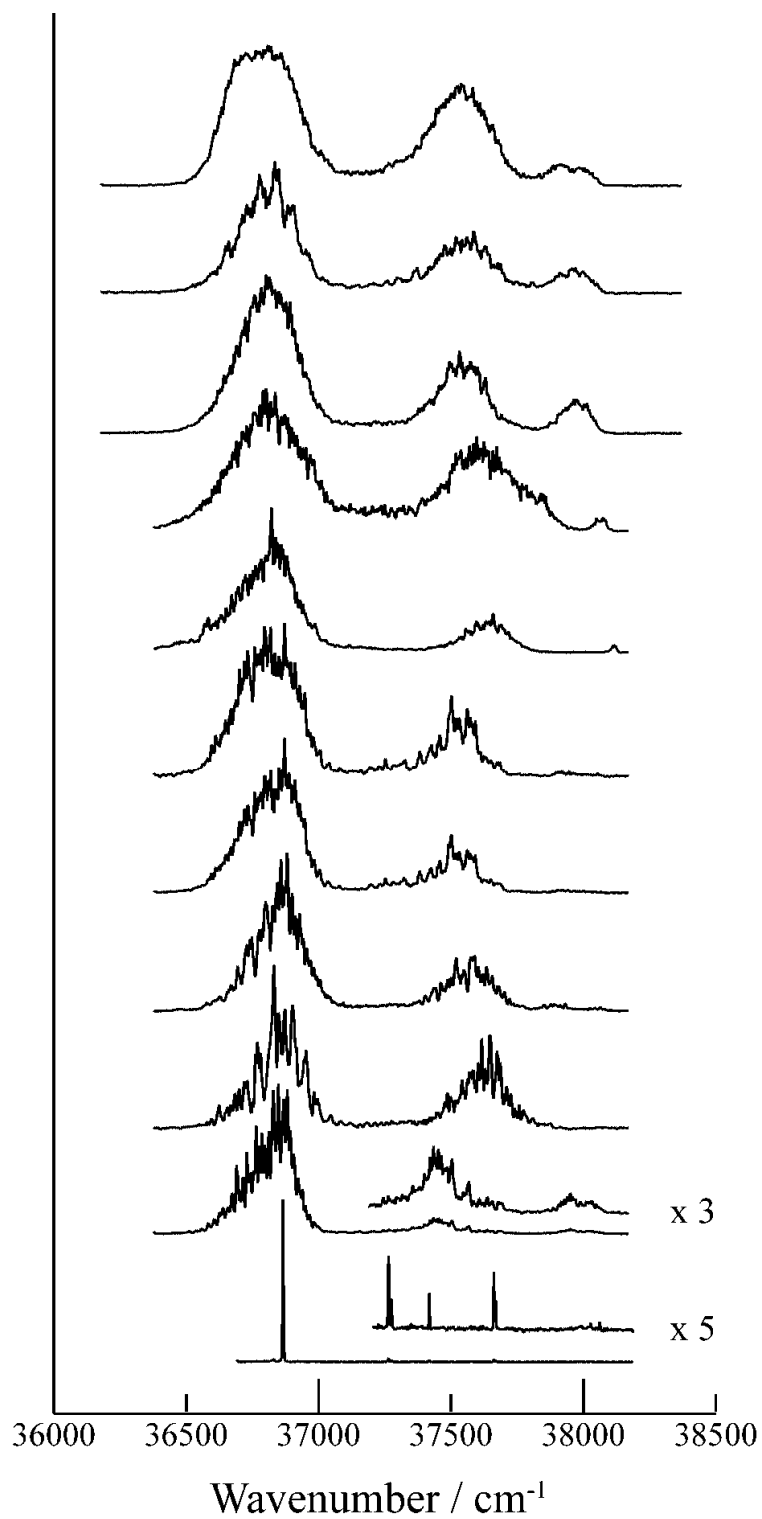


Figure 8(vi): $(1 + 1)$ REMPI spectra for $(pFT)_n$ ($n = 1-11$), each normalised to the most intense feature. The monomer spectrum is shown at the bottom, the $(pFT)_{11}$ spectrum is at the top. For the monomer and dimer, the blue region is magnified for clarity.

transition. Thus, it is possible that the spectra of the heavier clusters contain contributions from even higher species, since greater laser intensities are needed to produce spectra with an adequate signal-to-noise ratio. The spectra shown in Figure 8(vi) have been collected using a laser intensity that is high enough to give an improved signal-to-noise ratio, whilst minimising the effects of fragmentation.

With increasing cluster size, the onset of the origin band (at $\sim 36800\text{ cm}^{-1}$ in the monomer spectrum) becomes increasingly redshifted, suggesting that the clusters are more strongly bound in the S_1 state than in the ground state. In addition, the origin feature becomes broader: for the lower values of n , the broadening occurs primarily on the red edge of the band. As n increases, it seems that there is also some broadening to the blue. This broadening may result from the presence of a number of isomers, each with a unique S_1 origin transition and intermolecular vibrational structure.

As with the origin feature, the second band (at $\sim 37400\text{ cm}^{-1}$ in the monomer spectrum) appears to broaden with increasing cluster size, although it is not clear whether this broadening is more pronounced on the low- or high-energy side of the band. The observed shift for this band is significantly more pronounced than for the origin band. The band energy appears to become blueshifted from $n = 1$ to $n = 2$. The band then shifts significantly to the blue on going from the dimer to the trimer. This is followed by a gradual redshift until $(pFT)_7$, at which point another blueshift seems to occur. Thereafter, the redshifting trend resumes for the size range considered here.

The third band (at $\sim 38000\text{ cm}^{-1}$ in the monomer spectrum), like the second, appears to shift gradually to the red with increasing cluster size. In this case, no discontinuity appears going from $n = 1$ to $n = 2$ but does occur from $n = 2$ to $n = 3$, but a discontinuity does occur again at $n = 7$, although here it is difficult to discern whether the third band might merge with the second (and a new fourth band appears in the

(*p*FT)₇ spectrum), or whether another dramatic jump to the blue has occurred. Assuming the latter, from $n = 7$ to $n = 11$, the gradual redshifting resumes.

These shifts seen for the second and third bands reflect the change in the internal energies associated with these vibrational modes; the blueshift seen for these bands in the dimer, trimer and for *p*FT₇ may indicate the steric hinderance of these modes. The overall similarity of the cluster spectra to that of the dimer points to a dimer core. This suggests that the other *p*FT molecules do not affect the spectroscopy of the cluster appreciably, and perhaps that they are weakly-bound. The same conclusion was reached in a previous study of toluene clusters.²¹

The dramatic change in the appearance of the spectra between $n = 1$ and $n = 2$ suggests that the intensity associated with particular vibronic bands changes markedly between the monomer and the dimer. The fact that the appearance of the bands changes very little with increasing cluster size, suggest that these changes seem to carry through to the higher complexes. Kelley²⁵ has described large changes in intensities in electronic absorption spectroscopy upon dimerisation: briefly, coupling between the electronic transition dipoles on neighbouring molecules will split the electronic transitions into a broad band of states with a range of band intensities. The vibronic mode-specific changes in intensity seen in this work are not unexpected, since the vibrations will be affected to differing extents by complexation. The onset of the origin (0^0) band is seen to shift to lower energy as the cluster size increases. The energy of the $6b^1$ band (at $\sim 37400\text{ cm}^{-1}$ in the monomer spectrum) shifts to the blue in the dimer and the trimer spectra, then to the red with increasing cluster size. Thus, as well as the band intensity variation, there are also significant shifts in the energies of particular vibronic bands.

8.3.3 Structural considerations

For species with a donor and an acceptor substituent in the *para* positions ('push-pull' configurations), there are a number of dimer geometries, two of which have been described by Kelley.²⁵ These are shown in Figure 8(vii).

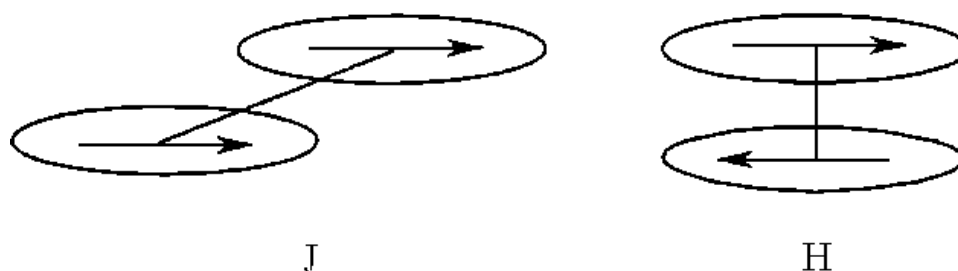


Figure 8(vii): *J- and H-type dimer geometries for species with a donor and acceptor substituent in the para positions, adapted from Figure 1 in Reference 25.*

In the J-type dimer configuration, the molecules are parallel stacked, but offset in such a way that the donor and acceptor substituents can interact. In the H-type dimer configuration, an antiparallel stacked structure allows the donor and acceptor substituents to interact, although a repulsive π - π interaction is likely when stacking the aromatic rings uniformly. In systems with strong hydrogen bonding, the J-type dimer is thought to be favoured.²⁵ The REMPI spectrum of the *p*FT dimer presented here does not provide much insight as to which isomer(s) might be present, although the presence of the strongly electronegative F atom (which can lead to the possibility of pseudo hydrogen bonding between the F atom on one molecule, and the methyl group on the other) perhaps suggests that, for the dimer, a J-type staggered parallel-stacked structure is favoured. Additionally, the redshift of the origin band in the dimer spectrum, relative to that in the monomer spectrum is indicative of a J-type geometry.²⁵ However, the large dipole for *p*FT (2.76 D calculated at the MP2/6-31+G*

level of theory by T. G. Wright), suggests that the antiparallel H-type structure must be considered. Finally, a major contribution from T-shaped isomers is not expected since the results of *ab initio* calculations on the toluene dimer¹ found the T-shaped geometry to be less stable than the parallel- or antiparallel-stacked conformations. Additionally, destabilisation of the T-shaped configuration interaction, induced by the presence of the fluorine atom, has been addressed by Riley and Merz.²⁶

8.4 Conclusions

Clusters of *para*-fluorotoluene have been prepared in a free-jet expansion and studied spectroscopically. Clusters containing up to sixteen *p*FT molecules were identified in the mass spectrum and the effects of both the pulsed valve/laser pulse delay and the laser intensity, on the cluster ion distribution were observed. Increasing the delay between opening the pulsed valve and firing the laser, *i.e.* probing increasingly warmer portions of the free-jet expansion, led to the observation of larger clusters. Additional increases in the delay however, led to the larger cluster ion signals decreasing. This is likely to arise from fragmentation of the larger clusters as a consequence of probing a portion of the free-jet expansion where the collisional cooling is less efficient (the clusters will have an increased internal energy). An increasing laser intensity, although necessary to collect spectra of the larger clusters with favourable signal-to-noise, led to photofragmentation. At a higher laser intensity, the fragments $C_2H_3^+$, $C_3H_3^+$ and $C_3H_2F^+$, as well as the atomic fragment C^+ , were observed.

(1 + 1) REMPI spectra for $(pFT)_n$ ($n = 1-11$) clusters have been presented. Although structure was apparent in the dimer spectrum, it was not reproducible and therefore no analysis has been attempted. Comparison of the high-quality monomer *p*FT spectrum with that of the dimer allowed tentative assignments of the observed vibronic bands.

Assignment of these features is complicated by changes in the band intensities and by the energetic shifts of these bands. The redshift in the onset of the origin (0^0) band indicates that the clusters are more strongly bound in the S_1 excited state, whilst the blueshift of some of the vibrational modes is indicative of steric hinderance of these modes, resulting from the complexation of one or more *p*FT molecules to the *p*FT chromophore. (1 + 1) REMPI spectra of clusters up to (*p*FT)₁₁ were collected, although in order to produce spectra with the best possible signal-to-noise ratio and with minimal fragmentation effects, a relatively high laser intensity was required. It is possible therefore, that the spectra of the larger complexes may be contaminated by fragmentation. The appearance of the bands in the spectra changed little beyond the dimer (*p*FT)₂, suggesting that the electronic spectroscopy of *p*FT complexes is largely determined by the (*p*FT)₂ species.

8.5 References

- ¹ D.M. Rogers, J.D. Hirst, E.P.F. Lee, T.G. Wright, *Chem. Phys. Lett.* **427** (2006) 410.
- ² S. Sun, E.R. Bernstein, *J. Phys. Chem.* **100** (1996) 13348.
- ³ K.S. Law, M. Schauer, E.R. Bernstein, *J. Chem. Phys.* **81** (1984) 4871.
- ⁴ P.R.R Langridge-Smith, D.V. Brumbaugh, C.A. Haynam, D.H. Levy, *J. Phys. Chem.* **85** (1981) 3742.
- ⁵ J. B. Hopkins, D.E. Powers, R.E. Smalley, *J. Phys. Chem.* **85** (1981) 3739.
- ⁶ M.O. Sinnokrot, E.F. Valeev, C.D. Sherrill, *J. Am. Chem. Soc.* **124** (2002) 10887.

- ⁷ Y.C. Park, J.S. Lee, *J. Phys. Chem. A*, **110** (2006) 5091.
- ⁸ A.L. Ringer, M.O. Sinnokrot, R.P. Lively, C.D. Sherrill, *Chem. Eur. J.* **12** (2006) 3821.
- ⁹ S. Tsuzuki, K. Honda, T. Uchimaru, M. Mikami, *J. Chem. Phys.* **122** (2005) 144323.
- ¹⁰ S. Ishikawa, T. Ebata, H. Ishikawa, T. Inoue, N. Mikami, *J. Phys. Chem.* **100** (1996) 10531.
- ¹¹ M. Schauer, E.R. Bernstein, *J. Chem. Phys.* **82** (1985) 3722.
- ¹² L.L. Connell, S.M. Ohline, P.W. Joireman, T.C. Corcoran, P.M. Felker, *J. Chem. Phys.* **96** (1992) 2585.
- ¹³ R. Chelli, F.L. Gervasio, P. Procacci, V. Schettino, *J. Am. Chem. Soc.* **124** (2002) 6133.
- ¹⁴ C.S. Parmenter, B.M. Stone, *J. Chem. Phys.* **84** (1986) 4710.
- ¹⁵ D.B. Moss, C. S. Parmenter, *J. Chem. Phys.* **98** (1993) 6897.
- ¹⁶ J.S. Baskin, T.S. Rose, A.H. Zewail, *J. Chem. Phys.* **88** (1988) 1458.
- ¹⁷ P.J. Timbers, C.S. Parmenter, D.B. Moss, *J. Chem. Phys.* **100** (1994) 1028.
- ¹⁸ K. Okuyama, N. Mikami, M. Ito, *J. Phys. Chem.* **89** (1985) 5617.

- ¹⁹ G. Varsanyi, L. Lang, *Assignments for Vibrational Spectra of Seven Hundred Benzene Derivatives* (Wiley, New York, 1974), p. 668.
- ²⁰ D.W. Squire, R.B. Bernstein, *J. Phys. Chem.* **88** (1984) 4944.
- ²¹ A. Musgrave, T.G. Wright, *J. Chem. Phys.* **122** (2005) 074312.
- ²² W. Lu, Y. Hu, Z. Lin, S. Yang, *J. Chem. Phys.* **104** (1996) 8843.
- ²³ K. Rademann, B. Brutschy, H. Baumgärtel, *Chem. Phys.* **80** (1983) 129.
- ²⁴ J.-H. Yeh, T.-L. Shen, D.G. Nocera, G.E. Leroi, I. Suzuka, H. Ozawa, Y. Namuta, *J. Phys. Chem.* **100** (1996) 4385.
- ²⁵ A.M. Kelley, *J. Chem. Phys.* **119** (2003) 3320.
- ²⁶ K.E. Riley, K.M. Merz, *J. Phys. Chem. B* **109** (2005) 17756.

9 *A simple model potential analysis of the bonding in alkali metal cation/Rg complexes (Rg = He–Xe) and Au⁺–Rg complexes (Rg = Ne, Ar, Kr, and Xe)*

9.1 *Introduction*

Solvation of singly-charged atomic metal ions M^+ is important in many areas, ranging from basic inorganic chemistry to biochemistry. The simplest interaction of M^+ with one ligand in the gas phase, is easiest to study both experimentally and theoretically, and the simplest "ligands" are rare gas (Rg) atoms. Potentials for such M^+ /Rg diatomic interactions are also important for understanding the ion transport properties of M^+ ions in many applications, for example plasma discharges. There is now an extensive set of reliable *ab initio* and experimental data for the potential curves of M^+ /Rg diatomic complexes,^{1,2,3,4,5,6,7,8,9,10,11,12} resulting in bond strengths, bond lengths and vibrational frequencies (an overview of work up to 2001 is given in Reference 1). There has been controversy in the past about whether the bonding in some M^+ /Rg complexes,^{1,13,14,15} especially those of transition-metal ions with Kr and Xe, is entirely "physical" *i.e.*, the attractive forces are due only to the leading, strong, $1/R^4$ -dependent ion-induced dipole term (plus other induction and dispersion attractive terms dependent on $1/R^6$, $1/R^7$, $1/R^8$, etc.),¹ or whether there is a "chemical" component due to Lewis acid/base covalent interactions, as the Rg atom begins to function as a "ligand" at shorter distances and thus binds in a classical coordinate-covalent manner with the M^+ ions. Breckenridge and coworkers^{1,6,7} have shown previously that using an entirely "physical" model potential, in which terms out to $1/R^8$ are properly included, almost all cases of M^+ /Rg bonding could be rationalized qualitatively by "physical" interactions, with no extra "chemical" bonding required.¹ However, there were a few exceptions,¹ notably the strongly-bound Au^+ –Xe complex,¹ for which a quite high-level *ab initio* relativistic potential curve had been calculated by Pyykkö and coworkers.¹⁵ It was tentatively concluded¹ that the Xe atom may have substantial extra

"chemical" attraction for the Au^+ ion which cannot be accounted for by simple "physical" bonding alone, as originally suggested by Pyykkö *et al.*^{13,15}

The filled-shell/filled-shell interaction of the alkali metal ions (Alk^+) with the atoms is the most likely case for a purely "physical" interaction (charge transfer from Alk^+ to the Rg atom is expected to be very small since the Rg ionisation energies are all significantly higher than those of the alkali metal atoms). Interactions in the Alk^+/Rg complexes have been analysed using the model potential analysis of Breckenridge and coworkers, using the spectroscopic constants (R_e , D_e and ω_e) derived from very high-level *ab initio* calculations of all 36 of the Alk^+/Rg potential curves,^{8,9,10,11,12} performed by T. G. Wright and others. The conclusion from the present study is that the interactions in all of these cases are indeed essentially "physical" in nature, but that the Breckenridge model potential cannot account quantitatively for all the effects in such bonding interactions. Interestingly the effective charge on the metal atom from such model potential calculations is consistently very slightly greater than 1.00. Possible sources for this small anomaly, including a minor breakdown of the model at small internuclear separations, where the "lengths" of the induced multipoles become significant compared to the internuclear separation R , are discussed herein.

High-quality *ab initio* curves (at the CCSD(T)/aug-cc-pV5Z level of theory) for all of the Rg complexes of the Au^+ ion have been calculated by T. G. Wright. These calculations have been extended to the basis set limit as part of the present study and this new, high-quality data provides an excellent opportunity to see if "chemical" attraction is required to explain the strong bonding observed for some of these complexes. In the present thesis, the Breckenridge model potential analysis¹ has been applied to the Ne, Ar, Kr and Xe interactions with Au^+ . These Au^+/Rg ionic complexes present a unique opportunity to examine the question of when "physical" attraction turns into "chemical" attraction in weakly-bound molecules.

9.2 Model potential

Breckenridge and coworkers have proposed the "long-range-forces" model potential for M^+-Rg species.¹ All the attractive terms out to R^{-8} are included in the potential, and the Born-Mayer repulsive term of the form Ae^{-bR} is used. This yields a model potential energy, $V(R)$, of the form:¹

$$V(R) = -\frac{\alpha_{RgD}Z^2}{2R^4} - \frac{C_6}{R^6} - \frac{\alpha_{RgQ}Z^2}{2R^6} + \frac{B_{Rg}Z^3}{R^7} - \frac{C_8}{R^8} - \frac{\alpha_{RgO}Z^2}{2R^8} - \frac{\gamma Z^4}{24R^8} + Ae^{-bR}$$

9(a)

Z is the "effective" charge on the M^+ ion and R is the internuclear distance. α_{RgD} , α_{RgQ} and α_{RgO} are the dipole, quadrupole and octopole polarisabilities of the Rg atom; B_{Rg} (which has a negative value) is the dipole–dipole–quadrupole hyperpolarisability of the Rg atom; γ is the higher-order second dipole hyperpolarisability of the Rg atom; and C_6 and C_8 are Z -independent coefficients representing the first (random-dipole/induced-dipole) and second (random-dipole/induced-quadrupole, random-quadrupole/induced-dipole) terms in the dispersion interaction. The higher-order B_{Rg} term is due to the dipole moment component induced on the Rg atom by the product of the electric field strength gradient and the electric field strength. The higher-order γ term is due to the dipole moment component on the Rg atom induced by the electric field strength cubed. The dispersion coefficients are calculated by (i) the Slater–Kirkwood approximation^{16,17} for the C_6 coefficients and (ii) a similar approximation derived by Koutselos and Mason¹⁸ for the C_8 coefficients. The model potential given in Equation 9(a) is valid at values of R that are large compared to molecular dimensions;^{19,20} at shorter distances, the potential becomes more approximate. By differentiating this model equation twice, two more equations are generated.¹ The

first-derivative equation (set to zero) locates the potential energy minimum, $-D_e$ (at R_e), and the second-derivative equation describes the curvature of the potential (related to ω_e) at R_e . If the R_e , D_e , and ω_e values of the particular state of the diatomic ion are known, or can be reliably estimated, then the three equations can be solved simultaneously to yield the effective charge, Z , and the two constants, A and b , which represent the repulsive term, Ae^{-bR} . (The three parameters R_e , D_e , ω_e were chosen¹ because they accurately describe the "depth" and "shape" of the potential curve near its minimum. They are also the most generally available spectroscopic parameters.) The main idea¹ of the Breckenridge model potential analysis is that if the model potential correctly describes the bonding (*i.e.* if the interaction is essentially purely "physical") then the derived Z value should be close to 1.00. On the other hand, if Z turns out to be substantially greater than 1.00, then the purely physical terms in the model potential are insufficient to explain the strength of the bonding and it is likely that "chemical" effects are present. For almost all cases studied in Reference 1 (except Au^+-Xe) Z was found to be close to 1.00 (1.00 ± 0.10) and this was taken to be evidence that the bonding in most well-characterised M^+-Rg complexes was essentially physical in nature.¹

The original version of the Breckenridge model potential¹ did not contain damping functions, which damp the purely long-range attractive forces at shorter ranges, where the electron clouds of the M^+ ion and the Rg atom interpenetrate. No attempt was made to include damping functions, because of simplicity in comparing many M^+/Rg diatomic complexes, and debate regarding their correct mathematical form.¹ Since the Tang-Toennies damping factors have been employed by many workers, the effect of including such damping functions, $f_n(R)$ has been examined in the present work. These have the form shown in Equation 9(b):

$$f_n(R) = 1 - \exp(-bR) \sum_{k=0}^n \frac{[bR]^k}{k!} \quad 9(b)$$

n is the modulus of the exponent of R in the long-range term that is to be damped, and b is taken to be the same value as that in the Born-Mayer repulsive term. These damping functions were incorporated into the model potential given in Equation 9(a) to give:

$$V(R) = -\frac{\alpha_{RgD} f_4 Z^2}{2R^4} - \frac{f_6 C_6}{R^6} - \frac{\alpha_{RgQ} f_6 Z^2}{2R^6} + \frac{B_{Rg} f_7 Z^3}{R^7} - \frac{f_8 C_8}{R^8} - \frac{\alpha_{RgO} f_8 Z^2}{2R^8} - \frac{\gamma f_8 Z^4}{24R^8} + Ae^{-bR} \quad 9(c)$$

The "damped" potential was differentiated once and twice (as for the "undamped" potential) and solved for A , b and Z .

For the Alk^+/Rg complexes, the values of α_{RgD} , α_{RgQ} , α_{RgO} , B_{Rg} , and γ_{Rg} are all reasonably well known from experiment or *ab initio* calculations.¹ Values of α_{Alk^+D} (the dipole polarisability of Alk^+), α_{Alk^+Q} (the quadrupole polarisability of Alk^+) and N (the effective number of outer-shell electrons) are required to calculate the C_6 and C_8 coefficients,^{1,16,18} and are accurately known.^{1,21} For the Au^+/Rg complexes, the values of α_{RgD} , α_{RgQ} , α_{RgO} , B_{Rg} , and γ_{Rg} are all reasonably well known¹ from experiment or *ab initio* calculations. N was taken¹ to be 10, α_{Au^+D} was taken to be¹ $1.74 \pm 0.10 \text{ \AA}^3$ and α_{Au^+Q} was estimated^{22,23} to be $2.8 \pm 0.5 \text{ \AA}^5$.

9.3 Results and discussion

9.3.1 Alk^+/Rg complexes

The values of Z , A and b derived by applying this model to the *ab initio* Alk^+/Rg potential curves are shown in Tables 9(I)–(V). (Note that there is not enough information about the necessary constants to perform the calculations for species involving Fr^+ and/or Rn .) The values were calculated by solving the three equations described above for A , b and Z using the MAPLE program.²⁴ Exact agreement was obtained with all the values reported previously,¹ except for Li^+-He where the values of Z , A and b in Reference 1 were listed incorrectly. As can be seen, the results for the value of Z are consistently slightly above 1.00 (1.02–1.09) and possible reasons for this will be discussed below. As in the previous work of Breckenridge *et al.*¹ it is concluded that the bonding in Alk^+/Rg complexes is essentially entirely physical in nature, with no additional "Lewis acid/base" or "metal–ion/ligand" type chemical interactions being required to explain the bonding.

The fitted model potentials for the lightest and heaviest systems (Li^+-He and Cs^+-Xe respectively) considered here are represented by the solid line curves in Figure 9(i), together with the *ab initio* data points for the potentials. The model potentials can be seen to agree extremely well with the *ab initio* data points over large ranges of the internuclear distances, from fairly large R all the way to R values on the inner walls of the potential curves substantially above the dissociation energy.

	A (cm ⁻¹)	b (Å ⁻¹)	Z
Li ⁺ -He	7.979×10^6 (4.419×10^6)	4.961 (4.772)	1.023 (1.030)
Li ⁺ -Ne	1.674×10^7 (1.020×10^7)	4.796 (4.651)	1.031 (1.036)
Li ⁺ -Ar	2.733×10^7 (1.163×10^7)	3.883 (3.652)	1.044 (1.058)
Li ⁺ -Kr	3.084×10^7 (1.059×10^7)	3.574 (3.294)	1.065 (1.087)
Li ⁺ -Xe	3.763×10^7 (1.106×10^7)	3.279 (2.976)	1.074 (1.102)

Table 9(I): values of A , b and Z for Li^+Rg calculated using the model potential analysis of Breckenridge et al.¹ with D_e , ω_e and R_e values determined from previous *ab initio* calculations.⁸⁻¹² Values in parentheses are obtained employing damping functions.

	A (cm ⁻¹)	b (Å ⁻¹)	Z
Na ⁺ -He	1.576×10^7 (1.262×10^7)	4.767 (4.715)	1.028 (1.030)
Na ⁺ -Ne	3.457×10^7 (2.866×10^7)	4.652 (4.612)	1.020 (1.020)
Na ⁺ -Ar	4.630×10^7 (3.322×10^7)	3.832 (3.764)	1.037 (1.039)
Na ⁺ -Kr	4.630×10^7 (2.994×10^7)	3.534 (3.445)	1.051 (1.055)
Na ⁺ -Xe	4.68×10^7 (2.66×10^7)	3.211 (3.100)	1.057 (1.064)

Table 9(II): values of A , b and Z for Na^+Rg calculated using the model potential analysis of Breckenridge et al.¹ with D_e , ω_e and R_e values determined from previous *ab initio* calculations.⁸⁻¹² Values in parentheses are obtained employing damping functions.

	A (cm ⁻¹)	b (Å ⁻¹)	Z
K ⁺ -He	1.828 × 10 ⁷ (1.528 × 10 ⁷)	4.202 (4.169)	1.061 (1.062)
K ⁺ -Ne	9.944 × 10 ⁷ (9.026 × 10 ⁷)	4.502 (4.485)	1.028 (1.028)
K ⁺ -Ar	1.002 × 10 ⁸ (8.466 × 10 ⁷)	3.751 (3.723)	1.041 (1.042)
K ⁺ -Kr	8.917 × 10 ⁷ (7.187 × 10 ⁷)	3.470 (3.435)	1.044 (1.045)
K ⁺ -Xe	8.859 × 10 ⁷ (6.824 × 10 ⁷)	3.185 (3.144)	1.047 (1.048)

Table 9(III): values of A , b and Z for K⁺-Rg calculated using the model potential analysis of Breckenridge *et al.*¹ with D_e , ω_e and R_e values determined from previous *ab initio* calculations.⁸⁻¹² Values in parentheses are obtained employing damping functions.

	A (cm ⁻¹)	b (Å ⁻¹)	Z
Rb ⁺ -He	2.200 × 10 ⁷ (1.896 × 10 ⁷)	4.019 (3.994)	1.076 (1.077)
Rb ⁺ -Ne	1.548 × 10 ⁸ (1.440 × 10 ⁸)	4.408 (4.397)	1.033 (1.033)
Rb ⁺ -Ar	1.751 × 10 ⁸ (1.562 × 10 ⁸)	3.762 (3.745)	1.042 (1.042)
Rb ⁺ -Kr	1.268 × 10 ⁸ (1.078 × 10 ⁸)	3.436 (3.412)	1.055 (1.056)
Rb ⁺ -Xe	1.270 × 10 ⁸ (1.046 × 10 ⁸)	3.179 (3.151)	1.054 (1.055)

Table 9(IV): values of A , b and Z for Rb⁺-Rg calculated using the model potential analysis of Breckenridge *et al.*¹ with D_e , ω_e and R_e values determined from previous *ab initio* calculations.⁸⁻¹² Values in parentheses are obtained employing damping functions.

	A (cm^{-1})	b (\AA^{-1})	Z
Cs ⁺ -He	2.456×10^7 (2.152×10^7)	3.789 (3.769)	1.086 (1.087)
Cs ⁺ -Ne	1.737×10^8 (1.626×10^8)	4.165 (4.156)	1.054 (1.054)
Cs ⁺ -Ar	1.977×10^8 (1.775×10^8)	3.614 (3.598)	1.060 (1.060)
Cs ⁺ -Kr	1.698×10^8 (1.479×10^8)	3.374 (3.355)	1.063 (1.064)
Cs ⁺ -Xe	2.025×10^8 (1.750×10^8)	3.185 (3.166)	1.058 (1.059)

Table 9(V): values of A , b and Z for Cs⁺-Rg calculated using the model potential analysis of Breckenridge *et al.*¹ with D_e , ω_e and R_e values determined from previous *ab initio* calculations.⁸⁻¹² Values in parentheses are obtained employing damping functions.

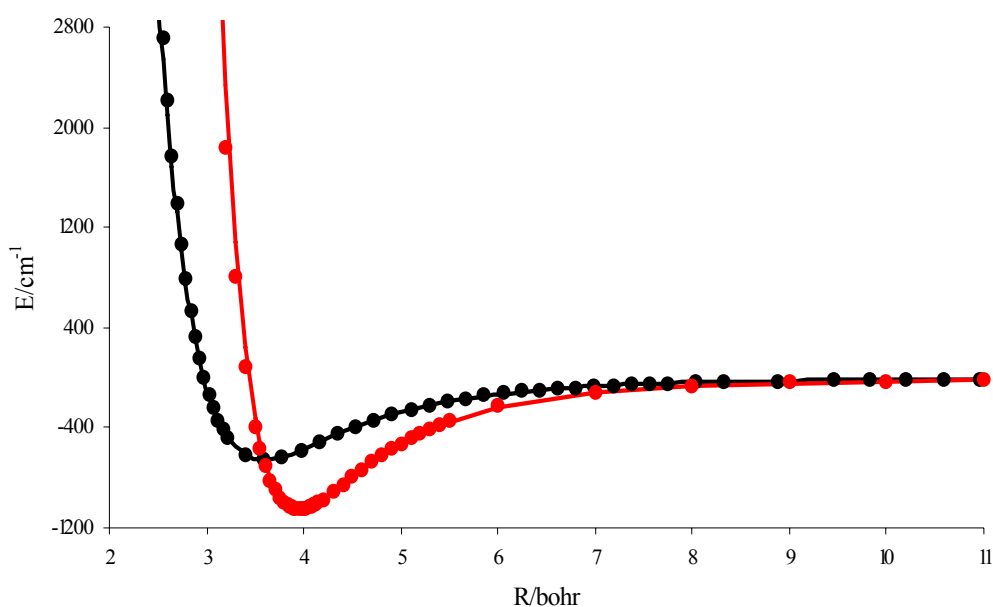


Figure 9(i): comparison of the fitted, undamped model potential (line) with the calculated *ab initio* points (data points) for Li⁺-He²⁵ (black curves) and Cs⁺-Xe¹² (red curves).

9.3.1.1 Damping functions

The values shown in Tables 9(I)–(V) in parentheses, are the values of A , b and Z obtained when damping functions are included in the model potential (see above). The effects are generally quite minor: the effective values of Z are seen to increase very slightly (the effect is largest for $\text{Li}^+\text{--Xe}$ and essentially negligible for the heavier Alk^+ ions). This may be rationalised by the fact that if the rapid, negative increase in the values of the R^{-n} terms is damped then (ignoring movement in the A and b values), Z needs to increase to account for this. In summary, the lack of damping functions cannot be the cause of the Z values being greater than 1.00.

9.3.1.2 *Ab initio* calculational inaccuracies

It is possible that errors in the calculated D_e , ω_e and R_e values lead to calculated Z values which are consistently larger than 1.00. This is unlikely however, given the excellent agreement between the results of the *ab initio* calculations used in the present study (performed by T.G. Wright) and those performed by others. For example, for $\text{Li}^+\text{--He}$ (for which the *ab initio* calculations should be most accurate), maximum errors of R_e , ω_e and D_e values for $\text{Li}^+\text{--He}$ are $\pm 0.002\text{\AA}$, $\pm 1\text{ cm}^{-1}$, and $\pm 5\text{ cm}^{-1}$ are found between the results of Wright *et al.*⁹ and Elford *et al.*²⁶ Using the extremes of these error limits in the direction that leads to the lowest Z value, the Z values decreased to 1.013 without damping and 1.020 with damping. Similarly for $\text{Li}^+\text{--Ne}$, using the extremes of the estimated error between the Wright values⁹ and an accurate high-level calculation by Røeggen and Skullerud²⁷ values of $Z = 1.012$ (1.016) without (with) damping were obtained. In conclusion, although errors in the *ab initio* calculation may lead to some lowering of the value of Z , they are not sufficient to lower Z to 1.00.

9.3.1.3 *Neglect of higher-order attractive terms in the model potential*

Adding higher-order terms in the attractive part of the model potential (R^{-9} , R^{-10} , etc.) will result in lower Z values, although the effects are not believed to be large enough to lower all the calculated Z values to 1.00 (or below). For example, it is known from the work of Bellert and Breckenridge (see Table 7 in Reference 1) that adding all three of the R^{-8} terms to the R^{-4} , R^{-6} and R^{-7} terms only lowers Z (no damping functions) from 1.05 to 1.04 for $\text{Na}^+\text{-Ar}$, and from 1.04 to 1.03 for $\text{Li}^+\text{-Ne}$. Adding higher terms should probably have even less effect. The lack of higher-order attractive terms in the model potential likely contributes to the Z values being slightly greater than 1.00, although is unlikely to explain the observation entirely.

9.3.1.4 *Errors in C_6*

In order to test whether the Slater–Kirkwood approximation may be leading to $Z > 1$, the value of Z was fixed to 1.00 and values of A , b and C_6 were calculated for $\text{Li}^+\text{-He}$. The value of C_6 obtained in this procedure was found to be unreasonable (1.2 atomic units undamped and 1.55 atomic units damped, compared with the accepted value of ~ 0.3 atomic units),²⁸ and arises as a result of a very small term trying to soak up a large difference. C_8 , or higher terms would be expected to give even more unphysical values. Thus, the Slater–Kirkwood approximation is reliable, as demonstrated by others,²⁹ and is not the cause of the high Z values.

9.3.1.5 *The form of the repulsion term*

One noteworthy weakness of the Born–Mayer potential is that it does not $\rightarrow \infty$ as $R \rightarrow 0$, but in fact tends to A . A more appropriate form of the repulsion term might therefore be $(A/R)\exp^{-bR}$ since then as $R \rightarrow 0$ the repulsion term does $\rightarrow \infty$. This

hypothesized form was tested on $\text{Li}^+\text{-He}$, although it was found to lead to slightly increased values of Z . If any effects due to A and b are ignored, then this may be understood as a form of damping (decreasing) the repulsive term at larger R values (owing to the A/R factor). It is likely that a repulsive potential term with more than two adjustable parameters is necessary to represent correctly the M^+/Rg repulsion all the way from larger R through R_e to smaller R . The form used herein cannot account fully for the increased values of Z , although it may possibly play some role. Although other more complicated forms of repulsion terms (usually containing more parameters) have been employed,^{30,31} they are not well suited to the simplicity of the present approach.

9.3.1.6 *Effects of polarisation of the outer-shell electron cloud of Rg towards Alk^+*

There have been substantial efforts over the years to understand the gas phase attractive interaction of M^+ ions with halogen X^- ions (isoelectronic with Rg atoms), using similar model potentials.^{32,33,34} However, any simple "long-range attraction" electrostatic model potential analysis is complicated by the short bond lengths of these strongly bound M^+X^- molecules, which can lead to severe electron-cloud polarisation and overlap. The earliest attempt at rationalizing such M^+/X^- interactions led to the Rittner potential³⁵ which had reasonable success, however, the Rittner model fails dramatically for the alkaline-earth halides: in the work of Törring *et al.*³⁶ it was postulated that this was due to the large polarisabilities of the alkaline-earth M^+ ions. Repulsion from the X^- ion led to the centre of the outer-shell electron charge being shifted away from the M^{2+} cationic core, such that its true distance from X^- was greater than R_e . In the present case, the distortion of the Rg atom's electronic cloud is described well by the model potential at long internuclear separations, when the lengths of the induced multipoles can be ignored compared to R . However, at shorter separations, the fact that one side of the multipole is closer to the M^+ nucleus than the

other must be considered. For example, the dominant R^{-4} term (see below for two pieces of evidence for this dominance) is derived¹⁹ assuming that a small dipole is induced on the Rg atom, with its centre exactly at the Rg nucleus. This is not strictly true, of course, since the polarisation of the Rg outer-shell electrons will actually begin to move the "centre" of the induced dipole towards the M^+ ion at short R . The R^{-4} term will break down, causing a somewhat stronger attraction than the simple R^{-4} term can describe. Qualitatively similar, but more complicated breakdowns will occur for the minor higher-order terms in the model potential at small R . A way of modelling this effect is to assume that the value of R to be used in the model potential is slightly shorter than the R_e value, and that the deviation (ΔR) of R from R_e at short values of R can be determined. A similar method was used by Törring and coworkers³⁶ where ΔR was found to have a strong correlation with the dipole moment of the alkaline-metal halides (the Törring model is also based on a dominant ion/induced-dipole term, after the ion/ion term in that case). If this idea is correct, and if the induced-dipole term is dominant, then the calculated dipole moments on the Rg atoms, induced by the M^+ ion, should be approximately proportional to ΔR , the shift in the Rg outer-shell electron cloud, multiplied by the "effective" number of outer-shell electrons in that cloud, which takes the value of N , used in the Slater–Kirkwood approximation. These values are 1.434, 4.45, 5.90, 6.70 and 7.79 for He–Xe.²¹

To calculate $\Delta R = R_e - R$, the shift necessary to reduce Z to 1.00, the three equations in the model potential analysis are solved simultaneously for b , A and R , with the value of Z fixed at 1.00. Calculated values of R_e , ΔR , $N \cdot \Delta R$, and induced dipole moments (μ_{ind}) are shown in Table 9(VI).

A graph of μ vs. $N \cdot \Delta R$ is shown in Figure 9(ii) and reveals a strong, positive correlation between μ_{ind} and $N \cdot \Delta R$.

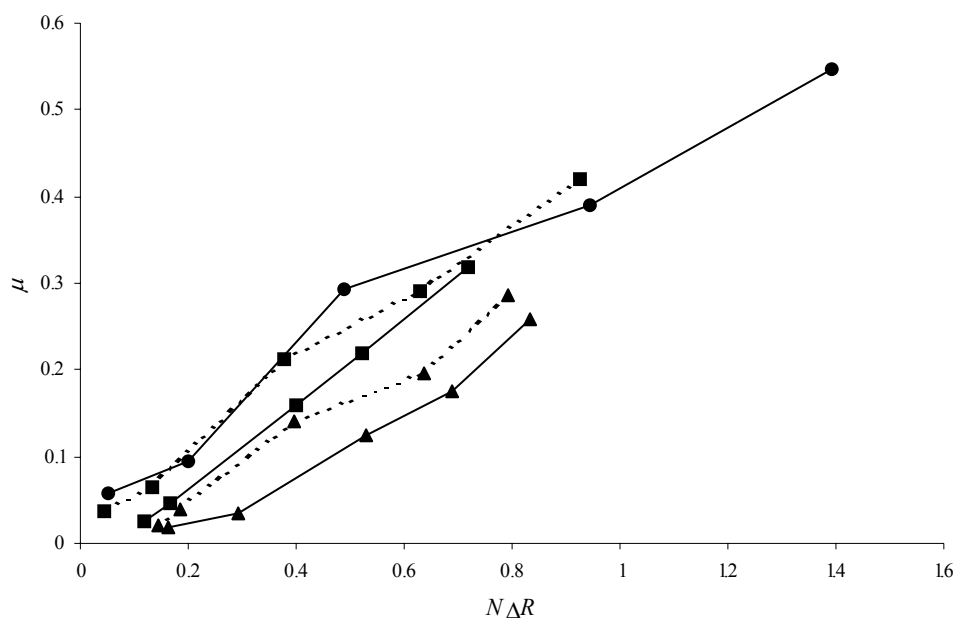


Figure 9(ii): plot of the induced-dipole on the Rg atom (μ_{ind}) against $N \cdot \Delta R$ for Li^+ -Rg (solid line and circles); Na^+ -Rg (dashed line with squares); K^+ -Rg (solid lines and diamonds); Rb^+ -Rg (dashed line with triangles); Cs^+ -Rg (solid line with triangles).

Species	R_e (Å)	ΔR (Å)	$N \cdot \Delta R$ (Å)	μ_{ind} (Å e)
Li ⁺ -He	1.896	0.027 (0.037)	(0.053)	0.0570
Li ⁺ -Ne	2.038	0.036 (0.045)	(0.200)	0.0953
Li ⁺ -Ar	2.364	0.055 (0.083)	(0.490)	0.293
Li ⁺ -Kr	2.520	0.092 (0.141)	(0.945)	0.391
Li ⁺ -Xe	2.716	0.109 (0.179)	(1.394)	0.548
Na ⁺ -He	2.324	0.031 (0.033)	(0.044)	0.0380
Na ⁺ -Ne	2.472	0.028 (0.030)	(0.134)	0.0648
Na ⁺ -Ar	2.780	0.059 (0.064)	(0.378)	0.212
Na ⁺ -Kr	2.920	0.084 (0.094)	(0.630)	0.291
Na ⁺ -Xe	3.104	0.101 (0.119)	(0.927)	0.419
K ⁺ -He	2.825	0.079 (0.083)	(0.119)	0.0257
K ⁺ -Ne	2.921	0.036 (0.037)	(0.165)	0.0464
K ⁺ -Ar	3.215	0.066 (0.068)	(0.401)	0.159
K ⁺ -Kr	3.356	0.075 (0.078)	(0.523)	0.220
K ⁺ -Xe	3.558	0.087 (0.092)	(0.717)	0.319
Rb ⁺ -He	3.070	0.098 (0.100)	(0.143)	0.0217
Rb ⁺ -Ne	3.140	0.041 (0.042)	(0.187)	0.0402
Rb ⁺ -Ar	3.425	0.066 (0.067)	(0.395)	0.140
Rb ⁺ -Kr	3.560	0.093 (0.095)	(0.637)	0.196
Rb ⁺ -Xe	3.750	0.099 (0.102)	(0.794)	0.287
Cs ⁺ -He	3.360	0.111 (0.113)	(0.162)	0.0182
Cs ⁺ -Ne	3.400	0.066 (0.066)	(0.294)	0.0343
Cs ⁺ -Ar	3.640	0.090 (0.090)	(0.531)	0.124
Cs ⁺ -Kr	3.760	0.102 (0.103)	(0.690)	0.175
Cs ⁺ -Xe	3.950	0.104 (0.107)	(0.834)	0.258

Table 9(VI): calculated values of R_e , ΔR , $N \cdot \Delta R$, and induced dipole moments (μ_{ind}) for the Alk^+/Rg species. Damped values are shown in parentheses. The induced-dipole

moments are calculated using: $\mu(\text{Å}e) = \frac{\alpha_{RgD}(\text{Å}^3) \cdot e}{(R_e(\text{Å}))^2}$ where e is the unit charge.

This is good evidence that the ion/induced-dipole term is dominant, and offers an explanation for the calculated Z values being slightly greater than 1.00 in all the Alk^+/Rg complexes. The increased Z values arise in part, as a result of the simple model potential treating the induced "dipoles" on the Rg atoms as being infinitely small "points" centred exactly at the Rg nuclei. This assumption is only valid at very large R , and at short R there is a finite shift of Rg electronic density toward the Alk^+ ions, resulting in an increased calculated effective charge on M^+ . As a further check that the R^{-4} ion/induced-dipole term is dominant the following calculation was performed for Li^+-He . The three model equations were solved fixing " R " at R_e for all attractive terms except the R^{-4} term, and fixing Z at 1.00. The value of R derived when R for *all* the terms in the model potential were allowed to vary (with Z fixed at 1.00) was found to be only 0.007 Å different from the R value determined from the R^{-4} term only. The R^{-4} term largely determines the R value, showing definitively that the R^{-4} term is completely dominant for the Alk^+/Rg complexes.

There are definite trends in the ΔR values shown in Table 9(VI). For the Li^+-Rg species ΔR increases with Rg: as Rg gets bigger, it gets more polarisable and so the centre of charge moves towards Li^+ leading to a larger ΔR value. Interestingly, for the other Alk^+ ions this trend is followed for Ne through Xe, but not for He, where there is a decrease on going from He to Ne. That is, the ΔR value is much greater than expected for Alk^+-He species. Similar anomalies for helium-containing species have been noted previously,¹ and for some cases have been attributed to the lack of p electrons on He.¹ There are no $p\pi-p\pi$ (or $p\sigma-p\sigma$) repulsive interactions in these species, whereas such repulsive interactions are present in all of the other Rg species. Thus He effectively has the ability to get closer to Alk^+ than other Rg atoms. The difference between R_e values for Alk^+-Ne and Alk^+-He complexes are: Li^+ (0.14 Å), Na^+ (0.15 Å), K^+ (0.09 Å), Rb^+ (0.07 Å), Cs^+ (0.04 Å), Fr^+ (0.02 Å). Thus He appears

to be less able to "penetrate" into the larger p -electron outer shells of K^+ through Fr^+ than Ne (which is actually not that much "larger" than He). Considering the Alk^+-He variation: as Alk^+ increases ΔR increases, but this trend is not consistent across the series, as the ΔR values for the other Alk^+-Rg systems show for each of the other Rg atoms: this probably indicates that several factors play a role. One possibility is that the simple Born–Mayer repulsive potential is not sufficiently flexible to represent this unusual "penetration" of the larger $Alk^+ p$ -shells by the He atom, and the best-fit of the three equations then causes the fitted value of Z to rise.

9.3.2 Au^+/Rg complexes

The results of applying this model potential analysis to the R_e , ω_e and D_e values obtained from the Au^+-Rg potential curves (calculated by T. G. Wright at the CCSD(T) level of theory using the basis sets aug-cc-pVQZ and aug-cc-pV5Z, employing small-core effective core potentials ECPs for Kr, Xe and Au) are given in Table 9(VII).

The values were calculated by solving the three equations, noted above, for Z , A , and b employing the MAPLE program. The values in parentheses are the values of A , b , and Z obtained when damping functions are included; the effects on Z of "damping" are quite minor for these complexes ($< 4\%$ change). Based on the results for the Alk^+-Rg complexes, it is suggested that if the derived model potential Z value is above 1.10 then "extra" Lewis-base chemical contributions to M^+-Rg bonding should be considered. As can be seen from Table 9(VII), the derived Z value for Au^+-Ne is below 1.10, consistent with only "physical" bonding. This might be expected for such an unlikely "ligand" as Ne, which has a very high ionisation potential of 21.6 eV (compared to 15.8 eV, 14.0 eV and 12.1 eV for Ar, Kr and Xe). For the other three

rare gases, however, Z is well above 1.10, rising in the sequence $\text{Ar} < \text{Kr} < \text{Xe}$, and is especially high for Au^+-Kr and Au^+-Xe . One possible "physical" reason for Z being so high for the Au^+-Ar , Au^+-Kr and Au^+-Xe cases is that higher-order attractive R^{-n} terms with $n > 8$ are still important. Shown in Table 9(VIII) are the effects on Z of successively deleting higher terms in the model potential.

	A (cm^{-1})	b (\AA^{-1})	Z
Au^+-Ne	9.39×10^7 (7.17×10^7)	4.49 (4.44)	1.08 (1.08)
Au^+-Ar	1.90×10^8 (9.93×10^7)	4.24 (4.08)	1.23 (1.24)
Au^+-Kr	2.52×10^8 (1.13×10^8)	4.08 (3.88)	1.32 (1.33)
Au^+-Xe	2.56×10^8 (9.54×10^7)	3.76 (3.51)	1.44 (1.47)

Table 9(VII): values of A , b and Z calculated by applying the undamped model potential analysis to the R_e , ω_e and D_e values calculated by T. G. Wright. Values shown in parentheses are obtained by incorporating damping functions into the model potential.

There is a large effect from the addition of the R^{-6} terms to the ion/induced-dipole term; addition of the R^{-7} and R^{-8} terms has a smaller effect. Although the addition of higher-order terms beyond R^{-8} to the model potential will probably decrease Z slightly, the decrease will not be to "physical" values below 1.10. Additionally, the inclusion of damping factors, which increases Z by decreasing the magnitude of the attractive terms will become more important as n increases beyond $n = 8$. The high effective values of Z obtained from the model potential analysis in this work, suggests the possibility that increasing "chemical" ligand effects are present for the Ar, Kr and Xe complexes of Au^+ .

	Au ⁺ -Ne	Au ⁺ -Ar	Au ⁺ -Kr	Au ⁺ -Xe
All terms included	1.08 (1.08)	1.23 (1.24)	1.32 (1.33)	1.44 (1.47)
Delete all R^8 terms	1.16 (1.16)	1.32 (1.32)	1.41 (1.42)	1.52 (1.53)
Delete all R^8, R^7 terms	1.17 (1.18)	1.36 (1.36)	1.47 (1.47)	1.60 (1.60)
Delete all $R^8, R^7,$ R^6 terms	1.40 (1.40)	1.57 (1.57)	1.68 (1.68)	1.81 (1.81)

Table 9(VIII): *effects on Z of successively deleting all but the R^4 terms in the model potential. Damped values are shown in parentheses.*

To provide further evidence for the emergence of chemical bonding in the Au⁺-Rg complexes, a natural bond order (NBO) analysis³⁷ was performed by T.G. Wright and others and the *ab initio* electron density near the R_e values of these complexes was examined to see if there is mixing of atomic orbitals, indicating the beginnings of "chemical" bond formation. Briefly, these analyses gave clear evidence that there is significant sharing of electron density between the Au⁺ and Rg centres for Rg = Kr and Xe, and thus that chemical bonding is occurring (the partial charges of Au^{+0.88}-Kr^{+0.12} and Au^{+0.79}-Xe^{+0.21} were calculated, compared with charges of Au^{+0.96}-Ne^{+0.04} and Au^{+0.94}-Ar^{+0.06} for the two lighter species). The main mode of electron density transfer was found to be from a filled $p\sigma$ orbital on the rare gas into the $6s\sigma$ orbital (LUMO) on the metal centre. A small amount of back bonding was identified, which increases monotonically from Au⁺-Ne to Au⁺-Xe, from the $5d_{z^2}$ σ orbital of Au⁺.

The conclusion from the above model potential analyses and the NBO analyses is that $\text{Au}^+\text{-Ne}$ can be described as a "physically-bound" complex, with the R^4 , R^6 , R^7 and R^8 terms being able to rationalise the bonding. (The natural bond order (NBO) analysis of the $\text{Au}^+\text{-Ne}$ *ab initio* wavefunctions showed the charge on Au^+ to be very close to 1.00). The dispersion terms (R^6 , R^8) play an important role in the bonding of Ne to Au^+ , because of the moderate polarisability of the $\text{Au}^+(5d^{10})$ outer shell of electrons. This is in contrast to the alkali metal ion/Ne complexes, where the leading ion/induced-dipole R^4 terms dominate. For example, $\text{Na}^+\text{-Ne}$ has a D_e value of 514 cm^{-1} , which is comparable to that of $\text{Au}^+\text{-Ne}$ (619 cm^{-1}). This is despite having a lower R_e value (2.47 \AA vs. 2.692 \AA for $\text{Au}^+\text{-Ne}$). However, in contrast to $\text{Au}^+\text{-Ne}$, where the effective Z value drops from 1.44 to 1.08 when the R^6 , R^7 and R^8 terms in the model potential are added to the R^4 term, the Z value for $\text{Na}^+\text{-Ne}$ only drops from 1.11 to 1.02. This is similar to the cases of $\text{Mg}^+\text{-Ar}$ vs. $\text{Na}^+\text{-Ar}$ discussed in Reference 1, where the R_e and D_e values are both quite similar, but for $\text{Na}^+\text{-Ar}$, the R^4 term contributes 71% of the bonding energy, while for $\text{Mg}^+\text{-Ar}$, the R^4 term contributes only 41%, mostly because of the large dispersion terms.

For $\text{Au}^+\text{-Ar}$, $\text{Au}^+\text{-Kr}$ and $\text{Au}^+\text{-Xe}$, the effective Z values show that "physical" bonding cannot account for the large bond energies calculated by T. G. Wright for the $\text{Au}^+\text{-Kr}$ and $\text{Au}^+\text{-Xe}$ complexes (6489 cm^{-1} and 10529 cm^{-1} respectively), consistent with there being "chemical" contributions to the $\text{Au}^+\text{-Kr}$ and $\text{Au}^+\text{-Xe}$ interactions. The bonding in the $\text{Au}^+\text{-Ar}$ complex lies on the borderline between the "physical" $\text{Au}^+\text{-Ne}$ complex and the increasingly "chemical" heavier $\text{Au}^+\text{-Rg}$ complexes. The NBO analyses reveal that the $\text{Au}^+\text{-Xe}$ and $\text{Au}^+\text{-Kr}$ chemical bonds mostly result from donation of $p\sigma$ electron density on the Rg atom to the empty, low-lying $\text{Au}^+(6s)$ orbital.

9.4 Conclusions

The model potential put forward recently by Breckenridge and coworkers¹ for M^+/Rg bonding has been considered in more detail, by applying the analysis to the filled-shell/filled-shell alkali metal cation/rare gas atom interaction. The interaction in these complexes is expected to be entirely physical and should therefore be well-described by the "long-range forces" model of Breckenridge *et al.*,¹ which incorporates all the attractive dispersion and induction terms out to R^{-8} . The effective charge on the metal cation calculated using this analysis was found to be consistently slightly greater than 1.00 for all the Rg systems studied, which is surprising since the Alk^+/Rg complexes are expected to be little influenced by "chemical" effects which could lead to higher "effective" values of Z to reproduce the higher D_e values.

The inclusion of damping factors, which dampen the long-range terms at short R where the Alk^+ and Rg atom electron clouds interpenetrate, was first considered, although this was found to lead to a slight increase in Z . Errors in the *ab initio* calculations were also considered. However, even when the analysis was repeated on the Li^+-He and Li^+-Ne systems using R_e , ω_e and D_e values which assumed the extremes of the error limits (operating in the direction which would act to decrease Z), Z was still found to be greater than 1.00. It is possible that errors in the *ab initio* calculations may cause a slight increase in the derived values of Z , although it is certainly not the only factor. The omission of higher terms (R^{-9} , R^{-10}) in the model potential was also ruled out as the cause of the increased Z values, and although their inclusion may lead to a slight decrease in Z it would not be sufficient to reduce Z to a more "physical" value of 1.00. The values of C_6 and C_8 were also ruled out as the cause of $Z > 1$. The Born-Mayer form of the repulsive potential was also considered as a possible cause for the increased values of Z . It was concluded that the inflexibility of the two-parameter repulsive term used herein could possibly play some role, and in

order to represent the M^+/Rg repulsive interaction correctly, from larger R through R_e to smaller R , a more complicated form of the repulsive term (containing more than two adjustable parameters) may be necessary. Based upon the simplicity of the current model potential, the Born-Meyer repulsive term is appropriate. Finally, the effect of the minor distortion of the Rg atom electron cloud was investigated. As a result of the Rg atom electron cloud becoming polarised towards Alk^+ during the interaction, the length of the induced multipoles become significant compared to the internuclear separation, resulting in the model potential breaking down at short R . By fixing $Z = 1.00$ and calculating the resulting "effective" separation of the M^+ ion point charge and the "centres" of the induced (and random) multipoles on the Rg atom, it was shown that there was indeed a strong correlation between the induced dipole and the product of the effective number of oscillating electrons and the shift in R . This suggests that one possible reason that the values of Z are slightly greater than 1.00 is due to this polarisation effect. In general, however, the model potential is still quite successful in semi-quantitatively describing the bonding in these M^+/Rg complexes as being "physical" in nature. Based on the results for the Alk^+-Rg complexes, it was concluded that if the derived model potential Z value is above 1.10 then "extra" Lewis-base chemical contributions to M^+-Rg bonding should be considered.

From the application of the model potential analysis to the Au^+-Rg complexes ($Rg = Ne, Ar, Kr$ and Xe), and NBO analyses (performed by T. G. Wright and others) of the charge distributions in these complexes, it is concluded that "physical" bonding is sufficient to explain the bonding in Au^+-Ne , but that increasingly larger amounts of "chemical" bonding is required to explain the larger bond energies along the series Au^+-Ar , Au^+-Kr and Au^+-Xe . For Au^+-Kr and Au^+-Xe , both the model potential analysis and the NBO results, indicate that a partial chemical bond is formed. For Au^+-Ar , although the model potential analysis yields a Z value > 1.2 , the effect of higher-order terms may bring this below 1.10. For Au^+-Ne , there is no strong

evidence of chemical bonding. These results are quite consistent with those of Pyykkö and coworkers,^{13,15} who suggested that the particularly strong bonding in Au⁺-Xe diatomic ion could have a major chemical component.

9.5 Future work

It would be desirable to have experimental measurements of the bond distances and bond strengths of all of the Au⁺-Rg complexes to compare with the very high level *ab initio* calculated values used in the model potential analysis of the bonding. An accurate determination of these values can be achieved by employing zero electron kinetic energy (ZEKE) spectroscopy (as used to study the vibrational modes of *para*-fluorotoluene – see Chapter 7). Recent efforts have been made to initiate a ZEKE spectroscopic study of the Au⁺-Rg complexes. In order to investigate these complexes, they must first be prepared in the gas phase. This required the design and utilisation of a laser vaporisation (LaVa) source. A solid Au rod was housed within a PEEK construct, surrounded by a stainless-steel jacket, through which liquid nitrogen is passed in order to cool the plume of Au atoms and ions ejected from the Au rod as a result of laser ablation. The Au rod is rotated and translated slowly by a small 4-phase stepper-motor to ensure a fresh area of the rod is continually ablated. The LaVa source is connected to the high vacuum side of the pulsed valve and ablated Au atoms and ions are picked up by the rare gas of interest (Ar held at 7–9 bar, or Kr or Xe seeded in Ar) as it passes over the surface of the rod. Ablated Au atoms undergo collisional cooling in a narrow channel lying beyond the Au rod. In order to further cool the ablated Au atoms, a liquid nitrogen cooling jacket and reservoir was designed and utilised. Au-Rg complexes are formed as the resulting gas mix expands into the vacuum. The resulting free-jet expansion passes to the extraction region of a time-of-flight mass spectrometer where it is intersected by the frequency-doubled output of a dye laser (Sirah Cobra Stretch). This first dye laser was used to perform a series of (1

+ 1) REMPI experiments, probing the $^2\Pi$ and $^2\Sigma^+$ states of the Au–Ar, Au–Kr and Au–Xe complexes, which correspond to the strong atomic transition Au ($6p \leftarrow 6s$). The results of these experiments on the Au–Ar complex have been presented in a recent publication.³⁸ The observation of the $^2\Pi$ and $^2\Sigma^+$ states of the neutral Au–Ar, Au–Kr and Au–Xe complexes is the first step to performing a ZEKE spectroscopic study, in which the spectroscopic constants of the cationic complexes can be determined.

9.6 References

- ¹ D. Bellert, W.H. Breckenridge, *Chem. Rev.* **102** (2002) 1595.
- ² S. Massick, W.H. Breckenridge, *Chem. Phys. Lett.* **257** (1996) 465.
- ³ J.G. Kaup, W.H. Breckenridge, *J. Chem. Phys.* **107** (1997) 2180.
- ⁴ J.G. Kaup, W.H. Breckenridge, *J. Chem. Phys.* **107** (1997) 4451.
- ⁵ E. Qing, L.A. Viehland, E.P.F. Lee, T.G. Wright, *J. Chem. Phys.* **124** (2006) 44316.
- ⁶ A.W.K. Leung, D. Bellert, R.R. Julian, W.H. Breckenridge, *J. Chem. Phys.* **110** (1999) 6298.
- ⁷ K.L. Burns, D. Bellert, A.W.K. Leung, W.H. Breckenridge, *J. Chem. Phys.* **114** (2001) 2996.
- ⁸ P. Soldán, E.P.F. Lee, T.G. Wright, *Mol. Phys.* **97** (1999) 139.

- ⁹ J. Lozeille, E. Winata, L.A. Viehland, P. Soldán, E.P.F. Lee, T.G. Wright, *Phys. Chem. Chem. Phys.* **4** (2002) 3601.
- ¹⁰ J. Lozeille, E. Winata, L.A. Viehland, P. Soldán, E.P.F. Lee, T.G. Wright, *J. Chem. Phys.* **119** (2003) 3729.
- ¹¹ L.A. Viehland, J. Lozeille, P. Soldán, E.P.F. Lee, T.G. Wright, *J. Chem. Phys.* **121** (2004) 341.
- ¹² H.L. Hickling, L.A. Viehland, D.T. Shepherd, P. Soldán, E.P.F. Lee, T.G. Wright, *Phys. Chem. Chem. Phys.* **6** (2004) 4233.
- ¹³ P. Pyykkö, *J. Am. Chem. Soc.* **117** (1995) 2067.
- ¹⁴ J.P. Read, A.D. Buckingham, *J. Am. Chem. Soc.* **119** (1997) 9010.
- ¹⁵ D. Schröder, H. Schwarz, J. Hrusak, P. Pyykkö, *Inorg. Chem.* **37** (1998) 624.
- ¹⁶ J.C. Slater, J.G. Kirkwood, *Phys. Rev.* **37** (1931) 682.
- ¹⁷ H.L. Cramer, D.L. Herschbach, *J. Chem. Phys.* **53** (1970) 2792.
- ¹⁸ A.D. Koutselos, E.A. Mason, *J. Chem. Phys.* **85** (1986) 2154.
- ¹⁹ R.S. Berry, S.A. Rice, J. Ross, *Physical Chemistry*, Wiley, New York, 1980, p. 408.
- ²⁰ A.D. Buckingham, *Adv. Chem. Phys.* **12** (1967) 107.

- ²¹ A.D. Koutselos, E.A. Mason, L.A. Viehland, *J. Chem. Phys.* **93** (1990) 7125.
- ²² M.V.K Sastri, P.L. Narasimhulu, K.D. Sen, *J. Chem. Phys.* **80** (1984) 584.
- ²³ E.A. Gislason, M.S. Rajan, *Chem. Phys. Lett.* **50** (1977) 25.
- ²⁴ MAPLE 10, MapleSoft, Waterloo, Ontario, Canada.
- ²⁵ P. Soldán, E.P.F. Lee, J. Lozeille, J.N. Murrell, T.G. Wright, *Chem. Phys. Lett.* **343** (2001) 429.
- ²⁶ M.T. Elford, I. Røeggen, H.R. Skullerud, *J. Phys. B* **32** (1999) 1873.
- ²⁷ I. Røeggen, H.R. Skullerud, *J. Phys. B* **25** (1992) 1795.
- ²⁸ R.J. Wheatley, W.J. Meath, *Chem. Phys.* **179** (1994) 341.
- ²⁹ R. Cambi, D. Cappelletti, G. Liuti, F. Pirani, *J. Chem. Phys.* **95** (1991) 1852.
- ³⁰ A.J. Stone, *The Theory of Intermolecular Interactions*, Clarendon Press, Oxford, 1996.
- ³¹ E.F. Archibong, C.-H. Hu, A.J. Thakkar, *J. Chem. Phys.* **109** (1998) 3072.
- ³² Y.P. Varshni, R.C. Shukla, *J. Mol. Spectrosc.* **16** (1965) 63
- ³³ R.L. Redington, *J. Phys. Chem.* **74** (1970) 181.

³⁴ M. Karplus, R.N. Porter, *Atoms and Molecules*, Benjamin, New York 1970.

³⁵ E.S. Rittner, *J. Chem. Phys.* **19** (1951) 1030.

³⁶ T. Törring, W.E. Ernst, S. Kindt, *J. Chem. Phys.* **81** (1984) 4614.

³⁷ J. E. Carpenter, F. Weinhold, *J. Molec. Struct. (Theochem)* **169** (1988) 41.

³⁸ R.J. Plowright, V.L. Ayles, M.J. Watkins, A.M. Gardner, R.R. Wright, T.G. Wright, W.H. Breckenridge, *J. Chem. Phys.* **127** (2007) 204308.